GRAIN GROWTH RATE TRANSITIONS IN BARIUM STRONTIUM TITANATE

by

Matthew J. Michie

A Dissertation

Submitted to the Faculty of Purdue University

In Partial Fulfillment of the Requirements for the degree of

Doctor of Philosophy

School of Materials Engineering

West Lafayette, Indiana

August 2019

THE PURDUE UNIVERSITY GRADUATE SCHOOL

STATEMENT OF COMMITTEE APPROVAL

Dr. John Blendell, Co-Chair
Department of Materials Engineering
Dr. Carol Handwerker, Co-Chair
Department of Materials Engineering
Dr. Eric Kvam
Department of Materials Engineering
Dr. Wolfgang Rheinheimer
Department of Materials Engineering
Dr. Fu Zhao
Department of Mechanical Engineering

Approved by:

Dr. David Bahr
Head of the Graduate Program

To Him who has many names.

"Merest breath...
All is mere breath
for writing books is endless,
and much study wears you out...
Here now is my final conclusion:
Fear God and obey his commands,
for this is everyone's duty.
God will judge us for everything we do,
including every secret thing,
whether good or bad."
Ecclesiastes 12: 8,12-13

ACKNOWLEDGMENTS

I would like to acknowledge my advisors and mentors John Blendell, Carol Handwerker and Wolfgang Rheinheimer for all of the support, patience and encouragement you have given me during my time at Purdue, you have helped me to develop into a better researcher as well as a better man. I would also like to acknowledge my wife and family who have provided endless support and encouragement along the way. Finally, I would like to gratefully acknowledges the support of the NSF Purdue-Tuskegee IGERT program: Global Traineeship in Sustainable Electronics (DGE Grant #1144843) for this research.

TABLE OF CONTENTS

LIST OF TABLES

LIST OF FIGURES

ABSTRACT

Author: Michie, Matthew, J. PhD
Institution: Purdue University
Degree Received: August 2019
Title: Grain Growth Rate Transitions in Barium Strontium Titanate
Committee Chair: John Blendell, Carol Handwerker

Understanding grain growth in dielectric ceramics is essential to controlling the electrical and mechanical properties necessary to produce ceramic capacitors and sensors. The effect of alloying barium titanate with strontium titanate on the equilibrium crystal shape was investigated in order to determine possible impacts on grain growth. The equilibrium crystal shape was studied through three experimental methods to identify possible changes in grain boundary energy or anisotropy with changing composition.

The first method was by imaging intergranular pores to observe faceting behavior and relative interfacial energies. Intergranular pores were reconstructed to determine the relative surface energies of the identified facets. The second method was to perform atomic force microscopy on surface facets to collect topography data. The topography data was combined with orientation data obtained by EBSD analysis from the same region, and used to calculate the normal vector of the surface facets. These datasets were plotted in a stereographic projection to study the faceting anisotropy. The third method involved collecting EBSD orientation data and images of surface faceting behavior. The surface faceting behavior of each grain was categorized by type of facet and plotted on a stereographic projection at the corresponding orientation. This allowed for the analysis of faceting transitions and the differentiation of faceted and continuous regions of the equilibrium crystal shape. The analysis of faceting behavior across compositions has implications on grain growth of the barium titanate/strontium titanate system.

1. INTRODUCTION

A dielectric ceramic is an electrical insulator that becomes polarized when an electric field is applied.[1] One of the most common applications for these materials is that of the multi-layer ceramic capacitor (MLCC). In 2017, the global ceramic capacitor market was valued at $6.128 billion USD and is expected to reach $9.167 billion USD by 2023.[2] As the electronics industry continues to grow, there is increasing pressure to make MLCCs smaller and to more precisely control the electrical properties of the capacitor. Section 1 will discuss how the properties of a ceramic are strongly influenced by the microstructure of the material. The motivation of this work is to better understand grain growth of dielectric ceramics and how one can influence the grain growth behavior. This information will aid in the manufacturing of new products and allow for better optimization of existing products.

This document presents a literary review of past works relating to the study of the equilibrium crystal shape of ceramic materials and its impact on grain growth, along with contributing new content. This first section covers the fundamentals of ceramic materials with an emphasis on grain growth and equilibrium crystal shapes, as well as discussing the interlink between these two concepts. Section 2 will discuss the selection of the barium strontium titanate ($BaSrTiO_3$) system as well as a literary review of the individual components barium titanate ($BaTiO_3$) and strontium titanate ($SrTiO_3$) that make up the $BaSrTiO_3$ system. Section 3 will discuss the processing techniques used to produce the samples used in this study. Section 4 will present and discuss the work relating to equilibrated pore shapes. This section will also cover the process used to obtain micrographs of intergranular pores, the 3D reconstruction methods used, and a discussion of the results. Section 5 will discuss experiments performing atomic force microscopy (AFM) of surface facets and discuss the results. Section 6 will discuss additional surface faceting

experiments that combine surface faceting type with electron backscatter diffraction (EBSD). Section 7 will discuss the results and conclusions when combining the data discussed in sections 4-6. Finally, Section 8 will discuss an environmental comparative analysis of $BaTiO_3$ and $SrTiO_3$ to assess the environmental impact of altering the composition of a tunable dielectric device.

1.1 Fundamentals of Ceramics

1.1.1 Basics of Ceramics

Ceramics are a material class of inorganic, nonmetallic compounds with a vast range of properties and structures.[3] Traditional ceramics have the defining properties of being hard, brittle, low thermal expansion, and high melting temperature; however, there are many ceramic materials that can vary from these traits. The work discussed in this paper will focus specifically on perovskite materials. The term perovskite is commonly used to refer to the mineral $CaTiO_3$, discovered by Count Perovskite in the 19th century; however, in this document the term will be referring to the general perovskite structure, ABX_3 where A and B are different cations and X is an anion.[1] The perovskite structure can exist in the cubic, tetragonal and orthorhombic as, shown in Figure 1.1, depending on the temperature and relative ion size.

The motivation for materials research revolves around the drive to create new materials that are better suited for an intended application. In order to change the properties of a material, one must understand the connection between the structure of the material, the properties of the material, and how the material is processed. This interconnection is commonly visualized in the triangle of Material Science, shown in Figure 1.2. This document aims to address all three of these concepts and how when experimentally changing one leg of this triangle will affect the others.

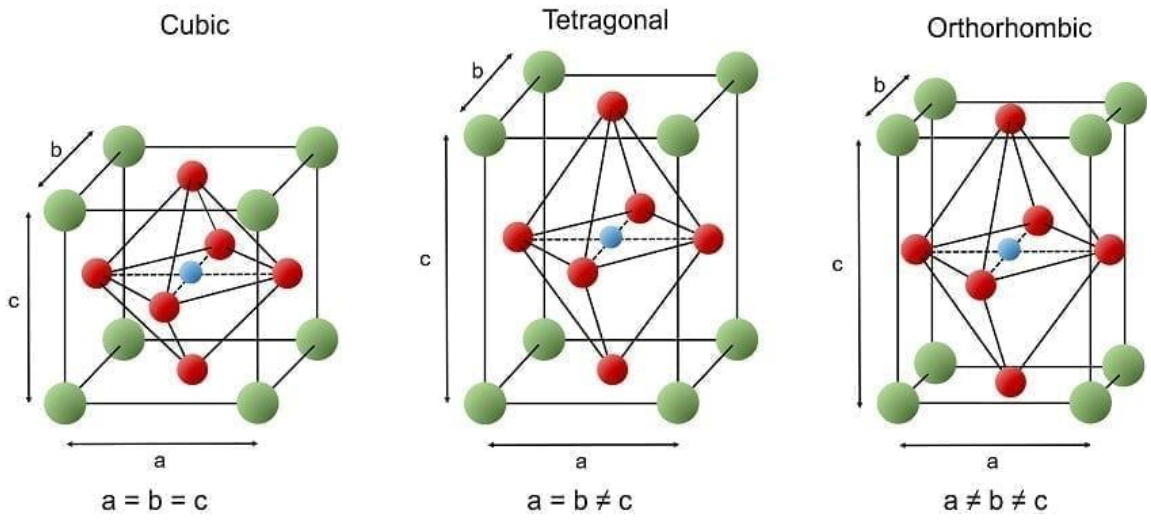

Figure 1.1: The three forms of the perovskite crystal structure.[4]

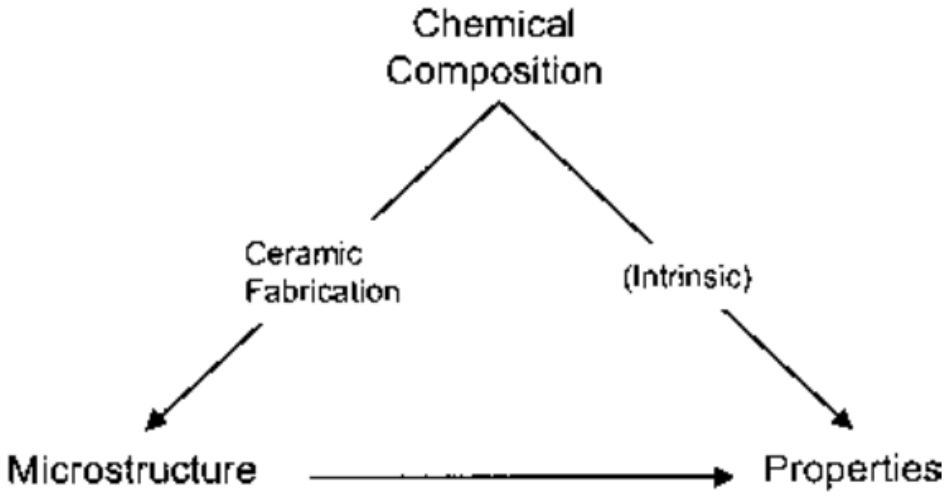

Figure 1.2: The triangle of material science representing the interaction between composition, microstructure and properties.[5]

1.1.2 Solid-State Sintering

Sintering is the process of firing and consolidating a body from powder particles.[3] This process occurs due to the driving force to reduce the interfacial energy of the system.[1] Sintering can be broken down into two components, coarsening and densification. Coarsening is

the process of reducing the total surface area by increasing the size of the particles. Densification is the removal of pores and solid-vapor interfaces to create new grain boundaries with lower interfacial energies. Both processes work by reducing the total interfacial energy of the system. These two processes are visualized in Figure 1.3. This relationship can also be represented in terms of the specific interfacial energy multiplied by the surface area which represents the total interfacial energy. More specifically, coarsening would be a change in surface area, with a constant specific interfacial energy and densification would include changing the total interfacial energy with constant surface area represented by Equation 1.[6]

$$\Delta(\gamma A) = \Delta\gamma A + \gamma\Delta A \qquad \text{Equation 1[6]}$$

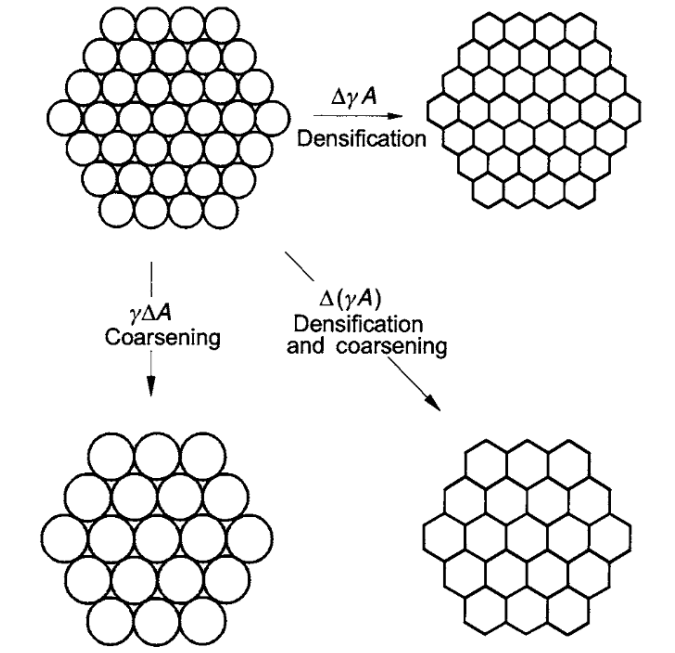

Figure I.5. Basic phenomena occurring during sintering under the driving force for sintering, $\Delta(\gamma A)$.

Figure 1.3: A visual representation of the process of sintering and densification.[6]

The sintering process can be broken down into 3 main steps. These steps are visualized in Figure 1.4. Stage 0 is adhesion between particles and must first occur before the other processes can begin. Stage 1 is when necking begins between the two particles and is driven by the curvature of the particles. Stage 2 is where diffusion continues to progress, and multiple necks begin to interact to the point of having interconnected pores. Stage 3 is the final stage, where the pores are now isolated and begin to shrink until a pressure equilibrium is reached. During this process the mechanism for mass transport will determine whether coarsening, densification, or both occur.

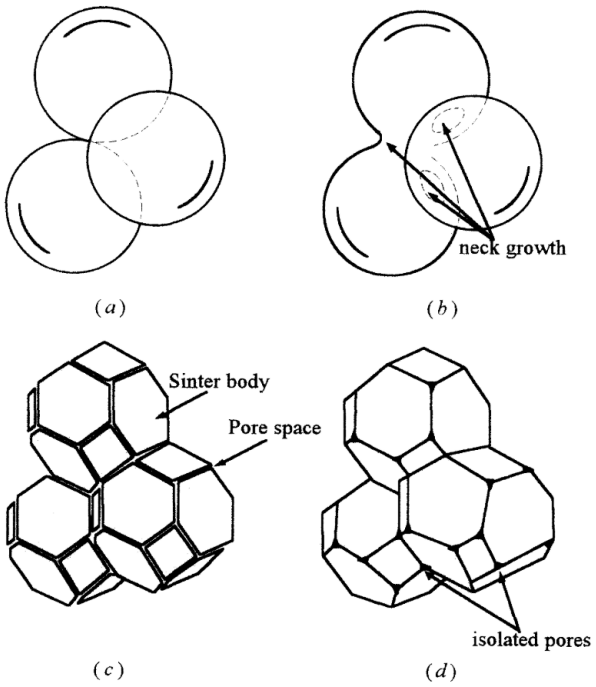

Figure 1.4: The three stages of sintering with (A) representing the initial stage, (B) the initial neck growth, (C) interconnected pore channels and (D) isolated pores. [1]

During the sintering process, there are six different pathways for matter transport to occur. These pathways are documented in Figure 1.5. These types of diffusion include lattice diffusion, surface diffusion, evaporation-condensation, and grain boundary diffusion. In terms of

densification and coarsening, these diffusion paths are shown Figure 1.6 for an ideal two particle system. It can be seen how, when transport occurs during densification, there is shrinkage while there is not in the coarsening process. As mentioned previously, the driving force of this process is to reduce the interfacial energy of the system. When starting with a powder compact, there are both solid-solid interfaces where the particles are in contact as well as solid-vapor interfaces. It is energetically favorable during sintering to create solid-solid interfaces, as there is a lower interfacial energy as compared to the solid-vapor interface.[7] In these solid-vapor interfaces, the pressure differences are related to the curvature of the grain boundaries and this curvature of the grain boundary is directly related to the diving force of the grain, as will be discussed in section 1.2.

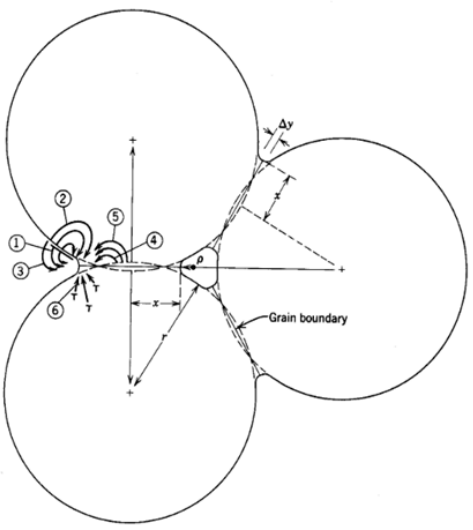

Alternate Paths for Matter Transport During the Initial Stages of Sintering

Mechanism Number	Transport Path	Source of Matter	Sink of Matter
1	Surface diffusion	Surface	Neck
2	Lattice diffusion	Surface	Neck
3	Vapor transport	Surface	Neck
4	Boundary diffusion	Grain boundary	Neck
5	Lattice diffusion	Grain boundary	Neck
6	Lattice diffusion	Dislocations	Neck

Figure 1.5: The six different mechanisms for matter transport during the initial stages of sintering.[3]

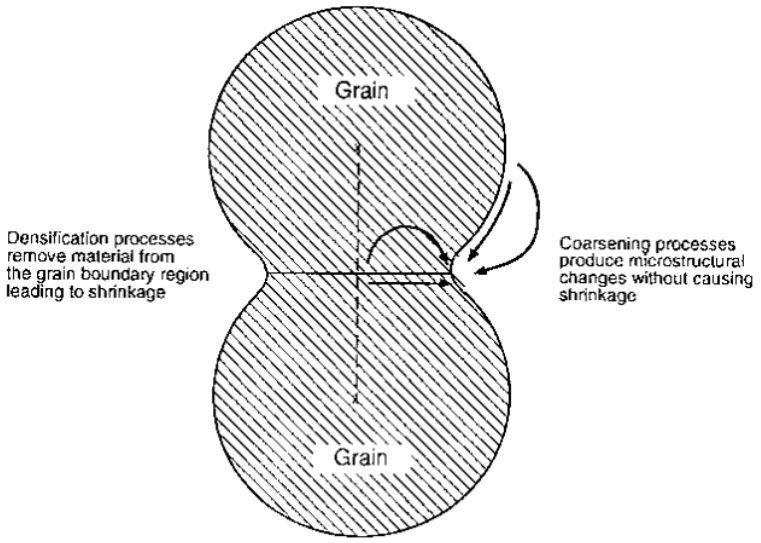

Figure 1.6: Transport mechanisms for densification and coarsening in an ideal two particle system.[5]

1.2 Fundamentals of Grain Growth

The triangle of material science shows there is a link between the grain size of a material and the resulting properties of a material. One example of this is how decreasing the grain size of a ceramic leads to a harder sample. Smaller grains can inhibit crack growth or pin defects. The grain size also can affect anisotropy in electrical properties and, when applied to ceramic capacitors, the grain size can affect leakage currents or failure mechanisms. This section will discuss how grain growth occurs and different models used to describe grain growth.

As discussed in section 1.1, the reduction of surface free energy is a driving force for sintering. The curvature of the resulting grains is a driving force for grain boundary migration. This curvature is directly related to the dihedral angle that is created at the intersection of three grain boundaries. This intersection is shown in Figure 1.7. The dihedral angle can be calculated from the interfacial energies, as shown in Equation 2. This relationship shows how differing

interfacial energies can change the angles of the grain boundary. When connecting multiple of these grain boundaries the curvature of the grain must change to accommodate the difference in the angles around the triple junction. This relationship is for an isotropic example and other models have been created for an anisotropic system. Herring described the surface free energy as the integral of specific surface free energy as a function of the outward normal.[8] It has also been described by Cahn and Hoffman in vector form that describes the free energy of an anisotropic surface at different orientations represented by a unit normal vector.[9] The curvature will then influence whether a grain will grow or shrink. This relationship can be seen in an ideal isotropic grain boundary in Figure 1.8. For an ideal system, when a grain has a dihedral angle of exactly 120° and is a six-sided grain, there is zero curvature, as shown in Figure 1.8C. As the number of sides of the grain boundary decreases, the angle inside the grain must increase to compensate, resulting in a convex boundary. This grain will shrink, as seen in Figure 1.8A and Figure 1.8B. When a grain has more than 6 sides the inside dihedral angle will shrink, resulting in a concave grain boundary. This grain will grow, as seen in Figure 1.8D.[10]

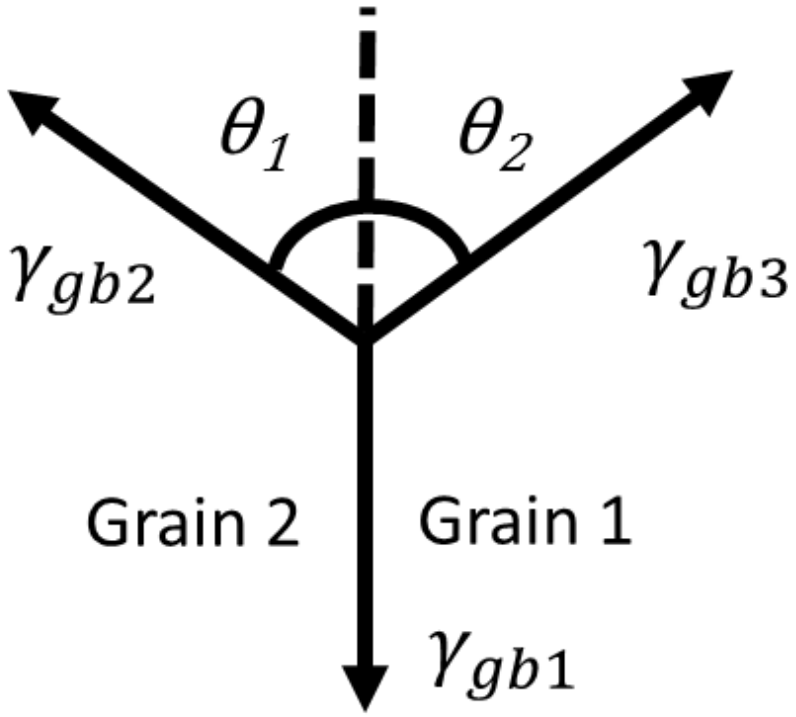

Figure 1.7: A schematic for the dihedral angle of a triple junction of three grains.

$$\gamma_{gb1} = \gamma_{gb2}\cos(\theta_1) + \gamma_{gb3}\cos(\theta_2) \qquad \text{Equation 2[1]}$$

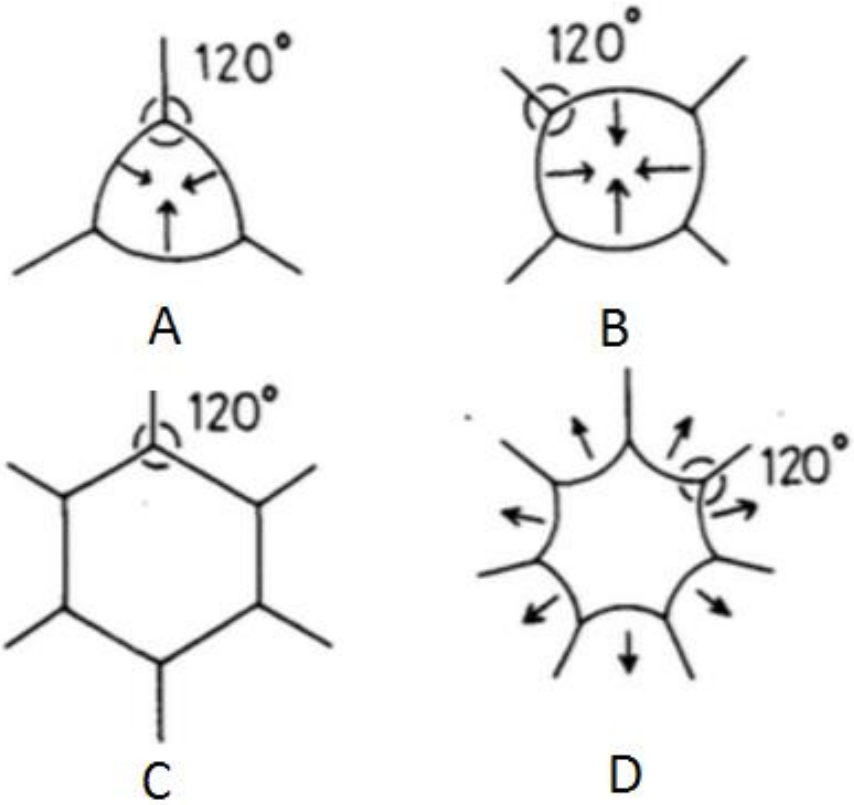

Figure 1.8: The effects of curvature and number of sides on isotropic grains where grains A and B shrink, grain C remains constant and grain D grows.[10]

1.2.1 Grain Boundary Formation

A first step to understanding grain growth is to understand the mechanics behind the formation of grain boundaries. Grain boundaries are defects in the bulk sample and have additional free energy. As discussed in section 1.1 these defects are present as it is energetically favorable for the system to form solid-solid interfaces as opposed to the solid-vapor interfaces of the bulk powder. This concept can be summarized by Equation 3 that describes the interfacial energy of a grain boundary is the sum of two free surfaces minus a binding energy.

$$\gamma_{GB} = \gamma_1 + \gamma_2 - B$$ Equation 3 [11]

A grain boundary between two neighboring grains can be described by 5 macroscopic parameters. Three parameters are used to describe the misorientations between the two grains. These three parameters are three angles of rotation to rotate one grain to match the orientation of the second grain. The two additional parameters are used to define the normal of the grain boundary. These two parameters are spherical angles that define the orientation of the grain boundary plane. As this normal vector is a unit vector, only two parameters of the coordinate system are needed. Experimentally, if these five parameters can be described then one can describe the interfacial energy of the grain. When this is done for two grains in contact then it possible to describe the energy of the grain boundary. This grain boundary energy then has implications on the on the larger grain growth of the system.

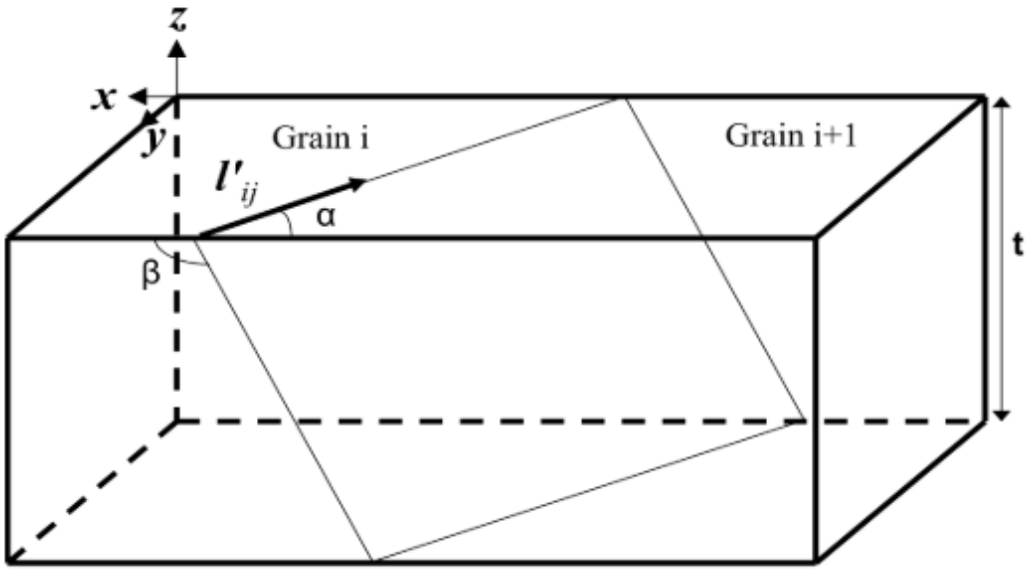

Figure 1.9: A schematic representing the five parameters of a grain boundary where α represents the trace angle and β represents the inclination angle. [12]

1.2.2 Isotropic Grain Growth

The simplest example of grain growth is the example of isotropic grain growth. The Burke-Turnbull model is the classic model of grain growth in simplistic terms. This model describes the velocity of grain boundary (V_b) as a function of driving force (F_b) and mobility (M_b) shown in Equation 4. The driving force can be broken down into a function of interfacial energy (γ_b) and curvature (κ), as shown in Equation 5. The mobility term is defined in Equation 6, where D_{eff} is the effective diffusivity, Ω is the atomic volume, δ is the grain boundary thickness, K_b is Boltzmann's constant and T is temperature. The effective diffusivity is defined by Equation 7, where D_0 is the maximum diffusion coefficient, Q is the activation energy, K_b is Boltzmann's constant, and T is temperature.[13] The experiments in this document will examine how both changes in the driving force and mobility may affect grain growth.

$$V_b = F_b M_b \qquad \text{Equation 4[13]}$$

$$F_b = \gamma_b \kappa \qquad \text{Equation 5[3]}$$

$$M_b = \frac{D_{eff}\Omega}{\delta K_b T} \qquad \text{Equation 6[3]}$$

$$D_{eff} = D_o \exp\frac{-Q}{K_b T} \qquad \text{Equation 7[1]}$$

The Burke-Turnbull model is limited by its assumptions for the driving force and mobility terms. In an isotropic model, it is assumed that the mobility term is constant for all grain boundaries; however, in real grain boundaries, the mobility can vary with the grain boundary structure. The driving force term in this model is an idealized scenario. When considering grain boundary movement, it possible to imagine the atoms jumping across the grain boundary when it is energetically favorable, as shown in Figure 1.10; however, there are many complications to

this simplistic model. Pores, impurities and defects can affect the structure of the grain boundary, creating a drag force. For this reason, grain boundary velocities calculated using only the Burke-Turnbull model are expected to be overestimations of measured data.

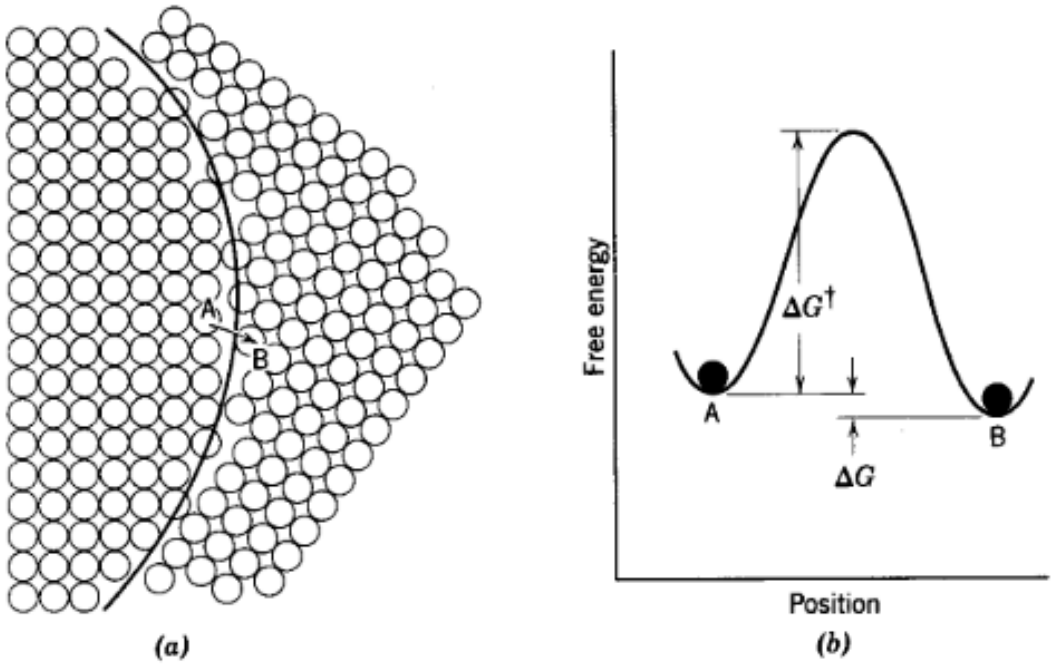

Figure 1.10: A grain boundary model where the atoms jump across the grain boundary (A) due to the free energy of the atom (B).[3]

1.2.3 Drag Forces

As discussed in 1.2.2, the driving force in a real system is influenced by many factors that may create a drag force on the movement of a grain boundary. The steady state scenario is when the driving force is balanced with the total drag force. The total drag force can be composed of intrinsic drag, solute drag, as well as pore or precipitate drag terms. The intrinsic drag of a system is defined by the diffusion rates of the atoms or ions across a grain boundary. The grain boundary structure can influence the intrinsic mobility of a grain boundary. It is expected that grain boundaries with special misorientation relationships, such as twin grain boundaries and low

angle grain boundaries, will have a lower intrinsic mobility.[14] Differing grain boundary structures that affect mobility are common in anisotropic systems; this anisotropic mobility of a grain can result in faceted microstructures.

1.2.3.1 Solute Drag

The first of these forces to be discussed is that of solute drag. In solute drag, impurities or solute can be either attracted or repelled by the grain boundary, resulting in an interaction potential. If a solute has an interaction potential, it can create a spatial concentration profile that is equal to the chemical potential of the solute.[14] Intrinsic defects in the material can also segregate out and similarly influence grain boundary migration. As the grain boundary migrates across the sample, the grain boundary will drive diffusion of the solute in the direction of migration. The steady state migration can be represented by Equation 8 as derived by Cahn. This equation describes the steady state drag force (F_s) as a function of the solute drag force per unit velocity and per unit solute concentration in the low-velocity limit (α), the bulk solute concentration (C_∞), and the approximate drift velocity of the solute (β^{-1}).[15]

$$F_s = \frac{\alpha C_\infty V_b}{[1 + (\beta V_b)^2]} \qquad \text{Equation 8[15]}$$

The force of intrinsic grain boundary migration is linear with respect to the velocity of the grain boundary, as seen in Figure 1.11A. The drag force for solute drag initially has a large force with a low velocity but, as velocity increases, the grain boundary can begin to break free and the force decreases, as shown in Figure 1.11B. The cumulative force of both intrinsic and solute drag is shown in Figure 1.11C. As the grain boundary migrates, it will disrupt the compositional profile of the solute. The changes in the compositional profile will vary depending on the solute being attracted to or repelled from the grain boundary. Profiles for both of these scenarios have

been calculated by Cahn.[15] The first plot is for a negative interaction energy or adsorption of the solute to the grain boundary, shown in Figure 1.12A. This plot shows an increasing velocity starting with (a), where Vβ=0 at equilibrium, transitioning to Vβ=1 where the impurity drag is at its maximum and ending at Vβ=3 which is considered a high velocity. During this transition, desorption begins everywhere along the interface with a higher concentration at the front half of the interface. As velocity increases, the desorption in front of the interface decreases, resulting in a lower drag force.

The profile for a positive interaction potential is shown in Figure 1.12B. The plot shows an increasing velocity from V_β=0 (a) to V_β=3 (c) with the maximum drag is shown in curve (b). At steady state, there is a depletion zone around the interface. As the velocity increases, the solute piles up in front of the interface until a critical velocity is reached and the interface begins to break free of the drag force.

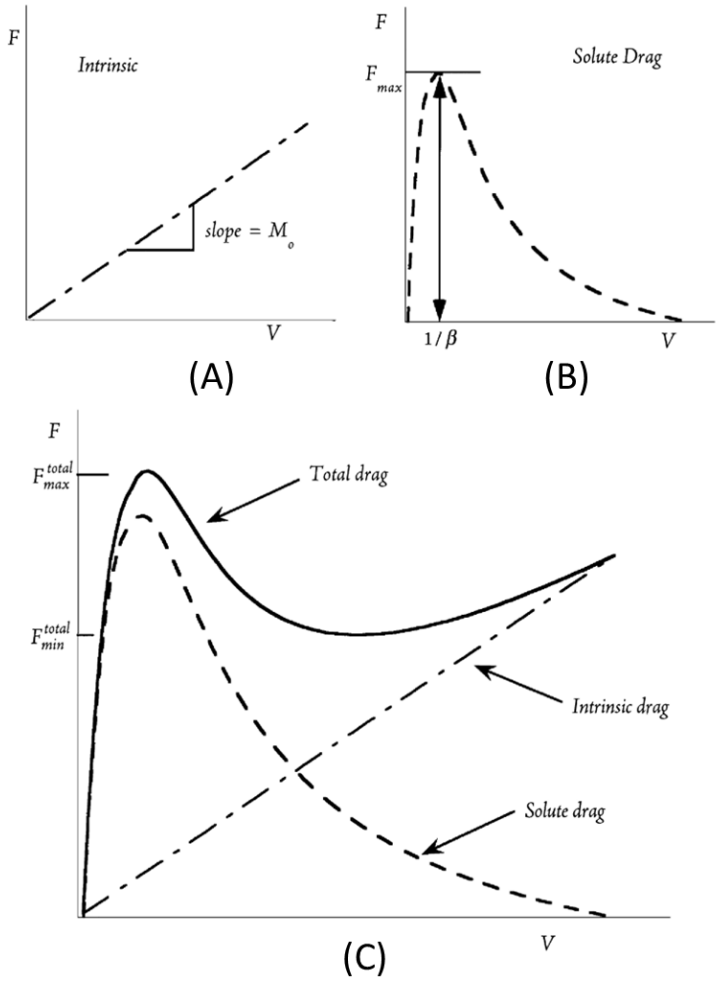

Figure 1.11: A plot of the force-velocity behavior of: (A) intrinsic drag, (B) solute drag and (C) the total drag composed of the solute and intrinsic drag.[16]

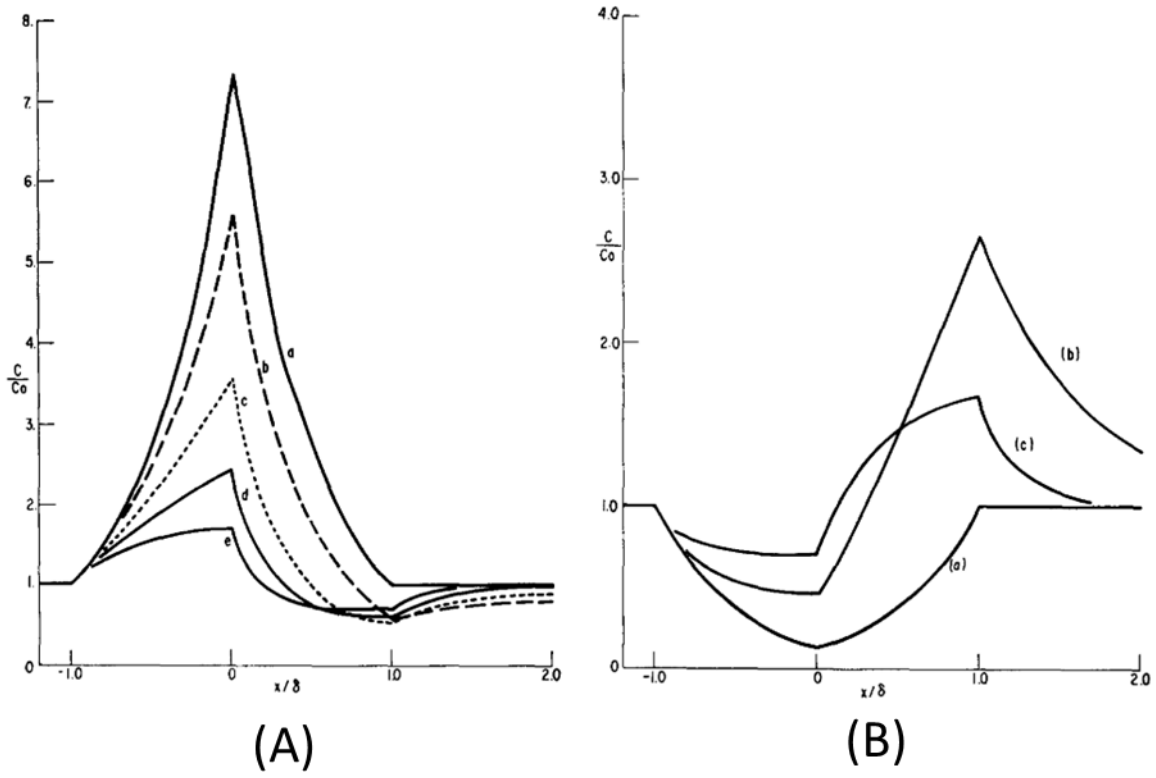

Figure 1.12: The compositional profiles where plot (A) represents a negative interaction potential where (a) represents equilibrium, (b) low velocity, (c) impurity drag maximum, (d) the inflection point of the drag-velocity curve, and (e) high velocity and (B) a positive interaction potential where (a) is at equilibrium, (b) is maximum drag, and (c) is high velocity.[15]

1.2.3.2 Pinning and Pore Drag

The mobility of a grain boundary can also be impacted by second phase particles and pores. The classic model of a grain boundary encountering a second phase inclusion was developed by C. Zener and C.S. Smith. This model considers an immobile inclusion of constant size. The inclusion results in a restraining force described in Equation 9, where r is the radius of the inclusion and θ is the angle between the inclusion and the normal of the interface.[5] This interaction can be seen in Figure 1.13. During this interaction, the particle reduces the area of the grain boundary and therefore reduces the free energy of the system. There

is an energy penalty for the grain to recreate the missing grain boundary. As a result, there is a change in curvature of the grain boundary until there is enough force for the boundary to break free of the particle.

$$F_r = (\gamma_{gb}\, cos\theta)(2\pi r\, sin\theta) \qquad \text{Equation 9[5]}$$

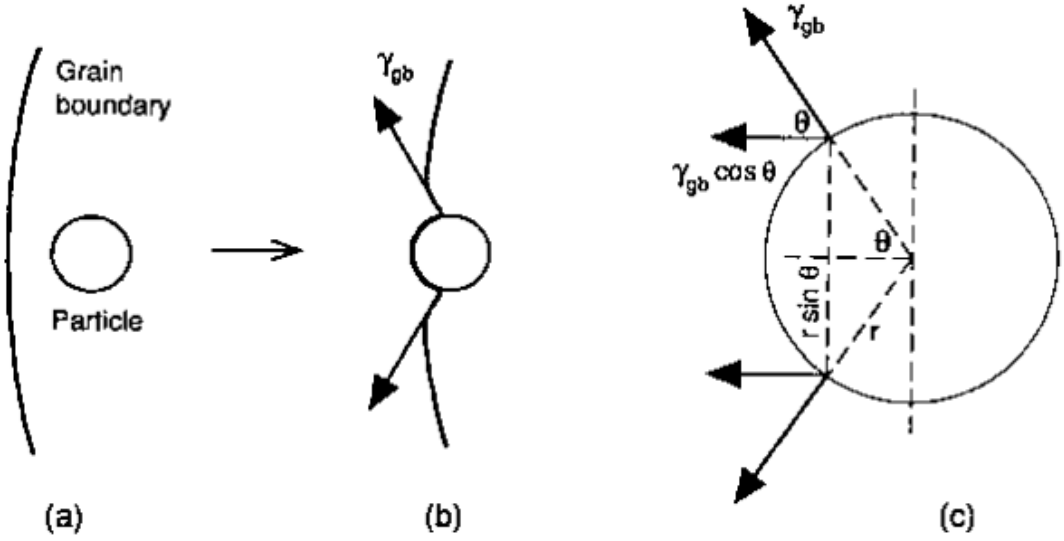

Figure 1.13: An immobile particle interacting with a grain boundary where (A) represents the approach, (B) the interaction with the grain boundary and (C) the geometry of the interaction between the particle and grain boundary.[5]

This concept can be applied to interactions with pores with the additional complication that pores also have a mobility and may travel with the grain boundary. During this interaction, the pore can change curvature with the interaction of the interface. As the grain boundary migrates, the pore will be dragged along, and the distortion will be dependent on the velocity of the boundary. This distortion is shown in Figure 1.14. As velocity increases, the pore will continue to elongate behind the leading edge until the grain boundary breaks free of the pore. Due to the influence of the pore on the curvature, the radius of the pore relative to the radius of the grain are

key components in determining if the pore will break free or stay attached to the grain boundary. This relationship will vary depending on composition of the system; however, it is possible to plot this data, as shown in Figure 1.15 for Fe doped MgO. This example differentiates between solute drag and pore drag, as well as identifying when it is expected for the pores to break free. A comparison of grain boundary motion for intrinsic, pore, and impurity drag can be seen in Figure 1.16.

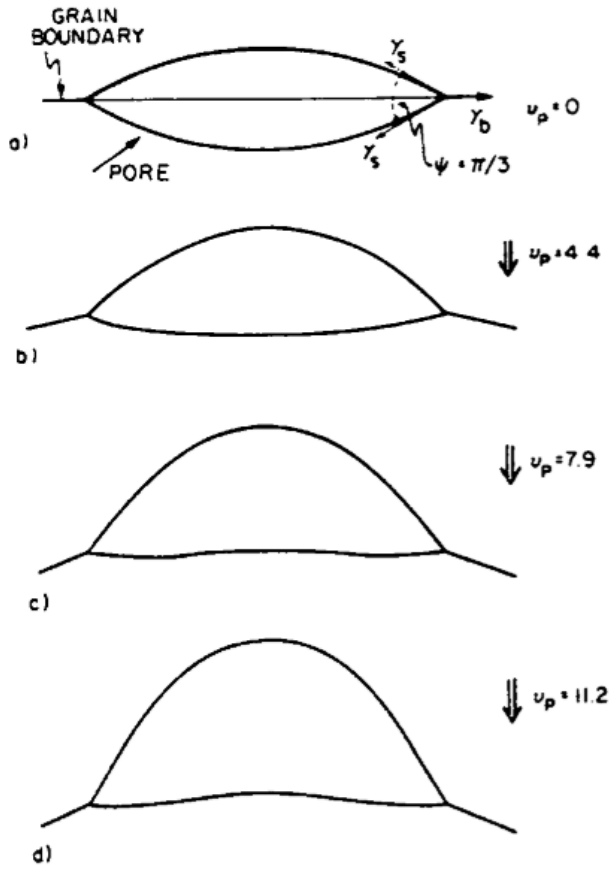

Figure 1.14: The transition of the pore shape when interacting with a grain boundary.[17]

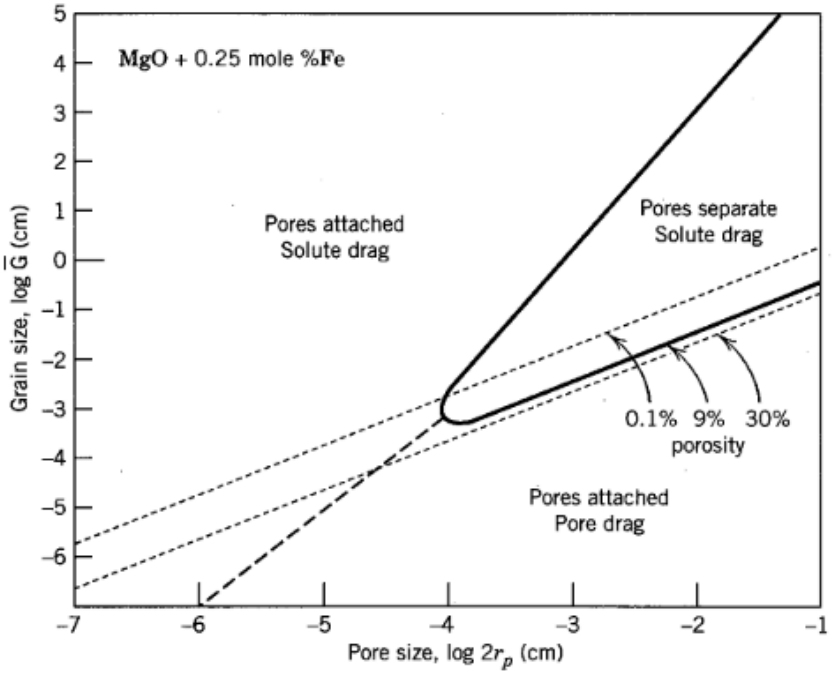

Figure 1.15: A plot of pore size vs. grain size that maps the behavior of solute drag and pore drag.[3]

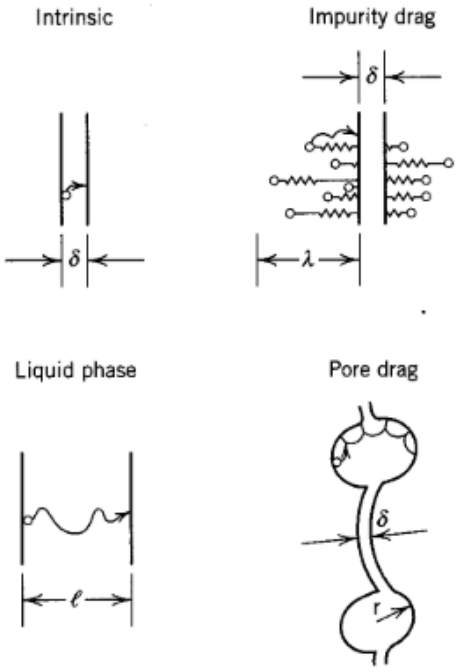

Figure 1.16: A schematic of how the motion of a grain boundary is impacted by intrinsic drag, impurity drag, a liquid phase and pore drag.[3]

1.2.4 Types of Grain Growth

There are multiple types of grain growth that can occur, the two most common classifications are normal and abnormal grain growth. Normal grain growth, also referred to as continuous grain growth, is when the shapes and sizes of the grains are within a narrow range with only minor variance between grains. Abnormal grain growth occurs when there are two populations of grains, one larger and one smaller. The larger grains grow at a much faster rate at the expense of the smaller grains. This abnormal grain growth is also commonly referred to as exaggerated grain growth or discontinuous grain growth.[5] As these abnormal grains grow, a bimodal distribution of the grain size can be observed; this distribution can be seen in Figure 1.17.

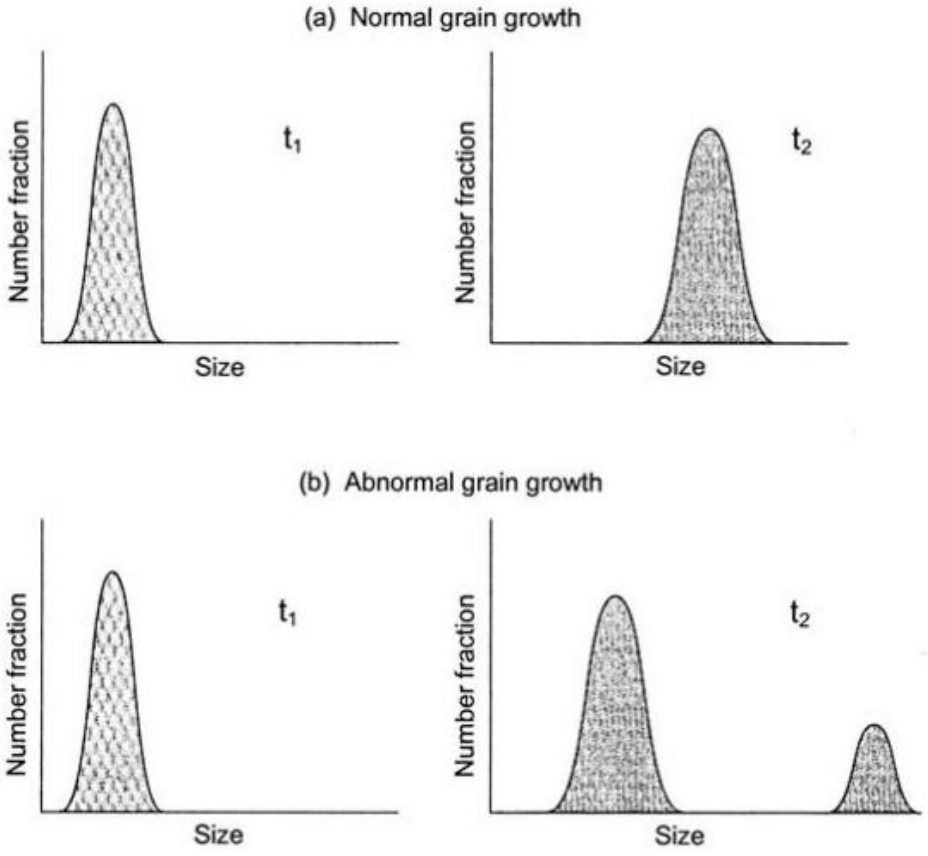

Figure 1.17: Plots of (A) normal grain growth and (B) abnormal grain growth, where time progresses to the right as grain growth occurs.[3]

Grain growth is commonly described using Equation 10. This equation defines G as the grain size, G0 as the initial grain size, t as time and k as the growth factor, also known as the grain growth constant. A standard practice for grain growth studies is plotting the grain growth constant or mobility on an Arrhenius plot. The Arrhenius plot uses log scale versus inverse temperature. An example plot of mobility and inverse temperature is shown in Figure 1.18. The mobility was calculated using Equation 11. On an Arrhenius plot, normal grain growth is expected to have a linear slope; variations from this expected result can indicate alternative grain growth types.

$$G^2 - G_0^2 = kt$$ Equation 10[18]

where $k = \frac{3}{G}\gamma_{gb}\left(\frac{D_b\Omega}{\delta K_b T}\right)$ for boundary-controlled diffusion.

$$V \approx 2\gamma M_b\left(\frac{1}{G_N} - \frac{1}{G_A}\right)$$ Equation 11[18]

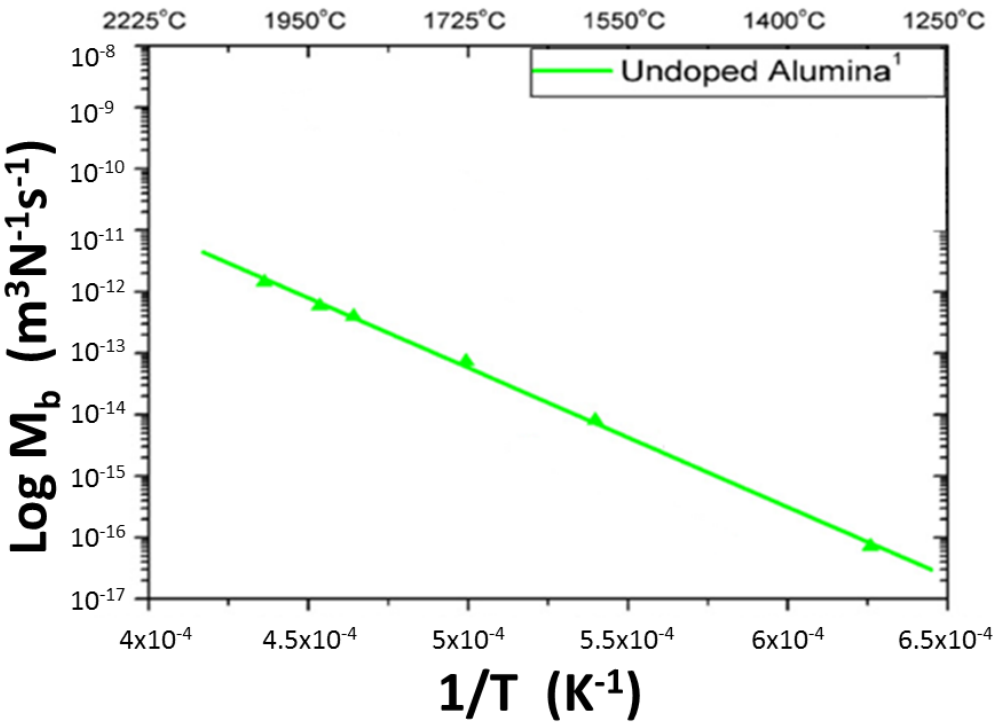

Figure 1.18: Plot of grain boundary mobility vs. temperature in undoped alumina.[19]

There are multiple possibilities as to why abnormal grain growth may occur. What is known is that, in isotropic systems, differing initial grain sizes is not sufficient for abnormal grain growth, determined by Wu et al., who simulated a large grain in a fine grained matrix, and the grains did not show indications of abnormal grain growth.[20] Cantwell et. al. suggested that structural changes could occur due to impurities.[21] Other authors, such as An et al., have proposed that faceting can inhibit grain boundary motion and non-faceted grains would be allowed to grow preferentially.[22] Additional explanations for abnormal grain growth include differences in mobility or energy, preferential segregation of impurities or dopants, the release of pores or solute from the grain boundaries, or the presence of a liquid phase. These options could create grains with a higher mobility or lower energy, and thus allow them to grow preferentially.

1.3 Grain Boundary Energy and Anisotropy

1.3.1 Anisotropic Grain Boundaries

In the models of grain growth discussed in previous sections, it was assumed that the grain boundaries were isotropic, having the same properties in any orientation. This assumption is one that does not hold when observing experimental results. Real grain boundaries can either be faceted or continuous. Faceted grain boundaries will break up into smaller steps of a stable orientation, while continuous grain boundaries are stable across a range of orientations and retain the overall curvature of the boundary. These continuous boundaries are also referred to as atomically rough boundaries. As a grain boundary migrates, the atoms cannot simply jump across the grain boundary, as modeled in section 1.2.2. Faceted grain boundaries move by nucleation and growth of the individual facets, as shown in Figure 1.19. The steps of the grain boundary can be anisotropic, having differing step energies. The nucleation and propagation of

these will be limited by the individual step energies. This anisotropy of step motion will result in one of the facets limiting the rate of migration.

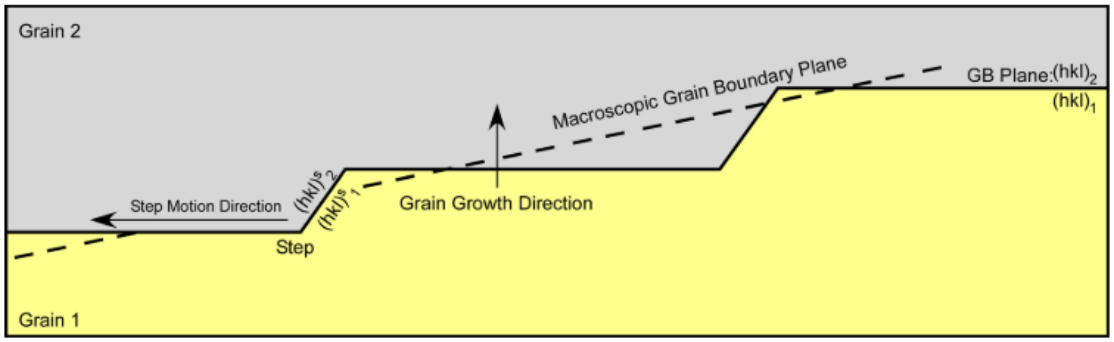

Figure 1.19: A schematic of faceting behavior as the macroscopic grain boundary migrates.[23]

It was previously stated the energy of the grain boundary is the sum of two surface energies minus a binding energy. If the assumption is made that the binding energy is isotropic, then one less parameter of five-dimensional space is required. This allows for the study of grain boundary anisotropy through surface energies. While it is possible for the binding energy to be anisotropic, especially in relation to temperature, it is a necessary assumption to simplify the experimental process.[24]

The energies of the facets can be plotted as a function of misorientation, as shown in Figure 1.20. This plot shows the change in energy of (100) and (111) plane of copper as a function of misorientation. The (100) plot shows how the energy of the grain boundary increases with misorientation until it reaches a maximum and then decreases due to symmetry. The plot of the (111) plane shows a similar trend except for an additional cusp at 60°, where there is a coherent twin boundary, also known as a Σ3 boundary which is calculated by the area of the coincident cite lattice divided by the area of the base lattice. While this coincident site lattice resulted in a

lower grain boundary energy, Sutton and Balluffi concluded that there is not a conclusive link between coincident sites and low energy boundaries.[25]

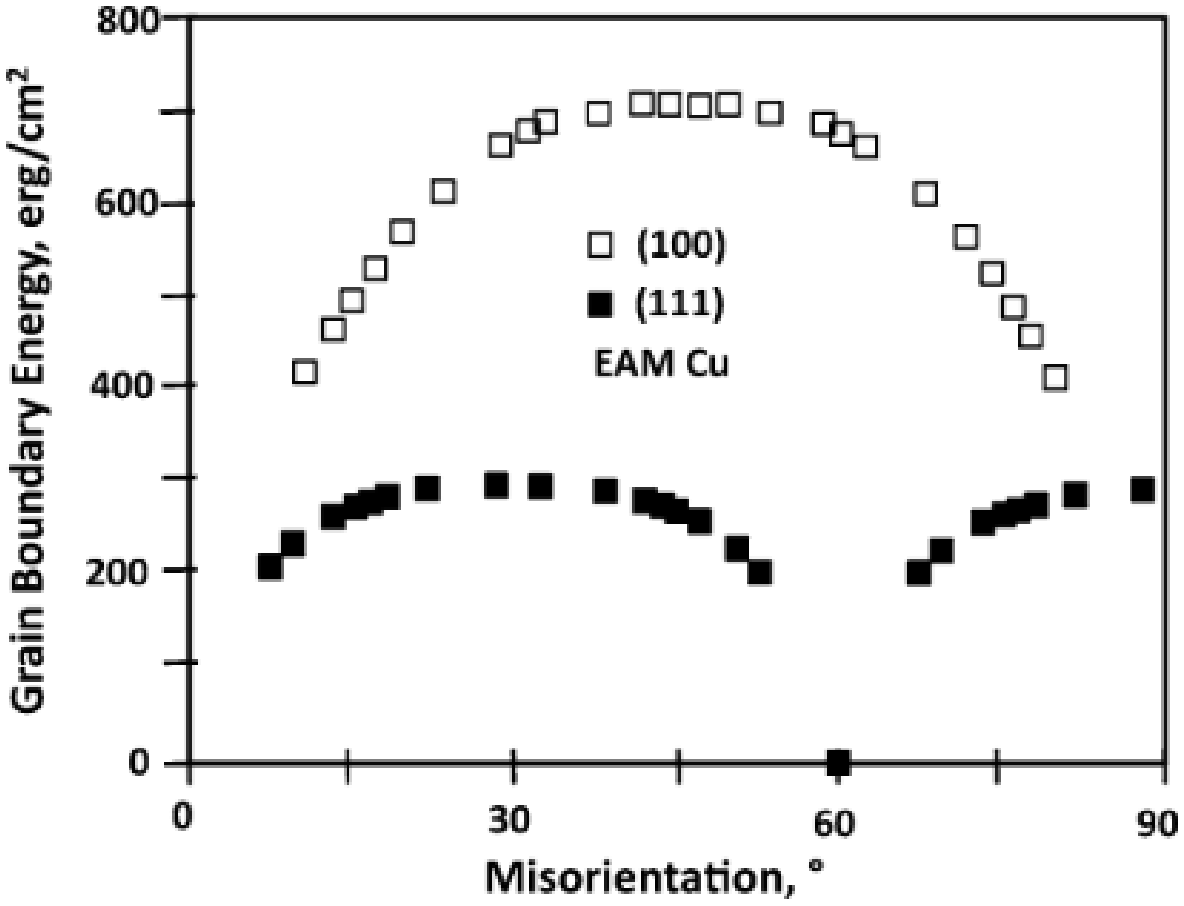

Figure 1.20: A plot of misorientation vs. grain boundary energy for (100) and (111) twist boundaries in the copper system.[26]

1.3.2 Grain Boundary Plane Distribution

A second way to experimentally study anisotropy of a system is through determining the grain boundary plane distribution (GBPD). The GBPD can be represented by a stereographic projection plotting grain boundary population as a function of orientation. As previously discussed, a grain boundary is defined by 5 parameters. Experimentally, the first 3 parameters

can be obtained through EBSD orientation measurement to determine the orientation of the grain surface. The final two parameters defining the normal of the grain boundary are much more difficult to experimentally observe, as the grain boundary goes into the sample subsurface at large range of possible orientations. To define the last two parameters, serial sectioning can be done, and images from the same locations are compared to determine the angle of the grain boundary.[27]

When performing this method, the surface images are converted into skeleton images, aligned and overlaid to produce an image as seen in Figure 1.21. Then, an algorithm is used to create a grain boundary mesh to connect the overlaying images and reconstruct the grain boundaries. This process is shown in Figure 1.22. It is then possible to determine all five of the grain boundary parameters and plot the distributions on a stereographic projection. An example plot for hot pressed polycrystalline magnesia is shown in Figure 1.23. The GBPD plots are represented as multiples of a random distribution (MRD) as a function of orientation. This process has been utilized to study multiple systems including: MgO, Y_2O_3, Ni, YSZ, $SrTiO_3$. Despite the difference in system type, there has been a correlation between low index, low energy surface planes, and higher MRD values. Additionally, there has been an inverse correlation between grain boundary energy and grain boundary population. A third conclusion from this body of work is that grain boundaries composed of low energy surfaces have low energies.[26] These conclusions from previous work are essential for studying grain boundary energy and anisotropy, as they provide a foundation for linking grain boundary energy and anisotropy to surface energy and anisotropy.

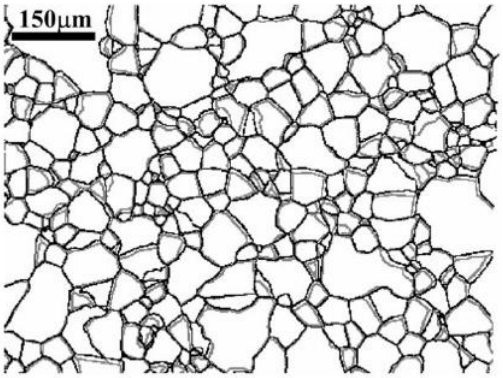

Figure 1.21: In image of two superimposed skeletal microstructures after serial sectioning.[28]

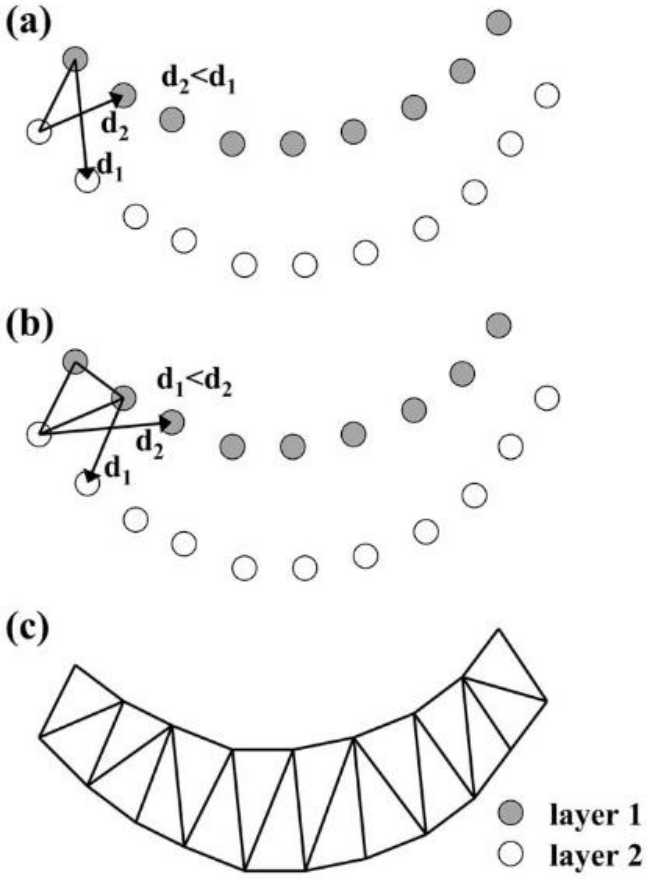

Figure 1.22: A schematic representing the process of creating a grain boundary mesh by connecting the triple junctions to the nearest neighboring vertexes.[28]

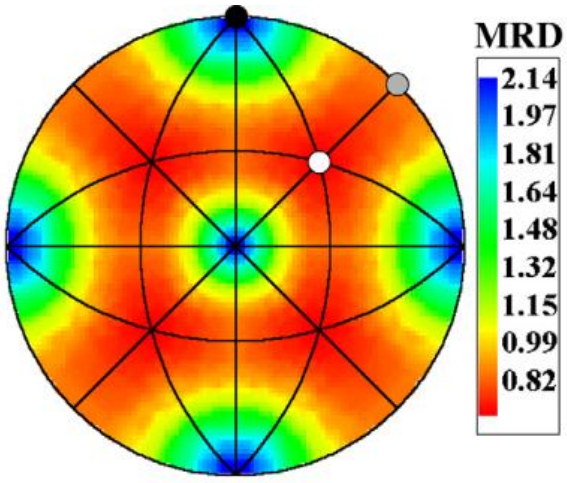

Figure 1.23: Shown the grain boundary plane distribution of hot pressed magnesia with peaks at the {100} planes.[28]

1.3.3 Wulff Shape

One method of studying the anisotropy of a material is through observing the Wulff shape or equilibrium crystal shape of a material. The Wulff shape is the minimum surface energy shape of an isolated particle. Experimentally, the Wulff shape is observed in small intergranular pores of a material allowing for a direct determination of anisotropy. The observed pores will show the facets, and thus the relative surface energy of each of the facets.

The Wulff shape is determined through the creation of a Wulff construction. To determine a 2D Wulff shape, one starts with a 2D polar plot of the surface energy as a function of orientation. At each orientation, a line is drawn from the center of the plot to the surface energy, and then a tangent line is drawn. The Wulff shape is the minimum energy shape, enclosed by the tangent lines across all orientations.[29] An example of this process is shown in Figure 1.24.

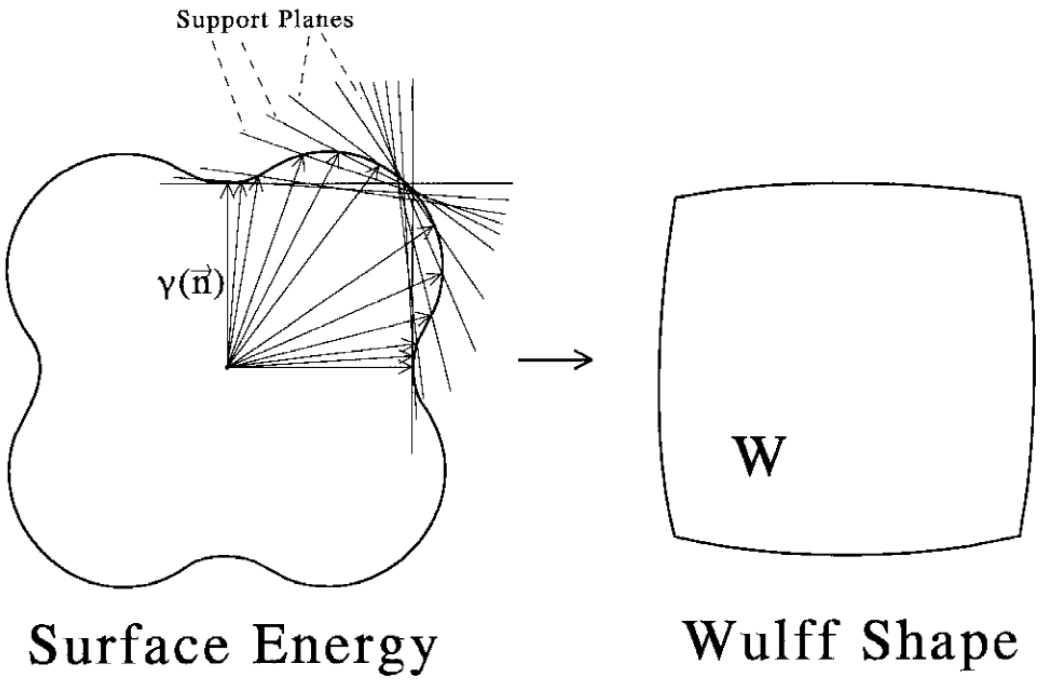

Figure 1.24: A schematic showing the process of creating a Wulff construction from the surface energy plot and the resulting Wulff shape.[29]

One primary concern when determining the Wulff shape of a material is differentiating between the true Wulff shape and the kinetic Wulff shape. The kinetic shape is one that is limited by low-mobility planes as opposed to low-energy planes.[30] Experimentally, ensuring that the pores most accurately represent the Wulff shape, the pores need to be isolated and as small as possible to minimize kinetic effects. A model by Kitayama has been developed to determine the processing requirements to equilibrate a pore; however, the model determines the time to equilibrate an oval pore to a rounded symmetrical pore.[31] This model is helpful for determining a critical experimental pore size but, it may still be possible that, even if a pore is spherical, the planes within the pore are not yet fully equilibrated.

After collecting the faceting information, it has been proposed that this information can be utilized to produce n-diagrams to have a tool to more easily represent the faceting behavior of a

material.[32] The n-diagram is analogous to a ternary phase diagram for faceting, where temperature, pressure and chemical potential are constant. The n-diagram is plotted on a stereographic projection, where the points representing stable facets and the lines represent transitions between facets. In an n-diagram it is possible to have areas analogous to two phase regions when there are rounded or continuous regions in the Wulff shape. An example of this diagram is shown in Figure 1.25, where Figure 1.25(A) represents a (100) cube, Figure 1.25(B-C) show the appearance and growth of the (111) facet until Figure 1.25(D), where the original (100) facet is no longer visible. An example n-diagram for the MgO-NiO system can be seen in Figure 1.26 with increasing NiO content. This example system shows an n-diagram with the addition of two-phase regions. In this example, the large single-phase regions would represent rounded areas of the Wulff shape.

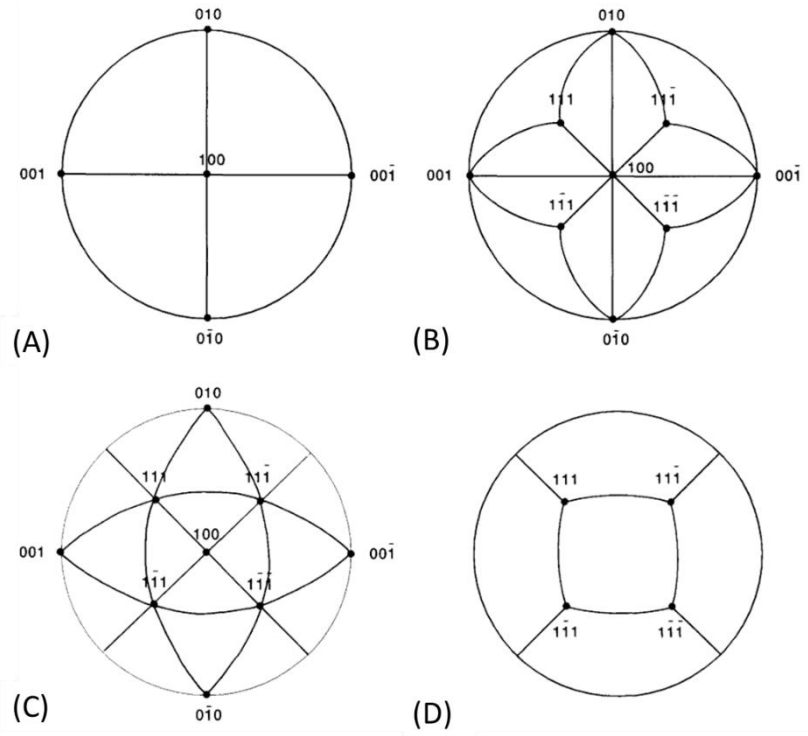

Figure 1.25: A series of n-diagram plots where (A) represents a {100} cube, (B) shows the addition of {111} facets, (C) shows growth of the {111} and (D) represents when the {100} facets have disappeared.[32]

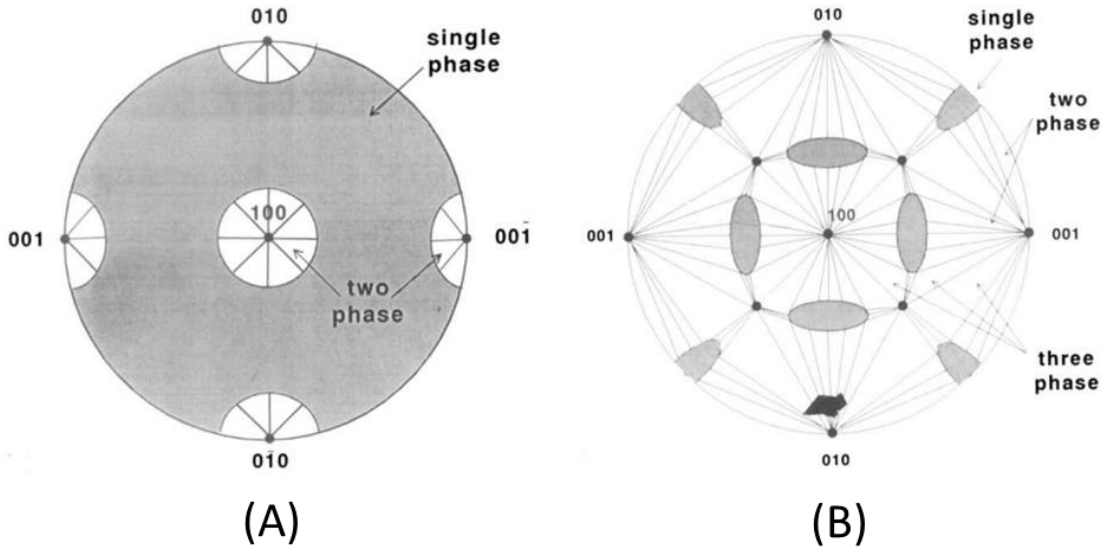

Figure 1.26 : A set of MgO-NiO n-diagrams with the composition of (A) having 99% MgO and (B) having 20% MgO.[32]

2. THE STRONTIUM TITANATE AND BARIUM TITANATE SYSTEMS

2.1 The $SrTiO_3$ System

When researching the current state of the art of dielectric ceramics, there has been a significant interest in grain growth of $SrTiO_3$. The work done in recent $SrTiO_3$ studies helped to motivate the work presented in this document. $SrTiO_3$ is a dielectric ceramic of the ABO_3 structure, known as a perovskite.[3] Perovskites are commonly used in the production of tunable ceramic capacitors as a grain boundary layer, piezoelectric actuators, and varistors.[33] $SrTiO_3$ was chosen as a model system in these previous studies as there are no phase transitions in the system at the temperatures of interest.[34] This section will discuss the previous work relating to grain growth, grain boundary anisotropy, and surface anisotropy related to $SrTiO_3$.

2.1.1 Grain Growth

A series of grain growth experiments were done on $SrTiO_3$ by Bäurer et al. These experiments observed a region of non-Arrhenius grain growth. In these experiments, $SrTiO_3$ was produced with a Sr/Ti ratio of 1.005,1.002 and 0.996, then sintered and annealed between 1100°C and 1600°C. Grain size measurements were made using the line intercept method and effective mobility was calculated by fitting the data to an Arrhenius law. One result was the determination that the changes in Sr/Ti ratio did not produce substantially differing mobility values. It was during this experiment that regions of abnormal grain growth were observed at temperatures above 1390°C. In the temperature range where abnormal grain growth occurred, the rate of grain growth slowed and was approximately stagnant at 1425°C.[34] The mobility of the abnormal grains was calculated in alignment with the methodology produced by Dillon et al.[35] Bäurer et al. proposed that there were two differing populations of grains in the temperature

region investigated: one of normal grain growth rate and one of abnormal grain growth rate. As this phenomenon was investigated in greater detail, it was seen that the rate of grain growth decreased in $SrTiO_3$ between 1350°C and 1425°C, as shown in Figure 2.1 by Rheinheimer et al.[36] In the data shown, the black points represent the collected data from grain growth experiments while the open data points are estimates of grain growth rates of large grains. The cause of this abnormal grain growth behavior has been the topic of much investigation. One proposed explanation for this non-Arrhenius behavior is that there were structural changes of the grains, such as a temperature dependent faceting/de-faceting transition.[34]

The concept of relating faceting behavior to grain growth served as the foundational motivation for this body of work. Previous works by Lee et. al. have proposed a relation between faceting behavior and normal or abnormal grain growth due to differences in migration mechanism between faceted and atomically rough.[37] It had also been observed that faceted grain boundaries can undergo a de-faceting transition with increased temperature.[38] Previous work in $SrTiO_3$ has studied the anisotropy and faceting behavior. Two of the experimental methods previously used include Wulff shape reconstruction and GBPD measurements. These previous experiments will be discussed as well as their relation to the observed abnormal grain growth behavior.

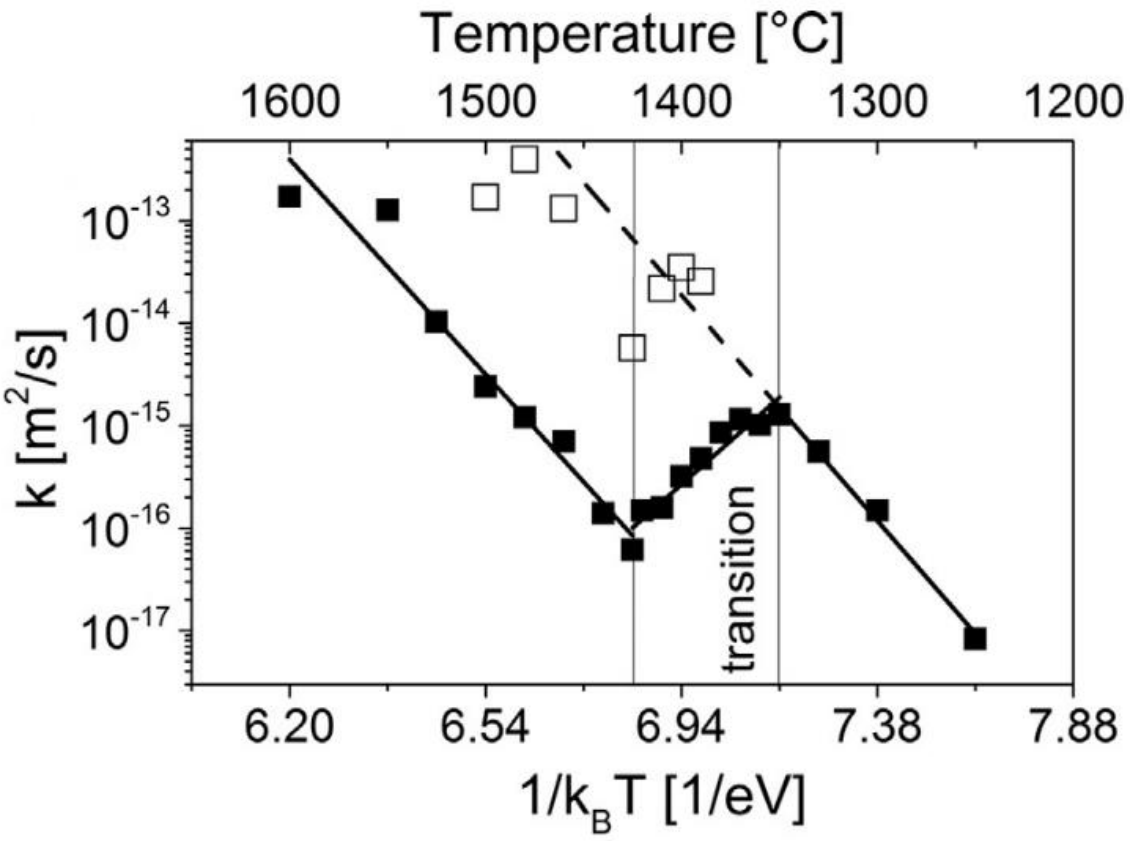

Figure 2.1: A plot of non-Arrhenius grain growth of $SrTiO_3$, where open points represent estimated growth rates of large grains.[36]

2.1.2 Surface and Grain Boundary Anisotropy

2.1.2.1 Wulff Shape

The first of the techniques previously used to study anisotropy and faceting behavior of $SrTiO_3$ that will be discussed is the observation and reconstruction of pore shapes. Rheinheimer et al. performed an experiment observing a series of $SrTiO_3$ pores across a temperature range of 1250°C to 1600°C in both oxygen and a reducing atmosphere of 95%N_2-5%H_2.[24] SEM micrographs were taken of small intergranular pores and these pores were reconstructed into 3D models, as shown in Figure 2.2. The 3D reconstructions were composed of four distinct facets, identified as (100), (110), (111), and (310), and an additional area labeled as microfaceted

regions were observed and reconstructed. These microfaceted regions were described as corrugated regions believed to be a kinetic or geometric constraint on the pores as they could not exist in the Wulff shape. Despite some proposed explanation of why these microfaceted regions exist, they have not yet been fully explained and the work of this paper will further investigate these regions in later sections.

When observing the pore shape with increasing temperature, it was observed that the pores became more isotropic, with an increased number of different facets. For the faceted grains in 95%N_2-5%H_2, it was observed that the pore shapes had less anisotropy compared to the pores processed at the same temperatures in oxygen. It was proposed that the observed differences in anisotropy due to temperature and atmosphere play a role in the grain growth anomaly.[24]

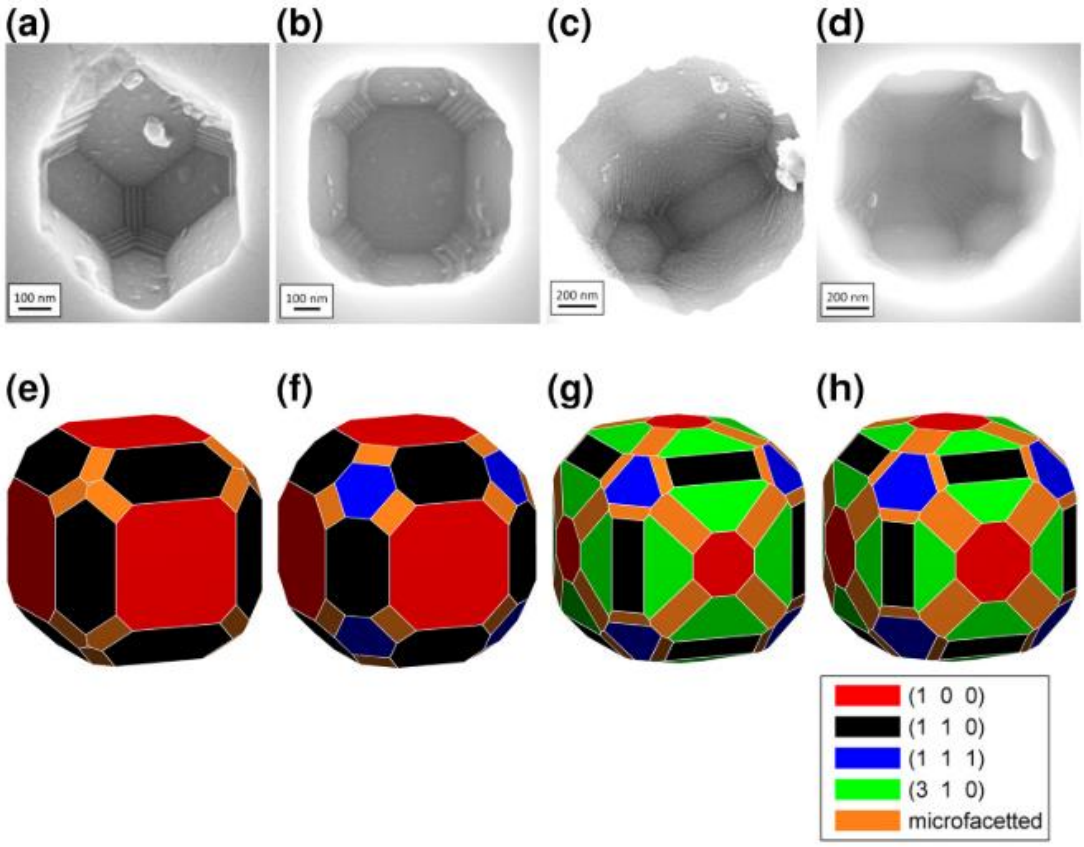

Figure 2.2:Sem images of pores annealed at (A) 1250 °C, (B) 1380 °C, (C) 1460 °C and (D) 1600 °C with their respective reconstructed pore shapes.[24]

2.1.2.2 Grain Boundary Plane Distribution

Experiments to study the grain boundary energy anisotropy have previously been performed by measuring the GBPD of $SrTiO_3$ by Saylor et. al., as well as in conjunction with the pore shape reconstruction from the last section. The Saylor et. al. experiment used $SrTiO_3$ samples that were annealed at 1650°C in air, polished, and then thermally etched at 1400°C for 6 min.[27] Two parallel serial sections were observed with a height difference of 5.2µm using orientation imaging microscopy (OIM). It was verified that the samples had no grain orientation texture or misorientation texture during analysis. The same process for determining GBPD discussed in section 1 was used here. The resulting grain orientations were plotted as a per orientation shown in Figure 2.3. It was determined that the {100} planes were the most frequently observed planes of the grain boundaries.

In the experiments performed by Rheinheimer et. al., similar GBPD measurements were made at 1300°C, 1350°C and 1425°C, and are shown in Figure 2.4.[24] The GBPD shows that there is increasing anisotropy of the grain boundary energy with increasing temperature. As previously discussed in section 1, there is an inverse correlation between the frequency of the grain boundary plane and its relative grain boundary energy. This difference from the pore shape anisotropy discussed in the previous section is attributed to a temperature dependence of the binding energy term. It was believed that the binding energy decreased at a slower rate than the surface energy in relation to temperature. This relationship between the grain boundary energy anisotropy and surface energy anisotropy can be seen in Figure 2.5. The increasing number of {100} planes with increasing temperature was suggested to be an indicator of the mobility of the planes. Previous grain growth simulations have shown a significant impact on the grain growth constant when a small number of low-mobility planes existed. This experiment concluded with the summary that, while previous GBPD experiments have considered the binding energy not to

be a significant impact, this showed that with changing temperature the assumption is no longer valid.

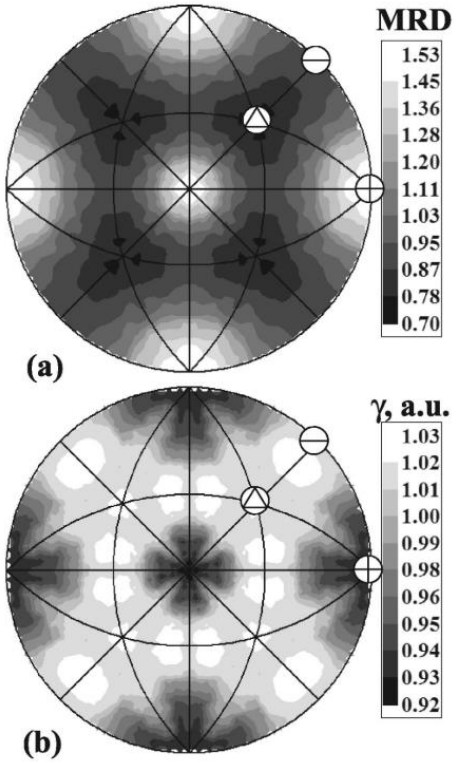

Figure 2.3:A plot of stereographic projections where A is the GBPD of $SrTiO_3$ and B is the surface energy at 1400°C.[27]

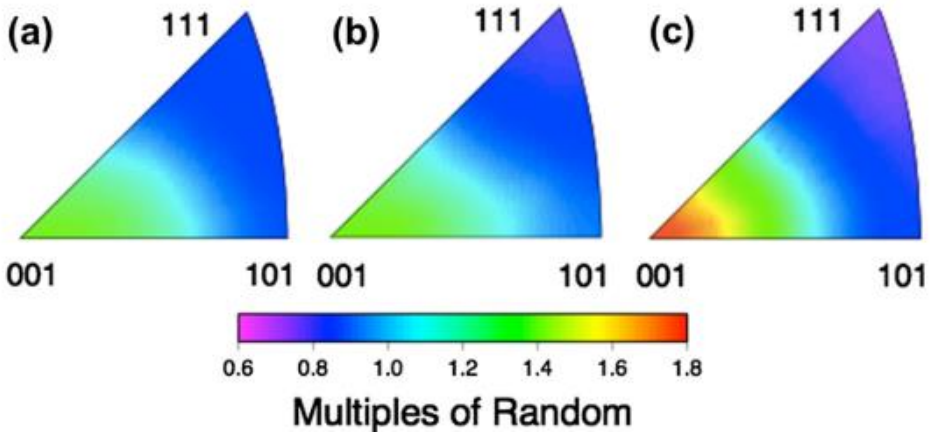

Figure 2.4: Plots of GBPD of $SrTiO_3$ at (A) 1300°C, (B) 1350°C and (C) 1425°C plotted as multiples of a random distribution.[24]

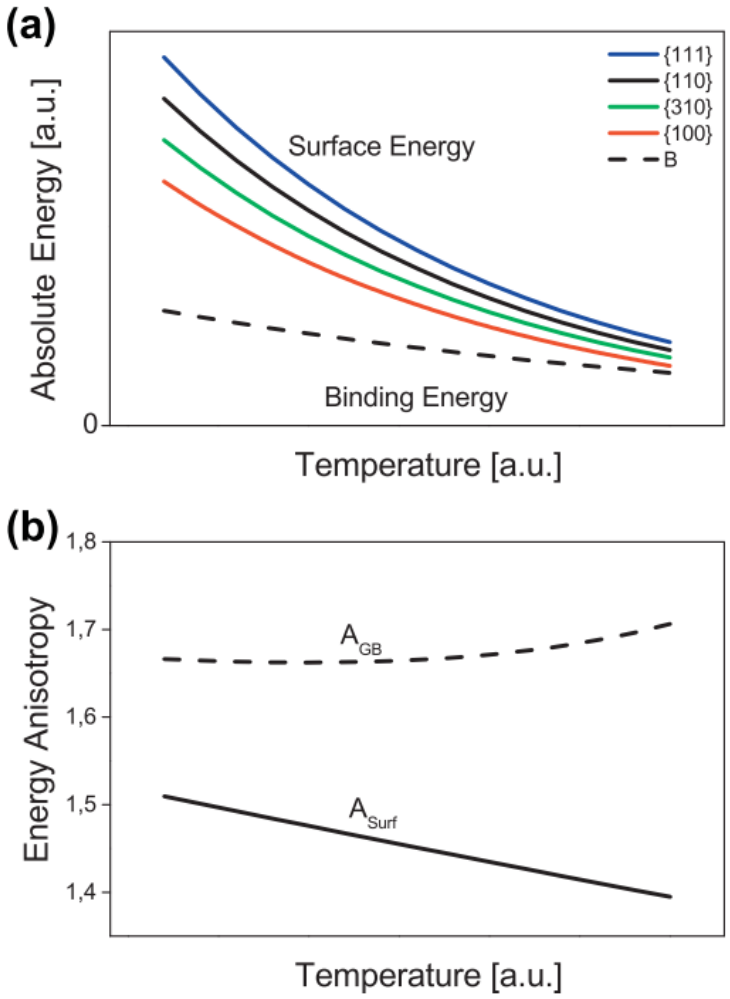

Figure 2.5: Plots of (A) absolute energy vs. temperature for the different planes of the pore shape and (B) a plot of the change in surface vs grain boundary anisotropy with respect to temperature.[24]

2.2 The $BaTiO_3$ System

The other system of interest is that of $BaTiO_3$. Grain growth and faceting behavior of $BaTiO_3$ has been studied in significant depth by Kang et. al. $BaTiO_3$ also has been observed to have abnormal grain growth as well as the connection between grain growth mechanism and faceting. It was determined that there is a relationship between the normal/abnormal grain growth transition and faceting behavior. In faceted $BaTiO_3$ grains, abnormal grain growth is seen, and

this abnormal grain growth is enhanced by the presence of {111} twins.[39] This abnormal grain growth behavior was further investigated in relation to processing atmosphere and it was observed that both normal and abnormal grain growth occur when samples are processed in either H_2 or O_2 atmospheres. [40] It was later noted that the rough to faceted transition could be induced with increased O_2. In this experiment, it was also seen that samples with a structural transition grew and densified at a reduced rate compared to samples with a rough boundary.[41] A later experiment produced rough and faceted $BaTiO_3$ samples after adding $SrTiO_3$ particles on the polished surfaces of the samples. In this experiment grain boundary migration occurred in rough boundaries while in the faceted samples migration was suppressed.[42] The previous experiments in $BaTiO_3$ showed a link between faceting behavior and grain growth behavior. When examining the abnormal grain growth behavior, the rate of grain growth increased with temperature in excess of a standard Arrhenius behavior, as shown in Figure 2.6.

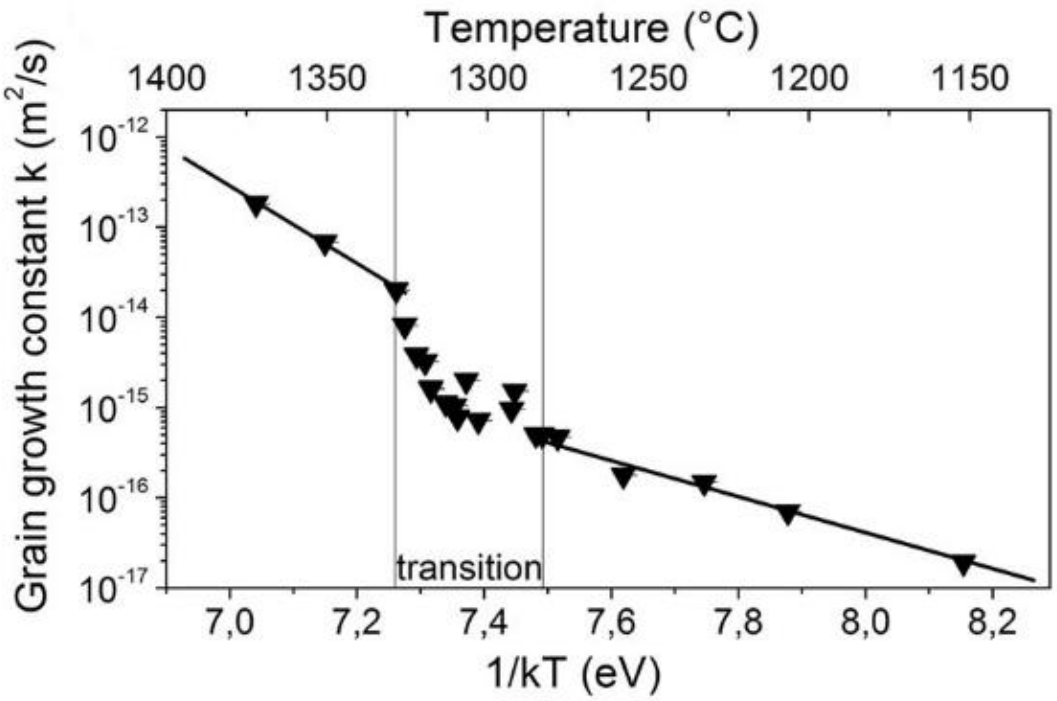

Figure 2.6: A plot of non-Arrhenius grain growth of $BaTiO_3$.[43]

Currently there have been few investigations into the equilibrium crystal shape of $BaTiO_3$. One study that has investigated the equilibrium crystal shape of $BaTiO_3$ is by Liou et. al.; however, the pores observed in this paper were non-equilibrated pores[44] In contrast to Wulff shape reconstructions in the $SrTiO_3$ system, this particular study was done using transmission electron microscopy (TEM), as shown in Figure 2.7. From this reconstruction, it was determined that the (100), (110) and (111) facets were present; however, from a TEM image it would be very difficult to see any additional facets. From this analysis it also not possible to determine the relative sizes of the viewable facets as the pore was elongated and considering the nature of a TEM image.

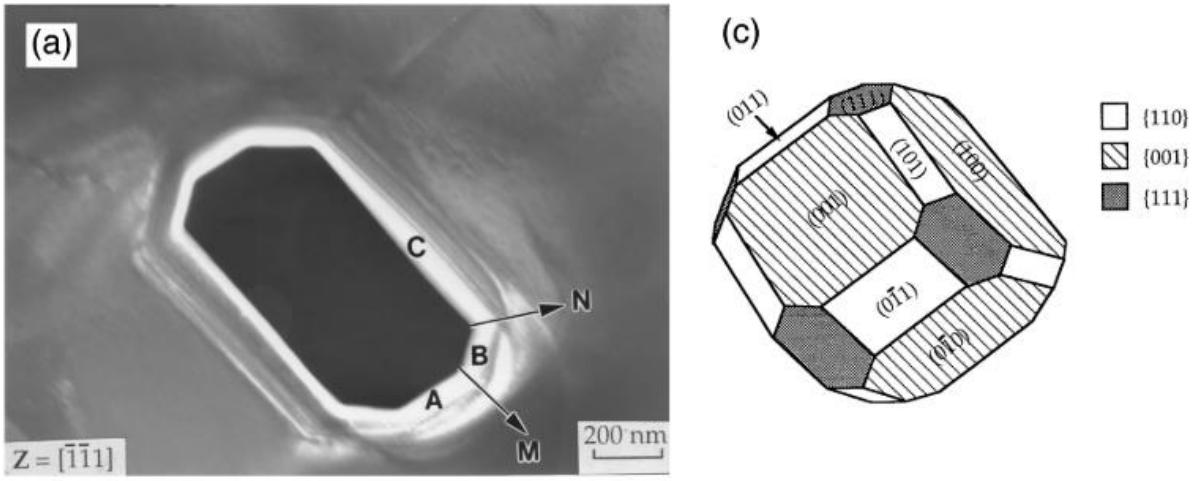

Figure 2.7: A micrograph of a $BaTiO_3$ pore shape obtained using TEM and the resulting reconstruction.[44]

2.3 $BaSrTiO_3$

$BaTiO_3$ was chosen as the secondary compound to alloy with $SrTiO_3$ as Barium and Strontium are full interchangeable on A site of the perovskite structure.[45] This work adds the

unique addition of observing the effect of varying the A site composition of the perovskite structure. This section will discuss differences in the $BaTiO_3$ and $SrTiO_3$ systems and further discuss the motivation behind alloying these two compounds.

Previous grain growth experiments on $BaTiO_3$ showed that it has a non-Arrhenius behavior, opposite of that of $SrTiO_3$.[43] There is a temperature region in $BaTiO_3$ where the rate of grain growth increases faster than the Arrhenius grain growth rate, as shown in Figure 2.8, comparing the grain growth rates of $BaTiO_3$ and $SrTiO_3$. One initial hypothesis of this work is that when alloying $BaTiO_3$ and $SrTiO_3$ together, due to the diverging non-Arrhenius behaviors it may be possible to see transitions across the composition range in the equilibrium crystal shape and faceting behavior.

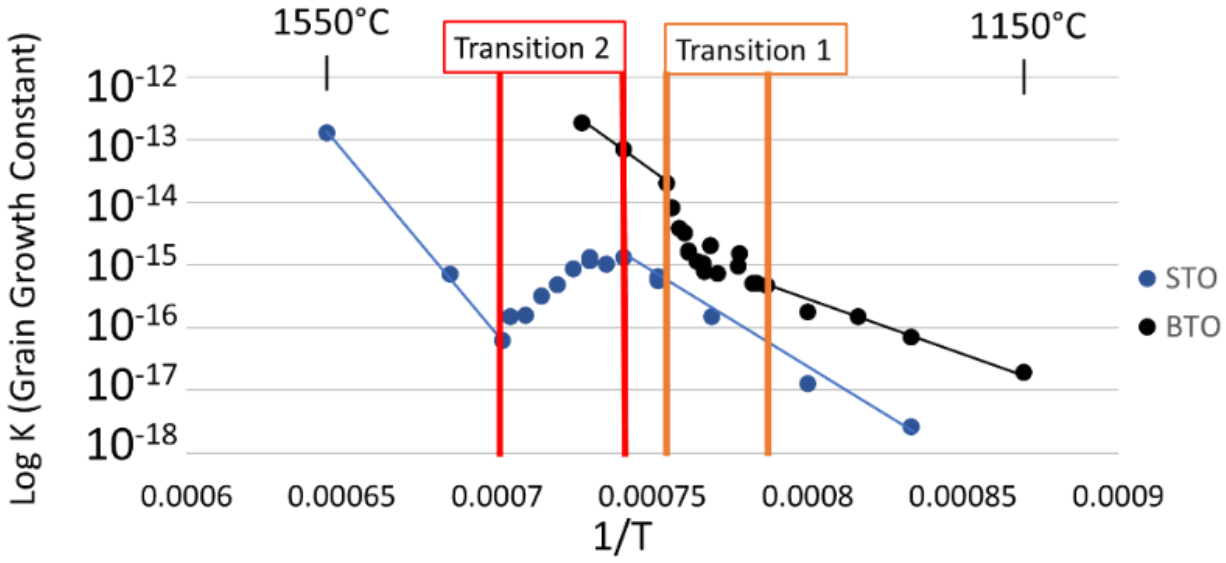

Figure 2.8: A cumulative plot of non-Arrhenius grain growth for $BaTiO_3$ and $SrTiO_3$.

One additional difference between $BaTiO_3$ and $SrTiO_3$ is in the type of vacancies that form. $SrTiO_3$ characteristically has defects at the strontium lattice position, while $BaTiO_3$ has defects in the titanium lattice position.[46][47] In relation to grain boundary movement, in $SrTiO_3$ it was observed increased strontium defects increased diffusivity and when additional titanium was added the grain boundary movement slowed.[48] The $BaTiO_3$ system, is heavily influenced by the B site and oxygen vacancies.[49]

A third difference of note between the two systems is the difference in melting temperature of the $BaTiO_3$ and $SrTiO_3$ line compounds. Phase diagrams for both systems are shown in Figure 2.9. The $BaTiO_3$ line compound has a melting temperature of 1625°C while the $SrTiO_3$ line compound has a melting temperature of 2040°C. When considering an alloy of these two materials, it is necessary to consider the effect of the melting temperature on samples of varying Ba-Sr ratio.

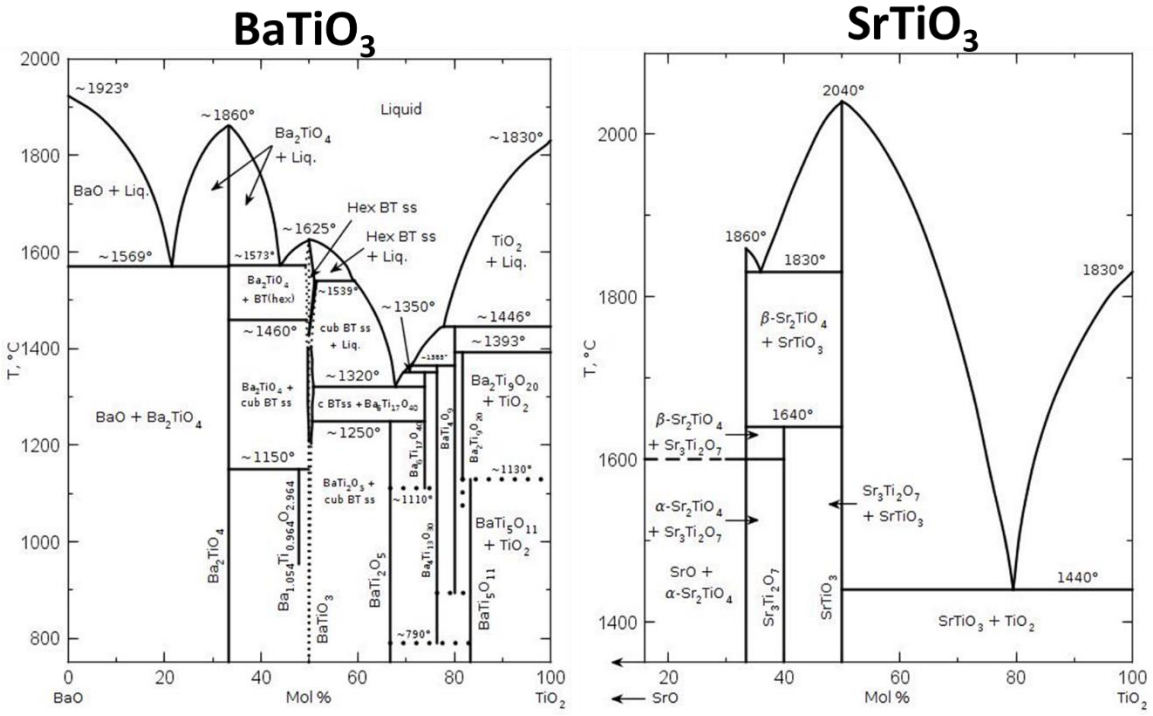

Figure 2.9: $BaTiO_3$ and $SrTiO_3$ phase diagrams [48][49]

3. PODWER PRODUCTION AND SINTERING

3.1 Mixed Oxide Route

$BaSrTiO_3$ powder was created using a mixed oxide route. This method was used to create samples for this work as it was previously used in the experiments by Bäurer et al.[48] Pure $BaTiO_3$ powder was processed along with 25%:75% Ba:Sr, 50%:50% Ba:Sr and 75%:25% Ba:Sr in $(Ba,Sr)TiO_3$. The base powders used for this experiment were 99.9% strontium carbonate ($SrCO_3$), 99.999% barium carbonate ($BaCO_3$), and 99.9% titanium oxide (TiO_2), all of which were sourced from Sigma Aldrich. $BaCO_3$, $SrCO_3$, and TiO_2 powders were combined in proportion to the corresponding composition and mixed in isopropyl alcohol with 2mm yttria-stabilized zirconia (YTZ) milling media using an attrition mill produced by Dayton Electric MFG. for 4 hours. The powder and alcohol were then separated using a Yamato RE500 roto evaporator. The powder was allowed to dry overnight in an oven at 60°C. The dry powder was sieved using a RX-29 Rotap by W.S. Tyler Inc. and a 160µm sieve. 10mm YTZ milling media was added during the sieving process to help break up large agglomerates. The mixed powders were calcined at 1100°C in air in alumina crucibles. Calcined powders were analyzed using a Bruker D8 Focus X-ray diffraction (XRD) instrument to verify the completion of the calcination process. The calcined powder then was attrition milled a second time, dried and sieved. The final powders had an average particle size of approximately 400nm. This measurement was done by measuring the average diameter of particles in a SEM micrograph.

Powder pellets of each composition were pressed using a 12mm diameter die in a hydraulic press. Pressing was done with an applied pressure of approximately 10 MPa. The resulting pellets were approximately 3mm in thickness.

3.2 Chemical Analysis

To confirm the homogeneity of the $BaSrTiO_3$ of varying compositions, the powder samples were analyzed using XRD. The resulting XRD patterns are shown in Figures 3.1-3.4. The calcination and mixing steps were determined to be complete once the patterns showed well-defined individual peaks. Powders that were not sufficiently calcined were milled a second time and calcined with increased temperature and time to allow for complete reaction of initial powders. Incomplete calcination was observed by the presence of double peaks in the X-ray pattern. Some samples showed an amorphous region near 30° that is attributed to the polymer sample holder used during analysis. The measured peaks were then compared to XRD standards, shown by the red lines in each corresponding figure. XRD analysis determined the mixing and calcination to be complete after the final calcination step.

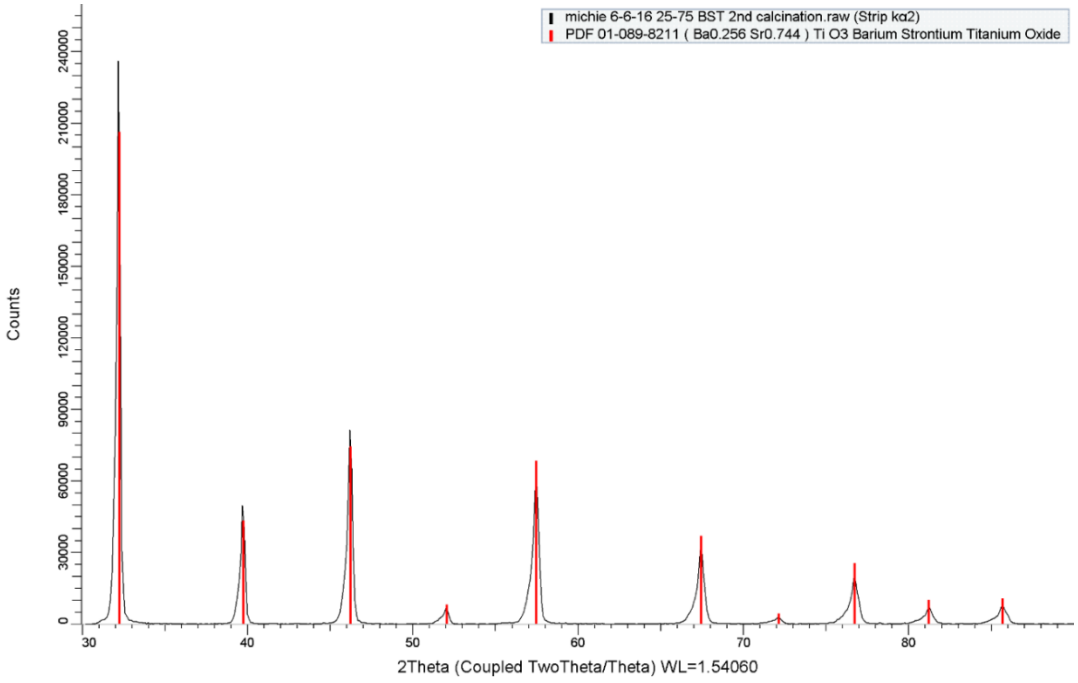

Figure 3.1: An XRD pattern of calcined $BaSrTiO_3$ powder of composition Ba25-Sr75 with matching reference pattern.

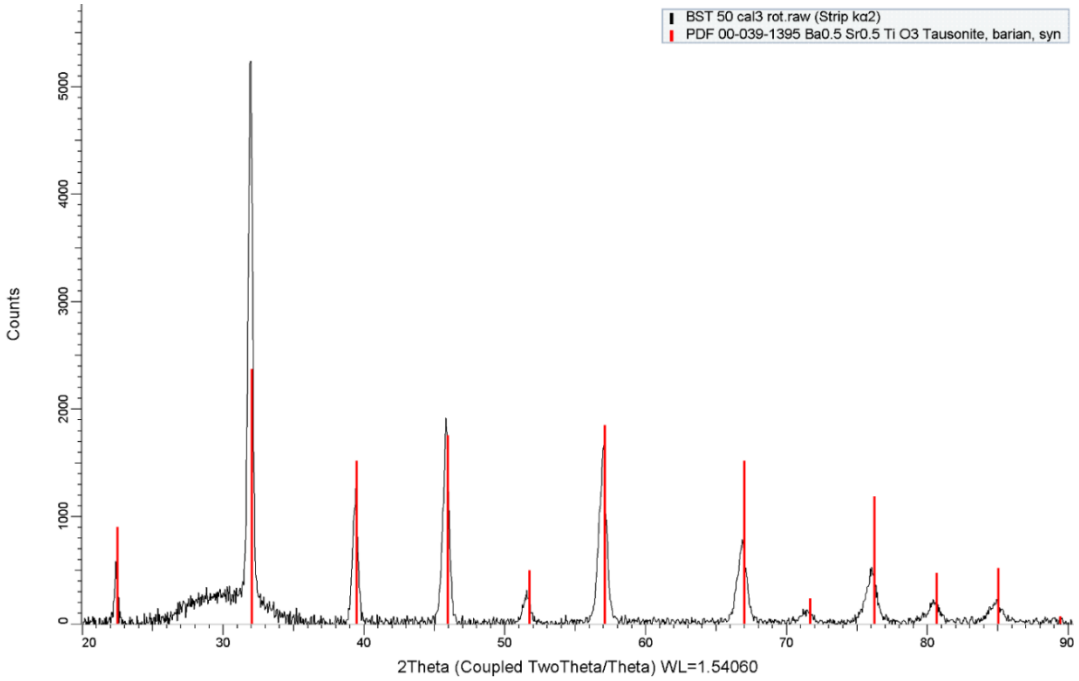

Figure 3.2: An XRD pattern of calcined $BaSrTiO_3$ powder of composition Ba50-Sr50 with matching reference pattern.

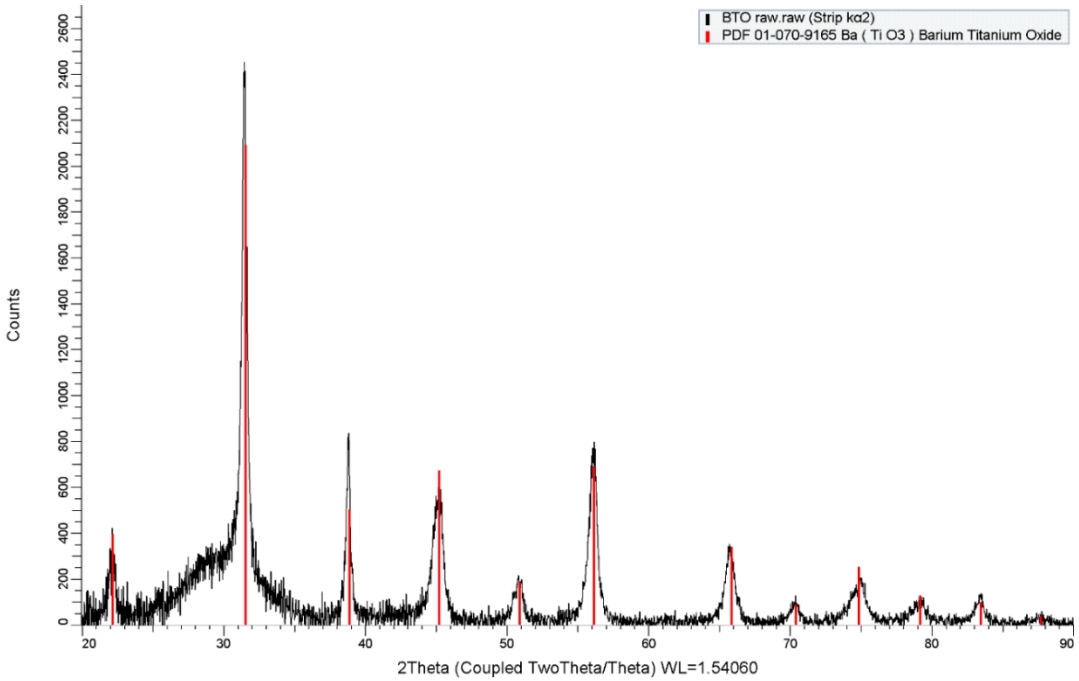

Figure 3.3: An XRD pattern of calcined $BaSrTiO_3$ powder of composition Ba75-Sr25 with matching reference pattern.

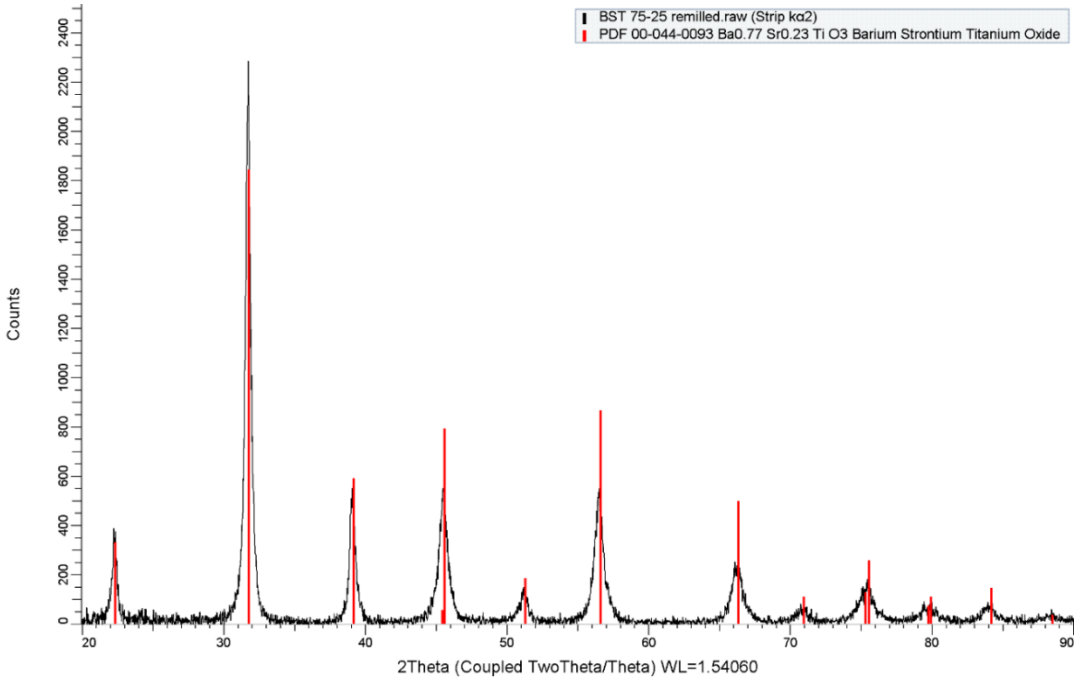

Figure 3.4: An XRD pattern of calcined $BaTiO_3$ powder with matching reference pattern.

3.3 Sintering and Thermal Etching

These samples were sintered in air at 1550°C for 10h. The sintering temperature was determined by the motivation to have as many small intergranular pores as close to equilibrium as possible and avoiding the melting temperature of the primary $BaTiO_3$ phase. With these constraints it was desired to sinter the sample at the highest temperature and longest time reasonable. The temperature of 1550°C was chosen as it was safely below the melting point of $BaTiO_3$ line composition of 1625°C.[50] A sintering time of 10h was used to ensure ample time to equilibrate based on the calculated time using the model proposed by Choi et. al.[52] Samples that were to be used for surface faceting were then thermally etched between 1100-1350°C for 10h. A grid was scratched into the surface of the samples to more easily find the same sample location for analysis using multiple techniques.

SEM micrographs were taken of the faceted surfaces of each composition and then EBSD was performed to obtain orientation information. A FEI Quanta SEM with an EDAX EBSD attachment was used for this analysis.

3.4 Polishing

The sintered pellets were then ground and polished. The samples were initially ground using increasingly fine silicon carbide paper until 1200 grit. The samples were then polished using 6µm, 3µm and 1µm Dimond suspensions. For the final polishing step, samples were polished using a GIGA-0900 vibratory polisher by PACE Technologies using SIAMAT 2 colloidal silica. After polishing, samples were cleaned in a sonicating bath to remove residual polishing media.

4. EQUILIBRIUM PORE SHAPE ANALYSIS

4.1 Introduction

This section will discuss the analysis of the equilibrium crystal shape or Wulff shape by observation of intergranular pores. As discussed in section 1, the equilibrium crystal shape is the shape of a grain with minimized surface energy in an isolated and unconstrained system. The Wulff construction is a section of the polar plot of a crystal representing the surface energy as a function of orientation. The Wulff shape is determined by drawing lines normal to the surface energy plot and the resulting shape formed from planes normal to the radius vectors. This equilibrium crystal shape is commonly observed experimentally through small, intergranular pores in the material of interest. This same procedure is used in this section of observe the Wulff shape of $BaSrTiO_3$.

As discussed in section 2, this work is motivated by the desire to better understand the non-Arrhenius grain growth behaviors of $BaTiO_3$ and $SrTiO_3$. It has been proposed that one possible contribution to this grain growth anomaly may be related to surface energy anisotropy. This section will explore how the surface energy anisotropy changes with Ba-Sr ratio.

4.2 Experimental Procedure

This experiment was used to analyze pure $BaTiO_3$ and three compositions of $BaSrTiO_3$. The samples were prepared as described in the powder processing section of section 3. The samples shown in this section were polished samples, and SEM micrographs of each sample were taken. The pores' images are of isolated pores within a grain. When choosing pores, the smallest available pores, free from debris or damage, were chosen for analysis.

The SEM images were reconstructed into 3D models using the Equilibrium Wulff Shape Generator software.[53] In the software, a cubic crystal system was chosen and the facet planes were manually chosen. The facets (100), (110), (111) and (310) were initially chosen, as the same facets were used in the $SrTiO_3$ work by Rheinheimer et al.[24] Additional facets were added to the 3D reconstruction based on the SEM images. These new facets were determined through trial and error to identify which facets most closely represented those in the micrographs. The 3D reconstruction was adjusted using the relative energy sliders in the software until the shape was approximately equivalent to the SEM micrograph. To increase the accuracy of this adjustment, the transparency of the SEM image was adjusted, and the image was overlaid on the 3D model to check relative sizes of each plane. This process is shown in Figure 4.1. This process was repeated for a minimum of 10 pores for each composition except for the Ba75-Sr25 composition. For this composition, only 5 pores were reconstructed, as the pores of this sample were much more deteriorated, and it proved difficult to image unobscured pores.

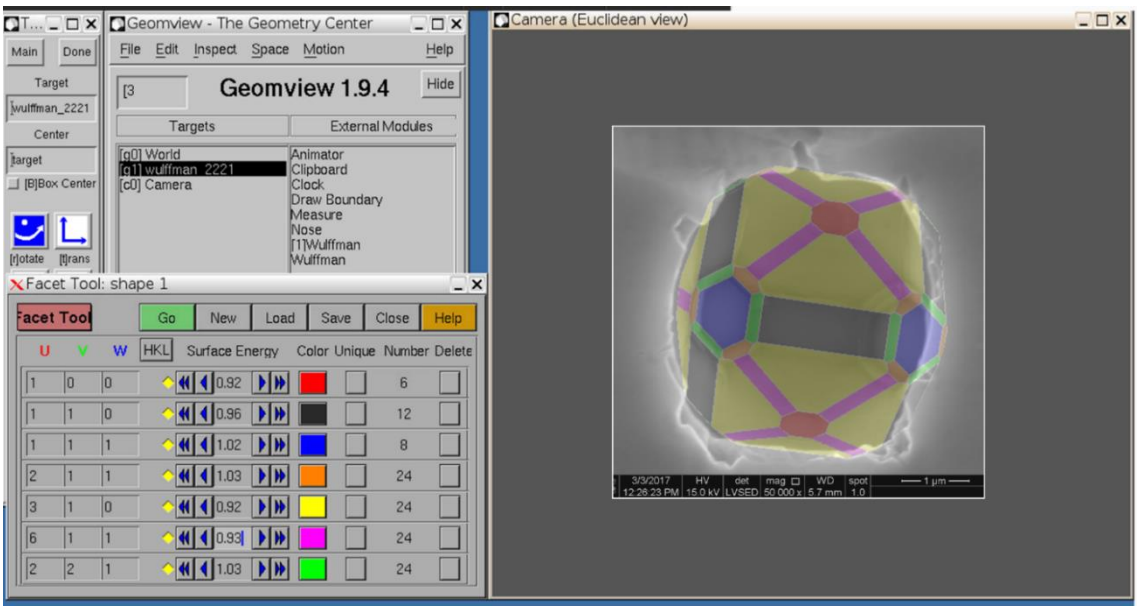

Figure 4.1: An image of the Wulff shape reconstruction process utilizing the equilibrium Wulff shape generator software. In this image, an SEM image with reduced opacity is overlaid on the reconstruction to verify the relative surface energies.

4.3 Results

Representative images for each composition are shown in Figure 4.2-4.5 for the four compositions tested. All samples were prepared as described in section 4.2 with the addition that the $BaTiO_3$ samples that were thermally etched as they were previously used in the experiment discussed in section 5. These pore images were visually reconstructed in the Equilibrium Wulff Shape Generator software shown in section 4.2. During this reconstruction (100), (110), (111), (211), (310) and (611) planes were observed on all compositions. The (221) facet was observed only on in the Ba50-Sr50 composition. An example reconstruction containing all the possible facets is shown in Figure 4.6. The relative energies for each composition are reported in Table 4.1. These results were then plotted in Figure 4.7 for all compositions with standard deviation error bars.

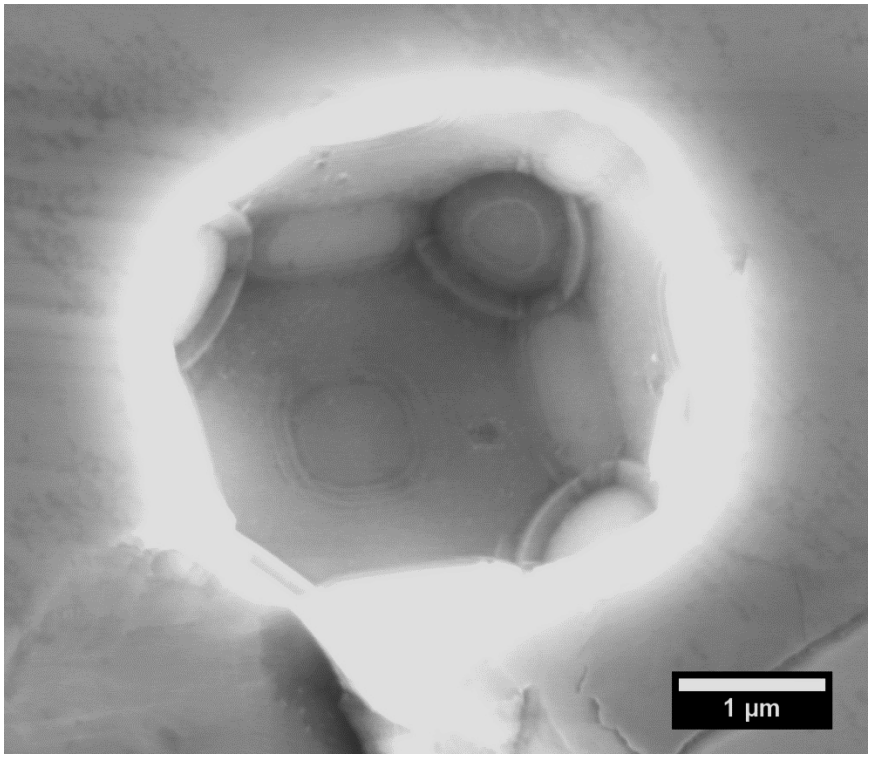

Figure 4.2: A representative SEM micrograph of a pore of $BaSrTiO_3$ of composition Ba25-Sr75.

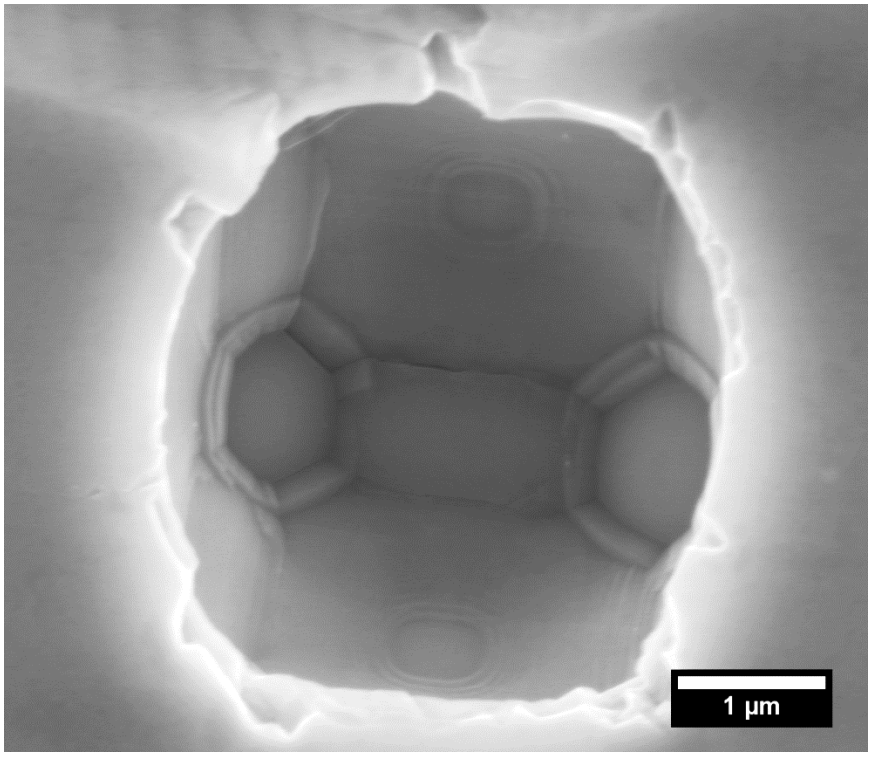

Figure 4.3: A representative SEM micrograph of a pore of $BaSrTiO_3$ of composition Ba50-Sr50.

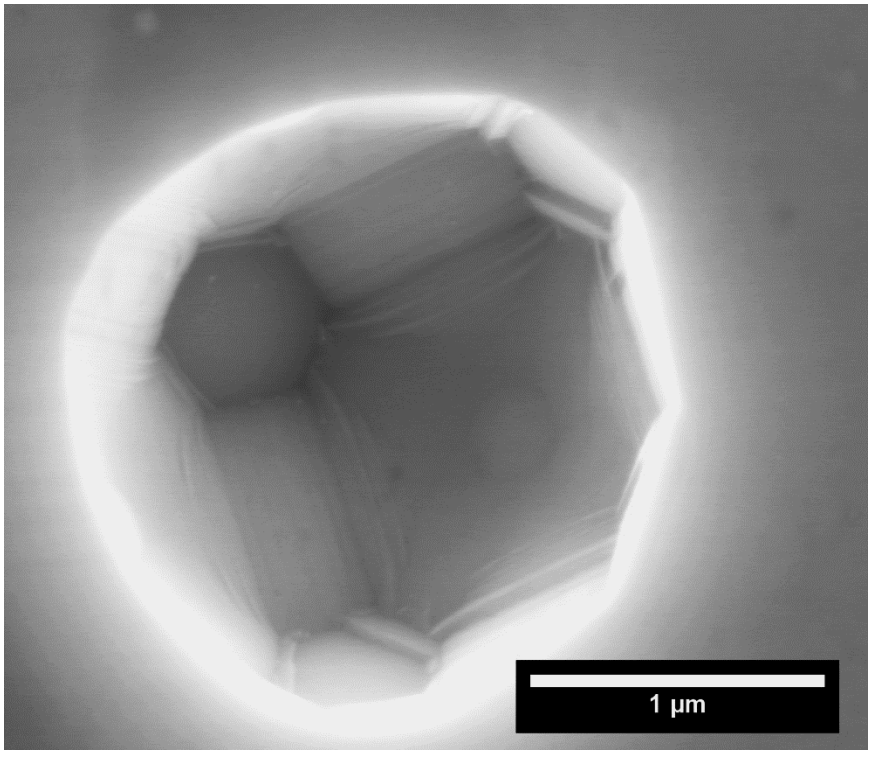

Figure 4.4: A representative SEM micrograph of a pore of $BaSrTiO_3$ of composition Ba75-Sr25

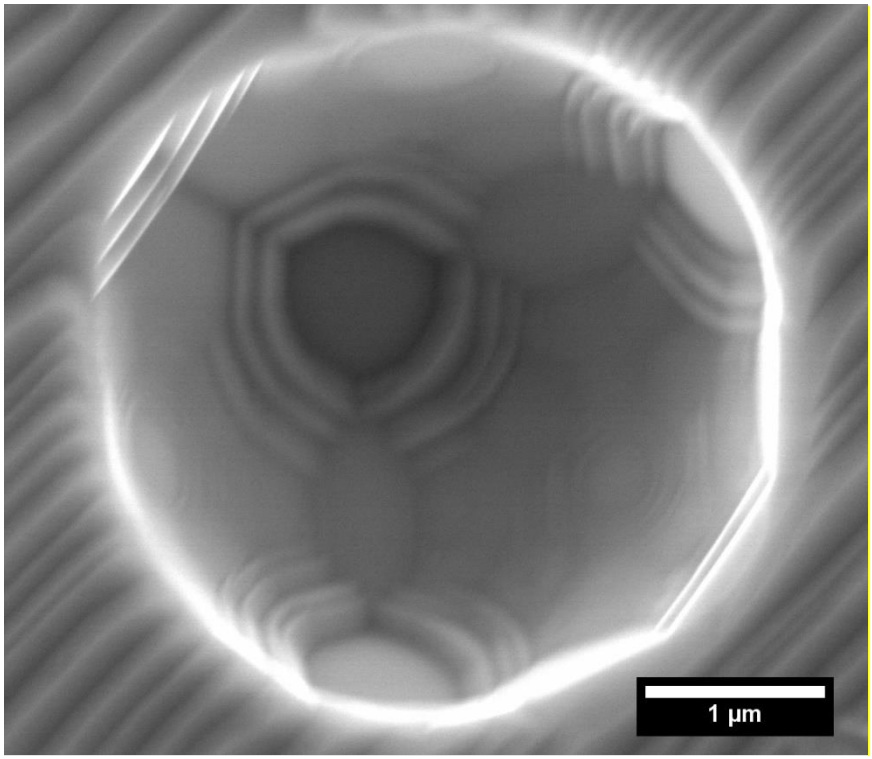

Figure 4.5: A representative SEM micrograph of a pore of $BaTiO_3$.

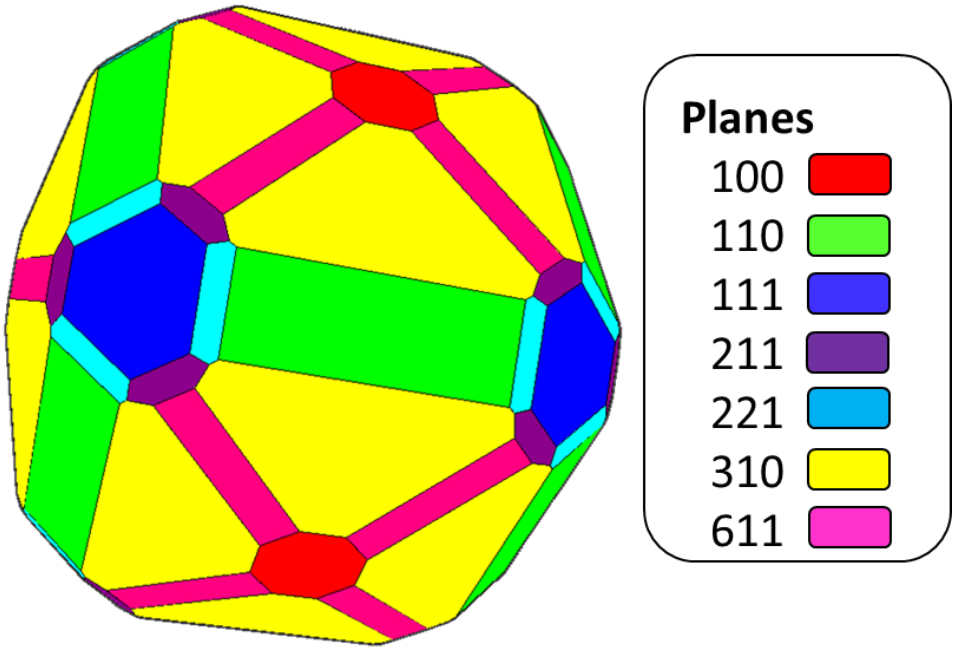

Figure 4.6: A representative pore reconstruction with all possible facets observed in the pore shape.

The reconstructions of each pore assumed that the Wulff shape is fully faceted. This assumption is necessary for an initial reconstruction of the Wulff shape. By only utilizing pore images, it is difficult to differentiate between a rounded plane with many stable orientations as opposed to one distinct facet. It is also difficult to determine the types of transitions from one facet to another only utilizing pore images. For this information, it is necessary to utilize additional techniques, as discussed in section 5 and 6.

The energy values calculated are relative values in relation to the other facets reconstructed. It is necessary to normalize these values to compare across compositions. The (111) facet was the most consistent in size when comparing pore to pore within a composition. For this reason, it was chosen to normalize the relative energy values to the (111) facet. When normalizing to the (111) facet it is no longer possible to compare the relative energies of the (111) facet. It is also for this reason the values of the (111) facet are 1 in Table 4.1 and are a constant value in Figure 4.7. As mentioned above, the (221) facet was only reconstructed in the Ba50-Sr50 composition, resulting in only one point plotted in Figure 4.7.

Table 4.1: Relative surface energies values obtained through pore reconstruction for all compositions.

Relative Surface Energy							
(hkl)	(100)	(110)	(111)	(211)	(310)	(611)	(221)
Ba25-Sr75							
AVG	0.866	0.930	1.000	0.998	0.887	0.887	N/A
STDEV	0.015	0.015	0.000	0.009	0.013	0.013	N/A
Ba50-Sr50							
AVG	0.905	0.941	1.000	1.024	0.909	0.917	1.016
STDEV	0.025	0.020	0.000	0.042	0.026	0.025	0.006
Ba75-Sr25							
AVG	0.901	0.951	1.000	1.007	0.915	0.915	N/A
STDEV	0.031	0.022	0.000	0.014	0.021	0.023	N/A
BaTiO3							
AVG	0.900	0.952	1.000	1.004	0.905	0.912	N/A
STDEV	0.052	0.030	0.000	0.030	0.043	0.045	N/A

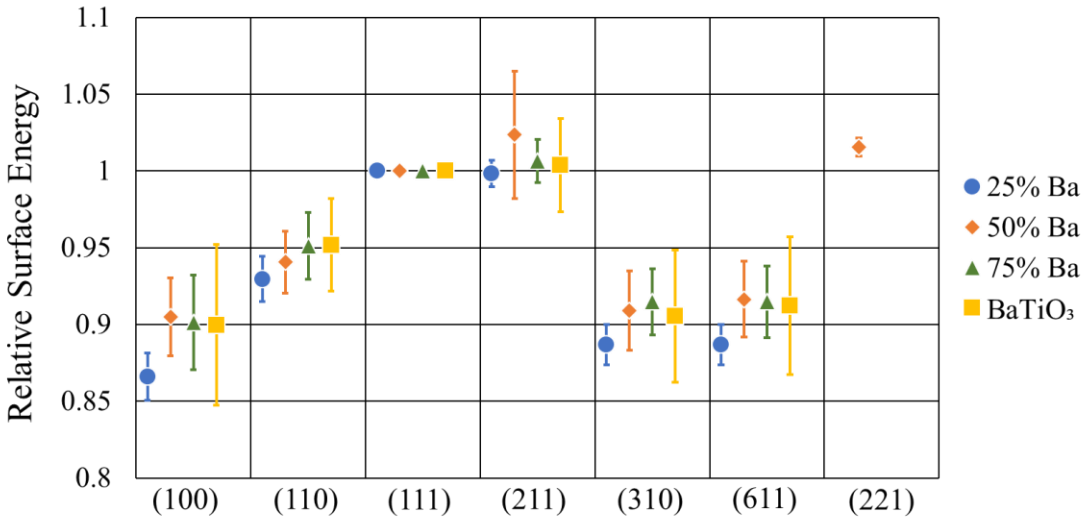

Figure 4.7: A plot of the average relative surface energies of each facet by composition.

4.4 Discussion

The pore reconstruction experiment has provided critical information for better understanding the Wulff shape of $BaSrTiO_3$. The first key information gathered is which surface facets may exist. From the data in section 4.3, the (100), (110), (111), (211), (310), (611) and (221) are all possible facets that may be seen in this system; however, it is necessary to understand the limitations of this method. This method involves visually comparing an intergranular pore to that of a 3D reconstruction and attempting to create a replica that most closely resembles the pore. This method can help to identify how many different surface facets exist; however, it does not precisely determine which facets exist. Determining which facets exist involves using previous research about the system as well as test fitting facets through trial and error.

From previous research of the $BaTiO_3$ and $SrTiO_3$ systems, the (100), (110), and (111) plane are common low energy planes and there is a high level of confidence that these planes would also exist in the intermediate compositions, as they exist in the end members. The additional four planes have a higher level of uncertainty. The (310) facet was observed in the $SrTiO_3$

reconstructions by Rheinheimer, discussed in section 2. This surface was also observed across all compositions, giving this facet a higher level of confidence. Features that have been labeled as the (221) and (611) surfaces are in the same location as the microfaceted regions presented by Rheinheimer. These facets, along with the (221) facet being only observed in one composition, leave a much higher level of uncertainty. These four planes may represent distinct facets or may be curved continuous regions of the Wulff shape. It is also possible that some artifacts of the observed pore shapes are not truly part of the Wulff shape but, instead, are kinetic artifacts that are not fully equilibrated.

To obtain pores shapes that are most closely represent the true Wulff shape, it is beneficial to process samples at high temperatures for a long as feasible. The model by Kitayama et al. was used as a reference for determining ideal processing parameters and pore sizes needed.[31] It was calculated that pores with an initial radius of 2µm would take approximately 3.5 hours to equilibrate at a temperature of 1550°C. The diffusion data from this calculation came from Jin et. al.[54] The experimental sintering time of 10 hours was chosen based on this calculation to ensure the observed pores were representative of the equilibrium shape.

When reconstructing facets that have higher degrees of uncertainty, the determination of which facets exist was compared across multiple pores. Observing the transitions between planes and number of sides of the surfaces can help identify what planes exist and limit possible choices of planes. One example is when reconstructing the (111) plane shown in Figure 4.6 in section 4.3. This surface had six sides, with three sides being shorter than the other three. Some of the neighboring planes and relative energies resulted in the (111) plane having only 3 sides. This method is limited in determining a small angle difference in possible planes. For example, the

(611) plane was determined the have the closest fit; however, a (511) or (711) plane could result in a Wulff shape that appears similar.

When observing the relative energies of each facet, there was a large variance between pores at the same composition. Some of this variance was due to kinetic differences in the pores. When choosing pores to image, the smallest resolvable pores were chosen; however, there was a distribution of pore sizes in the observed facets, the average pore size was approximately 2µm. The differences in pores size were likely primarily responsible for some of the differences in apparent relative surfaces energies within a composition. Another possible source of variance is due to the viewing angle of the pores. The observed width of a facet may appear smaller than the true width if not viewing from the normal direction of the plane. Due to the mechanics of electron microscopy, it was difficult to obtain clear images some pores. It was frequently difficult to obtain good contrast; if the pore was too deep, the electrons may have difficulty reaching the detector. Pore selection was critical, as it is possible to have had pores that were filled with contaminants, were damaged during polishing, or were too large to be useful in obtaining accurate data. As shown in Table 4.1 in section 4.3, the standard deviation is greater than the variance in energy across compositions. Utilizing only pore reconstructions, it was not possible to determine changes in faceting behavior with composition with the one exception of the (221) facet only appearing in the Ba50-Sr50 composition. Overall, this experiment has provided critical information; however, more analysis is needed for an accurate representation of the Wulff shape. Sections 5 and 6 will introduce two additional experiments informed by the results of this section.

5. SURFACE FACETING AFM ANALYSIS

5.1 Introduction

The motivation of this study is to accurately determine the faceting behavior of barium strontium titanate alloys. The pore shape experiments in section 4 provided a foundation as to what facets may exist in the pore shape; however, more work is needed to refine this reconstruction of the Wulff shape. This experiment uses atomic force microscopy (AFM) to observe surface facets of grains. This method will allow for the verification of the facets chosen in section 4 or the refinement of what facets appear in the Wulff shape. Unlike in pore shape measurements, where the facets are reconstructed only from images, this technique will allow for the measurement of exact type of facet. Additionally, while this method will not allow for direct measurement the relative surface energies of the facets, it will help determine which facets are in contact with one another.

The data from this experiment will be plotted on a stereographic projection. To more easily keep track of the reconstructed facets, the reconstructed facet information has been mapped onto a triangle of a stereographic projection, as shown in Figure 5.1. The black triangle on the pore reconstruction corresponds to the stereographic triangle. The colors on the stereographic triangle correspond to the colored facets of the reconstruction. The black tie lines on the stereographic triangle correspond to which facets are in contact with one another. These plots are comparable to the n-diagram concept by Cahn and Handwerker.[32] The pore shape in Figure 5.1 is used, as it has all of the possible facets observed from the pore shapes in section 4, despite the (212) facet only being reconstructed in a select composition. This reconstruction will be discussed in greater detail in section 5.4.

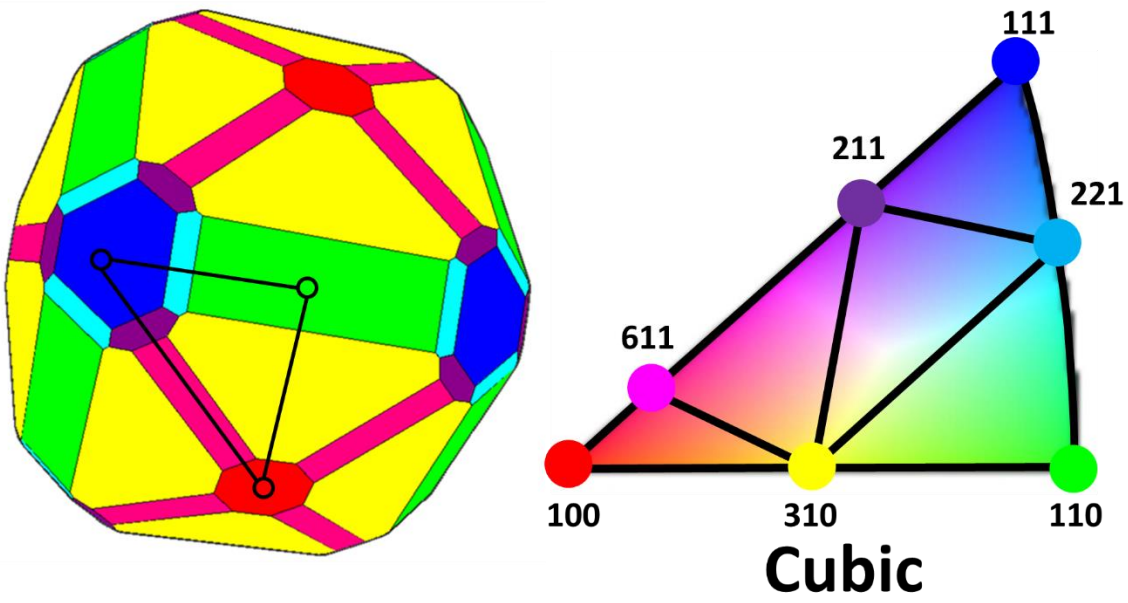

Figure 5.1: Pore shape reconstruction with labeled facets plotted on a single traingle of a stereographic projection.

5.2 Experimental Procedure

Samples in this experiment were processed as described in section 3. For this work, Ba25-Sr75 and Ba75-Sr25 were analyzed and compared. These compositions were chosen to represent both a barium rich sample and a strontium rich sample. The Ba25-Sr75 composition was thermally etched at 1100°C and the Ba75-Sr25 composition was thermally etched at 1300°C. These etching temperatures allowed for faceted surfaces to be easily seen using electron microscopy. The samples were observed in the SEM and a location with well-defined facets was chosen. EBSD was then performed on this area to determine the orientation of the grains. The same location of the sample was analyzed using atomic force microscopy (AFM). This process was simplified by scratching a reference grid on the sample to find the same grains when transitioning from the SEM to the AFM. A high-resolution scan of the interior region of each

grain was made, being careful to avoid the grain boundary in the scan. This resulted in a scan containing only the facets of each grain. The SEM images and AFM images were then compared and overlaid. A rotation angle between the two samples was calculated to correct for misalignment when transferring the sample from the SEM to the AFM.

The AFM data was exported to a text file containing the topography data with corresponding x and y positioning. This file was analyzed by a series of MATLAB scripts, located in appendix B. These scripts were an adapted and expanded version of the MATLAB script developed by Lowing, D.[55] An initial script inputs the AFM data file, Euler angles of the same grain from the EBSD analysis, and the misalignment angle from transferring instruments. The AFM data provides z height data with x and y coordinates in the laboratory reference frame. The EBSD data provides the orientation of each grain and the Euler angles used to rotate the grain between a crystal reference frame and a laboratory reference frame. This script converts the AFM data into the crystal reference frame and provides the normal vectors of the AFM data. The misalignment angle calculated corrects for the misalignment between the SEM laboratory reference frame and the AFM laboratory reference frame.

The script fits 9-point grids to the AFM dataset and uses a least squares plane fitting method to determine the normal direction of the grid. The normal vectors are then rotated with a Bunge rotation matrix using the Euler angles from EBSD and correcting for the laboratory frame misalignment. This results in a new dataset of normal vectors of the AFM surface in the crystal reference frame. The script then performs an R^2 calculation to determine the goodness of fit and eliminates datapoints below a specified threshold. The R^2 cutoff was typically set to 90% to limit this noise. The goal of this procedure is to determine the normal directions of the facets. The data from the peaks and troughs of the facets will create additional noise that can make visualization

of the data difficult. This data was then plotted on a stereographic projection as both a scatter and contour plot. Additional scripts were developed to plot the data in ways that would allow for more accurate interpretation. The first method used was to use the cubic symmetry of the system and copy the datapoints into all sections of the stereographic projection. The script for this procedure can also be found in appendix B. It was later decided that this method created too much additional noise in the data and may lead to inaccurate data interpretation. The additional plotting method developed uses cubic symmetry to fold all vectors into one triangle of the stereographic projection. This data is used to plot both a scatter plot and an intensity plot. The plots from all grains measured, utilizing all the plotting methods developed, can be seen in appendix C.

5.3 Results

Ba25-Sr75 and Ba75-Sr25 samples were analyzed using an AFM, as described in section 5.2. The area studied of the Ba25-Sr75 sample is shown is Figure 5.2. An SEM micrograph was taken to observe the faceting behavior and an EBSD map of the area was taken. This section will discuss the data collected from grains 1 and 3 shown in Figure 5.2. After performing EBSD analysis, topography measurements were taken in the AFM, as shown in Figure 5.3. When transferring the sample from the SEM to the AFM, it was expected that there would be a small angle difference in the orientation of the sample. The red line on Figure 5.2 running parallel to the facets on grain 1 corresponds to the red line in Figure 5.3. This line was compared to green line in Figure 5.3 that is aligned parallel to the facets of grain 1. It was determined that there was a 6° rotational difference between the rotation of Figure 5.2 and Figure 5.3. This value was inputted into the MATLAB script along with the Euler angles of the grain determined by EBSD

and the raw topography data from the AFM image. The AFM data used in each dataset were individual images of the interior of each grain, avoiding imaging the grain boundary.

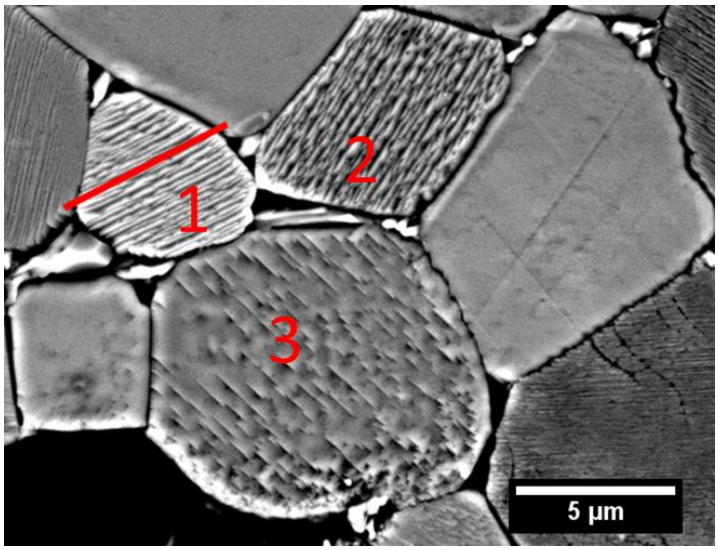

Figure 5.2: A SEM micrograph of thermally etched Ba25-Sr75 with grains labeled.

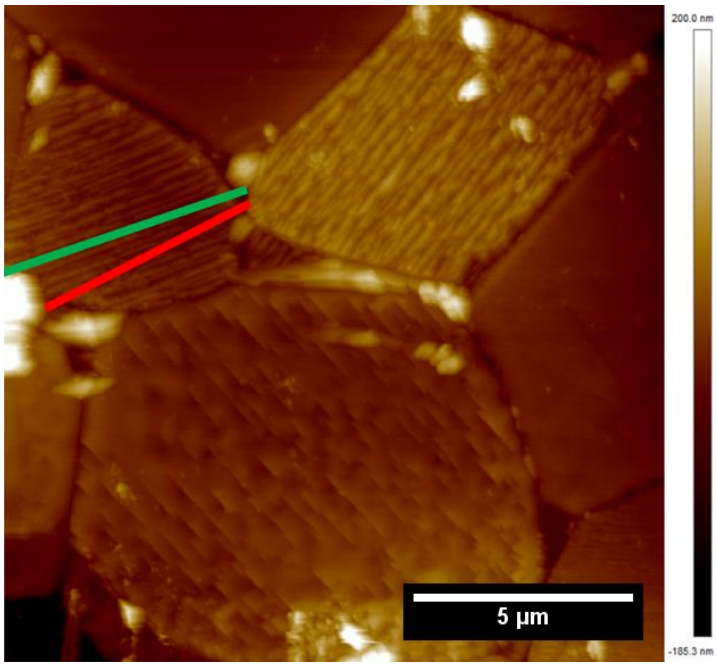

Figure 5.3: An AFM image of the Ba25-Sr75 composition with lines overlaid to show the angular correction between SEM and AFM reference frames.

The AFM topography data for each grain was processed through the MATLAB scripts described in appendix B and plotted on a stereographic projection. For each grain, the Euler angles collected by the EBSD map plus the added correction for the misorientation between the SEM and AFM laboratory reference frame were manually entered. To simplify this process, the EBSD map was processed to determine a single average orientation per grain, and that set of Euler angles was used for this analysis. The orientation across each grain typically was typically less than 0.5° except when points were identified as equivalent Euler angles due to symmetry. The MATLAB script plots a scatter plot and contour plot of the processed dataset and then mirrors the data points into one triangle of the stereographic projection.

As a proof of concept to verify, a smooth flat grain was chosen to verify that the MATLAB script was correctly rotating each dataset. This grain was found in the Ba75-Sr25 sample and is shown in Figure 5.4. This plot shows the grain orientation represented by the black square located in the center of the peak in the heat map, as would be expected for a smooth flat grain. This plot shows that the AFM data collected is being represented as expected in the stereographic projection, as well as demonstrating that the rotation matrix is properly rotating the AFM data from the laboratory reference frame to the crystal reference frame. It is now possible to continue to analyze the remaining grain from the Ba25-Sr75 and Ba75-Sr25 compositions.

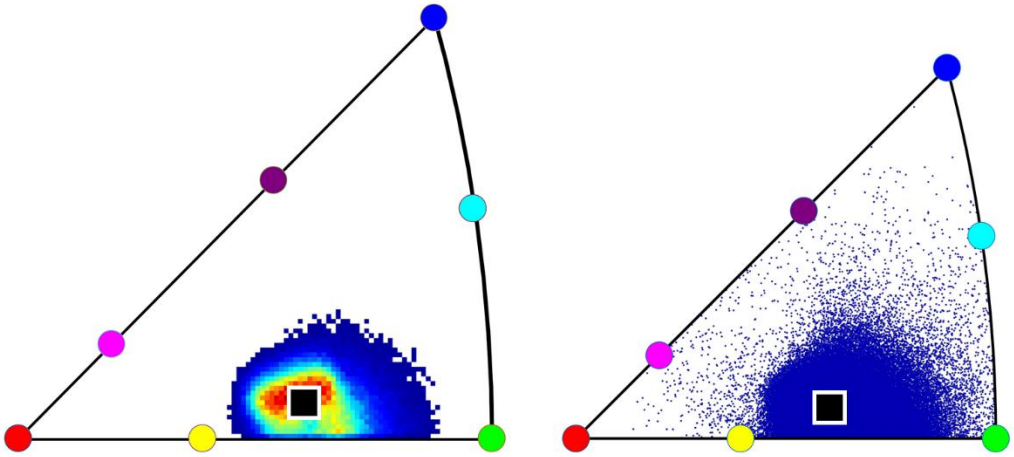

Figure 5.4: Normal vector distribution of surface facets for sample Ba75-Sr25 grain 3 with all data folded into a single stereographic triangle.

Observing the SEM image in Figure 5.2, grain 1 of composition Ba25-Sr75 had long facets that span the length of the grain. The surface of the grain had broken up into two dominant facets, with a small influence from a third facet. Areas where the surface facets were discontinuous and did not span the whole length of the grain imply there was some influence of a third facet. When analyzing Figure 5.5 and Figure 5.6, it is expected to see a minimum 2 facets present in the projections. This is seen in the two distinct peaks in the contour plot of Figure 5.5. The two peaks represent a concentration of normal vectors. The two peaks can also be observed in Figure 5.5 in the two concentrated regions of the heat map.

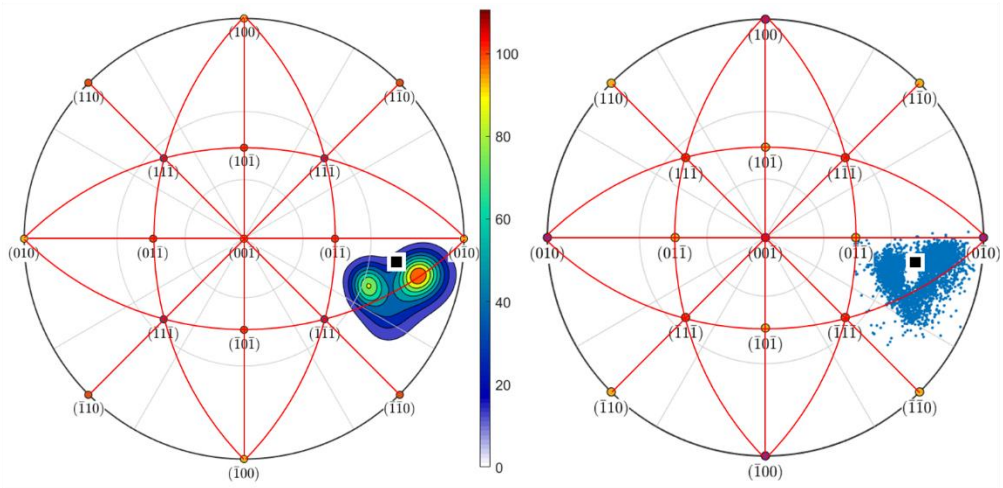

Figure 5.5: Normal vector distribution of surface facets for sample Ba25-Sr75 grain 1

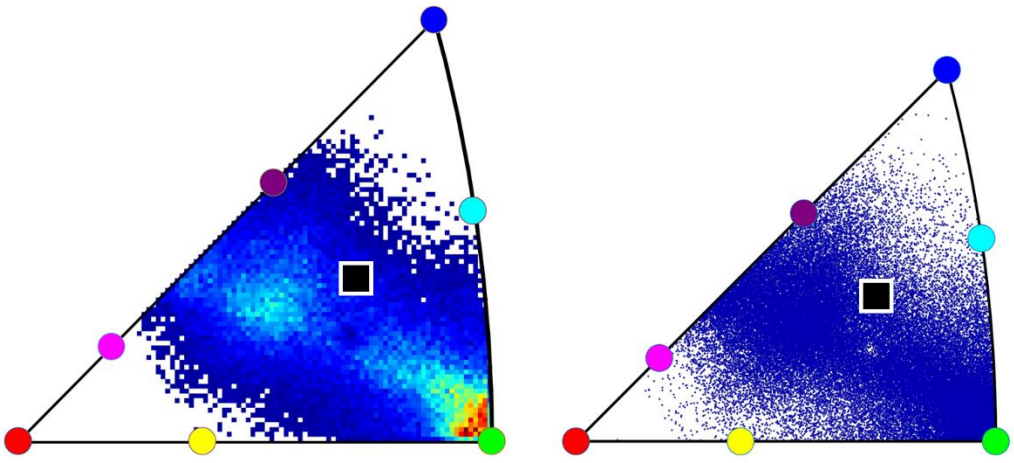

Figure 5.6: Normal vector distribution of surface facets for sample Ba25-Sr75 grain 1 with all data folded into a single stereographic triangle.

To allow for more accurate analysis of the datasets, the facet locations of the reconstructed Wulff shape have been added to the stereographic triangle of Figure 5.6, with each colored dot representing the corresponding facet in Figure 5.1. The surface normal of the grain being analyzed was also added to the figure as seen by the black square. As previously discussed, it is expected to see two or three concentrated areas for the faceting behavior of grain 1. With one facet only having a relatively small impact on the surface faceting, it was expected that this facet may be difficult to see in Figure 5.6 and the influence on the histogram heat map is much less. With all samples analyzed using this method, it will be difficult to see the appearance of the smaller contributing facets due to the noise in the data.

The concentration of normal vectors near the (110) pole suggests that the (110) facet is present in the surface faceting behavior. The second facet in Figure 5.5 is located between the (100) and (111) facets near what was identified as the (211) facet from the Wulff shape reconstructions. This faceting behavior has multiple possible interpretations. The simplest interpretation is that there is a facet between the (100) and (111) in contact with the (110) facet. This interpretation is complicated by the location of the peak on the heat map in Figure 5.6. As this peak does not align with the (211) or (611) facet as determined by the facets in the Wulff shape reconstruction it is feasible that the (211) facet may be a (311), (411) or some other facet between (100) and (111). The small angle difference between these facets would likely be difficult to see in SEM images. An additional complexity is that the peak shown in Figure 5.6 is not directly between (100) and (111), but closer to the interior of the triangle. This may mean that there is a facet present that is not on this line. This most intense area of this peak was calculated to be located at an orientation of (0.874,0.225,0.429). An approximation of this facet may be a (412) facet.

A second interpretation is that the (211) previously identified, or the possible (311) or (411) region, is not a facet but a rounded continuous region, or that there is a continuous transition between the two facets. If this surface were a curved continuous region, the normal vectors would appear as a larger area on the stereographic projection, as opposed to one single location. Additional data is needed to verify if the Wulff shape contains a continuous region.

The faceting behavior of Ba25-Sr75 grain 2 is plotted in Figure 5.7. The corresponding SEM image in Figure 5.2 suggests that there are three facets present in the surface faceting. Figure 5.7 shows one distinct peak, as well as 1-2 additional concentrated regions. The maximum located on the right side of Figure 5.7 is located closer to the (110) than the (221) facet shown in the reconstruction. This peak was calculated to be located at (0.688,0.245,0.682). This suggests that a (331) peak may be more accurate than the (221) peak originally constructed.

The additional faceting maximums have a higher level of uncertainty. The high intensity streak from the possible (331) peak to the line between (100) and (111) suggests this facet is in contact with the facet or continuous region along this line. The intersection location of this streak suggests the possibility of a facet closer to the (111) than the reconstructed (211). If this region is continuous instead of faceted, this behavior may suggest that the continuous region extends above the (221) location, and there is a possibility that a two-faceted region of surface facets may exist between the possible continuous region and the neighboring facets.

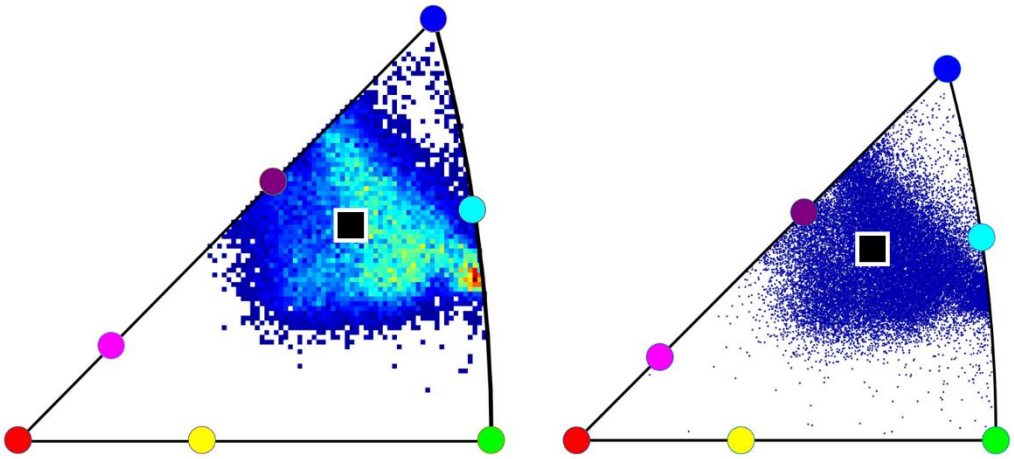

Figure 5.7: Normal vector distribution of surface facets for sample Ba25-Sr75 grain 2 with all data folded into a single stereographic triangle.

Data for grain 3 of the Ba25-Sr75 composition, collected in the same manner as described above, is plotted in Figure 5.8. The SEM micrograph in Figure 5.2 shows grain 3 to have facets that are spaced sporadically, and which do not span the length of the grain. From this image it is expected to have up to three different facets appear on the stereographic projections. The contour plot of Figure 5.8 shows two distinct peaks, with one more intense than the other, as well as a bulge at the bottom of the contour plot. For this data set, it is beneficial to observe the scatter plot of Figure 5.8 to more clearly see the faceting behavior. There are three groupings of scatter points; the approximate locations of these groupings have been identified by the three red circles. These three groupings represent the expected behavior for grains that had three surface facets. This data was then folded into one stereographic triangle and is shown in Figure 5.9.

The heat map data show one distinct peak, with a peak that was calculated to be located at (0.857, 0.363,0.363). This aligns with the previously suggested (311) plane from grain 1;

however, the three groupings observed in Figure 5.8 become harder to see. The data extends down the (611) peak identified in the reconstruction, supporting the claim that that these two planes are in contact with each other in the Wulff shape. The rounding of the data from the suggested (311) plane into the interior of the stereographic triangle would be consistent with a continuous region near (311).

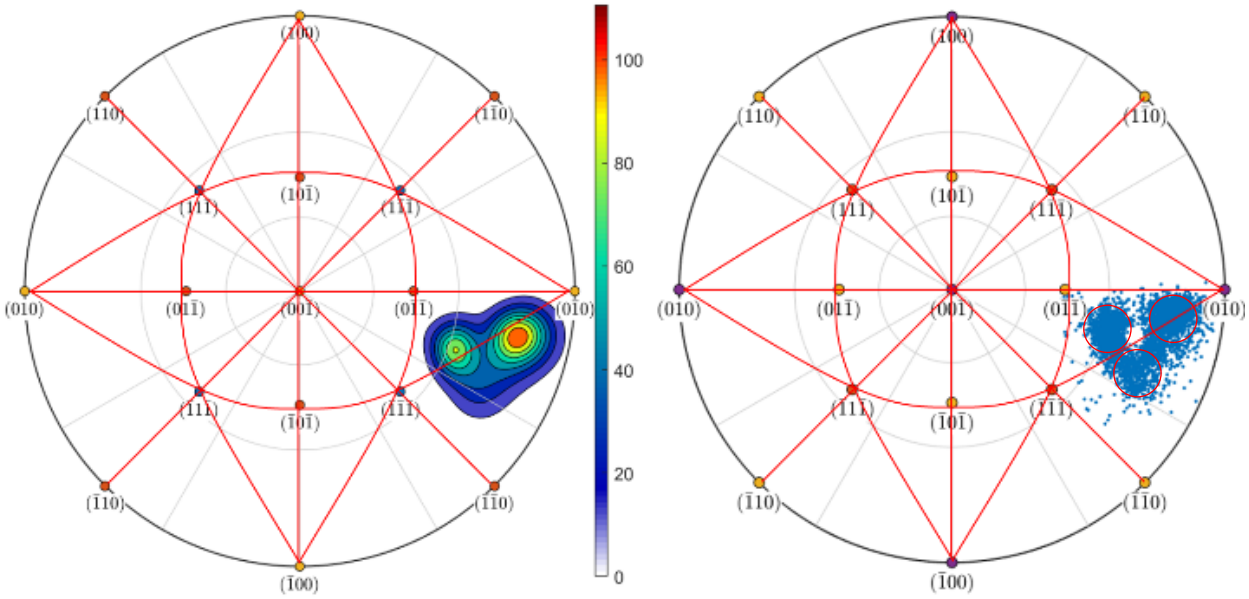

Figure 5.8: Normal vector distribution of surface facets for sample Ba25-Sr75 grain 3, with red circles overlaid on the scatter plot to indicate possible facet locations.

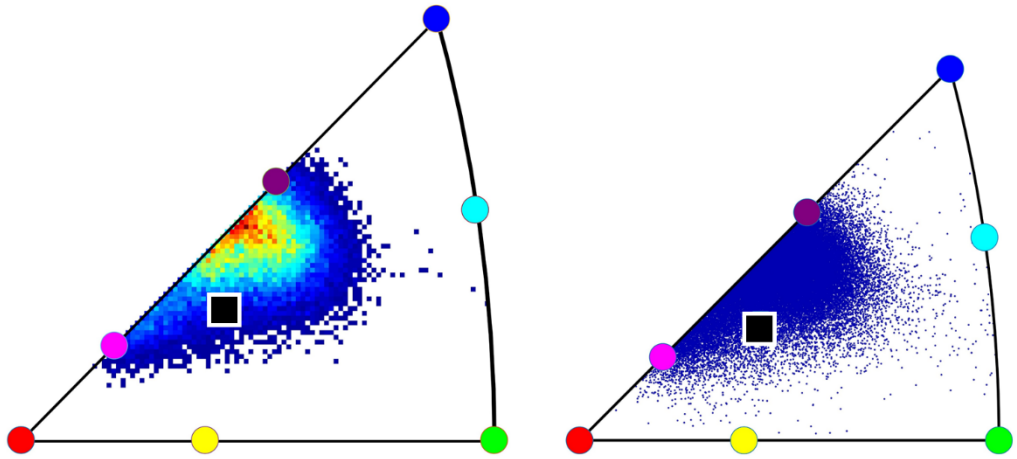

Figure 5.9: Normal vector distribution of surface facets for sample Ba25-Sr75 grain 3 with all data folded into a single stereographic triangle.

A fourth grain of B25-Sr75 was analyzed, and the resulting plots is shown in Figure 5.10. This grain appeared smooth and flat across a large portion of the grain; and this is seen in the maximum of Figure 5.10. The peak of the heat mat is in the same approximate location as the grain orientation represented by the black square on the plot. This would indicate that the largest influence on the data in this plot is not faceted data but the flat grain surface. The data does show a smaller influence from a facet that is either the (111) or a facet between the (111) and (211). This is consistent with the observation seen in grain 2.

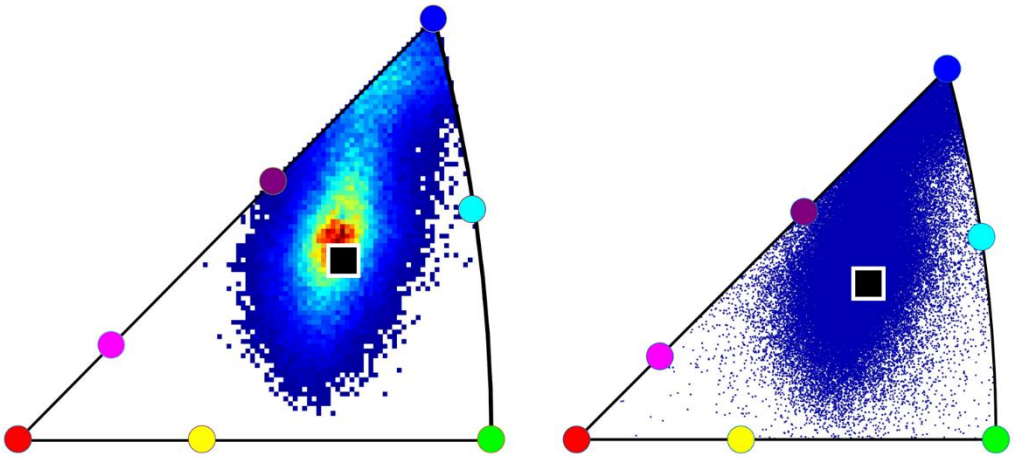

Figure 5.10: Normal vector distribution of surface facets for sample Ba25-Sr75 grain 4 with all data folded into a single stereographic triangle.

The datasets from grains 1-3 were combined and plotted in Figure 5.11. Grain 4 was removed from this data set due to the peak from the grain orientation obscuring the plot. This plot summarizes the observations from the individual plots. A strong (110) peak is seen along with what has been approximated as a (311) peak. This (311) peak is not a small distinct peak but a much larger border area, suggesting that it is likely a continuous region instead of a distinct facet. There is also a less intense peak at what is approximated to the (331). The further implication of this data will be discussed in section 5.4.

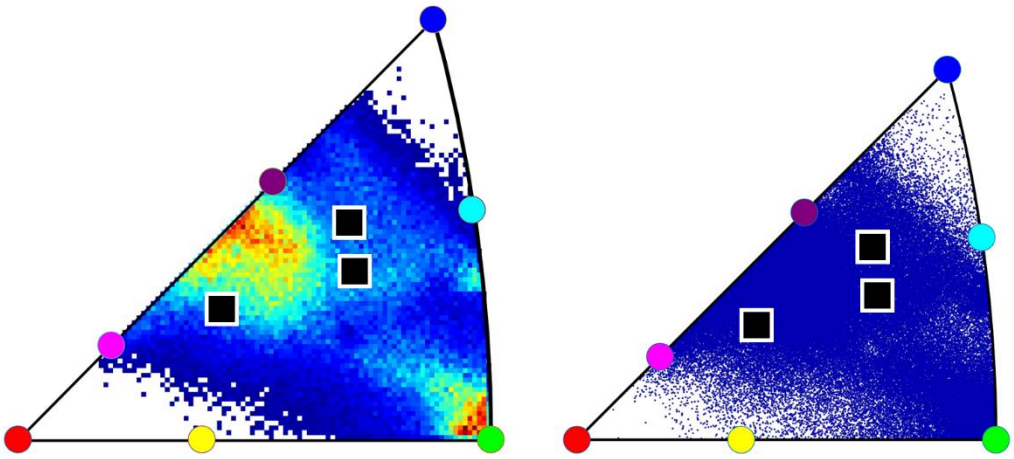

Figure 5.11: Normal vector distribution of surface facets of grains 1-3 for composition Ba25-Sr75 with all data folded into a single stereographic triangle.

The other composition analyzed using this method is that of Ba75 -Sr25. The same procedure as described above was used to analyze the grains labeled in Figure 5.12. Grain 2 shown in the SEM image is plotted in Figure 5.13. There is one distinct peak between (221) and (111), suggesting a possible facet. The heat map also shows a higher concentration between the (221) and the (111). This is similar to the behavior seen in Ba25-Sr75 grain 2 and 4. Figure 5.14 displays a similar faceting behavior for grain 4 of Ba75-Sr25. Both grains 2 and 4 have rather rough surfaces when observed in the SEM image. This would suggest that the surface is breaking up into 3 facets. Observing the heat maps of these two grains, it is possible that the (111) facet is being observed along with the two surrounding facets that were originally reconstructed as the (211) and (221) facets; however, these plots would suggest these two facets are located closer to the (111) facet.

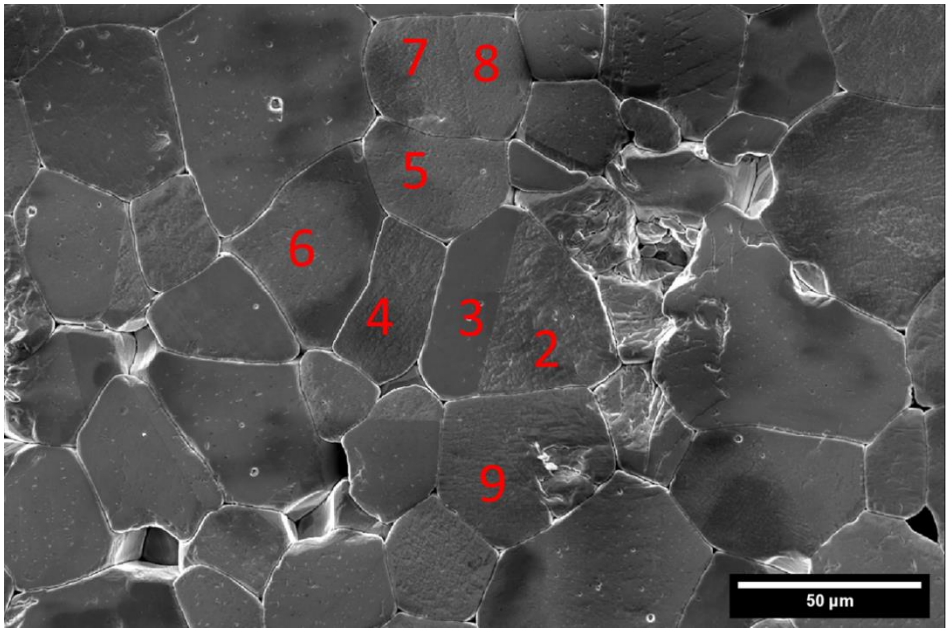

Figure 5.12: A SEM micrograph of thermally etched $BaSrTiO_3$ of composition Ba75-Sr25 with the grains analyzed labeled.

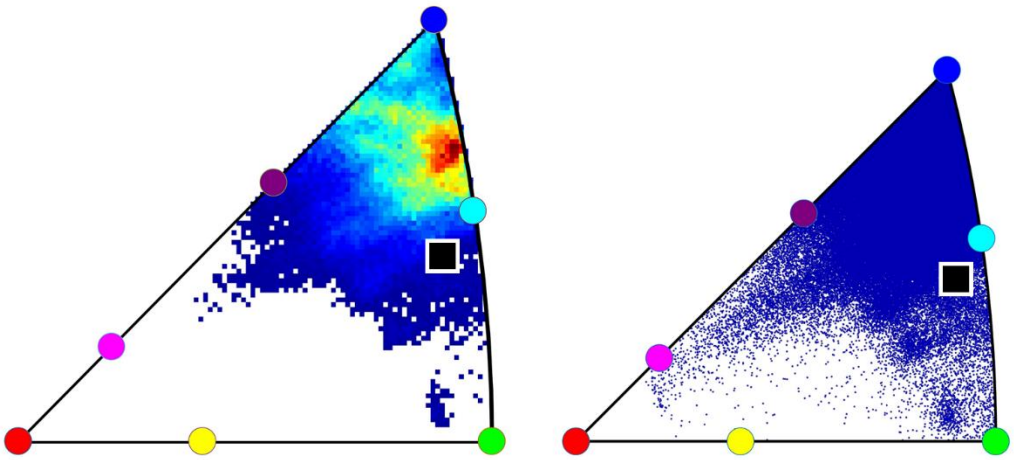

Figure 5.13: Normal vector distribution of surface facets of grain 2 for composition Ba75-Sr25 with all data folded into a single stereographic triangle.

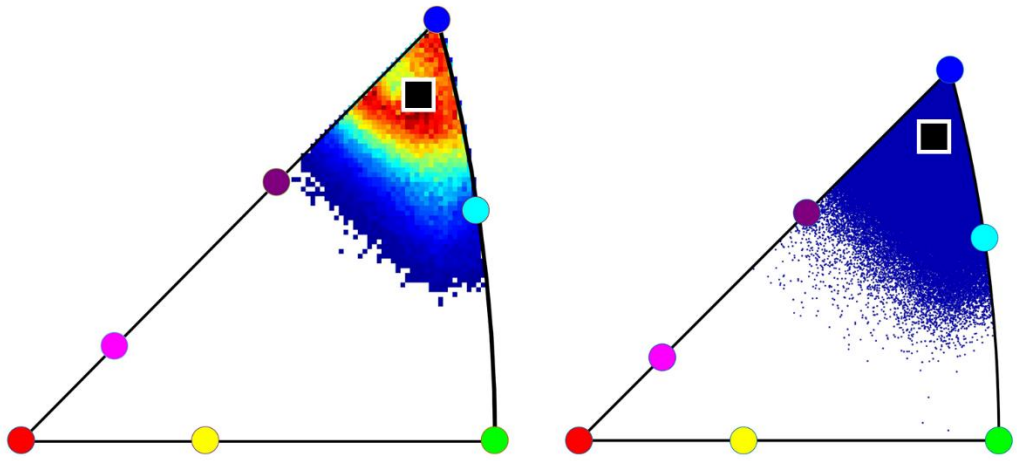

Figure 5.14: Normal vector distribution of surface facets of grain 4 for composition Ba75-Sr25 with all data folded into a single stereographic triangle.

Grain 5 of the Ba75-Sr25 composition is plotted in Figure 5.15. The data in this plot spans from the (110) facet to the (211) facet. This suggests that these two facets may be in contact with one another in the Wulff shape. This is similar to Ba25-Sr75 grain 1 with the exception that the peak is at the interior of the plot instead of being located at the (110) facet. The peak on the interior of the triangle could represent an additional unidentified facet or could be due to a continuous region. It is necessary to be mindful not only of whether the plane is faceted or curved, but also whether the transitions between planes are continuous or have missing orientations. As an example, when a plane in the Wulff shape is rounded, it is likely that the edge of the of the continuous region will be observed. The rounding of the plane will result in a range or orientation values when observed in the AFM. The larger range of values are expected to appear as a broad area extending into the interior of the stereographic triangle as opposed to one distinct peak. It is also possible that a peak is an artifact of how the data is collected. A grain that

breaks up into three distinct facets may have concentrations of normal vectors due to the peak of the facets. When analyzing AFM data, it is important to also consider the tip geometry. The sharpness of the AFM tip will impact the resolution of the scans. The AFM probes used in this experiment had a tip radius of approximately 5nm and the sided of the facets were on the order of 100nm; however, an AFM tip that is rounded or damaged may flatten the topographic peaks and would result in additional normal vectors representing the peak of the facet as opposed to the sides of the facet. In this scenario, it would be expected that this peak or artifact would be near the orientation of the grain. In Figure 5.15 the peak of the heat map does not overlap with the grain orientation indicated by the black square on the plot. This same behavior is seen in Figure 5.16 and Figure 5.17.

Samples Ba75%-Sr25% grains 2,5,6 and 8 all show grain normal orientations outside of the datasets collected. It is expected that the grain orientation would likely be between the identified peaks of each dataset. There are multiple possibilities that could explain this situation. It is possible that there is an error in the correction angle calculated. The Ba25-Sr-75 composition had observed grains that were dominated by two facets. When adjusting for the rotation correction it is much easier to determine the angle of rotation when there is a well-defined plane to rotate around, as seen in Figure 5.3. The grains observed in the Ba75-Sr25 composition were either smooth or three faceted grains, making it more difficult to find a characteristic landmark in which to rotate. It is also possible that when the EBSD data was processed there was a small difference in the average grain orientation calculations as the Euler angles for data processing and the grain orientations were calculated as different times.

Figure 5.16 plots grain 8 and presents data spanning from the (211) facet to the line between (100) and (110). The intersection of this point is closer to the (110) plane than the reconstructed

(310) plane. It is possible that this plane may be closer to a (210). Figure 5.17 plots grain 6 that spans from the same region between the (310) and the (110) and intersects the line between the (110) and the (221). This intersection is similar to that of the intersection in grain 2 of the Ba25-Sr75 composition.

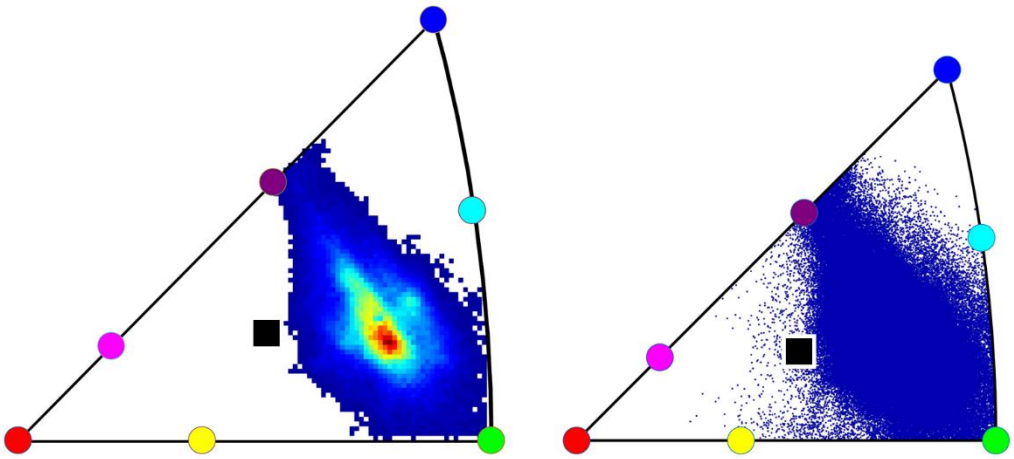

Figure 5.15: Normal vector distribution of surface facets of grain 5 for composition Ba75-Sr25 with all data folded into a single stereographic triangle.

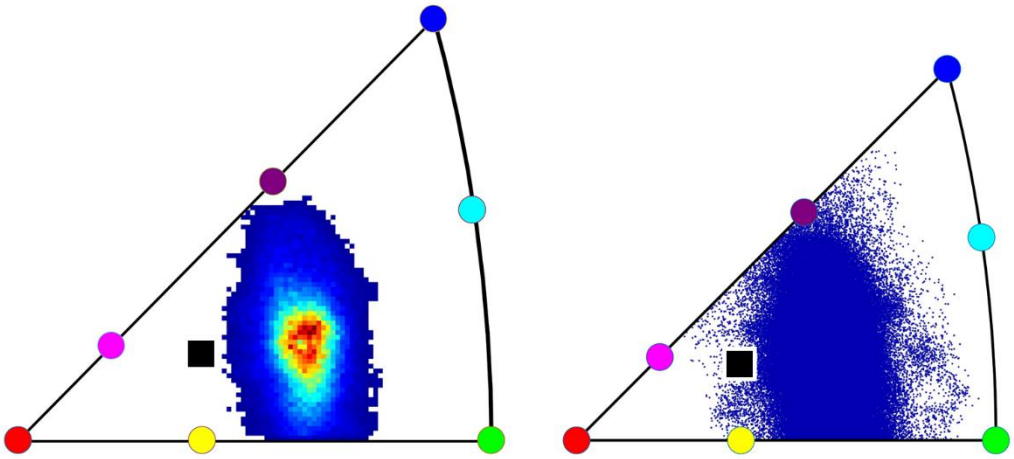

Figure 5.16: Normal vector distribution of surface facets of grain 8 for composition Ba75-Sr25 with all data folded into a single stereographic triangle.

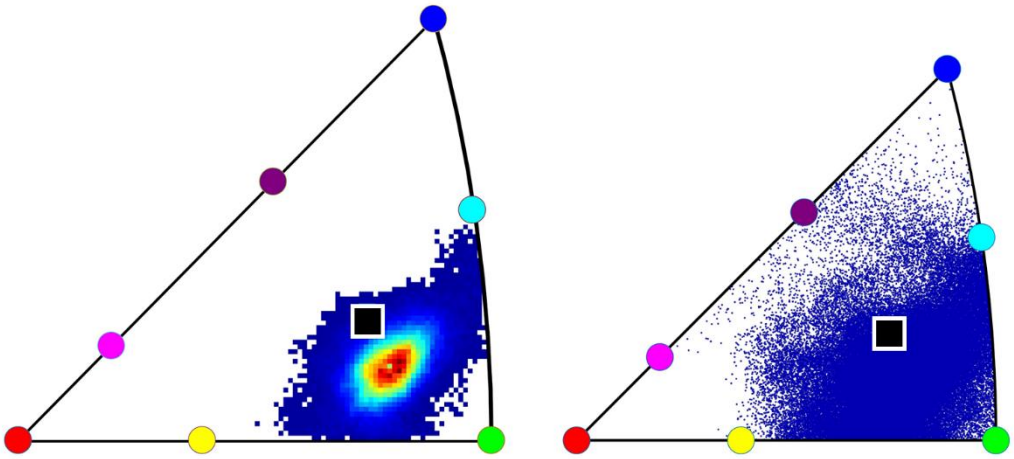

Figure 5.17: Normal vector distribution of surface facets of grain 6 for composition Ba75-Sr25 with all data folded into a single stereographic triangle.

Figure 5.18 presents the plot of grain 7, showing a large area or two of concentrated normal vectors. The central peak being located near the grain orientation may suggest a possible influence of flat or rounded regions of surface faceting. The large peak near the (211) facet was calculated to have an orientation of (0.848,0.353,0.392). This peak is similar to the possible (311) facet discussed from the Ba25-Sr75 composition. The large distribution of intensity around this area is also consistent with a continuous region, as suggested from the analysis of the Ba25-Sr75 grain.

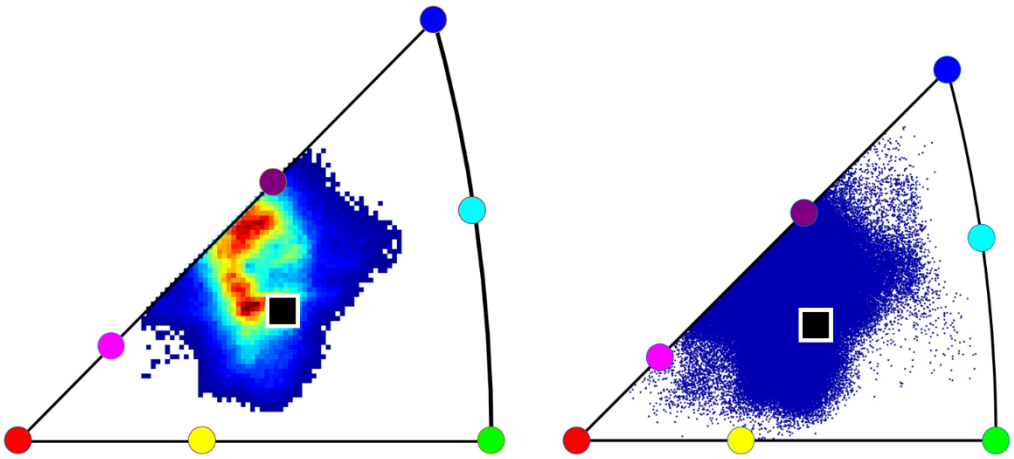

Figure 5.18: Normal vector distribution of surface facets of grain 7 for composition Ba75-Sr25 with all data folded into a single stereographic triangle.

The data from all grains except for grain 3 was combined and plotted in Figure 5.19. Grain 3 was excluded as it was a smooth grain that primarily represented the grain orientation and would skew the dataset. The peaks from grain 5, 6 and 8 are the most intense peaks in Figure 5.19. There are multiple possible explanations for these peaks, and these will be explored at greater depth in section 5.4.

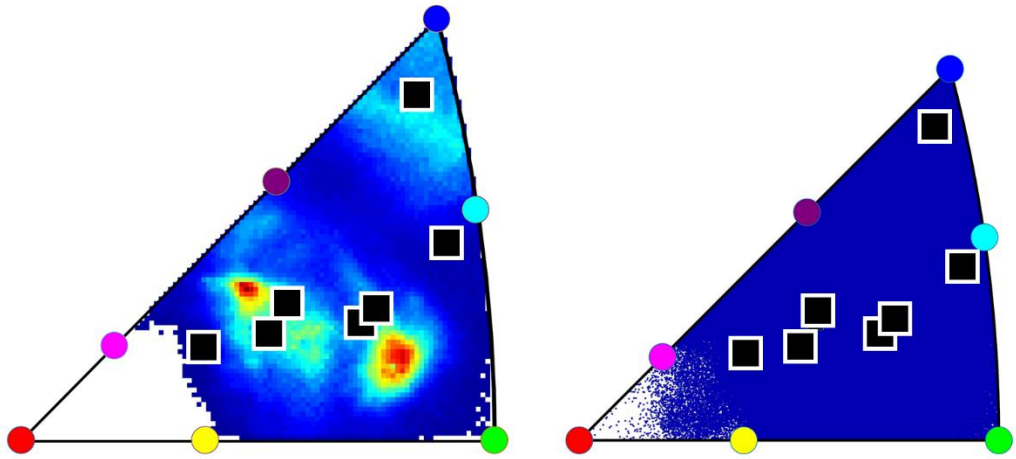

Figure 5.19: Normal vector distribution of surface facets of all grains except grain 3 for composition Ba75-Sr25 with all data folded into a single stereographic triangle.

5.4 Discussion

This section will discuss the data collected in Section 5.3 as well as the implications of the data on the Wulff reconstruction. The data collected suggests that there are a series of refinements that need to be made to the initial pore reconstruction in Figure 4.6. The first of these corrections is that there should not be a tie line between the (221) and (310) facets, as seen in Figure 5.1. This conclusion is made from Figure 5.6 of Ba25-Sr75 and Figure 5.15 of Ba75-Sr25. In both figures, there is a line of datapoints extending from the (110) facet to a region between the (100) and (111) facet. If both facets appear together on a single grain, the two facets must be in contact with one another in the Wulff shape, so the original tie line must be corrected. The corrected stereographic plot is shown in Figure 5.20 to show a new tie line between the (110) and (211) facets. This change in which tie lines exist results in a change in the Wulff

shape, seen in Figure 5.21. This new Wulff shape has the energy of the (211) facet adjusted to show that is in contact with the (110) facet. This representation has been exaggerated to be seen easier, as the experiments in this section do not give additional information regarding the relative energies.

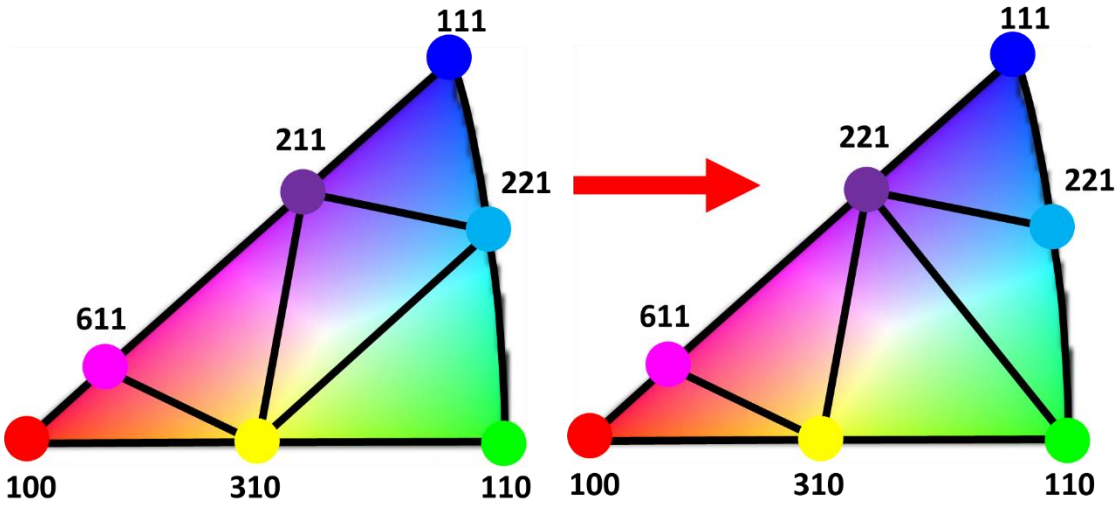

Figure 5.20: A transition in faceting behavior removing the tie line between (221) and (310) and inserting a new tie line between (211) and (110).

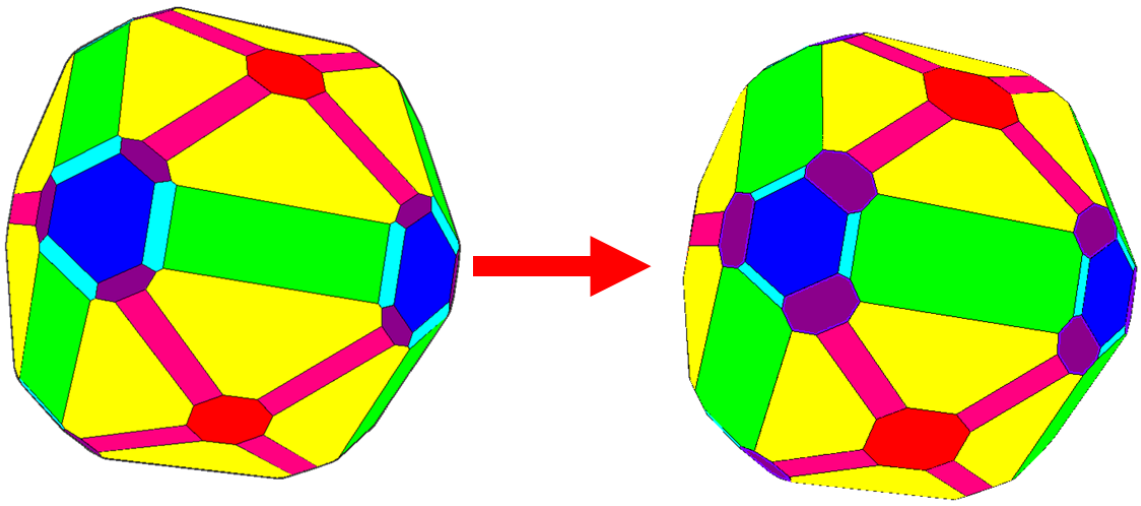

Figure 5.21: A reconstruction representing the transition in facing behavior by lowering the energy of the (211) plane.

A second conclusion from the data in section 5.3 that applies to both compositions is that there is evidence to suggest that the location of the facet initially identified as the (211) needs to be adjusted. Utilizing the peak of the heat map plots, it was determined that the (311) is much more likely the correct location of the facet. The other information about this (311) region is that, when observing Figure 5.11 and Figure 5.18, it can be seen that there is a much broader area of normal vectors instead of a small distinct peak. This would imply that there is not a (311) facet, but a continuous region of multiple stable orientations. This is supported by the other areas of intensity shown in Figure 5.11. There are two areas of higher intensity transitioning from the (311) region to the (110) facet and the area below the (221) facet. Comparable to a two-phase region in a ternary phase diagram, in a faceting diagram it expected to observe a 2 faceted region between a continuous region and a facet. These regions would appear as triangular regions that are broad near the continuous region and narrow to a point at the facet. With the assumption that the (311) is a continuous region, Figure 5.22 has been updated to show the anticipated behavior, with the grey areas representing two-faceted regions. In this region it would be expected to see a series of rotating tidelines extending from the facet and spreading across the width of the continuous region. A grain with a normal orientation within one of these regions would be expected to break up into two facets composed of the facet and the continuous region.

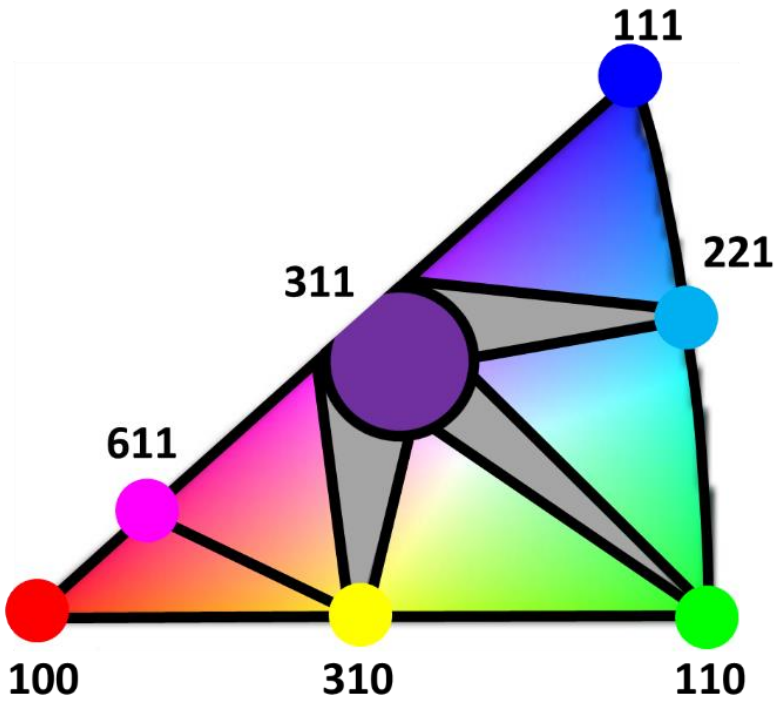

Figure 5.22: A proposed faceting diagram with a larger continuous (311) plane and two-faceted regions represented by the grey triangles.

One additional discrepancy is the location of the (221) facet. Figure 5.7 shows a peak below the (221) facet, which was approximated as a (331) facet; however, the data from Ba75-Sr25 has multiple possible interpretations. Figure 5.17 shows data that intersects between the (110) and (111) facets below the (221) supporting a possible (331) facet; however, other data sets suggest different conclusions. Figure 5.13 shows a large intensity peak above the (221) facet, closer to the (111) facet. To help determine the probability of these new facets, an additional reconstruction was made in Figure 5.23, reconstructed with a (311) and (331) facet. Visually, the changes in the reconstruction are minor angle differences that likely would be unable to be differentiated in pore shape images. Despite the (331) facet as being verified as a possible facet, further investigation is needed to determine the faceting behavior between the (110) and the

(111). It may be possible that that there are two distinct facets in this region, or that the (221) region is also a continuous region. It is also possible that there is a change in faceting behavior with the change in Ba-Sr ratio. The analysis in section 6 will continue to explore this region.

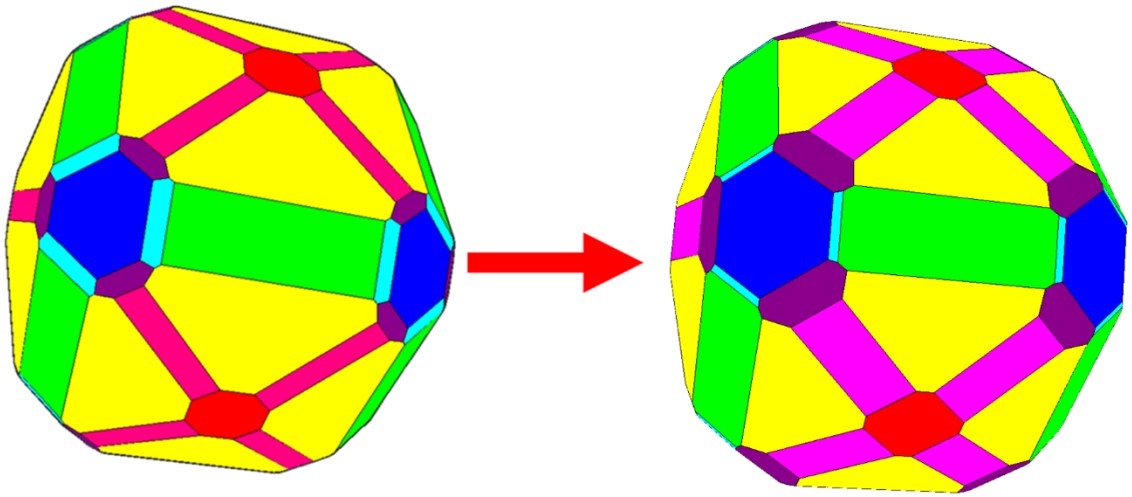

Figure 5.23: The proposed modified pore reconstruction utilizing surface faceting information.

The peaks located inside the Ba75-Sr25 sample in grains 5,6 and 8 differed from the expected faceted behavior. All three of these peaks were located near each other, so additional analysis is needed to determine the cause of these peaks. To better understand this behavior, additional reconstructions were made to determine the feasibility of an additional facet being present. The peaks determined in the heat map plot were converted to (hkl) values and reconstructed. The reconstruction of the peak from grain 8 added to the existing reconstruction can be seen in Figure 5.24. The new facet is represented by the black plane between the (311) and (331) facets. This facet is not one that was observed in the pore shape analysis; however, there are still high levels of uncertainty regarding the facets surrounding the (111) facet. It is possible this peak may be an artifact of the transition between the (311) facet, considering the probability that near the (311) is a continuous region.

It may also be possible that this new facet is result of the kinetic transition. This peak may be appearing due to the grains not being fully equilibrated and there is a not equilibrated region between the (311) and the (331). It is possible that there is a rounded region around the (111). If the sample is still equilibrating, there may be intermediate kinetic facets that would not appear in the Wulff shape, or that the previously seen microfaceted regions from $SrTiO_3$ studies were a result of how the samples were cooled. Section 6 will continue to investigate this faceting behavior.

The analysis in this section is not without limitation. For both compositions, there was only a limited number of grains collected, and additional data could greatly improve the faceting reconstructions. When observing the scatter plots of Figure 5.11 and Figure 5.19, there are large regions of the stereographic projection without data. The Ba25-Sr75 composition was missing data near the (111) facet and both compositions were missing data from near the (100) facet. When observing the locations of the grain orientations, there were no measured grains collected from these regions. Grains from these regions would be needed to verify the faceting behavior of the neighboring orientations.

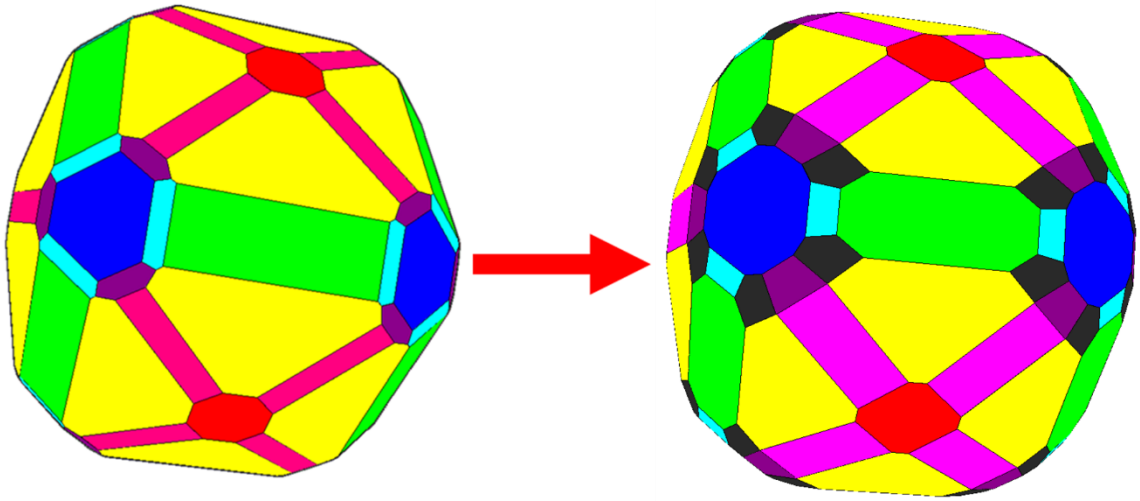

Figure 5.24: A possible pore shape reconstruction with the addition of a black facet located at (0.85, 0.18, 0.49) representing the observed peak in faceting behavior.

Future used of this technique should further explore the limitations and possible sources of error. As previously mentioned, this technique can be impacted by the alignment when transferring a sample from the SEM to the AFM. The data can also be influenced by the sharpness or damage to the AFM tip that may create a rounding of the observed surface facets and peaks in the dataset that are not representative. It is also possible, that the flatness of the sample may contribute to error in measurement. If the sample is not perfectly flat there may be a need to add an additional correction factor; however, this difference should be the same in both the SEM and AFM. This possible source of error would be greatly impacted by how the AFM data is processed. If the AFM data is not plane fit, then the angle of the surface should be the same in both instruments. It would be necessary to compare the sample AFM measurements to a standard to know the proper plane fitting parameters.

To obtain a proper representation of the Wulff shape grains a larger number of orientations would be needed. The scatter plots should cover all orientations in the stereographic projection.

In order to do this, specific gains can be chosen from EBSD orientation and scanned using AFM to fill in missing orientations.

6. SURFACE FACETING ANALYSIS

6.1 Introduction

The goal of the experiment discussed in this section is to create a diagram that maps the faceting behavior of the equilibrium crystal shape. This diagram is comparable to the concept of N-diagrams by Cahn and Handwerker.[32] N-diagrams are analogous to a phase diagram, but for faceting behavior of a grain. The diagrams in this section will be plotted on a single triangle of the stereographic projection and can help infer which planes, seen in the Wulff shape, are facets, and which are continuous. These plots can also depict faceting tie lines, which illustrate planes in contact with one another and are a useful tool to help differentiate transition types from one plane to another.

6.2 Experimental Procedure

The N-diagrams in this paper are created by imaging numerous thermally etched grains in the SEM and then obtaining orientation information through EBSD. Each grain that is imaged is organized by faceting behavior into one of 3 categories. This category is determined by observing the faceting behavior of the etched grain in SEM micrographs. Grains of type 1 are grains that appear smooth or flat. These grains would represent an orientation that is either perfectly aligned with a facet or on a continuous region with no missing surface orientation. Grains of type 2 are grains that have two distinct surface facets that span the width of the grain. Grains of type 2 are expected to appear in grains with an orientation between two facets or between a facet and a continuous region. As a polished grain facets when heated the surface will equilibrate into the two facets that will result in the same macroscopic curvature. Grains with orientations between three will result in type 3 grains that have three distinct facets. Individual

grains are plotted on a stereographic projection and symbols are given to each of the 3 categories. This projection is then folded into a single triangle of the stereographic projection using symmetry operations. This process is accomplished by utilizing the MATLAB script located in appendix B.

The orientation map of grains to be analyzed was processed to give each grain one constant orientation. The grains were numbered using the OIM 8 software, and the orientation information was exported into a text file containing the Euler angles of the mapped grains. Using SEM images, each grain was determined to have 1, 2 or 3 facets. This value was added to the text file to be processed by the MATLAB script. The Euler angle values were plotted on a stereographic projection with each faceting category being plotted with a different icon. These data points are then folded into one stereographic triangle using symmetry operations. The distribution of the faceting behavior in the stereographic triangle can be used to better understand faceting behavior and faceting transitions.

6.3 Results

Faceting datasets from three (Ba,Sr)TiO_3 compositions and from $BaTiO_3$ were compared. The first dataset, of composition Ba25-Sr75, is shown in Figure 6.1. The grains are plotted on a stereographic projection with the (100), (110), (111), (310), (211), (611) and (221) facets labeled by the colored dots corresponding to reconstruction from section 4 in Figure 4.6. In the faceting diagrams in this section, the black squares represent grains that appeared flat or smooth in the SEM images. The blue diamonds represent grains that appeared to have 2 dominant facets with little to no influence of a third facet. The red circles represent grains that had 3 facets observed in the SEM. The first set of data being analyzed is the smooth grains of Figure 6.1. Most of the smooth grains are at the bottom of the triangle and span the entire width of the triangle. This

behavior suggests the possibility of a continuous region at the bottom of the diagram. If the (310) plane were not a facet but within a continuous region, it may explain the groupings of smooth grains. The small grouping of smooth data points higher up near the (111) may also suggest a continuous region; however, the small number of datapoints do not allow for a reliable conclusion.

The two-facet grains grouped between the (211) and the (221) suggest a possible tie line between these planes and the width of the data points suggests the possibility of a continuous region. The additional two-facet grains near the (110) facet suggest a possible tie line between the (110) and the larger grouping of two-facet grains. The three-faceted grains are expected to be located everywhere there is not a single facet, continuous region or tie line.

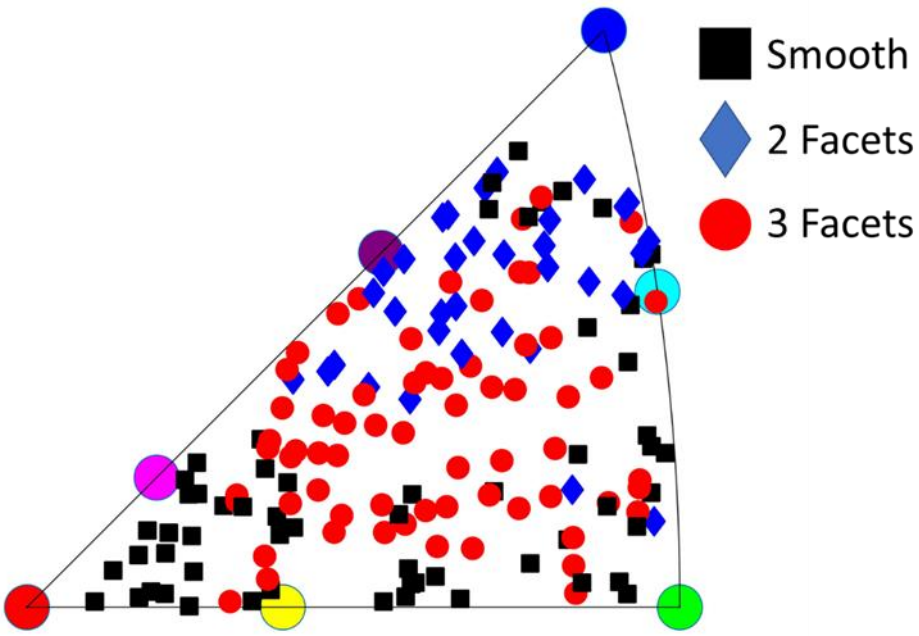

Figure 6.1: A plot of surface faceting distribution plotted on a stereographic projection and labeled by faceting type for composition Ba25-Sr75 with all data folded into a single stereographic triangle.

Figure 6.2 shows the resulting plot from the Ba50-Sr50 composition. This plot shows a spread of smooth grains across the bottom of the plot akin to that of Figure 6.1. There is a larger group of smooth grains near the (221), which may suggest a possible continuous region. The two-faceted grains have a larger grouping around the (221) and span towards the (221), (110) and the region between then (110) and the (310). This further suggests the possibility of the (211) facet being within a continuous region and having tie lines between the (221), (110), and possibly the (310).

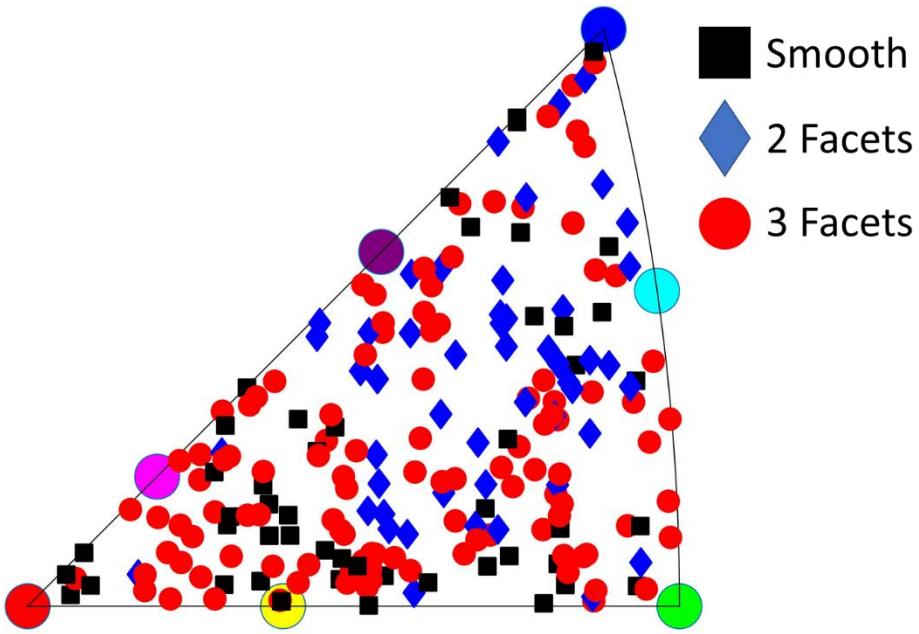

Figure 6.2: A plot of surface faceting distribution plotted on a stereographic projection and labeled by faceting type for composition Ba50-Sr50 with all data folded into a single stereographic triangle.

Figure 6.3 shows the plot of the Ba75-Sr25 composition sample. In this sample, there are many more smooth grains. The smooth grains can be seen spanning the bottom of the triangle,

from the (100) to the (110), as well as a large group of smooth grains on the right side of the stereographic triangle. As discussed previously, there is likely a continuous region around the (311) and the (310). It is also possible that the area around the (111), is rounded and the smooth grains around the (111) facet would support this hypothesis. The distribution of these grains supports the possibility that there is a continuous region in both areas, possibly near the (310) and the (221). There are a smaller number of two-faceted grains in Figure 6.3 compared to the previous two samples, making analysis more difficult. There are some small groupings of two-faceted grains near the (310), (110) and (221).

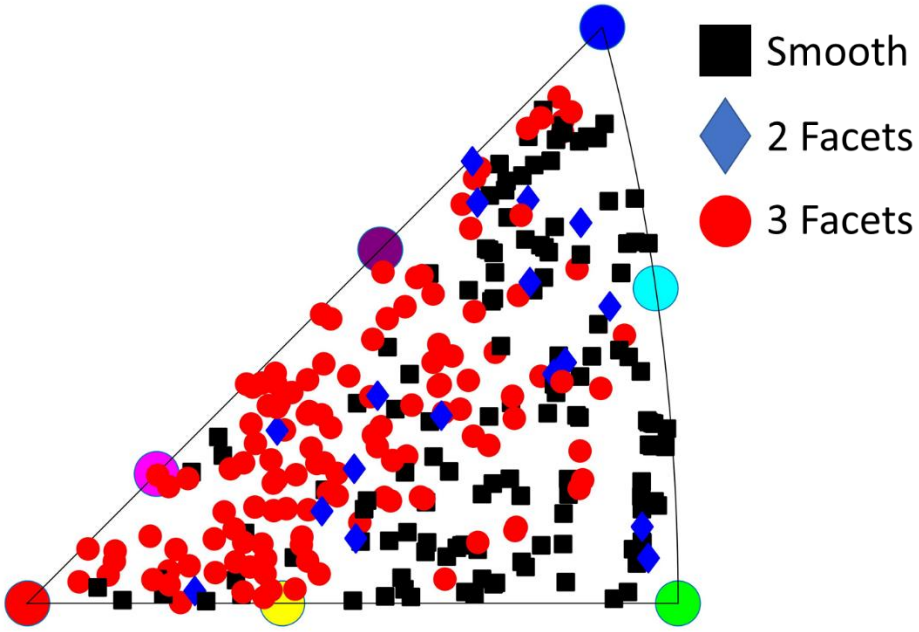

Figure 6.3: A plot of surface faceting distribution plotted on a stereographic projection and labeled by faceting type for composition Ba75-Sr25 with all data folded into a single stereographic triangle.

Figure 6.4 shows the resulting plots for the $BaTiO_3$ sample. This plot has a grouping of smooth facets near the (310), suggesting the possibility of a continuous region. This plot contains

a large number to two-faceted grains occupying a large region of the center of the triangle, with a concentration near the (211) as well as between the (110) and (221), between the (211) and (111), between the (110) and (310), and possibly near the (611). These groups of two-faceted grains likely represent multiple tie lines crossing the stereographic triangle. In section 6.4 these results will be discussed in greater detail and compared to the results in section 5.

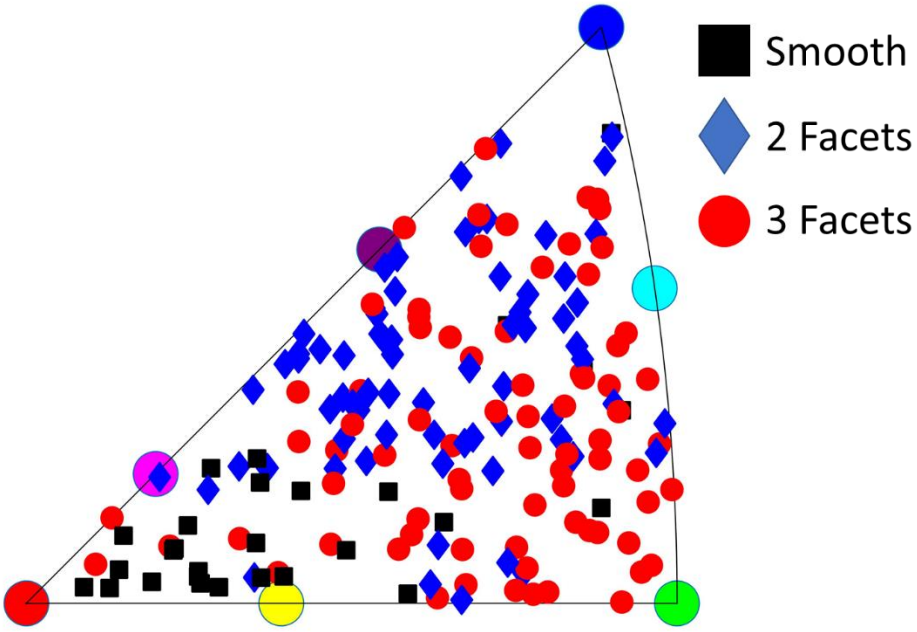

Figure 6.4: A plot of surface faceting distribution plotted on a stereographic projection and labeled by faceting type for $BaTiO_3$ with all data folded into a single stereographic triangle.

6.4 Discussion

This section will discuss the results from section 6.4 in conjunction with the conclusions from section 5. From section 5, the major conclusions were that instead of a tie line between the (221) and (310), as originally proposed, there is a tie line between the (110) and the line between the (100) and (111). It was also concluded that the (211) facet is more likely to be a (311) facet and

the (221) facet is more likely to be a (331) facet. Observing the datasets surrounding the (311), it is likely that this plane observed in the pore shape is a rounded region with multiple stable orientations instead on one distinct facet. It is necessary to compare the results from this section to determine if the previous observations are validated. When comparing the Ba25-Sr75 composition, the faceting maps data has groupings of two-facet grains that would line up with the expected tie lines between the (311) and the (331), and possibly the (110). When verifying that the region near (311) is continuous, the data has mixed conclusions. It would be expected to see a grouping of smooth faceted grains in a continuous region and then have a large group of two-faceted grains that narrow to a point when coming near a facet. This data has a large group of two-faceted grains but does not have smooth grains near the (311). This may be due to a lack of data and not measuring enough grains of the correct orientations, or that the range of orientations represented by the continuous region is small and difficult to detect though this method.

Within this composition, the other discrepancy is the large number of smooth grains between (100) and (110). A continuous region was not detected in the AFM faceting experiment. When observing the scatter plot of Figure 5.11, there is very little data in this region especially near the (100). Additional grains with an orientation in the lower section of this stereographic triangle would be needed to verify these observations. When observing the faceting plots in this section across all compositions, there is consistently a group of smooth grains between the (100) and the (110), except for the $BaTiO_3$ sample, which had a group of smooth facets that only extend halfway between the (310) and the (110). With all compositions displaying this activity, there is a much higher confidence that there a continuous region between the (100) and the (110). This claim is supported by the width of the data points in Figure 5.16 and Figure 5.17. If the (310)

plane was a facet, it would be expected that the data would narrow to a peak at the location of the facet. The width of these data sets may represent tie lines between a continuous region and other facets.

The other constant observation across all compositions, except the $BaTiO_3$ sample, is a group of smooth grains on the right side of the stereographic triangle. This may either represent a continuous region such as the (331) facet being continuous or may be a measurement error. It is possible that three-faceted grains that have very small facets may be mistaken for a smooth grain unless observed at a high magnification. It possible that some of the smooth grains from these datasets are three-faceted grains. These observations and the observations from sections 4-5 will be discussed in section 7 and related back to possible influences on grain growth.

Considering future used of this technique, it will be necessary to further refine the final datasets. Multiple grains of differing faceting behavior should not exist at the same orientation. The overlapping facets are most likely an indicator of a kinetic effect and that some surface facets were not equilibrated. Considering a flat surface transforming into a faceted surface the kinetic transition is toward the more faceted surface. In areas of the same orientation, the grains with the higher number of facets should be closer to equilibrium. This technique could be refined by filtering out datapoints at the same orientation to make the final dataset easier to interpret.

7. COMBINED WULFF SHAPE CONCLUSIONS

The objective of this document is to study the faceting behavior of $BaSrTiO_3$ alloys and relate this behavior back to grain growth of the bulk sample. Sections 4-6 have explored different techniques to more accurately represent the equilibrium crystal shapes, and this section will discuss how to combine the data obtained in sections 4-6. This section will summarize the main conclusions from each section and discuss what conclusions can be made when comparing the three types of data.

When studying the equilibrium crystal shape, there are multiple types of data needed to accurately reconstruct a model Wulff shape. Firstly, the different orientations and locations of the surfaces must be found. These are represented by the crystallographic planes that make up each Wulff shape. Determining the surfaces of the Wulff shape is complicated by the possibility that the planes can be flat facets, with one distinct normal vector, or rounded continuous regions with a range of normal vectors. It is also possible that between two planes there can be either a continuous transition or a transition with missing orientations.

The second type of relevant data to collect is the relative size of each of the surfaces that make up the Wulff shape. The relative size of the surface represents the relative interfacial energy (γ) of each plane. Understanding the relative interfacial energies is necessary to predict which planes are of the lowest energy, and the resulting impact on grain growth.

The third aspect to discuss is the type of transition from one surface to another. While it is possible for a plane to be faceted or atomically rough it is also possible to have differing transition type that either are continuous or have missing orientations. There are 5 possible transition types, and these can be visualized in Figure 7.1. Type 1 is a continuous transition between two planes and, when observed in the surface faceting experiment, would be

represented by smooth grain along the stereographic projection. Type 2 is a discontinuous transition between two facets, which would be represented by surface faceting that breaks up into two grains. Type 3 is a curved region transitioning to a facet without any missing orientations. The surface faceting for type 3 would look the same as type 1. Type 4 is the same as type 3, but with missing orientations. The surface faceting of type 4 transitions would show a region of smooth grains and a region of grains with 2 facets. Type 5 is a transition between two curved planes that have a discontinuous region. These transition types are important because both whether a facet is faceted or rough and the type of transition that is present will change the Wulff shape and have a potential impact on grain growth.

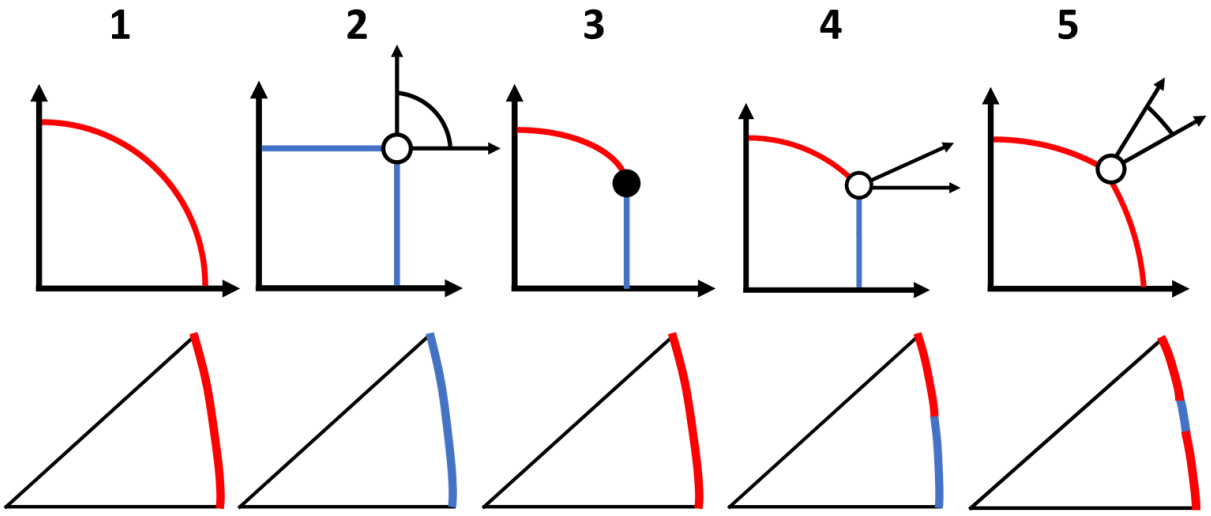

Figure 7.1: A plot of the 5 faceting transition types with red lines representing curved surfaces and blue lines representing flat facets. The bottom plots represent the expected surface faceting behavior for each transition type. The red line corresponds to smooth flat surface facets and the blue lines represent two-faceted surfaces.

7.1 Combined Wulff Shape Analysis

Section 4 discussed the overall form of the Wulff shape, allowing for an initial determination of which facets exist in the Wulff shape and the relative sizes of each facet. In this analysis, it was

assumed all observed planes were flat facets. It was also determined that through this method the differences in relative energy could not be easily compared due to the large standard deviation within each composition. Significantly more data would be needed to be collected, as well as ensuring the pores are all the same size to reduce variance due to kinetics.

Section 5 utilized the information from Section 4 and attempted to refine the reconstruction of the Wulff shape. From this analysis is was determined that the (221) facet was more accurately represented by the (311) facet and the (211) facet was more accurately represented by the (311) facet. The (311) area showed strong evidence that the region is likely a rounded continuous region and is in contact with the (110) facet, instead of the (111) facet being in contact with the (310), as previously reconstructed. It was also determined that there is evidence to support the claim that there is a rounded region around the (111) plane; however, to more accurately determine whether this rounded region is a rounded plane or rounded transition, more data is needed.

Section 6 attempted to obtain comparable information to section 5, but in a manner that would have a higher throughput. The results support the previous conclusions of a continuous region around the (310), the direction of the tie lines extending from the (110) plane and showed greater evidence of a rounded region around the (111) plane. This study added the conclusion that there is likely a continuous region around the (310) plane. These conclusions as a whole set a groundwork for creating an N-diagram for the $BaSrTiO_3$ system.

7.2 Implications for Grain Growth

Having an accurate n-diagram for this system would be of great benefit for better understanding the $BaSrTiO_3$ system; however, there are still disagreements on exactly how

particular faceting behaviors would affect grain growth. As discussed in section 1, grain boundaries move through nucleation and propagation of facets or steps. When two faceted boundaries interact, it is possible that mismatched facets can impede grain growth. It is also possible that introducing facets can create reentrant angles and assist in the propagation of step movement. When the Wulff shape has a larger number of facets the grain interactions become more complex, but there are more possible planes for the boundary to align to. If one continues to add additional facets to an equilibrium shape, the system becomes more rounded and closer to an isotropic shape.

Previous work in MgO studying abnormal grain growth has observed some abnormal grains with faceted boundaries, while other abnormal grains were curved. It was also reported that those abnormal grains with the highest mobility were curved.[56] It has also been reported that non-faceted abnormal grain growth can occur in alumina.[57] Other research has categorized grain boundary motion at high and low mobility, and states that faceting occurs in both high and low mobility boundaries, separating roughing transitions from faceting behavior.[58] Additional work is required to determine exactly how the observed faceting behavior of the $BaSrTiO_3$ system directly affects the abnormal grain growth observed in the $BaTiO_3$ and $SrTiO_3$ systems.

7.3 Future Work

The information collected from this study provides initial results for creating a detailed n-diagram of the faceting behavior for the $BaSrTiO_3$ system. It has provided some new insights into possible faceting behavior of the system. The next step in this line of research would be to collect additional data, to provide better statistical data, and determine the faceting behavior near orientations that had low numbers of grains. It would also be beneficial to perform grain growth studies of the $BaSrTiO_3$ with varying Ba:Sr ratios. With a set of complete n-diagrams and

corresponding grain growth behavior, it would provide valuable insight to predicting and controlling the resulting microstructure.

To assist in this process, it would be ideal if the Matlab scripts used in these experiments were integrated with the image processing to allow for higher throughput. The most time-consuming process of the AFM faceting work is the need to individually scan each grain. If this process could be streamlined through taking cropped datasets from larger high-resolution images it would greatly increase the amount of data that could be obtained. The most time-consuming process of the surface faceting work is identifying the type of surface faceting. If the surface faceting images could be automatically processed it would provide more consistent results in less time.

8. BARIUM TITANTE AND STRONTIUM TITANATE COMPARATIVE ENVIRONMENTAL ANALYSIS

The Electronic ceramics industry is one that is growing rapidly, and the ceramic capacitor market is expected to be valued at $9.167 billion by 2023.[2] With the rapid growth of this industry, it is necessary to evaluate the environmental impact this growth will have, and the risks associated with the production of these new components. The research discussed in this document is studying specifically the $BaSrTiO_3$ system with a variable Ba-Sr ratio. $BaSrTiO_3$ is a material of interest for the creation of tunable microwave devices, and the individual components of $BaTiO_3$ and $SrTiO_3$ are used in a wide range of dielectric components. The question that this section aims to address is what the potential environmental implications of are adjusting the barium and strontium ratios in these tunable electronic ceramics. To address this question, the SimaPro 8.5.2 software will be used in conjunction with the Ecoinvent 3 lifecycle inventory database to analyze the components by composition.

To compare the environmental impact on a device level, the example device of a multi-layer ceramic capacitor (MLCC) will be used, as it is one of the most common dielectric ceramic devices produced. This process will determine if the impact of the different ceramic materials is significant compared to the component being produced. There are two common types of MLCC produced. The first is the precious metal electrode (PME) type capacitor. These capacitors use Palladium and silver as the electrode materials, and the electrodes are terminated with silver. The second type is the base metal electrode (BME) MLCC. These capacitors were developed in the 1960s and use nickel for the electrode material and the electrodes are terminated with copper and coated in nickel. BME capacitors are commonly used to save on material cost as compared to PME capacitors. A diagram of these two MLCC types can be seen in Figure 8.1. MLCCs are

produced by stacking alternating layers of dielectric ceramic and nickel paste, pressing these layers into green bodies, cutting the green bodies into the correct size, sintering the green bodies, and finally terminating the ends of the capacitors. A detailed flowchart of this process can be seen in Figure 8.2. This section will focus on BME type capacitors, as manufacturers are continuing to transition towards production BME capacitors to minimize cost.[59]

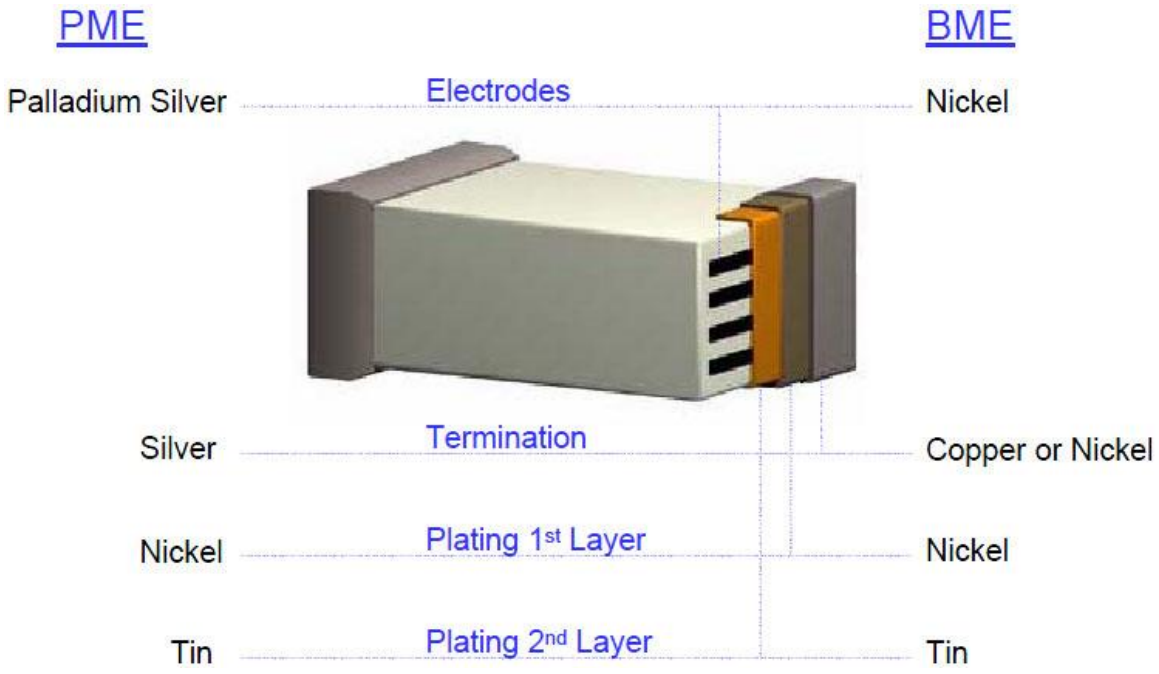

Figure 8.1: Diagram of a multi-layer ceramic capacitor with corresponding material representing a precious metal electrode capacitor(PME) and a base metal electrode (BME) capacitor.[60]

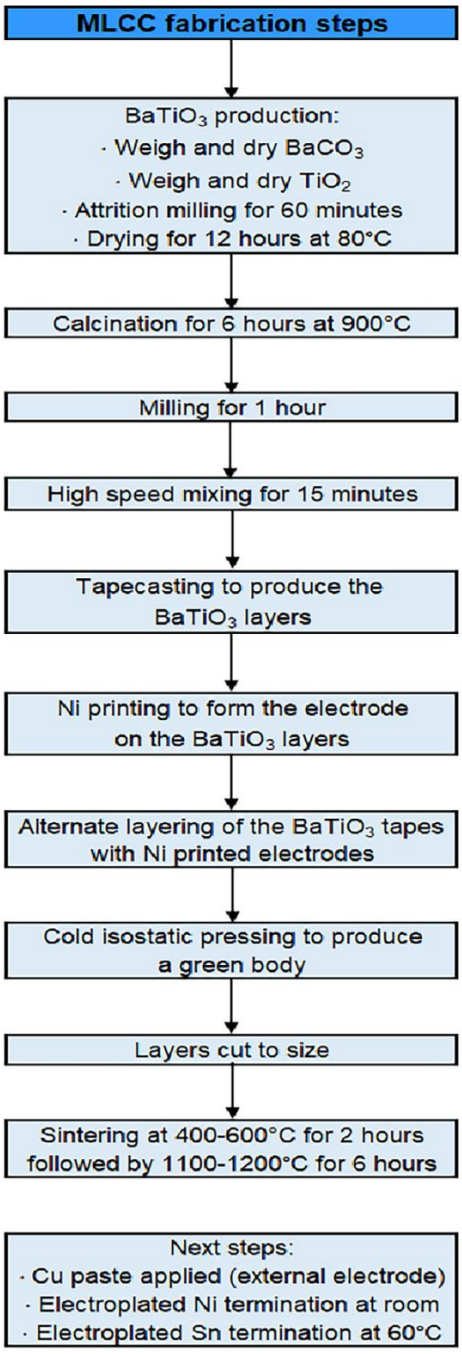

Figure 8.2: A flow chart of MLCC production steps.[61]

To determine the environmental impact of changing the Ba-Sr ratio in a capacitor, a comparative analysis is being performed of two BME capacitors, one composed of $BaTiO_3$ dielectric layers and the other composed of $SrTiO_3$ dielectric layers, in addition to a comparative

analysis of the individual components of the capacitor. $BaTiO_3$ and $SrTiO_3$ are commonly produced through hydrothermal synthesis and solid-state reactions between the respective carbonate and titanium dioxide (TiO_2). The solid-state reaction route will be used for this analysis as this method is commonly used in large scale production.[61]

This analysis assumes the use and end of life of both capacitor types to be the same. The differences in these devices are primarily in the mining and processing of raw materials. In the production of capacitors of differing compositions, it is possible the sintering temperatures of these materials may vary; however, for this study, it will be assumed that the production of the capacitors is the same. The functional units chosen are 1kg of capacitors and 1kg of powder. The environmental impact categories of this study being assessed are ozone depletion, global warming, smog, acidification, eutrophication, carcinogens, non-carcinogens, respiratory effects, ecotoxicity and fossil fuel depletion. The Ecoinvent 3 database was used to gather data for each of the chemical components in each of the corresponding environmental impact categories. The TRACI 2.1 environmental impact assessment tool was used to assess the collected data from each of the listed impact categories. The TRACI tool is a problem oriented or mid-point approach where a system's streams are classified according to the impact categories in which they contribute.[62] The top producing companies for MLCCs are commonly located in the United States and Japan. Due to many large MLCC manufacturers being in the United States, such as Kemet, Vishay and AVX, the TRACI methodology was chosen as it was developed by the US Environmental Protection Agency and would accurately represent the environmental impact of a US based manufacturer.

The first assessment will be comparing the environmental impact of barium titanate (BTO) and strontium titanate (STO). The barium strontium titanate composition is a solid solution that

will form across the composition range. This comparison will assess the difference in environmental impacts between two ceramic layers. A comparative plot across the 10 impact categories can be seen in Figure 8.3. When comparing the environmental impact of the two titanate compounds it is necessary to compare the impact of the individual chemical components to assess what component is responsible for change in each impact category. Barium titanite is produced through a solid-state reaction between barium carbonate and titanium dioxide and strontium titanite is produced through a reaction between strontium carbonate and titanium dioxide. As these reactions do not use the same mass of titanium dioxide these comparisons need to be adjusted for stoichiometry. Figure 8.3 compares the resulting product of 1kg of barium titanate to 1kg of strontium titanite, while Figure 8.4 has been normalized to 1kg of titanium dioxide and the mass of the carbonates have been adjusted for correct stoichiometry.

When comparing the impact categories of barium and strontium titanate, strontium titanate has a higher environmental impact in 6 of the 10 categories. Of the 10 categories only 4 categories have differences of more than 10%. Those categories are ozone depletion, non-carcinogens, ecotoxicity and fossil fuel depletion. As these four categories have the largest discrepancies, they will be the focus of the analysis. Of these categories, a process analysis was done to determine the cause of the differences in each category. In the ozone depletion category, the primary differences between BTO and STO are the high rate of petroleum and gas production in the manufacturing process of STO. This higher use of fossil fuels is also responsible for the higher impact in the fossil fuel consumption category. The non-carcinogenic effect is the most dramatic difference between the two. The primary process responsible for this difference is the production of barium sulfide and barium carbonate. The production of barium carbonate is an essential step and the primary cause of environmental impact of this category. Barium carbonate

is classified an acute oral toxin category 4 on its safety data sheet. Barium carbonate also acts as an oral, dermal and inhalation irritant. It is for these same reasons that the ecotoxicity impact category has a higher impact from BTO. As the desired product is toxic due to the barium carbonate content, it is necessary to explore the potential effects of increasing the barium content of a capacitor.

To gain a full understanding of the impact of the production of BTO and STO, it is necessary to also compare the impact of the barium and strontium carbonate with that of titanium dioxide, which is used to make the titanate compounds. Figure 8.4 shows that the titanium dioxide is the component of the ceramic material with the highest environmental impact in 7 of the 10 categories. The remaining 3 categories – non-carcinogens, respiratory effects, and ecotoxicity – have barium carbonate as the primary source of the environmental impact due to its nature as a toxin, as previously discussed. In the ozone depletion category, TiO_2 with chlorine gas is the primary contributor to the environmental impact. TiO_2 is commonly produced through a chloride or a sulfide route. The chloride route was chosen for this analysis, as it is the newer of the two methods and makes up 57% of the market.[63] This process does produce chlorine gas, which results in additional impact on the ozone. In the global warming category, TiO_2 has higher heating required during manufacturing and this heat comes from natural gas and coal, contributing to global warming. This heating from fossil fuels is also the primary contributor to the smog, acidification and fossil fuel consumption categories. In the eutrophication category, there is waste residue from the production of TiO_2 that needs to be treated before being sent to the landfill, and this is the primary contributor of eutrophication. In the carcinogen category, the Ecoinvent database lists TiO_2 production as a carcinogen. At this point in literature there is much debate as to whether TiO_2 causes cancer and is it not listed as a carcinogen in a standard safety

data sheet. In 2016 the French agency ANSES proposed TiO_2 be listed as a class 1B carcinogen.[64] Upon further review, there was not sufficient evidence to link TiO_2 to causing cancer, so it has been reclassified as a substance suspected of causing cancer when inhaled.[65] It is necessary to understand there is a possibility that TiO_2 is cancer causing, but further study is still needed.

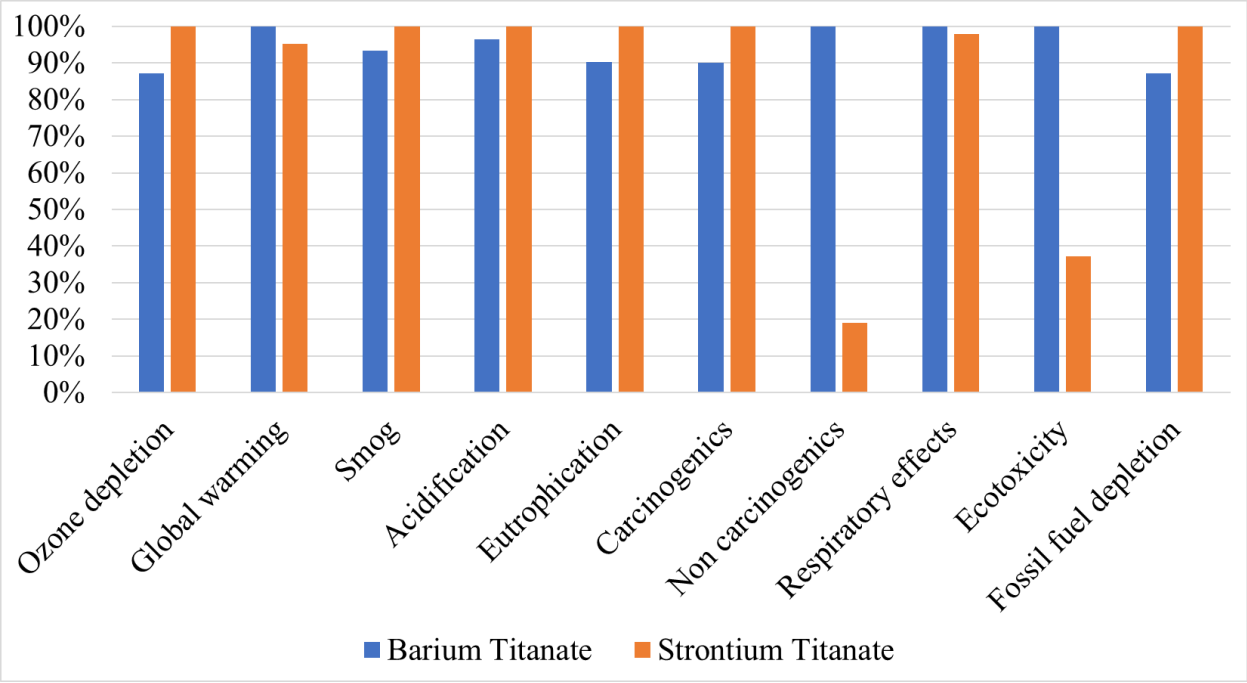

Figure 8.3: A plot of environmental impact across 10 impact categories comparing $BaTiO_3$ vs $SrTiO_3$ of equivalent mass.

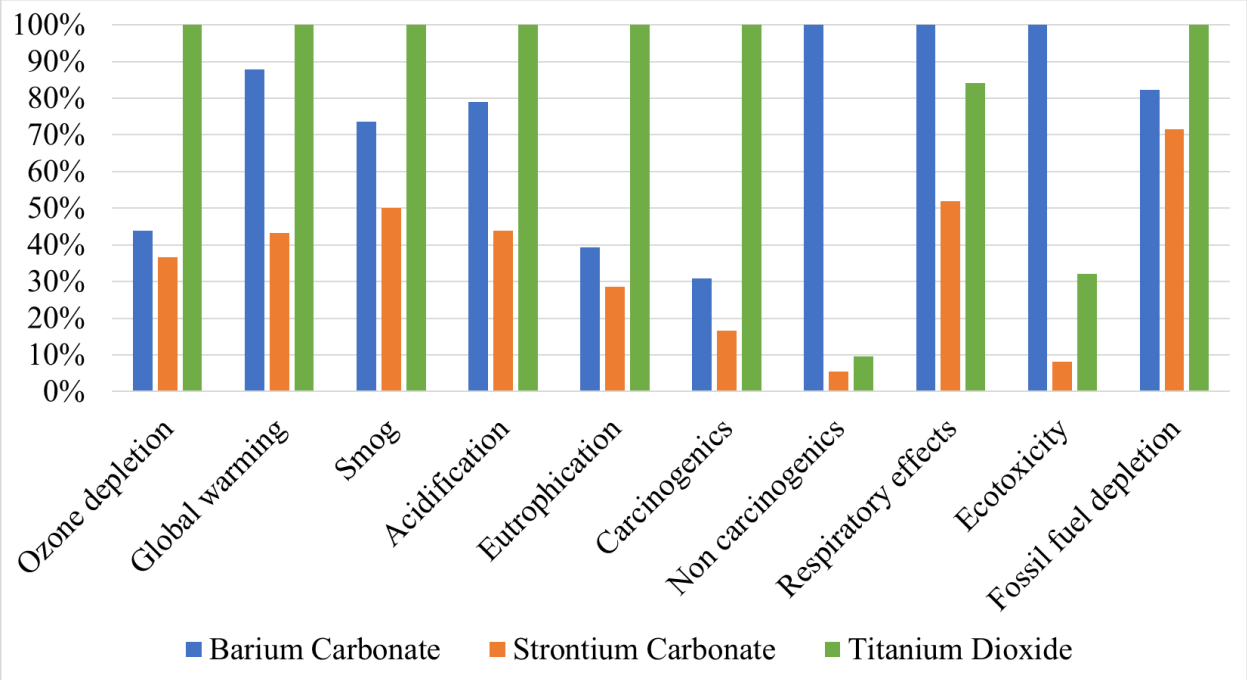

Figure 8.4: A plot of environmental impact across 10 impact categories comparing Barium carbonate, strontium carbonate and titanium dioxide of equivalent mass.

When comparing these environmental effects, it is necessary to define a scope of the work and decide as to whether the impact of changing the ratio of Ba-Sr has a substantial effect on the environment. In this study, the comparison is being made on the scale of an electronic component. As shown in Figure 8.2, the production of the ceramic layers is only one step of the production of a ceramic capacitor. With a component framework, it is possible to compare 1kg of BTO capacitors with that of 1kg of STO capacitors, as shown in Figure 8.5. This figure shows that there is very little change in environmental impact in 8 of the 10 categories studied. The two exceptions are those of non-carcinogens and ecotoxicity. The nickel that makes up a large volume percentage of the capacitor has a larger impact than the ceramic components in many of the impact categories. The major contributions include coal and fossil fuels for heating, sulfidic

tailings from processing and respiratory effects from the nickel mining. In both capacitor types, the nickel and copper contribution remain the same.

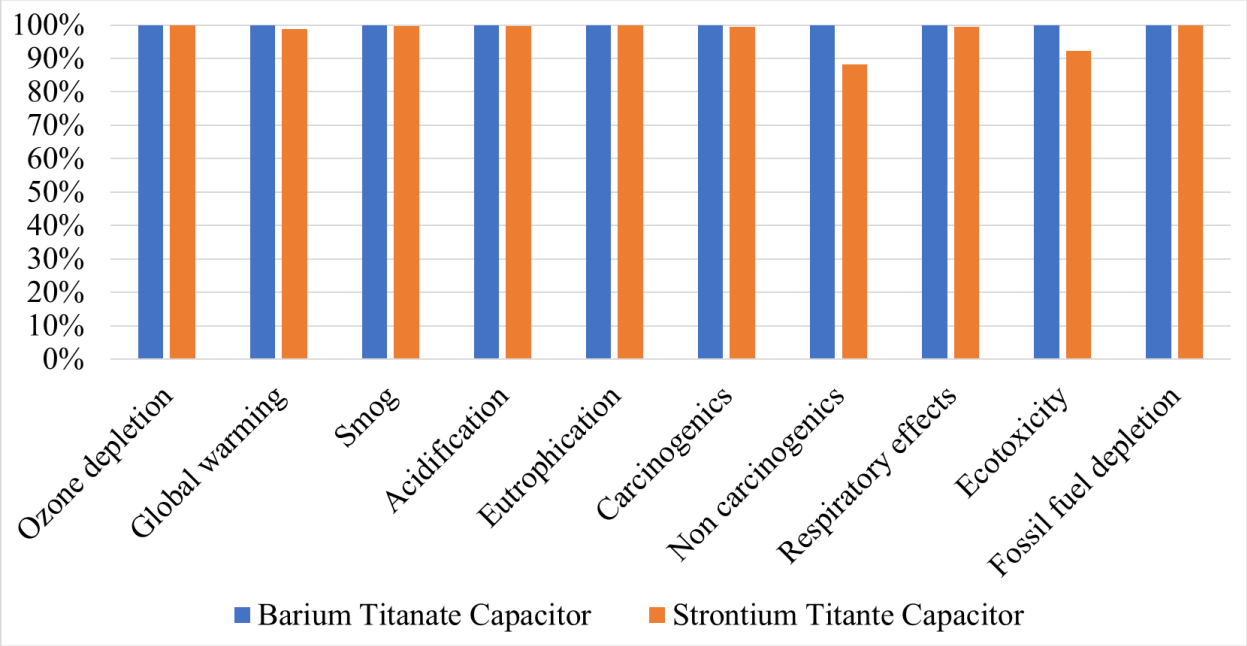

Figure 8.5: A plot of environmental impact across 10 impact categories comparing a $BaTiO_3$ capacitor vs $SrTiO_3$ capacitor composed of base metal electrodes.

In summary, when transitioning from a $SrTiO_3$ capacitor to a $BaTiO_3$ capacitor, the major changes in environmental impact come from handling barium sulfide and barium carbonate, as they are oral toxins. The goal of this study is to help researchers and industry determine the impact of altering the composition of $BaSrTiO_3$ devices. If the principal investigator is considering adding barium carbonate to an existing dielectric, they should be aware of the potential risks of handling a toxic substance and it necessary to be especially mindful of the end of life of the product. By the time of disposal, most electrical components have only existed for 5% of their intended lifespan; due to reliability concerns, most electrical components are disposed of instead of recycled.[66] When considering a standard use case for this study, it is very rare that $SrTiO_3$ is used by itself. Instead, it is commonly alloyed with $BaTiO_3$ or other

dielectric ceramics. When considering a scenario where $BaTiO_3$ is already in use and one is considering a change in the Sr to Ba ratio for a component, the environmental impact of such a change is minimal, but due to the widespread usage of these capacitors this small impact could have long term cumulative effects.

APPENDIX A. PORE SHAPE ANALYSIS

Appendix A contains the pore images used to create the 3D reconstruction discussed in section 4.

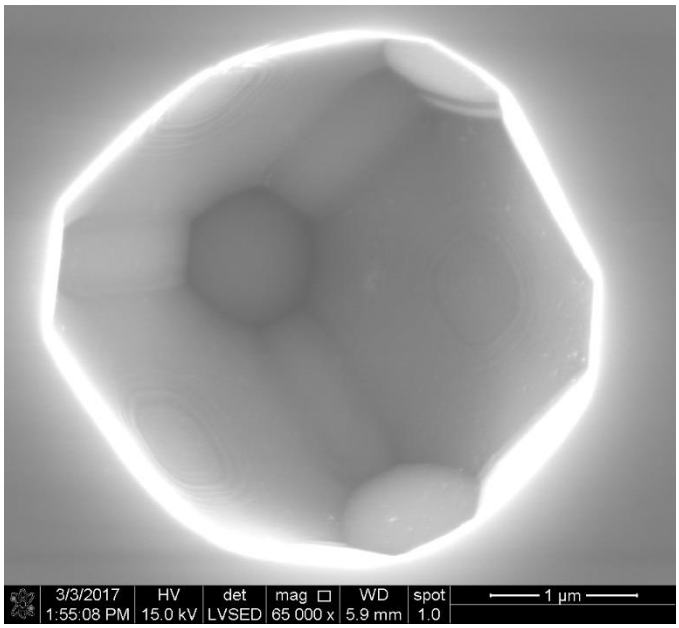

An SEM micrograph of Ba25%-Sr75% pore 1 used for 3D reconstructions.

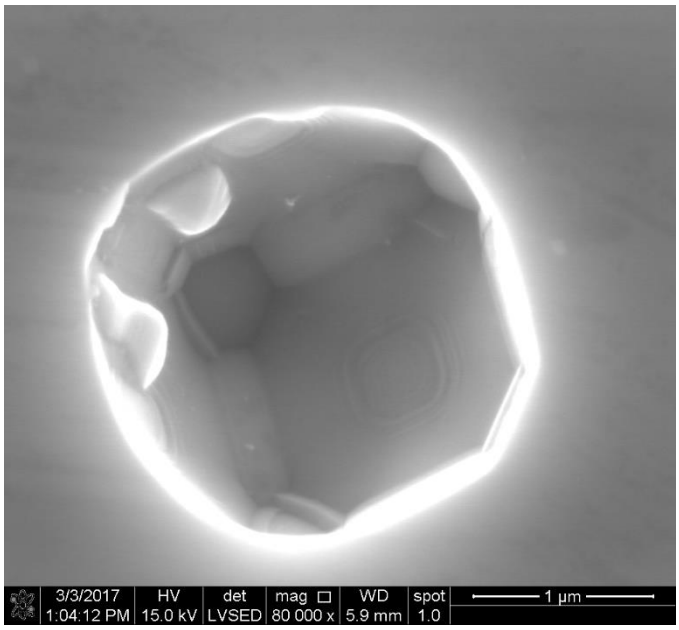

An SEM micrograph of Ba25%-Sr75% pore 2 used for 3D reconstructions.

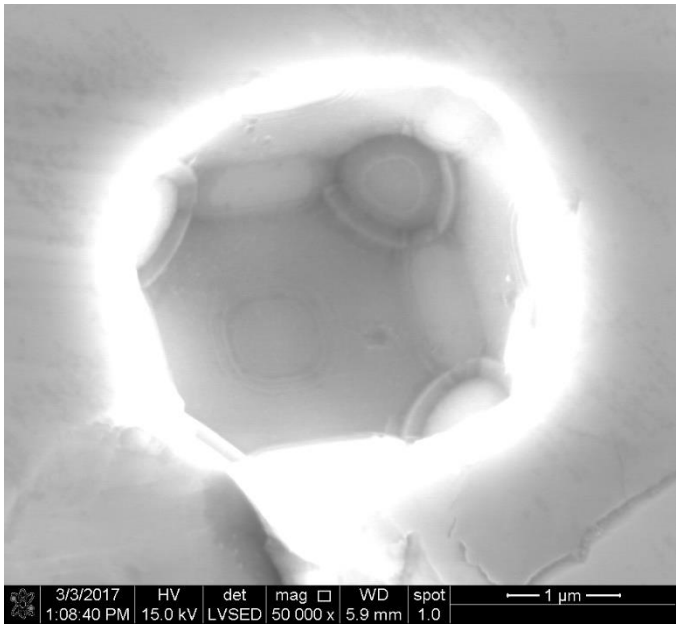

An SEM micrograph of Ba25%-Sr75% pore 3 used for 3D reconstructions.

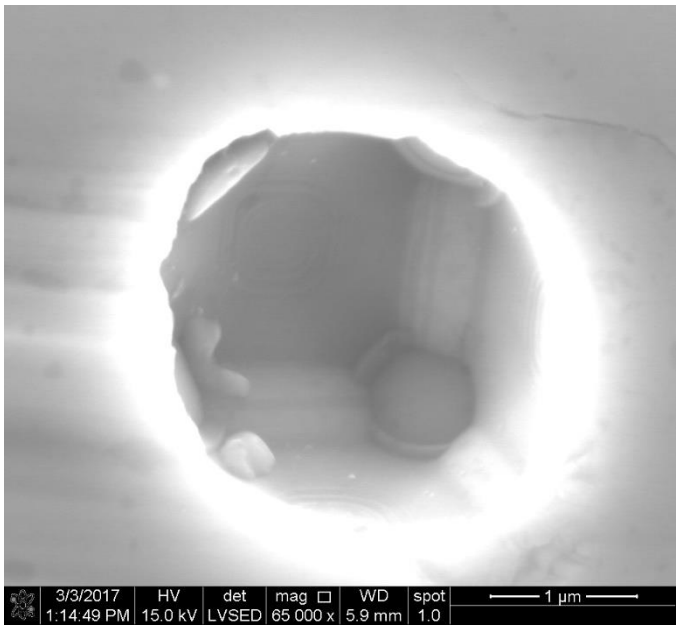

An SEM micrograph of Ba25%-Sr75% pore 4 used for 3D reconstructions.

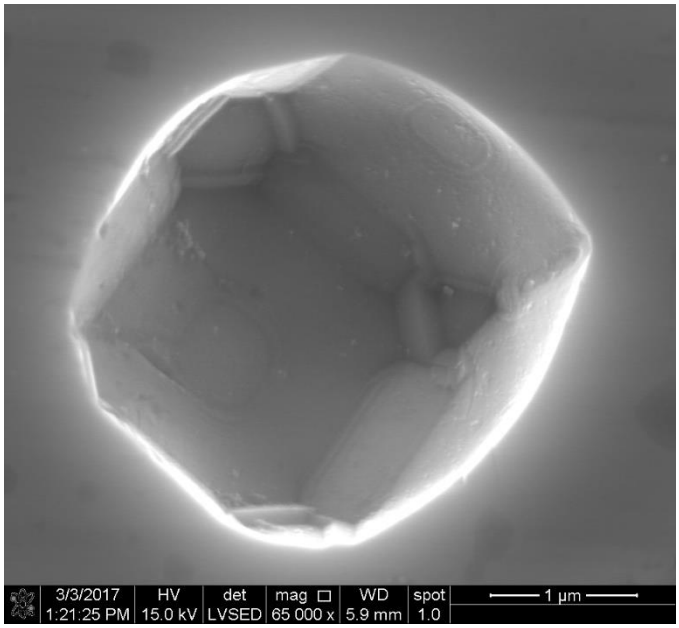

An SEM micrograph of Ba25%-Sr75% pore 5 used for 3D reconstructions.

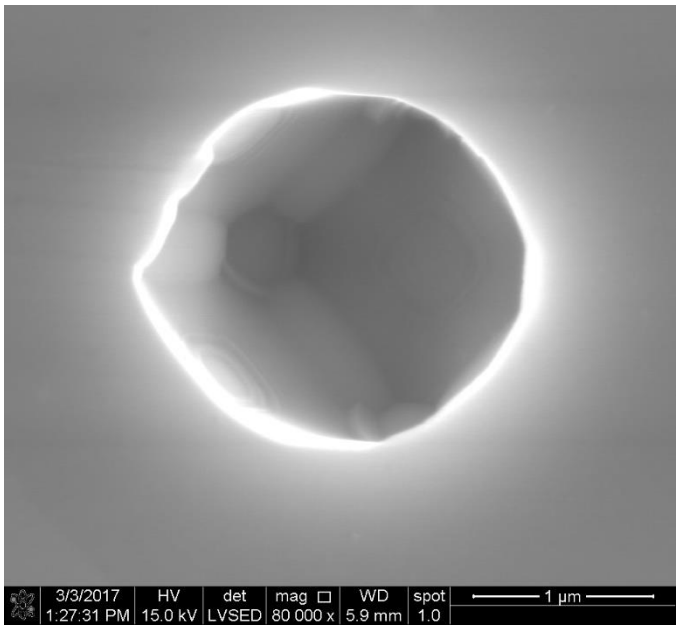

An SEM micrograph of Ba25%-Sr75% pore 6 used for 3D reconstructions.

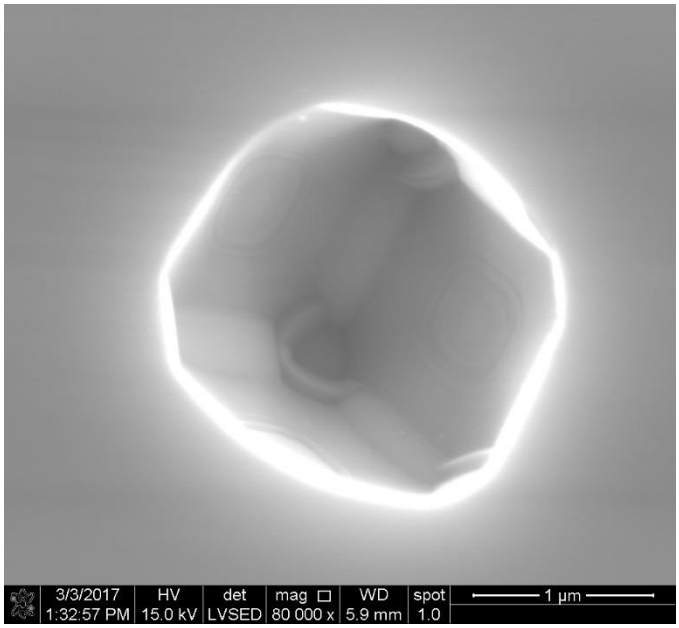

An SEM micrograph of Ba25%-Sr75% pore 7 used for 3D reconstructions.

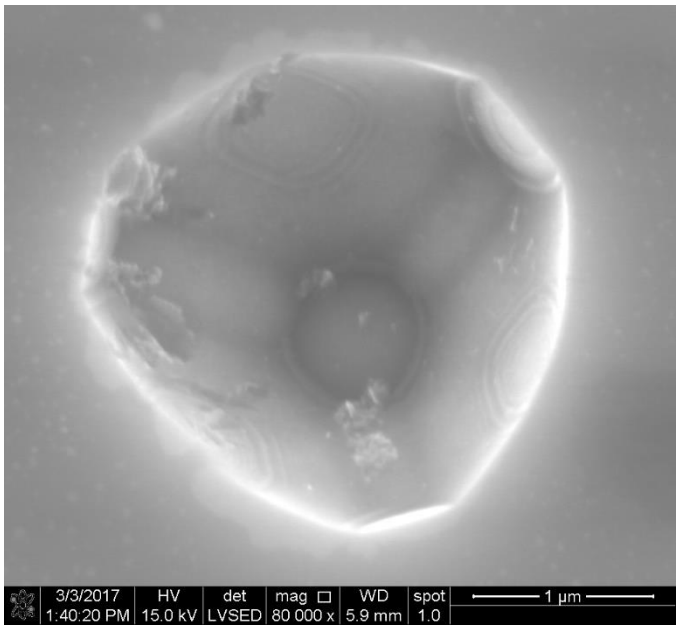

An SEM micrograph of Ba25%-Sr75% pore 8 used for 3D reconstructions.

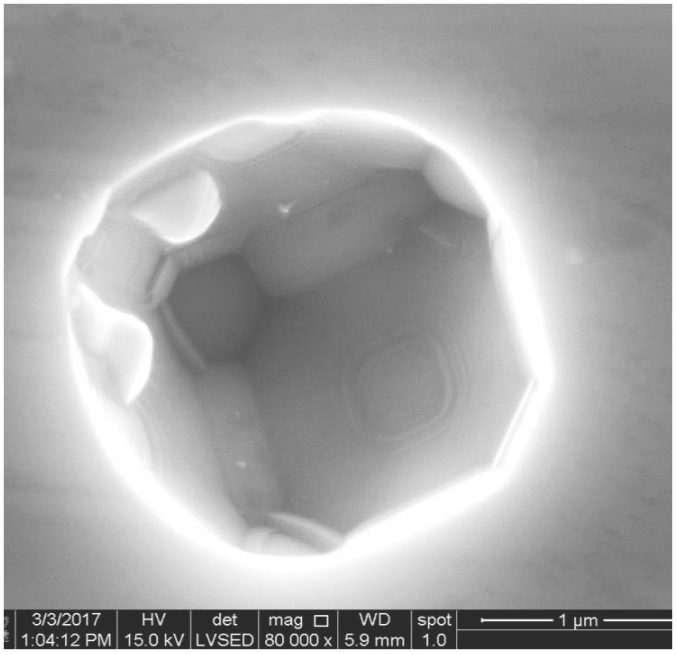

An SEM micrograph of Ba25%-Sr75% pore 9 used for 3D reconstructions.

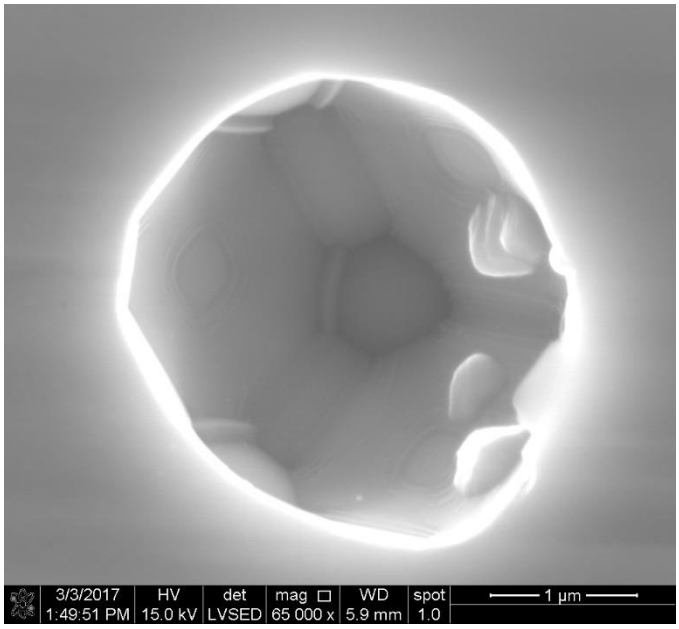

An SEM micrograph of Ba25%-Sr75% pore 10 used for 3D reconstructions.

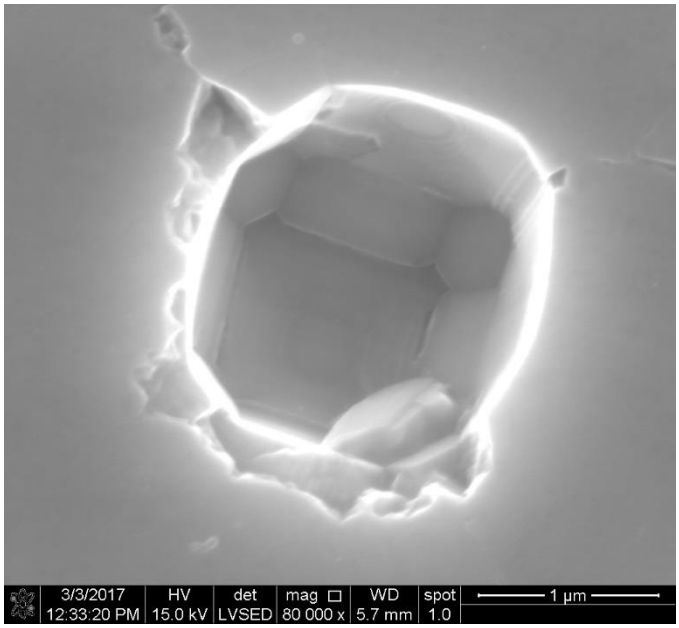

An SEM micrograph of Ba50%-Sr50% pore 1 used for 3D reconstructions.

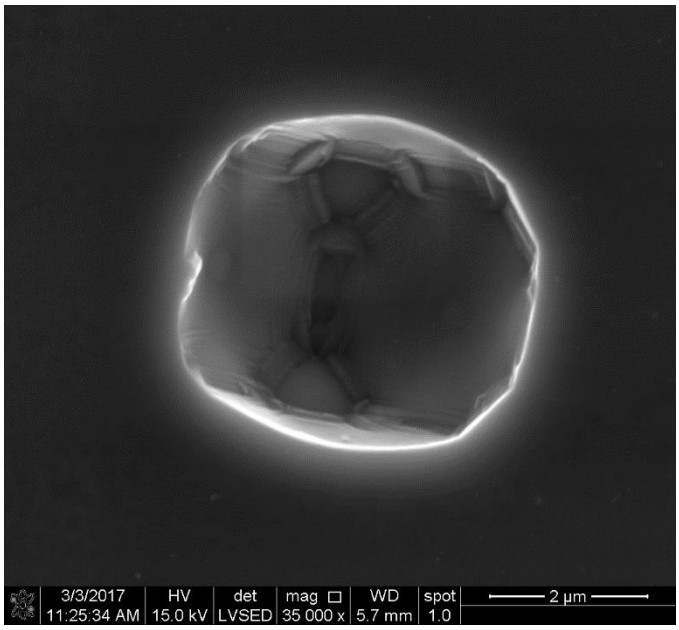

An SEM micrograph of Ba50%-Sr50% pore 2 used for 3D reconstructions.

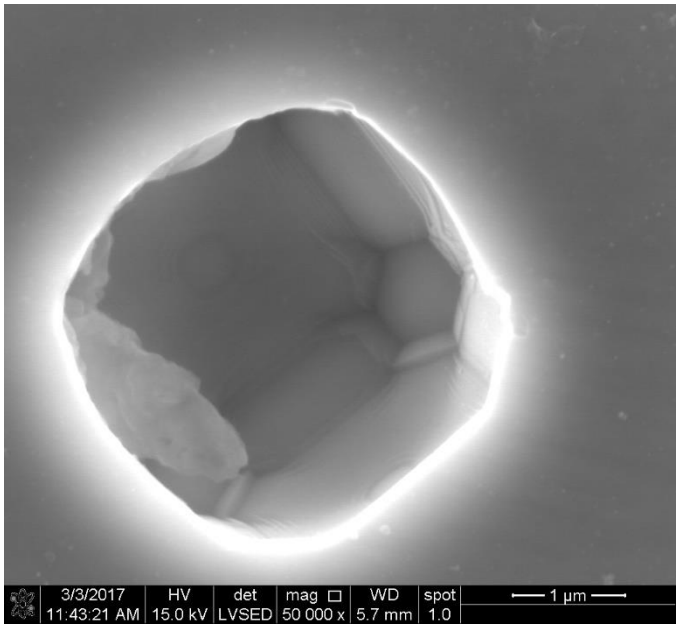

An SEM micrograph of Ba50%-Sr50% pore 3 used for 3D reconstructions.

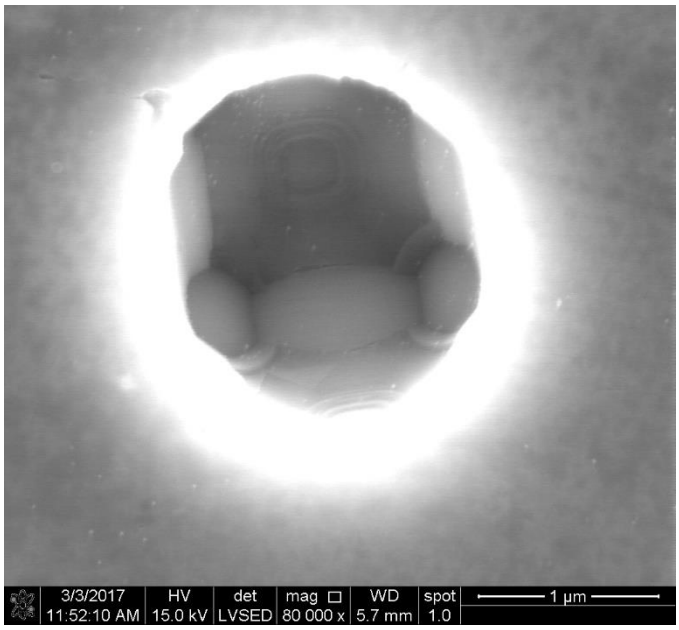

An SEM micrograph of Ba50%-Sr50% pore 4 used for 3D reconstructions.

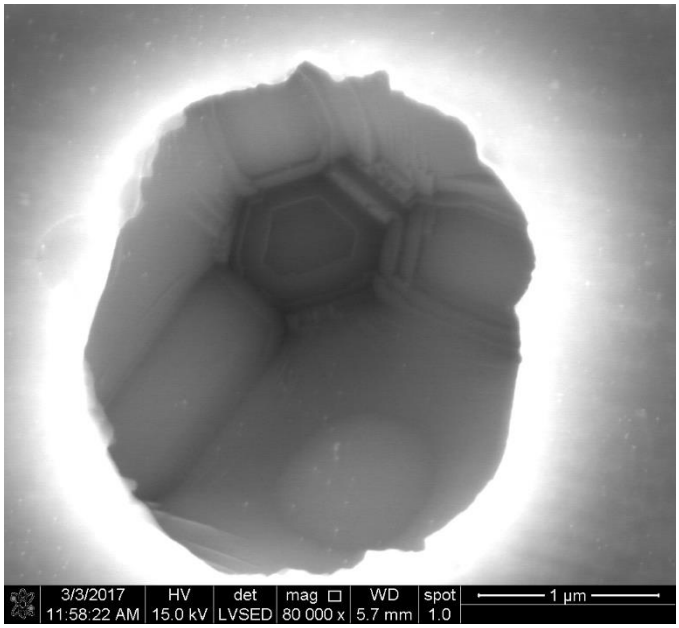

An SEM micrograph of Ba50%-Sr50% pore 5 used for 3D reconstructions.

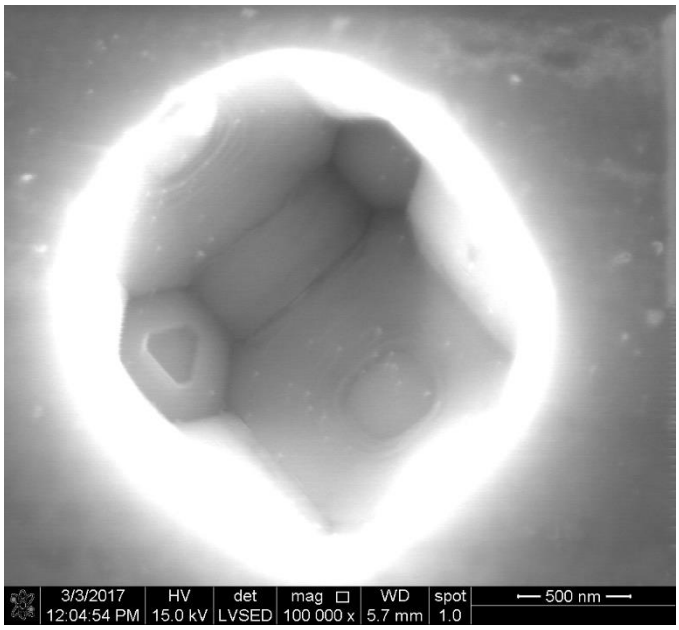

An SEM micrograph of Ba50%-Sr50% pore 6 used for 3D reconstructions.

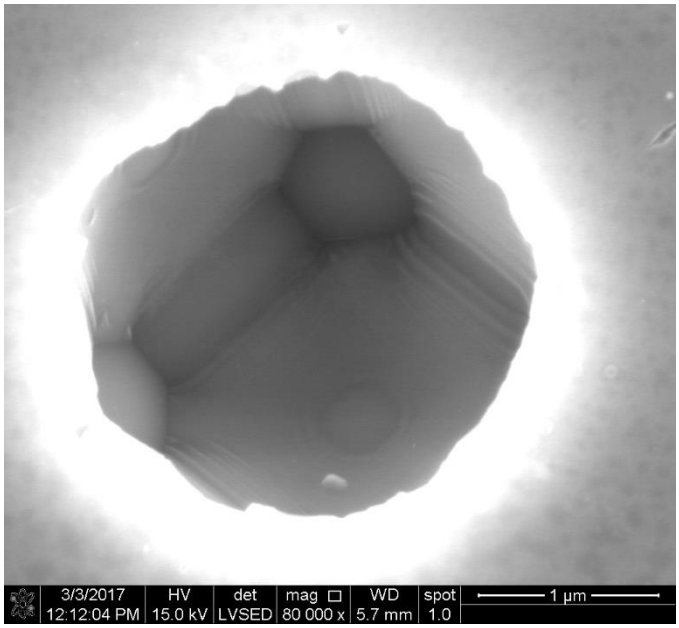

An SEM micrograph of Ba50%-Sr50% pore 7 used for 3D reconstructions.

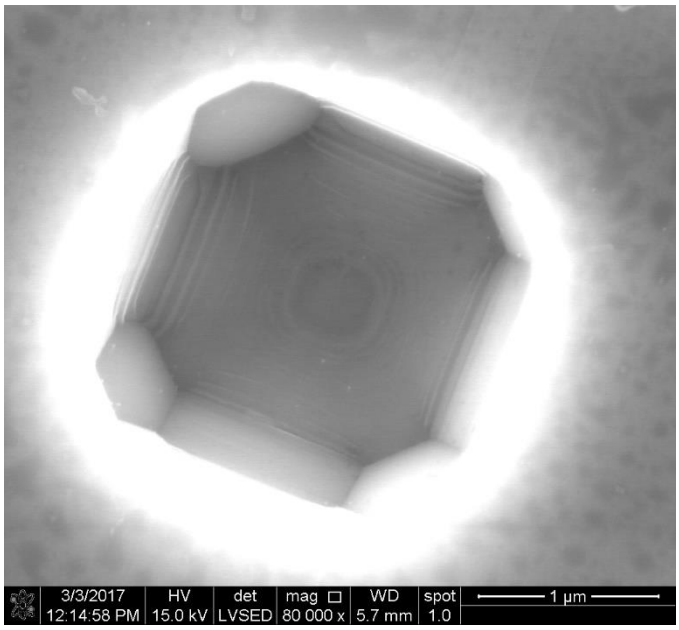

An SEM micrograph of Ba50%-Sr50% pore 8 used for 3D reconstructions.

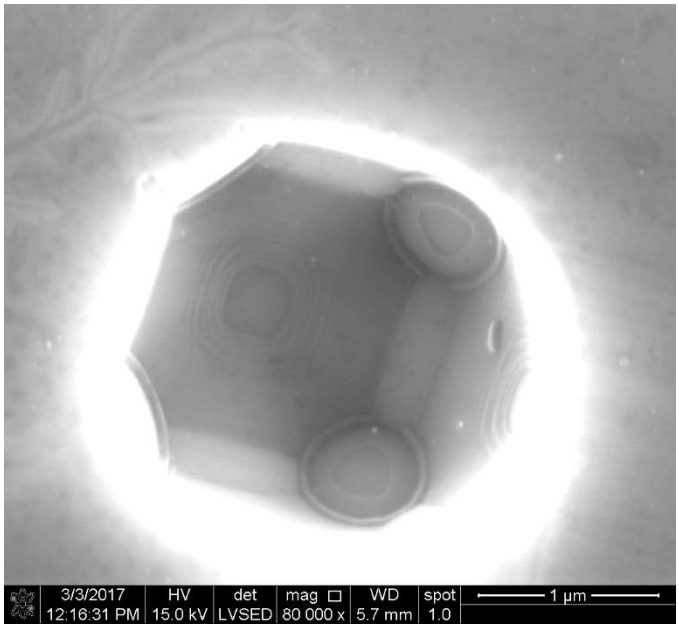

An SEM micrograph of Ba50%-Sr50% pore 9 used for 3D reconstructions.

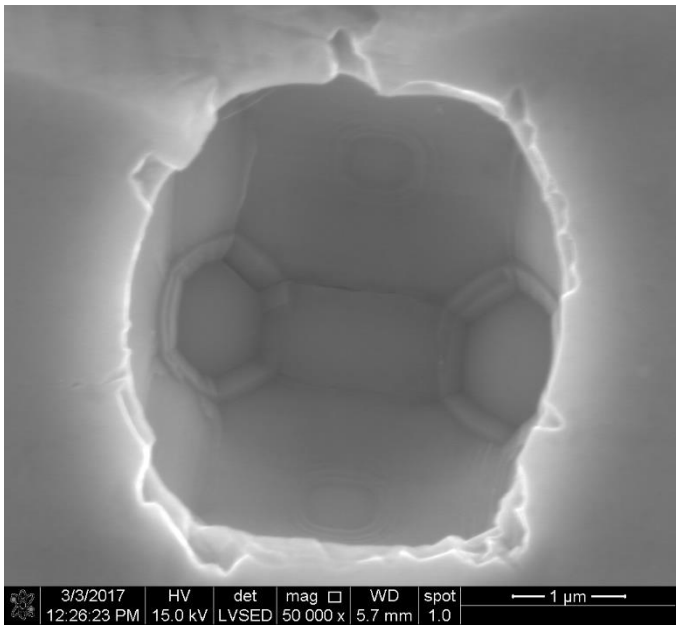

An SEM micrograph of Ba50%-Sr50% pore 10 used for 3D reconstructions.

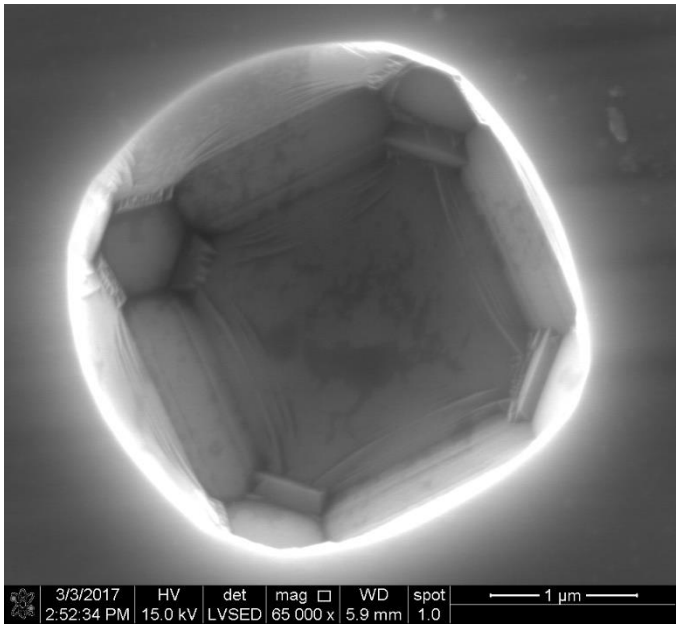

An SEM micrograph of Ba75%-Sr25% pore 1 used for 3D reconstructions.

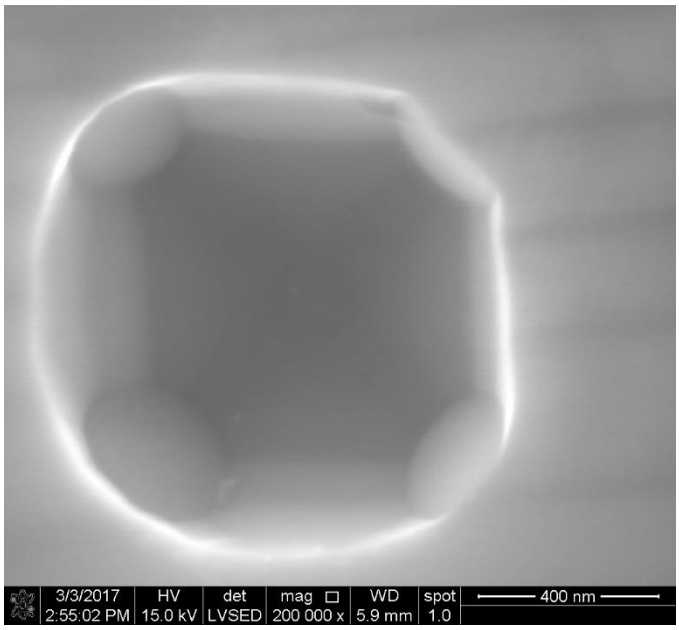

An SEM micrograph of Ba75%-Sr25% pore 2 used for 3D reconstructions.

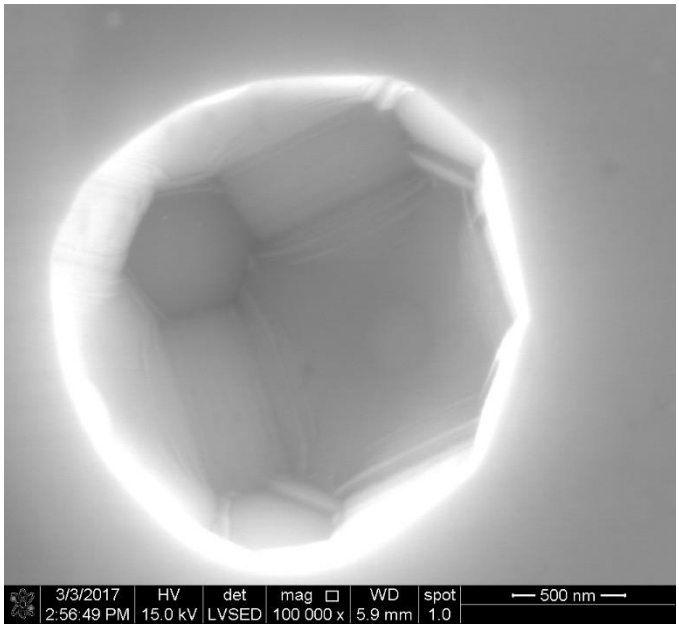

An SEM micrograph of Ba75%-Sr25% pore 3 used for 3D reconstructions.

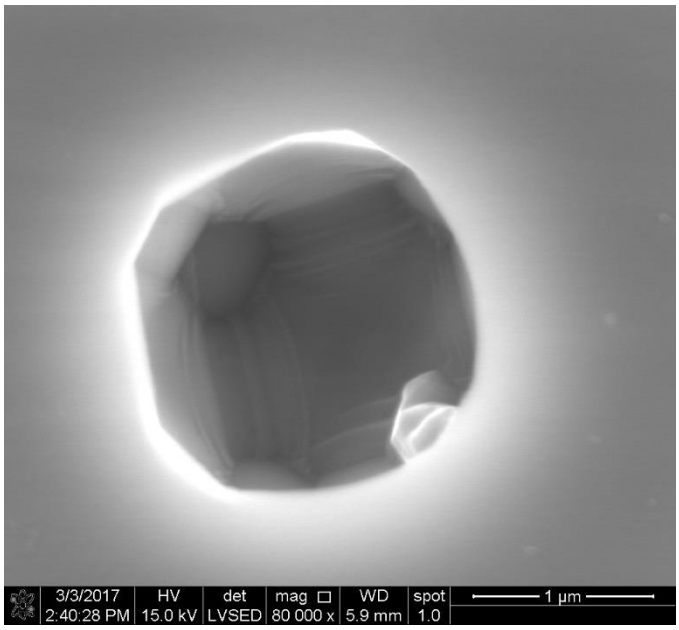

An SEM micrograph of Ba75%-Sr25% pore 4 used for 3D reconstructions.

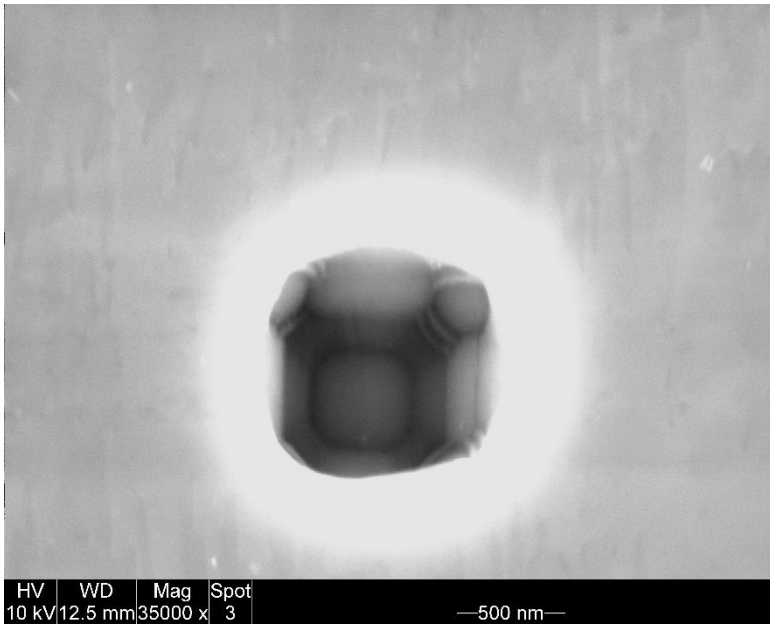

An SEM micrograph of Ba75%-Sr25% pore 5 used for 3D reconstructions.

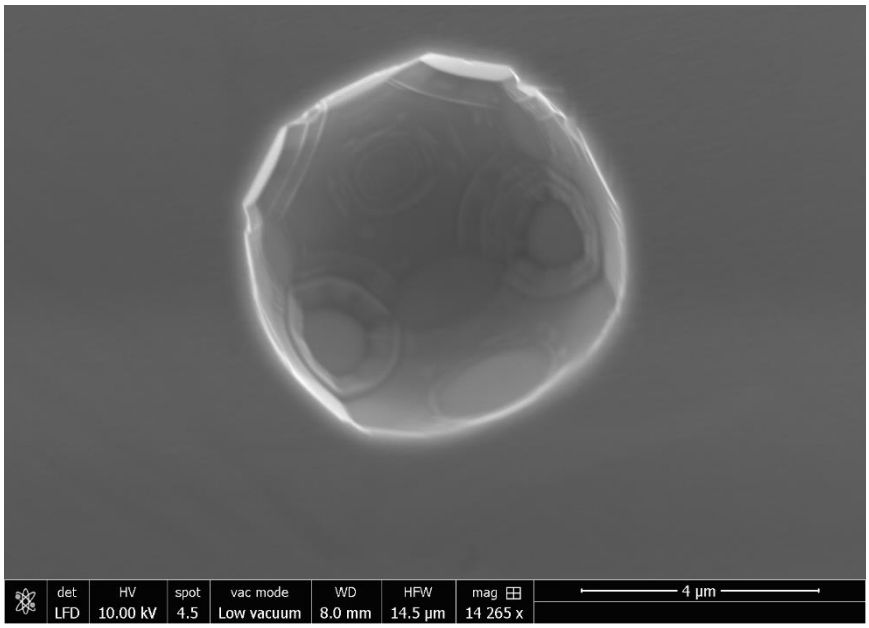

An SEM micrograph of $BaTiO_3$ pore 1 used for 3D reconstructions.

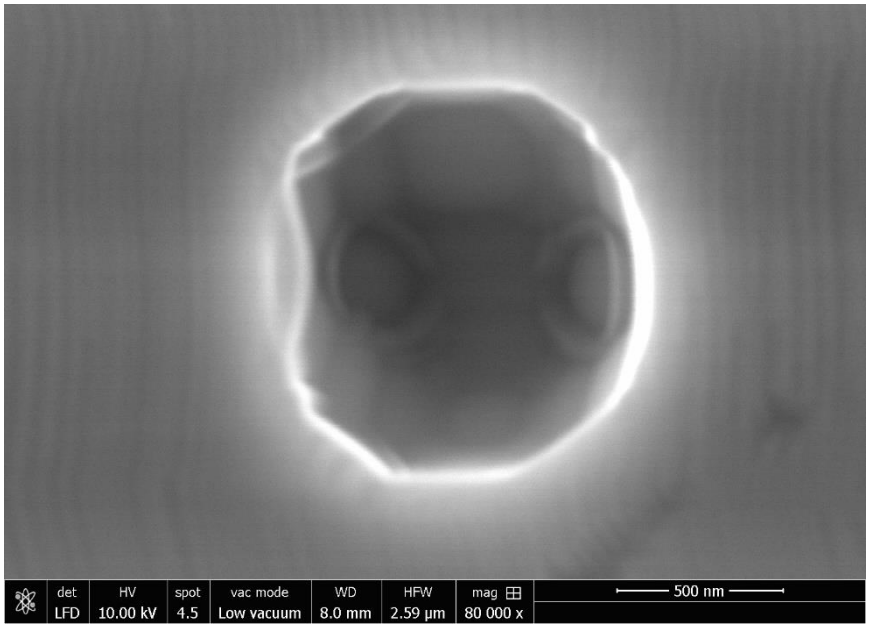

An SEM micrograph of $BaTiO_3$ pore 2 used for 3D reconstructions.

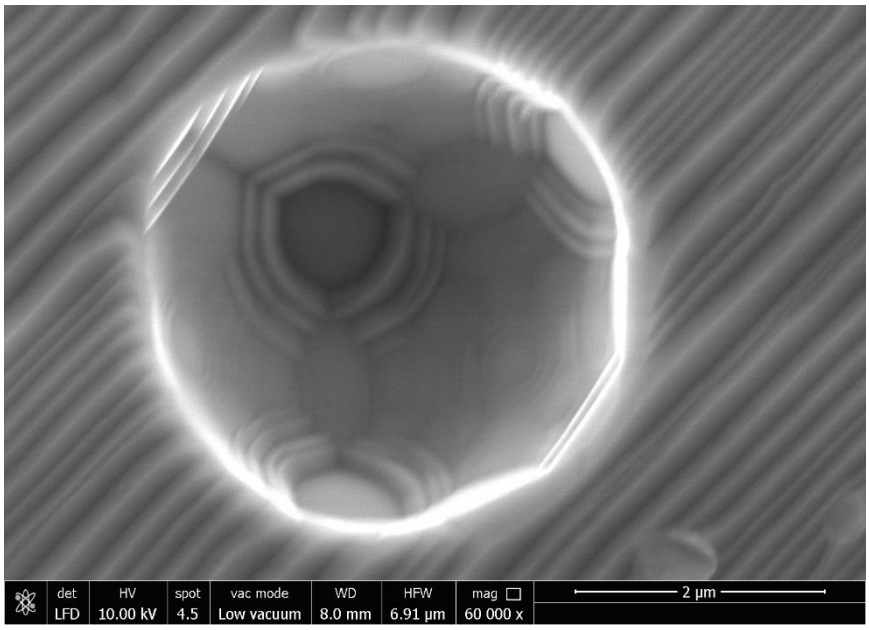

An SEM micrograph of $BaTiO_3$ pore 3 used for 3D reconstructions.

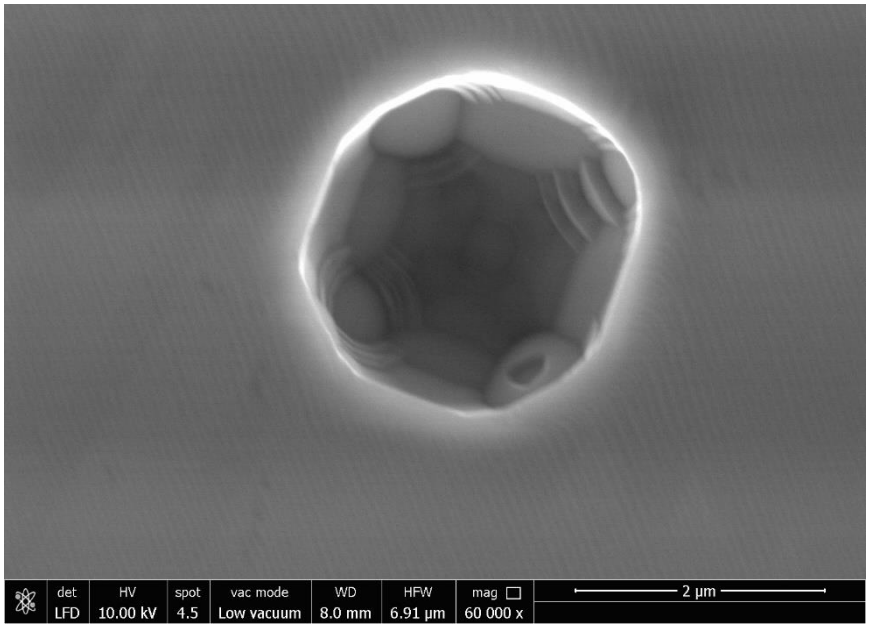

An SEM micrograph of $BaTiO_3$ pore 4 used for 3D reconstructions.

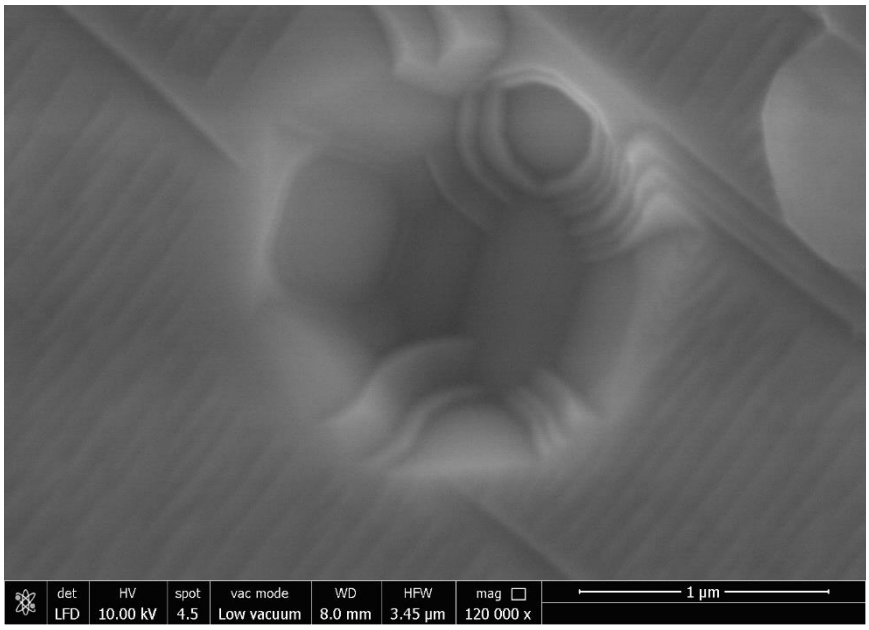

An SEM micrograph of $BaTiO_3$ pore 5 used for 3D reconstructions.

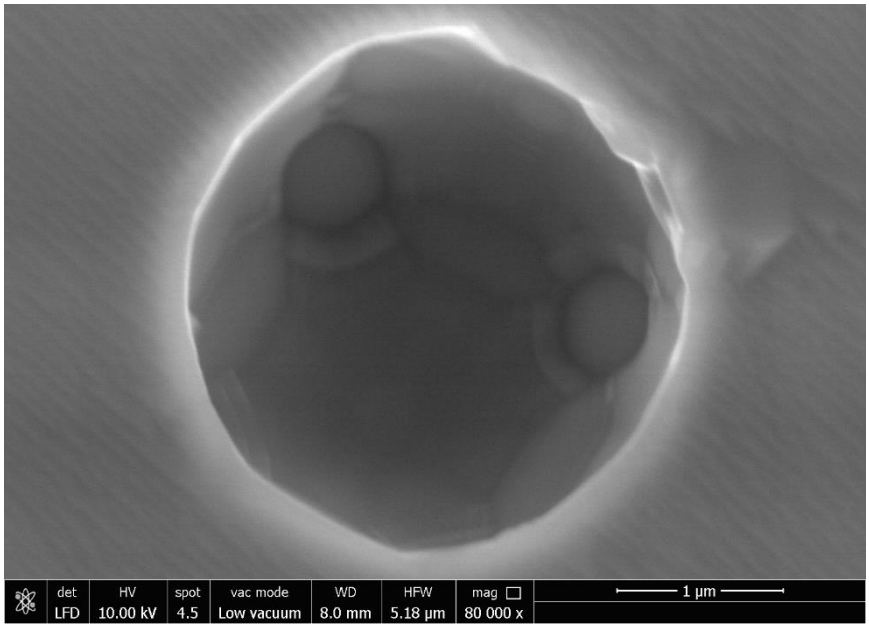

An SEM micrograph of $BaTiO_3$ pore 6 used for 3D reconstructions.

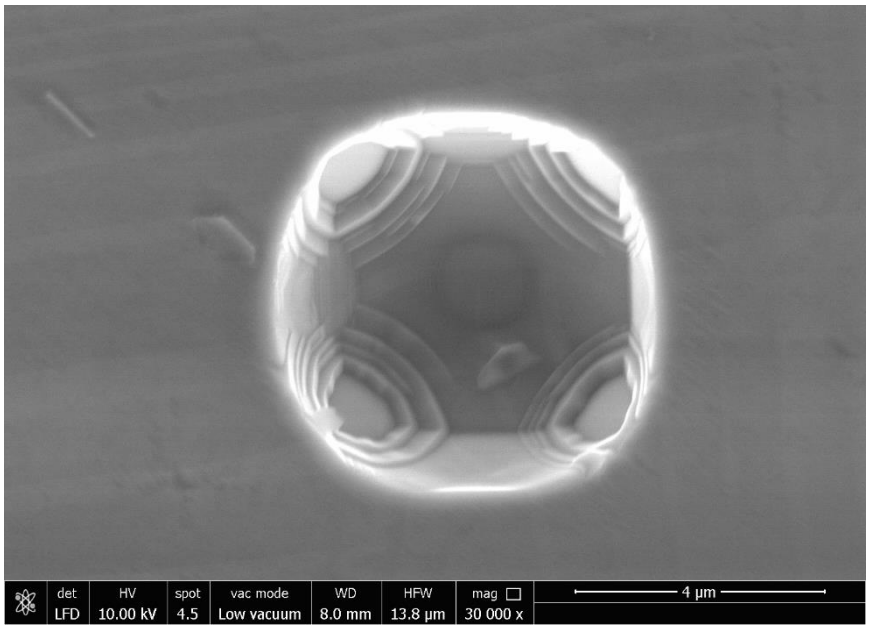

An SEM micrograph of $BaTiO_3$ pore 7 used for 3D reconstructions.

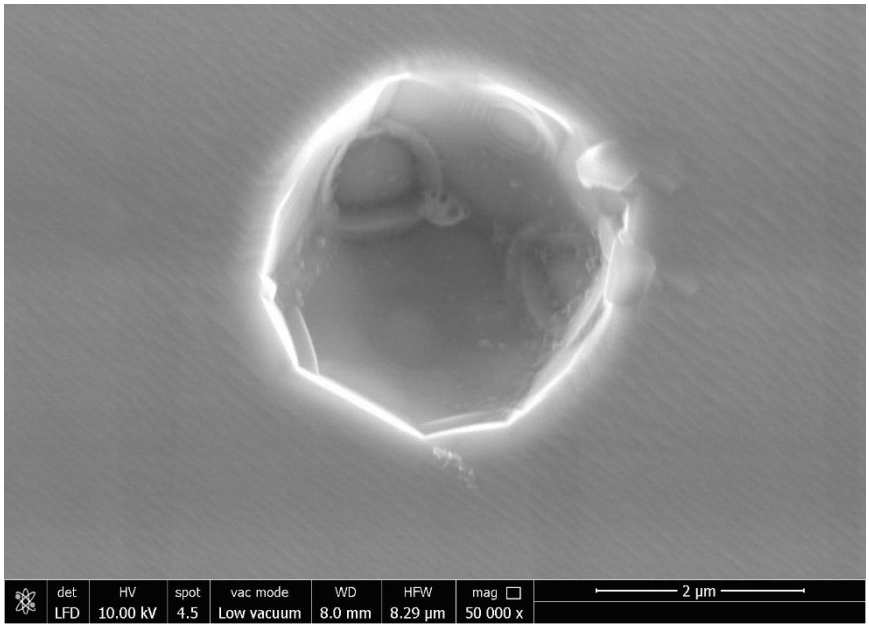

An SEM micrograph of $BaTiO_3$ pore 8 used for 3D reconstructions.

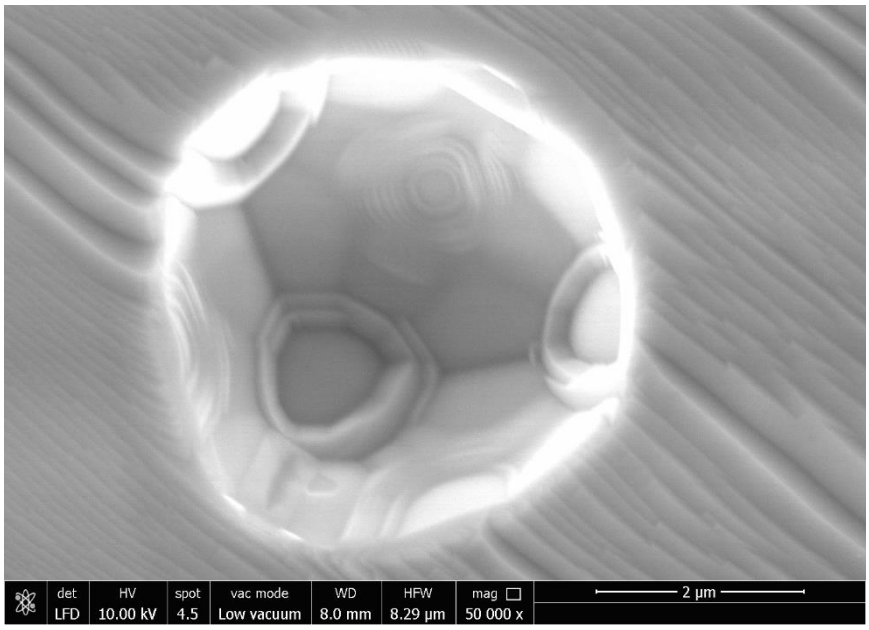

An SEM micrograph of $BaTiO_3$ pore 9 used for 3D reconstructions.

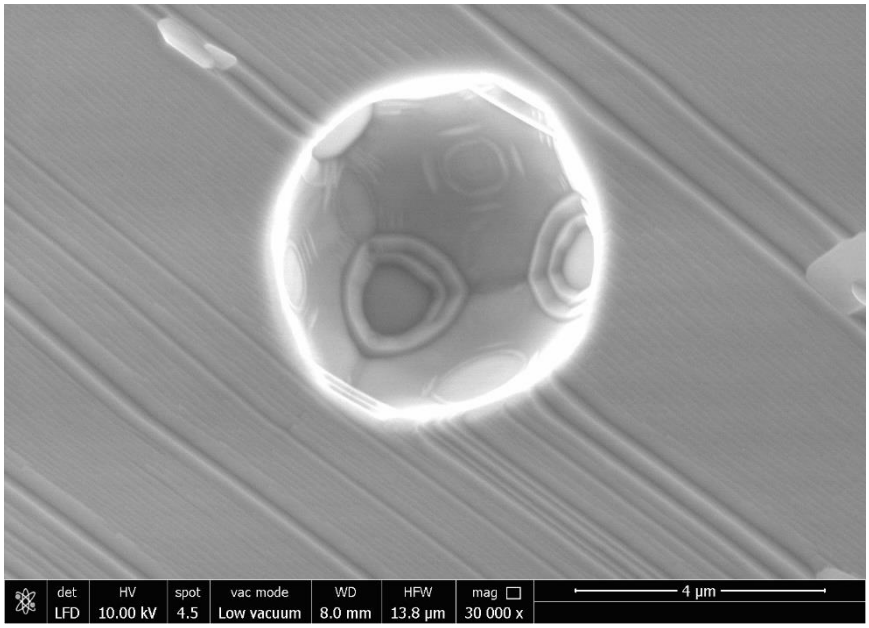

An SEM micrograph of $BaTiO_3$ pore 10 used for 3D reconstructions.

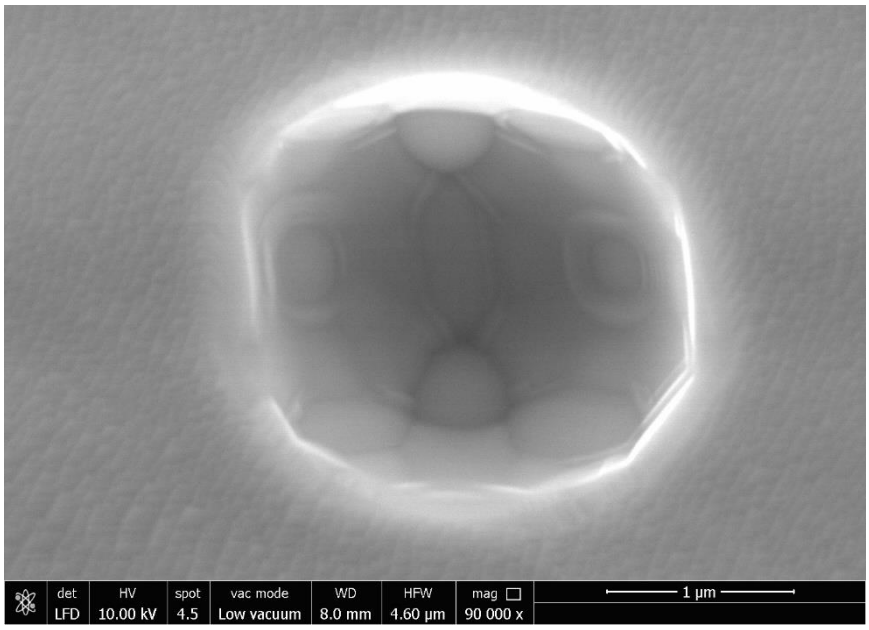

An SEM micrograph of $BaTiO_3$ pore 11 used for 3D reconstructions.

APPENDIX B. MATLAB SCRIPTS

This appendix contains the collective MATLAB code used to process the data used in this document. Appendix B contains 6 separate scripts and prior to the beginning of each script there is a brief description of the purpose of each script. Significant portions of this code are altered version of the code originally created by David Lowing.[55]

MATLAB Script 1- this script extracts the AFM data from a raw nasoscope image file and converts it into a text document.

```
function [data_mtx] = TextFileExtraction(afm_text)

%Imports text file making a structure and then pulls out necessary data

%segments
filename = afm_text; %sets text file name
delimiterIn = ' '; %sets delimeter basis
data = importdata(filename,delimiterIn); %converts data from text to structure
data_array = data.data; %isolate data matrix from structure
header = data.textdata; %isolate header from structure

%confirm this will work dependig on text format
%extraction!!
[r,c] = size (data_array); % Measures row and column size
while c>1 %while loop removes all columes except c1
```

```
    data_array(:,2) = [];
    [r,c] = size (data_array); % Measures row and column size
end
%Header information extraction
line_count = char(header(67)); %isolate header line
Key   = '"\Samps/line: '; %set search key
Index = strfind(line_count, Key); %find key in string
Value = sscanf(line_count(length(Key):end), '%g', 1); %set double to number following string

line_count = char(header(63)); %isolate header line
Key2 = '"\Scan size: '; %set search key
Index = strfind(line_count, Key2); %find key in string
Value2 = sscanf(line_count(length(Key2):end), '%g', 1); %set double to number following string

%Z reshaping and conversion
Mtx_1 = reshape(data_array, Value, []); % reshape matrix to correct dimensions
data_mtx = flip(Mtx_1); %flips matrix to match other formats
zcon = Value/Value2; % number of points divided by total length of x
data_mtx = data_mtx * zcon; %converting z height from nm to points
end
```

MATLAB Script 2- This script is the main plane fitting script used to create a surface mesh to represent the AFM data and determine the normal vectors of the surfaces. The inputs for this script are the converted AFM data, 3 Euler angles obtained from EBSD and correction angle to account for the difference between the AFM and SEM laboratory frame.

```
function [Rval_array, crystal_normal_cell] = Plane_Fit_Main_Script_New(afm_text)
%This script is designed to create a series 3x3 arrays from given data and
%run them through a plain fit script then output an array containing the
%best plane fit for each point in the form of a plane normal.

[data_array] = TextFileExtraction(afm_text);

%inputs
%-number of lines and points per line (assumed to be the same)
%-the z height data array
warning('off','curvefit:fit:iterationLimitReached') % Turns off Matlab warning
[r,c] = size (data_array); % Measures row and column size
crystal_normal_cell = cell(r,c); % Creates cell array matching input size
Rval_array = zeros(r,c); % Creates double array matching input size
x = 1:3; % Creates 1x3 vector
y = 1:3; % Creates 1x3 vector

angle1 = Angle1 % EBSD angle 1
```

```
angle2 = Angle2 % EBSD angle 2

angle3 = Angle3 % EBSD angle 3


correction = CorrectionAngle % SEM to AFM correction angle + is Clockwise


u = (180-angle3) + correction % 180 - EBSD angle swapping 1 and 3 correct this one***

v = 180-angle2 % EBSD angle 2 stays the same

w = 180-angle1 %180 - EBSD angle swapping 1 and 3


R1 = [cosd(u) sind(u) 0; -sind(u) cosd(u) 0; 0 0 1]; % Z rotation matrix

R2 = [1 0 0; 0 cosd(v) sind(v); 0 -sind(v) cosd(v)]; % X' rotation matrix

R3 = [cosd(w) sind(w) 0; -sind(w) cosd(w) 0; 0 0 1]; % Z" rotation matrix

Rfull = R1*R2*R3; % Creates Euler angle rotation matrix


n=2;

m=2;

while n <= r-1

   while m <= c-1

% Extracts data points and fits them to a plane cycles 50 times to get best fit

      point_array = [data_array(n-1,m-1) data_array(n-1,m) data_array(n-1,m+1);

data_array(n,m-1) data_array(n,m) data_array(n,m+1); data_array(n+1,m-1) data_array(n+1,m)

data_array(n+1,m+1)];

      [X, Y, Z] = prepareSurfaceData(x, y, point_array);
```

```
        [fitresult, gof] = createFit(X, Y, Z); %does the fitting for the plane ****
%       formula(fitresult);
%       Rval = gof.rsquare;
        Rval_array(n,m) = gof.rsquare;
        coe = coeffvalues(fitresult);
%       coeffnames(fitresult);
        if Rval_array(n,m) > 0.0
% Creates 4 points on the calculated plane then 2 lines and solves the cross product
            Z1 = (coe(1,1))+(coe(1,2)*1)+(coe(1,3)*1); % Calculates z-1
            Z2 = (coe(1,1))+(coe(1,2)*3)+(coe(1,3)*3); % Calculates z-2
            Z3 = (coe(1,1))+(coe(1,2)*3)+(coe(1,3)*1); % Calculates z-3
            Z4 = (coe(1,1))+(coe(1,2)*1)+(coe(1,3)*3); % Calculates z-4
            P1 = [1 1 Z1]; % Creates point using z-1
            P2 = [3 3 Z2]; % Creates point using z-2
            P3 = [3 1 Z3]; % Creates point using z-3
            P4 = [1 3 Z4]; % Creates point using z-4
            V1 = [P1(1)-P2(1), P1(2)-P2(2), P1(3)-P2(3)]; % Creates vector between point 1,2
            V2 = [P3(1)-P4(1), P3(2)-P4(2), P3(3)-P4(3)]; % Creates vector between point 3,4
            vec = cross(V1, V2); % Cross product of 2 vectors
% Normalizes the vector and applies the EBSD rotation using a rotation
% matrix
            normal = vec/norm(vec); % Normalizes vector
            normal = normal'; % Transposes vector
```

```
            crystal_normal = Rfull* normal; % Applies EBSD based rotation matrix
            crystal_normal = crystal_normal'; % Transposes vector
% Packages the vector as a cell and stores it in a cellarray
            normal_vector = {crystal_normal(1,1), crystal_normal(1,2), crystal_normal(1,3)};
            crystal_normal_cell(n, m) = {normal_vector};
        else
% sets Rval and relative vector cell to zero making it a null result if it does
% not pass the quality control test
            Rval_array(n,m) = 0;
            normal_vector = {0, 0, 0};
            crystal_normal_cell(n, m) = {normal_vector};
        end
         m = m+1; %column loop counter
    end
    m = 2; %Column loop counter reset at end of row
    n = n+1 %Row loop counter
end


warning('on','curvefit:fit:iterationLimitReached') % Turns on Matlab warning
```

MATLAB Script 3- This script is used to plot the data from MATLAB script 2 as well as MATLAB script 4. This script removes points below the R^2 value threshold and plots the data on a stereographic projection. Please note this script uses the MTEX suite and it must be running to plot.

```
function Data_Processing_Script(Rval_array, crystal_normal_cell)

[r,c] = size (Rval_array);
n=2;
m=2;
while n <= r-1
    while m <= c-1
        if Rval_array(n,m) > 0
            vector = [crystal_normal_cell{n,m}{1,1}, crystal_normal_cell{n,m}{1,2},
crystal_normal_cell{n,m}{1,3}];
            vector = vector * -1;
            fid = fopen('Vector_List.txt', 'a+');
            fprintf(fid, '%f %f %f\r\n', vector);
            fclose(fid);
        end
        m = m+1;
    end
    m = 2;
```

```
    n = n+1
end


figure;
fname = fullfile('Vector_List.txt');
v = loadVector3d(fname,'ColumnNames',{'x','y','z'});
contourf(v,'projection','eangle','grid','upper')%change eangle to earea?
mtexColorbar
annotate([vector3d.X,vector3d.Y,vector3d.Z],'label',{'X','Y','Z'},'backgroundcolor','w')
cs = crystalSymmetry('m-3m')
hold all
plotHKL(cs,'projection','eangle','grid_res',15*degree,'BackGroundColor','w')
hold off
%saveas(gcf,'1')


figure;
fname = fullfile('Vector_List.txt');
v = loadVector3d(fname,'ColumnNames',{'x','y','z'});
scatter(v,'MarkerSize', 2,'projection','eangle','grid','upper')
mtexColorbar
annotate([vector3d.X,vector3d.Y,vector3d.Z],'label',{'X','Y','Z'},'backgroundcolor','w')
cs = crystalSymmetry('m-3m')
hold all
```

```
plotHKL(cs,'projection','eangle','grid_res',15*degree,'BackGroundColor','w')

hold off

%saveas(gcf,'2')


%delete Vector_List.txt % if you want to delete file to prevent overwriting next dataset
```

MATLAB Script 4- This script is a rotational script that utilized the data from MATLAB script 2 and copies the data points to appear in all triangles of the stereographic projection via a rotation matrix. After this script is run use MATLAB Script 3 to plot.

```
function [facet]=Rotation_Script(Rval_array, crystal_normal_cell)

[r,c] = size (Rval_array);
%M = zeros(r, c);
q=1
n=2;
m=2;
while n <= r-1
   while m <= c-1
      if Rval_array(n,m) > 0.9
         vector = [crystal_normal_cell{n,m}{1,1}, crystal_normal_cell{n,m}{1,2},
crystal_normal_cell{n,m}{1,3}];
         Facet(q,:)=[vector(1,1); vector(1,2); vector(1,3)];
         vector = vector * -1;
         fid = fopen('Vector_List.txt', 'a+');
         fprintf(fid, '%f %f %f\r\n', vector);
         fclose(fid);
         q=q+1;
      end
```

```
        m = m+1;
    end
    m = 2;
    n = n+1
end


%%%
%here gamma and orientation can be defined
%     Nr   (h k l)  gamma   color   Transparenz
%trans=1;
%Facet(1,:)=[1;0;0;  .85;     1;0;0;       1]; %100: 1.0
%Facet(2,:)=[1;1;0;  1.04;    0;0;0;     1]; %110: 1.11
%Facet(3,:)=[1;1;1;  1.08;   0;0;1;       1]; %111: 1.1
%Facet(4,:)=[4;1;1;  1.02;   0;1;0;      1]; %310: 1.06
% Facet(5,:)=[2;2;1;  1.0344;   1;.5;.1;      1]; %221: 1.15
% Facet(6,:)=[2;1;1;  1.0696;   1;.5;.1;      1]; %221: 1.15
% % Facet(7,:)=[4;1;1;  1.055;   1;.5;.1;   1]; %311: 1.1
% Facet(8,:)=[5;1;1;  1.0527;   1;.5;.1;   1]; %311: 1.1
% % Facet(9,:)=[3;2;2;  1.26;   1;.5;.1;      1]; %221: 1.15
% % Facet(10,:)=[6;1;0;  1.03;   0;1;0;      1]; %310: 1.06
% % % Facet(11,:)=[3;2;1;  1.084;   1;.5;.1;      1]; %310: 1.06
% Facet(12,:)=[3;1;1;  1.069;   1;.5;.1;      1]; %310: 1.06
% % Facet(13,:)=[3;3;2;  1.148;   1;.5;.1;      1]; %310: 1.06
```

```
arg1=size(Facet,1); %reading # of rows from above
facet=zeros(8*6*arg1,3); % making a array of zeros
for i=1:arg1
   facet(i,:)=Facet(i,:); % repopulating zero array with above

facet(i+arg1,:)=[Facet(i,1);Facet(i,3);Facet(i,2)];     %Facet(i,4);Facet(i,5);Facet(i,6);Facet(i,7);F
acet(i,8)];
facet(i+(2*arg1),:)=[Facet(i,2);Facet(i,1);Facet(i,3)]; %Facet(i,4);Facet(i,5);Facet(i,6);Facet(i,7);
Facet(i,8)];
facet(i+(3*arg1),:)=[Facet(i,2);Facet(i,3);Facet(i,1)]; %Facet(i,4);Facet(i,5);Facet(i,6);Facet(i,7);
Facet(i,8)];
facet(i+(4*arg1),:)=[Facet(i,3);Facet(i,1);Facet(i,2)]; %Facet(i,4);Facet(i,5);Facet(i,6);Facet(i,7);
Facet(i,8)];
facet(i+(5*arg1),:)=[Facet(i,3);Facet(i,2);Facet(i,1)]; %Facet(i,4);Facet(i,5);Facet(i,6);Facet(i,7);
Facet(i,8)];
end;
facet=unique(facet,'rows'); % gets rid of double rows

% this section actual symmetry calculations
F=size(facet,1); % read size array
for f=1:F
    facet(f+F,:)=[-facet(f,1);-facet(f,2);-
facet(f,3)];%facet(f,4);facet(f,5);facet(f,6);facet(f,7);facet(f,8)];
```

```
end;
F=size(facet,1);
for f=1:F
   facet(f+F,:)=[-
facet(f,1);facet(f,2);facet(f,3)];%facet(f,4);facet(f,5);facet(f,6);facet(f,7);facet(f,8)];
end;
F=size(facet,1);
for f=1:F
    facet(f+F,:)=[facet(f,1);-
facet(f,2);facet(f,3)];%facet(f,4);facet(f,5);facet(f,6);facet(f,7);facet(f,8)];
end;
F=size(facet,1);
for f=1:F
   facet(f+F,:)=[facet(f,1);facet(f,2);-
facet(f,3)];%facet(f,4);facet(f,5);facet(f,6);facet(f,7);facet(f,8)];
end;
facet=unique(facet,'rows');

[r,c] = size (facet);
%M = zeros(r, c);
q=1
n=2;
while n <= r-1
```

```
        vector = [facet(n,1), facet(n,2), facet(n,3)];
        vector = vector * -1;
        fid = fopen('Vector_List2.txt', 'a+');
        fprintf(fid, '%f %f %f\r\n', vector);
        fclose(fid);
    n = n+1
end

figure;
fname = fullfile('Vector_List2.txt');
v = loadVector3d(fname,'ColumnNames',{'x','y','z'});
contourf(v,'projection','eangle','grid')
mtexColorbar
annotate([vector3d.X,vector3d.Y,vector3d.Z],'label',{'X','Y','Z'},'backgroundcolor','w')
cs = crystalSymmetry('m-3m')
hold all
plotHKL(cs,'projection','eangle','grid_res',15*degree,'BackGroundColor','w')
hold off

figure;
fname = fullfile('Vector_List2.txt');
v = loadVector3d(fname,'ColumnNames',{'x','y','z'});
scatter(v,'MarkerSize', 2,'projection','eangle','grid')
```

```
mtexColorbar
annotate([vector3d.X,vector3d.Y,vector3d.Z],'label',{'X','Y','Z'},'backgroundcolor','w')
cs = crystalSymmetry('m-3m')
hold all
plotHKL(cs,'projection','eangle','grid_res',15*degree,'BackGroundColor','w')
hold off

%delete Vector_List.txt
%delete Vector_List2.txt
```

MATLAB Script 5- This script plots the data processed in MATLAB script 2 and folds it into a single tringle of the stereographic projection using a rotation matrix. This script outputs a scatter plot as well as heat map plot.

```
%getting and preparing the data
close all;
clear;

%put filename of list of surface normal vectors here:
filename='FILENAME.txt';
%do you want to save as tif? (1:yes,else:no)
save=1;

%insert HKL to plot normal% Use largest number as h 2nd as k and 3rd as l
% hkl= [h k l];
%
% lat_hkl= 90-acosd(hkl(3)/norm(hkl))
% long_hkl= atand(hkl(2)/(hkl(1)))
%
% hx= hkl(1)/sqrt(hkl(1)^2+hkl(2)^2+hkl(3)^2);
% ky= hkl(2)/sqrt(hkl(1)^2+hkl(2)^2+hkl(3)^2);
% lz= hkl(3)/sqrt(hkl(1)^2+hkl(2)^2+hkl(3)^2);
```

```
%
% x_stereo= lz/(0.5+0.5*hx);
% y_stereo= ky/(0.5+0.5*hx);
%
% x_hist= x_stereo/0.85*102+1
% y_hist= y_stereo/0.85*102+1
%%
%Read file and prepare data for processing
v=dlmread(filename);
v=abs(v);
for i=1:size(v,1)
    v(i,:)=sort(v(i,:),'descend');
    v(i,:)=v(i,:)/norm(v(i,:));
    theta_v(i)=acosd(v(i,3));
    phi_v(i)=atand(v(i,2)/v(i,1));
end;
%%


%%
%Plot all normal vectors in a stereographic projection of the unit triangle
%(100), (110), (111)
fig1=figure('Position',[0 0 600 600]);
axesm('stereo');
```

```
a=plotm(90-theta_v,phi_v,'MarkerSize',1,'marker','s','MarkerEdgeColor',[0 0
0.7],'LineStyle','none');
xlim([0 0.93]);
ylim([0 0.83]);
theta0=0:0.1:90-54.7;
for i=1:size(theta0,2)
   phi1(i)=45;
end;
plotm([0 0],[0,45],'-','color','black','linewidth',2);
plotm([0 90-54.7356],[0,45],'-','color','black','linewidth',2);
plotm(theta0,phi1,'-','color','black','linewidth',2);
set(gca,'ycolor','w')
set(gca,'xcolor','w')
box off;
axis off;
plotm(0,0,'MarkerSize',20,'marker','o','MarkerFaceColor','red','LineStyle','none')%100
plotm(0,45,'MarkerSize',20,'marker','o','MarkerFaceColor','green','LineStyle','none')%110
plotm(35.2644,45,'MarkerSize',20,'marker','o','MarkerFaceColor','blue','LineStyle','none')%111
plotm(0,18.4349,'MarkerSize',20,'marker','o','MarkerFaceColor','yellow','LineStyle','none')%103
plotm(24.0948,26.5651,'MarkerSize',20,'marker','o','MarkerFaceColor',[0.5,0,0.5],'LineStyle','no
ne')%112
plotm(9.3359,9.4623,'MarkerSize',20,'marker','o','MarkerFaceColor','magenta','LineStyle','none')
%116
```

```
plotm(19.4712,45,'MarkerSize',20,'marker','o','MarkerFaceColor','cyan','LineStyle','none')%212
%
plotm(lat_hkl,long_hkl,'MarkerSize',15,'marker','s','MarkerFaceColor','black','LineStyle','none')%
hkl


if save==1
    print('-djpeg','-r600',[filename '_scatter_with_normal.tif'])
end;
%%


%%
%extracting the stereographically projected vectors for further processing
dataObjs = findobj(a,'-property','YData');
Y = dataObjs(1).YData;
dataObjs = findobj(a,'-property','XData');
X = dataObjs(1).XData;
%%


%%
%calculate a histogram of the stereographig projection to get the point
%densities
n=100;
m=0.828427125/(n-1);
```

```
b=hist3([X;Y]',{0:m:0.85 0:m:0.74});
for i=1:size(b,1)
    for j=1:size(b,2)
        xi=i*0.8284/n;
        eta=j*0.7321/n;
        x=-2*(-1+(xi/2)^2+(eta/2)^2)/(2+2*(xi/2)^2+2*(eta/2)^2);
        y=2*(eta/2)/(1+(xi/2)^2+(eta/2)^2);
        z=2*(xi/2)/(1+(xi/2)^2+(eta/2)^2);
        theta_calc(i,j)=acosd(dot([1 0 0],[x y z])/(norm([1 0 0])*norm([x y z])));
        b(i,j)=b(i,j)/cosd(theta_calc(i,j));%as point density was calculated in stereographic
projection, it has to be corrected by direction in space to remove projection area changes
    end;
end;
b=b';%prepare for plotting
b=-1+b/max(max(b));%normalize to 1
%%


%%
%plot point densities
fig2=figure('Position',[600 0 600 600]);
c=0.95;
subplot('Position',[0.1 0.17 c*.828427125 c*0.732050808]);
d=colormap(jet);
```

```
d(1,:)=[1 1 1];
colormap(d);
surf(b);
%contourf(b); %topo style
%shading interp; %smoothed heat map
shading flat;
%shading faceted; %shows grid
line([m*n n*1.02],[m*n m*n],[0 0],'color','black','linewidth',2);
line([m*n n*1.02*0.73/0.84],[m*n n*1.02*0.73/0.84],[0 0],'color','black','linewidth',2);
%add white lines to cover
%line([m*n n*1.02*0.73/0.84],[m*n+1.4 1.4+n*1.02*0.73/0.84],[0 0],'color',[0.999, 0.999,
0.999],'linewidth',5);
viscircles([-230 0],331,'color','black','linewidth',2);
%add white lines to cover
%h=viscircles([-229.3 0],331,'color',[0.999, 0.999, 0.999],'linewidth',2);
h.Children(1).Color = [0.999, 0.999, 0.999];      %change the color of the thinner inside line
h.Children(2).Color = [0.999, 0.999, 0.999];      %change the color of the edging
axis off;
xlim([0 101]);
ylim([0.8 89]);
view(2);

%% add color markers to plot%%
```

```
hold on;
plot(1,1,'MarkerSize',20,'marker','o','MarkerFaceColor','red','LineStyle','none')%100
plot(101,1,'MarkerSize',20,'marker','o','MarkerFaceColor','green','LineStyle','none')%110
plot(88.8,88.8,'MarkerSize',20,'marker','o','MarkerFaceColor','blue','LineStyle','none')%111
plot(39.9,1,'MarkerSize',20,'marker','o','MarkerFaceColor','yellow','LineStyle','none')%103 **
plot(54.9,54.9,'MarkerSize',20,'marker','o','MarkerFaceColor',[0.5,0,0.5],'LineStyle','none')%112
**
plot(20.7,20.7,'MarkerSize',20,'marker','o','MarkerFaceColor','magenta','LineStyle','none')%116*
*
plot(97,49,'MarkerSize',20,'marker','o','MarkerFaceColor','cyan','LineStyle','none')%212

%plot(y_hist,x_hist,'MarkerSize',15,'marker','s','MarkerFaceColor','black','LineStyle','none')%hkl

if save==1
    print('-djpeg','-r600','-painters',[filename '_contour_with_normal.tif'])
end;
%%

%%
%plot a color legend for the point densities
fig3=figure('Position',[1150 0 200 400]);
ax = axes;
colormap(jet);
```

```
c = colorbar(ax,'Location','west');

ax.Visible = 'off';

if save==1

    print('-djpeg','-r600',[filename '_legend_with_normal.tif'])

end;

%%
```

MATLAB Script 6- This script plots the data from section 6 of this document. The input of this script is a text file of 4 columns. The first 3 columns are the 3 Euler angles of each grain determined by EBSD. The fourth column is a number to represent the type of faceting. For this paper the values of 1 represented smooth grains, values of 2 represented grains that broke up into 2 surface facets and values of 3 represented grains that broke up into three surface facets.

```
close all;
clear;

%imports ebsd Euler angle list & determines size
filename='FILENAME.txt';
%do you want to save as tif? (1:yes,else:no)
save=1;

ebsd=dlmread(filename);
s=size(ebsd);
s1=s(:,1);

%creates unit vector (0,0,1) x sixe of ebsd file
blank_vectors = zeros(s1,3);
z = ones(s1,1);
blank_vectors(:,3) = z;
```

```
final_vectors = zeros (s1,3);

colormatrix = zeros (s1,1);

colormatrix(:,1) = ebsd(:,4);


% %inputs

% %-number of lines and points per line (assmed to be the same)

% %-the z height data array

% warning('off','curvefit:fit:iterationLimitReached') % Turns off Matlab warning

% [r,c] = size (data_array); % Measures row and column size

% crystal_normal_cell = cell(r,c); % Creates cell array matching input size

% Rval_array = zeros(r,c); % Creates double array matching input size

% x = 1:3; % Creates 1x3 vector

% y = 1:3; % Creates 1x3 vector


n=1;

while n <= s1

angle1 = ebsd(n); % EBSD angle 1

angle2 = ebsd(n+s(:,1)); % EBSD angle 2 ***62,69,43 ect is # of rows switch to variale***

angle3 = ebsd(n+s(:,1)+s(:,1)); % EBSD angle 3



u = (180-angle3); % 180 - EBSD angle swapping 1 and 3 correct this one***

v = 180-angle2; % EBSD angle 2 stays the same
```

```
w = 180-angle1; %180 - EBSD angle swapping 1 and 3



R1 = [cosd(u) sind(u) 0; -sind(u) cosd(u) 0; 0 0 1]; % Z rotation matrix

R2 = [1 0 0; 0 cosd(v) sind(v); 0 -sind(v) cosd(v)]; % X' rotation matrix

R3 = [cosd(w) sind(w) 0; -sind(w) cosd(w) 0; 0 0 1]; % Z'' rotation matrix

Rfull = R1*R2*R3; % Creates Euler angle rotation matrix



%blank_vectors(:,3) = z



normal = blank_vectors(1,:)/norm(blank_vectors); % Normalizes vector

normal = normal'; % Transposes vector

crystal_normal = Rfull* normal; % Applies EBSD based rotation matrix

crystal_normal = crystal_normal'; % Transposes vector



final_vectors(n,:) = crystal_normal;



n= n+1;

end



% final_vectors(:,4)=ebsd(:,4);



% fileID = fopen('colors_test.txt','w'); %creats .txt file
```

```
% final_vectors_T=final_vectors'; %trasposes matrix to print properly
% fprintf(fileID,'%1.6f %1.6f %1.6f %1.0f\r\n',final_vectors_T); %prints with 6 decimal places
% fclose(fileID);
%-----------------------------------------------------------------------------------------------------------

final=abs(final_vectors);

for i=1:size(final,1)
    final(i,:)=sort(final(i,:),'descend');
    lat_final(i)=90-acosd(final(i,3)/norm(final(i,:)));
    long_final(i)=atand(final(i,2)/final(i,1));
end;



figure;
axesm('stereo'); %sets lot type to Stereo
xlim([-0.001 0.829]); %crops to single triangle
ylim([-0.001 0.732]);
% set(gca,'ycolor','w')
% set(gca,'xcolor','w')
box off;
axis off;
plotm(0,0,'MarkerSize',20,'marker','o','MarkerFaceColor','red','LineStyle','none')%100
```

```
plotm(0,45,'MarkerSize',20,'marker','o','MarkerFaceColor','green','LineStyle','none')%110
plotm(35.26,45,'MarkerSize',20,'marker','o','MarkerFaceColor','blue','LineStyle','none')%111
plotm(0,18.43,'MarkerSize',20,'marker','o','MarkerFaceColor','yellow','LineStyle','none')%103
plotm(24.09,26.56,'MarkerSize',20,'marker','o','MarkerFaceColor',[0.5,0,0.5],'LineStyle','none')%
112
plotm(9.335,9.46,'MarkerSize',20,'marker','o','MarkerFaceColor','magenta','LineStyle','none')%11
6
plotm(19.47,45,'MarkerSize',20,'marker','o','MarkerFaceColor','cyan','LineStyle','none')%212
%%
%Orientierungslinien in den polarplot einzeichnen
lat0=-90:1:90;
long3=-90:1:90;
for i=1:181
    long0(i)=0;
    long1(i)=45;
    long4(i)=90;
    lat1(i)=atand(tand(45)*sind(long3(i)-90));
    lat2(i)=atand(tand(45)*sind(long3(i)+90));
end;
plotm([0 0],[-90,90],'-','color','black');
plotm([45 -45],[-90,90],'-','color','black');
plotm([-45 45],[-90,90],'-','color','black');
% plotm(lat0,long0,'-','color','black'); %y axis
```

```
plotm(lat0,long1,'-','color','black');
plotm(lat0,-long1,'-','color','black');
plotm(lat1,long3,'-','color','black');
% plotm(lat2,long3,'-','color','red');
plotm(lat0,long4,'-','color','black','LineWidth',2);
plotm(lat0,-long4,'-','color','black','LineWidth',2);
%%



c = 1;
while c <= s1
    if colormatrix(c) == 1
        a=plotm(lat_final(c),long_final(c),'MarkerSize',10,'marker','s','MarkerFaceColor','black',
'MarkerEdgeColor','black','LineStyle','none');
    elseif colormatrix(c) == 2
        a=plotm(lat_final(c),long_final(c),'MarkerSize',10,'marker','d','MarkerFaceColor','blue',
'MarkerEdgeColor','blue','LineStyle','none');
    elseif colormatrix(c) == 3
        a=plotm(lat_final(c),long_final(c),'MarkerSize',10,'marker','o','MarkerFaceColor','red',
'MarkerEdgeColor','red','LineStyle','none');
    elseif colormatrix(c) == 4
        a=plotm(lat_final(c),long_final(c),'MarkerSize',10,'marker','p','MarkerFaceColor','cyan',
'MarkerEdgeColor','cyan','LineStyle','none');
```

```
    elseif colormatrix(c) == 5
        a=plotm(lat_final(c),long_final(c),'MarkerSize',10,'marker','+','MarkerFaceColor','green',
'MarkerEdgeColor','green','LineStyle','none');
    elseif colormatrix(c) == 6
        a=plotm(lat_final(c),long_final(c),'MarkerSize',10,'marker','^','MarkerFaceColor','magenta',
'MarkerEdgeColor','magenta','LineStyle','none');
    else
        a=plotm(lat_final(c),long_final(c),'MarkerSize',10,'marker','*','MarkerFaceColor','white',
'MarkerEdgeColor','white','LineStyle','none');
    end

    c=c+1;
end

if save==1
    print('-djpeg','-r600',[filename '_faceting_plot.tif'])
end;

%figure;
% subplot(1,2,1);
% subplot('Position',[0.05 0.3 0.4 0.4])
%axesm('stereo');%
```

```
%a=plotm(lat_final,long_final,'MarkerSize',5,'marker','s','MarkerFaceColor','red',
'MarkerEdgeColor','red','LineStyle','none');
% xlim([0 0.83]);
% ylim([0 0.73]);

% dataObjs = findobj(a,'-property','YData');
% y = dataObjs(1).YData;
% dataObjs = findobj(a,'-property','XData');
% x = dataObjs(1).XData;
```

APPENDIX C. AFM FACETING DATA

Appendix C contains the complete dataset for Section 6 of this document. For composition Ba25-Sr75 this includes the original plot on the full stereographic, a plot of the data being rotated by a symmetry operation to show the data in all triangles of the stereographic projection and plots of the dataset folded into one stereographic triangle. The First two of these figures compare datasets with different R^2 value cutoffs. For Ba75-Sr25 the same plots are shown, except the symmetry plots on the whole stereographic projection as they were not generated.

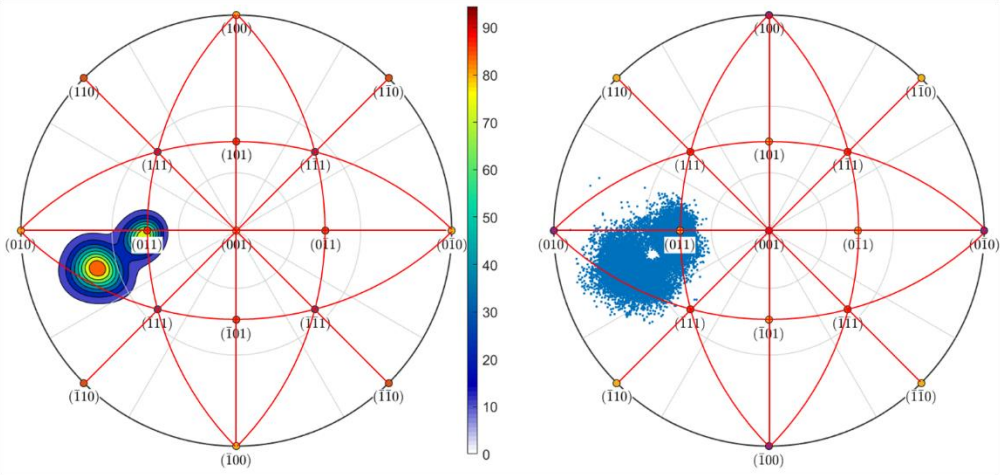

Plot of Ba25-Sr75 grain 1 with an R^2 value >0.9

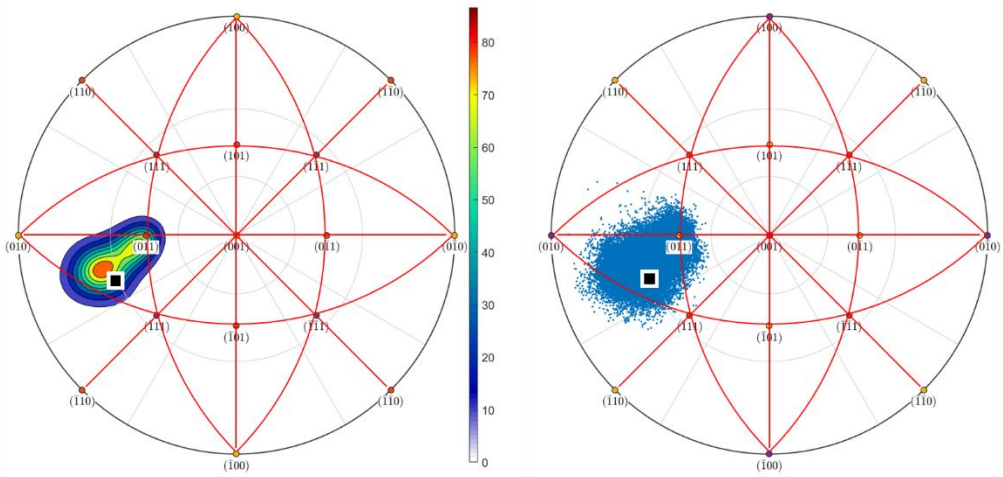

Plot of Ba25-Sr75 grain 1 with an R^2 value >0

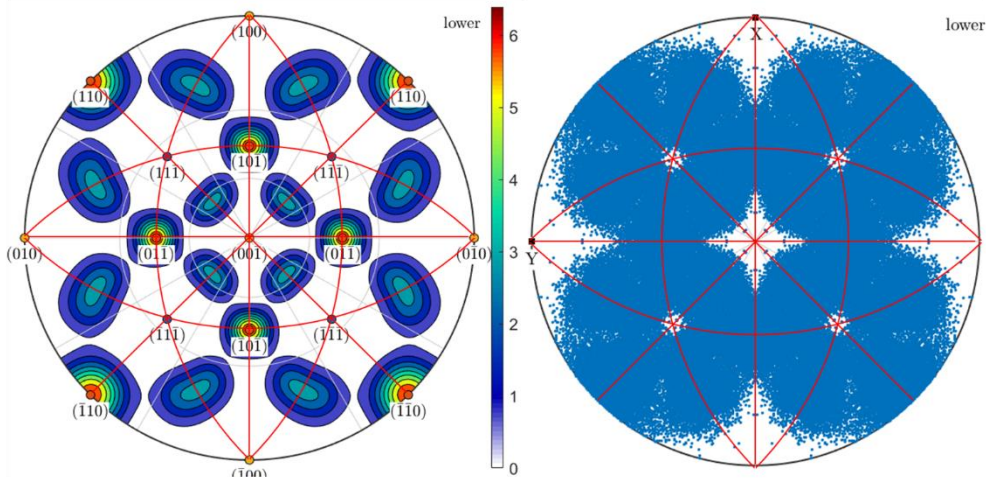

Plot of Ba25-Sr75 grain 1 with symmetry

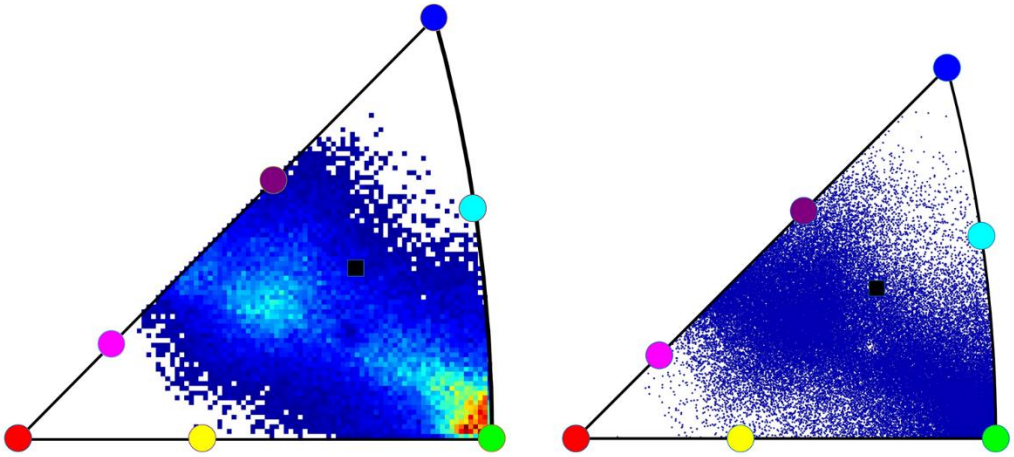

Plot of Ba25-Sr75 grain 1 with all data folded into one triangle of the stereographic projection

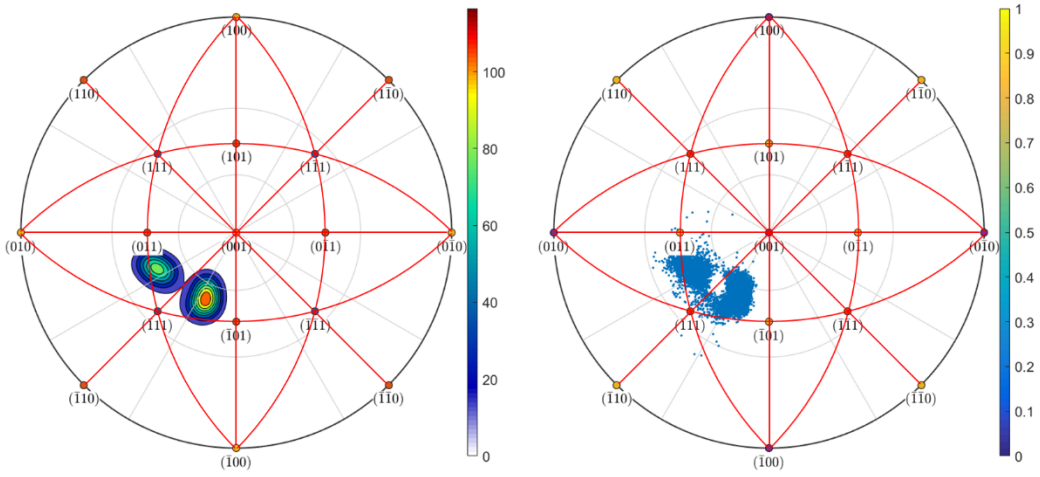

Plot of Ba25-Sr75 grain 2

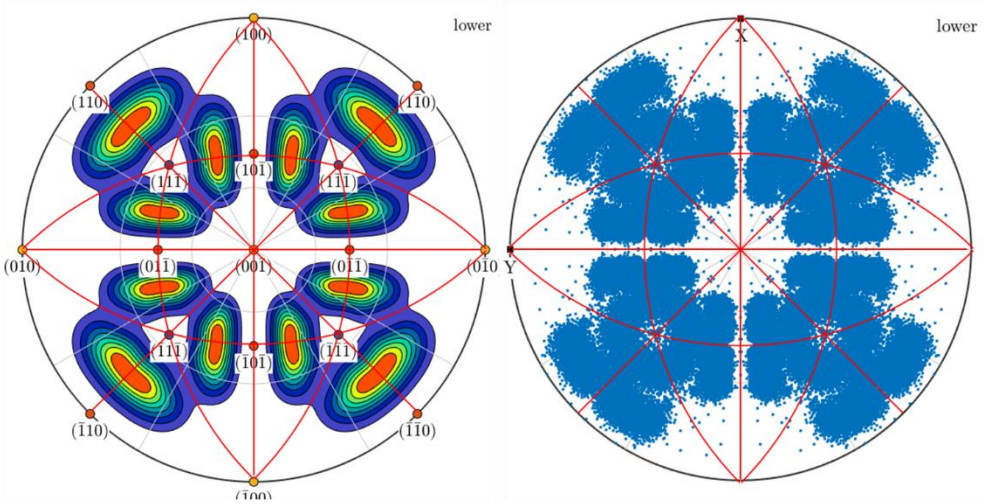

Plot of Ba25-Sr75 grain 2 with symmetry

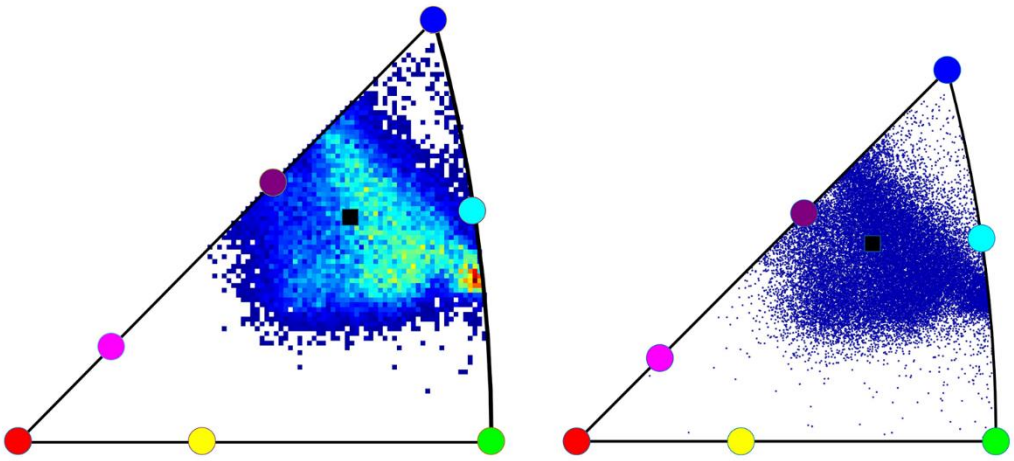

Plot of Ba25-Sr75 grain 2 with all data folded into one triangle of the stereographic projection

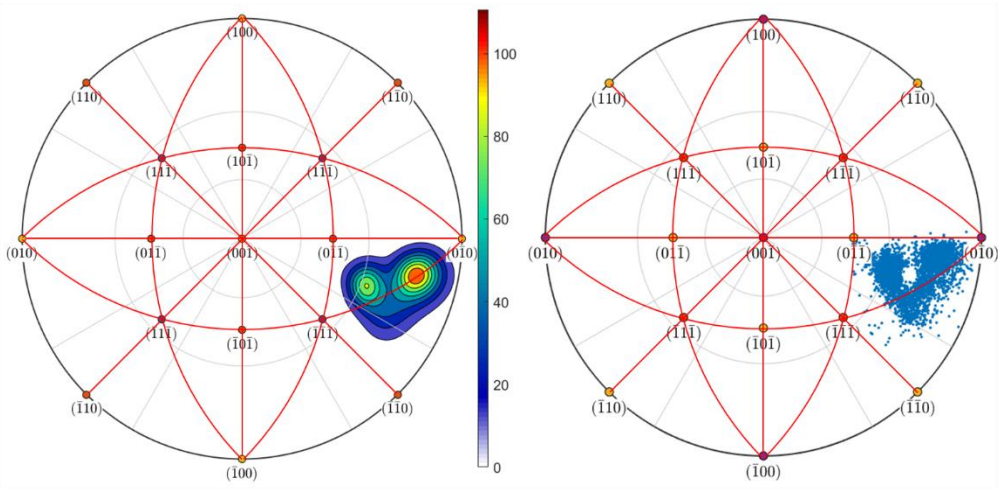

Plot of Ba25-Sr75 grain 3

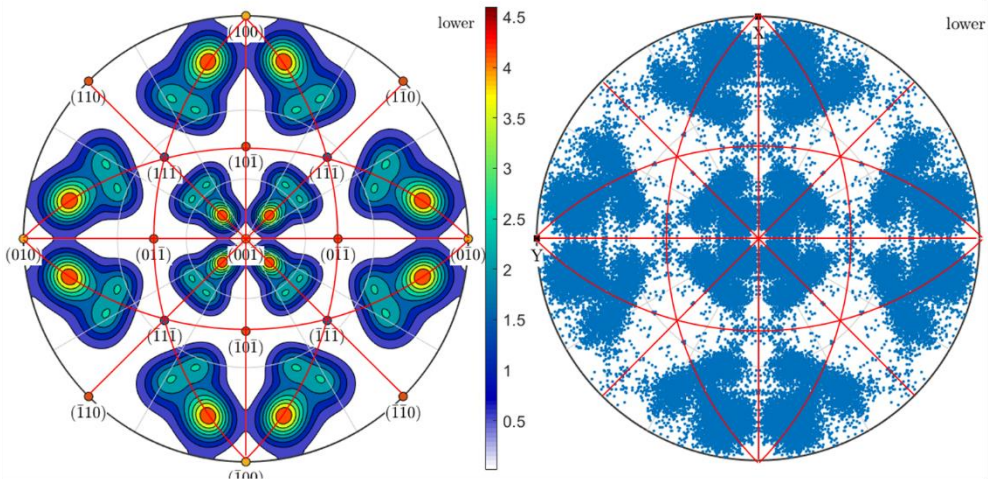

Plot of Ba25-Sr75 grain 3 with symmetry

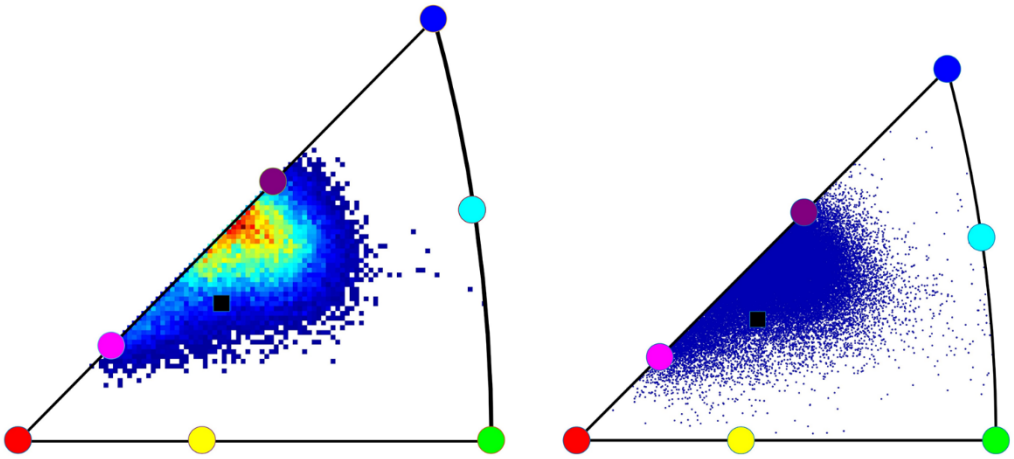

Plot of Ba25-Sr75 grain 3 with all data folded into one triangle of the stereographic projection

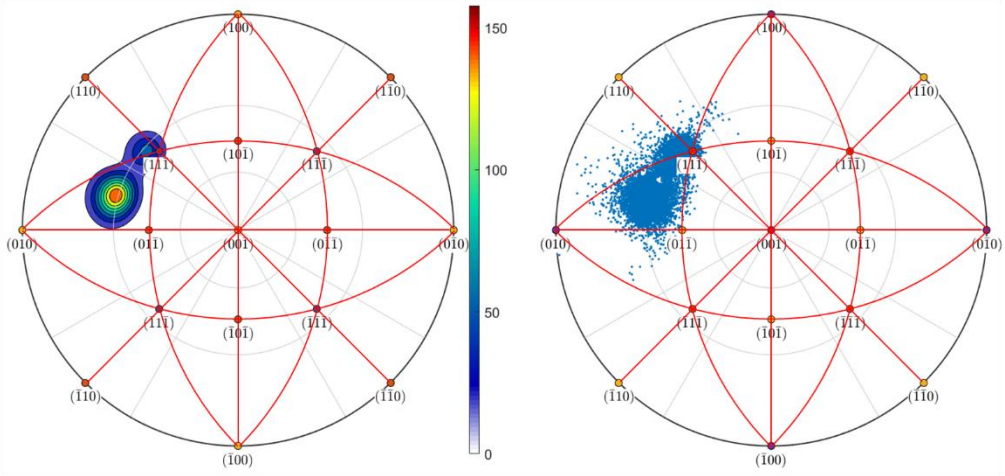

Plot of Ba25-Sr75 grain 4

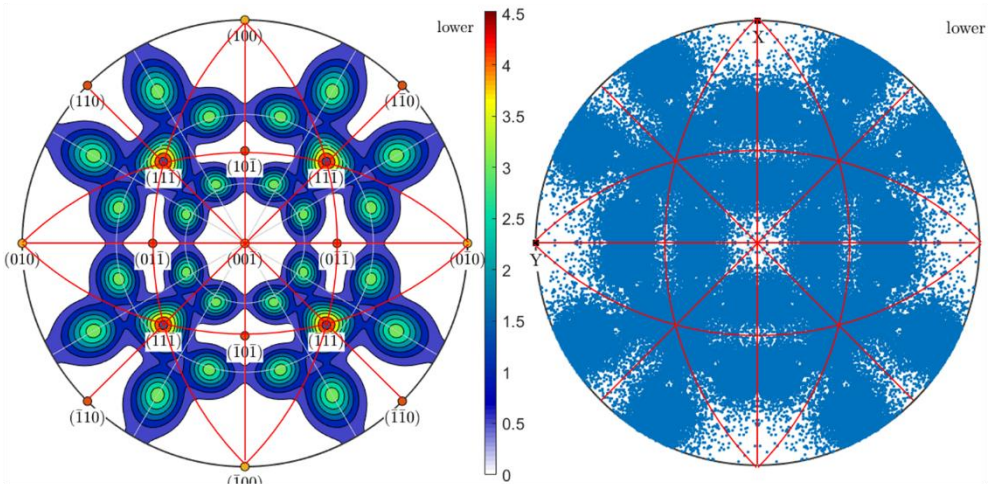

Plot of Ba25-Sr75 grain 4 with symmetry

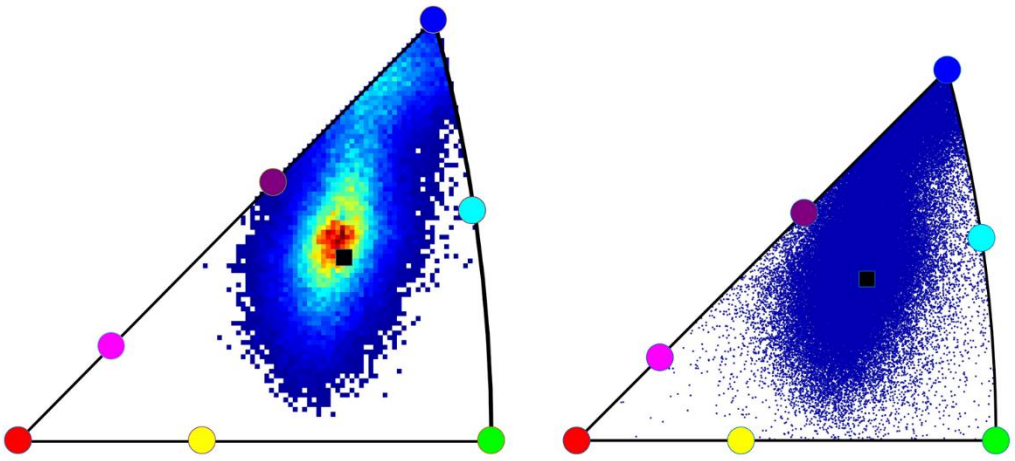

Plot of Ba25-Sr75 grain 4 with all data folded into one triangle of the stereographic projection

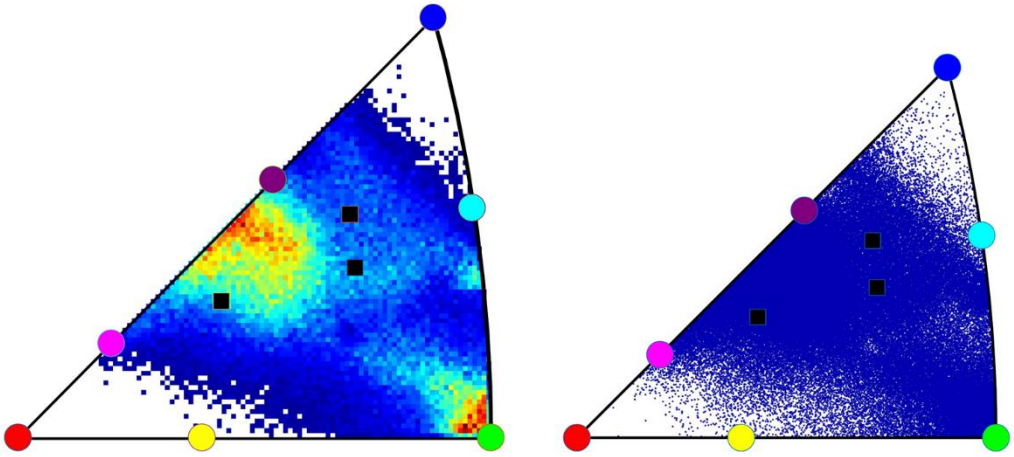

Plot of Ba25-Sr75 grains 1-3 with all data folded into one triangle of the stereographic projection

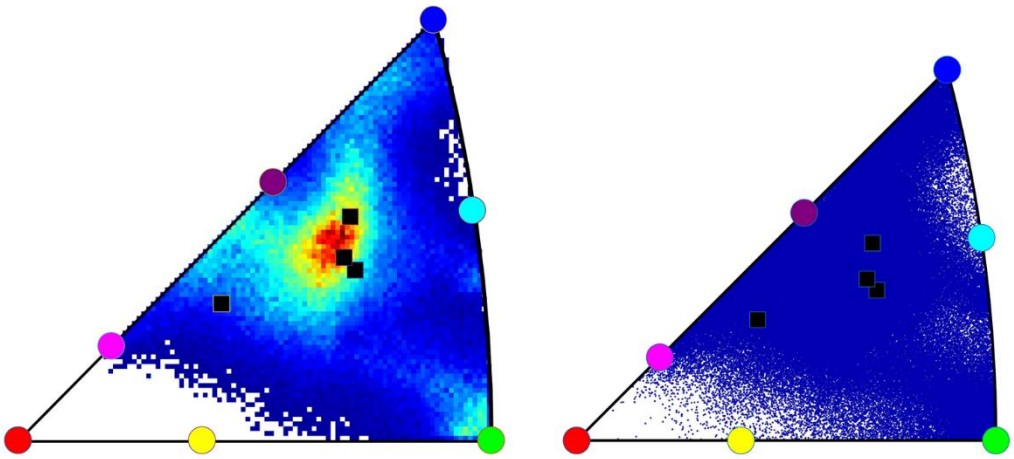

Plot of all Ba25-Sr75 grains with all data folded into one triangle of the stereographic projection

Please note that there is no Ba75-Sr25 grain 1 sample the samples begin with grain 2 in reference to the labeling of the surface grains from Section 5.

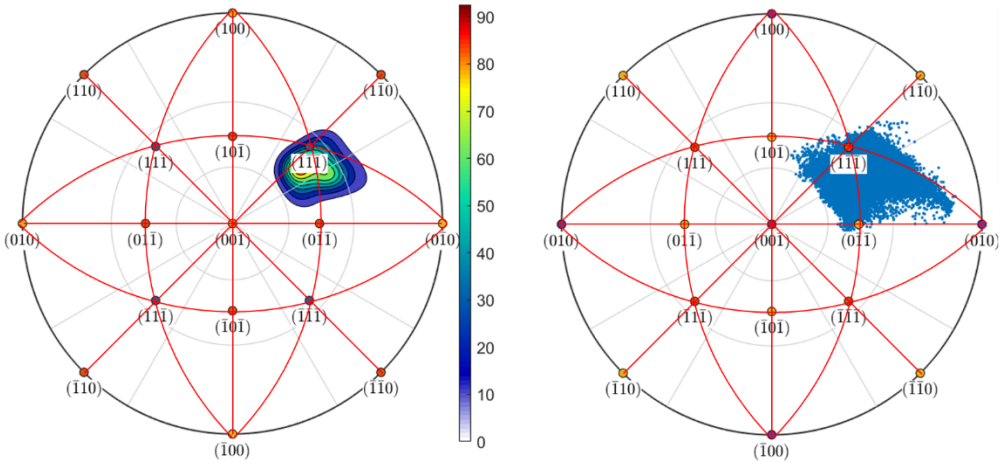

Plot of Ba75-Sr25 grain 2

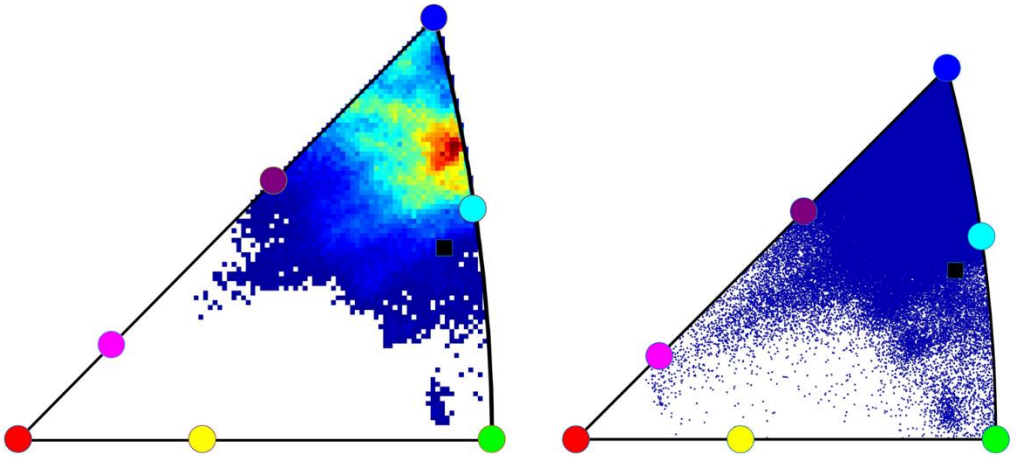

Plot of Ba25-Sr75 grain 2 with all data folded into one triangle of the stereographic projection

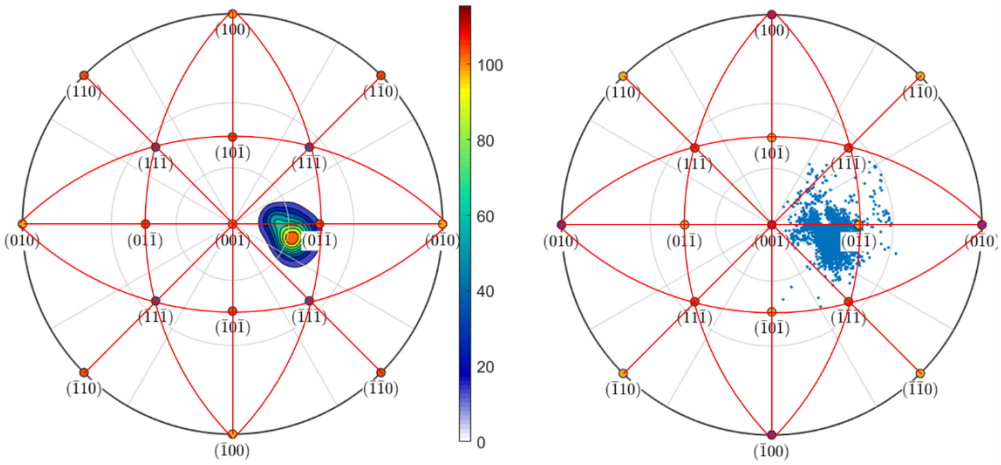

Plot of Ba75-Sr25 grain 3

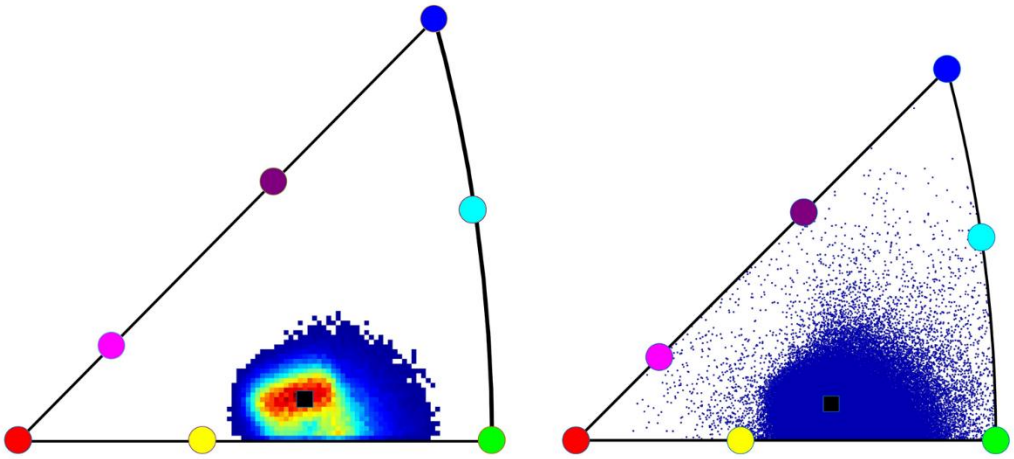

Plot of Ba25-Sr75 grain 3 with all data folded into one triangle of the stereographic projection

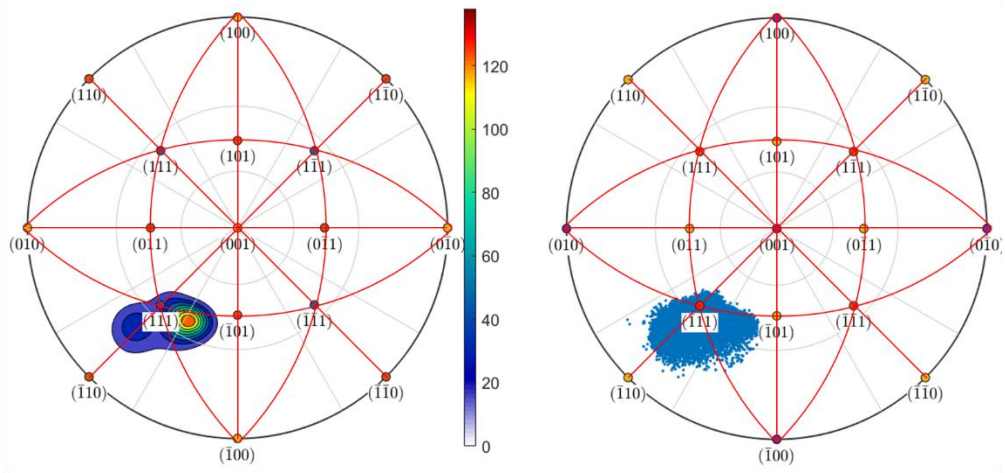

Plot of Ba75-Sr25 grain 4

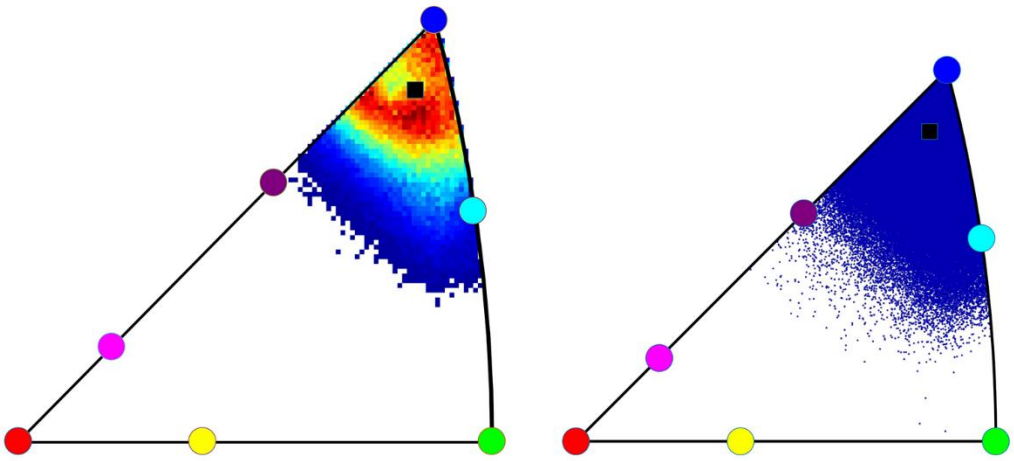

Plot of Ba25-Sr75 grain 4 with all data folded into one triangle of the stereographic projection

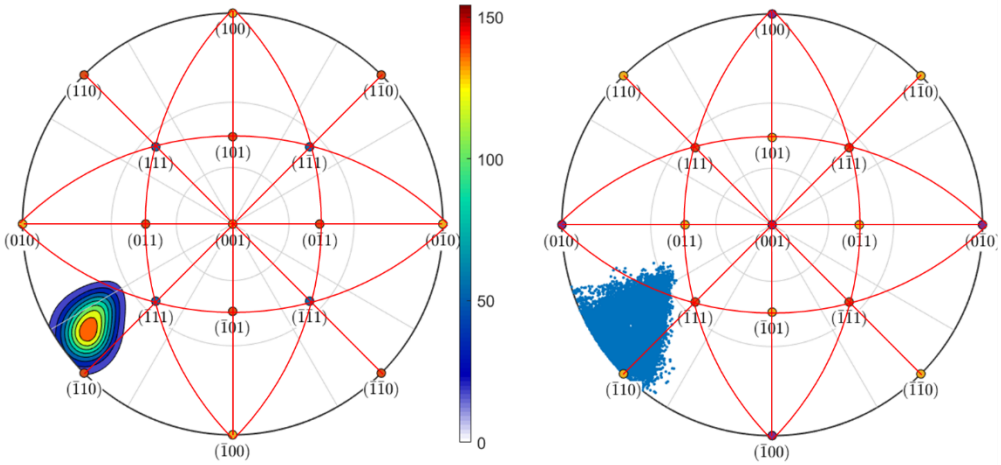

Plot of Ba75-Sr25 grain 5

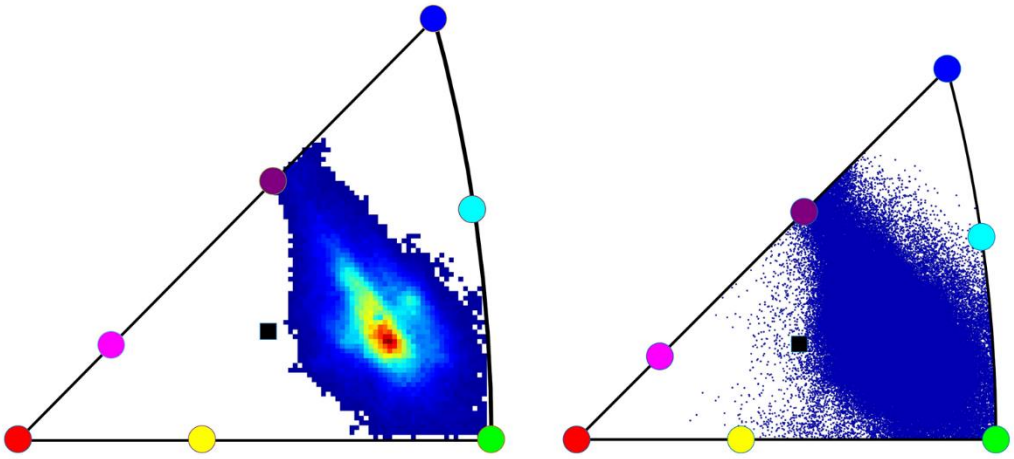

Plot of Ba25-Sr75 grain 5 with all data folded into one triangle of the stereographic projection

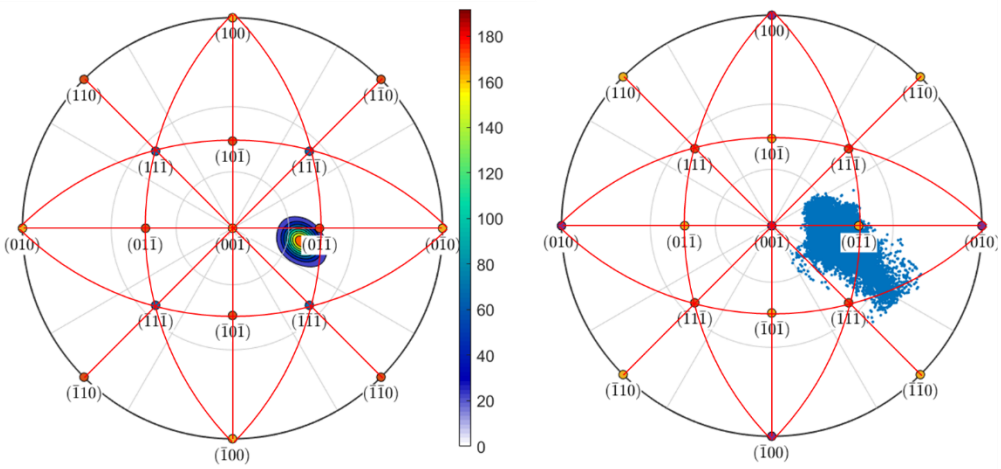

Plot of Ba75-Sr25 grain 6

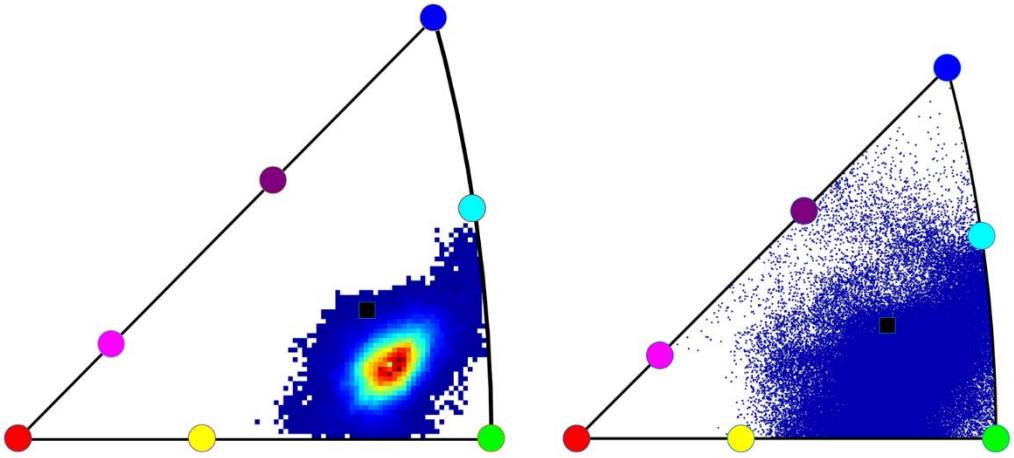

Plot of Ba25-Sr75 grain 6 with all data folded into one triangle of the stereographic projection

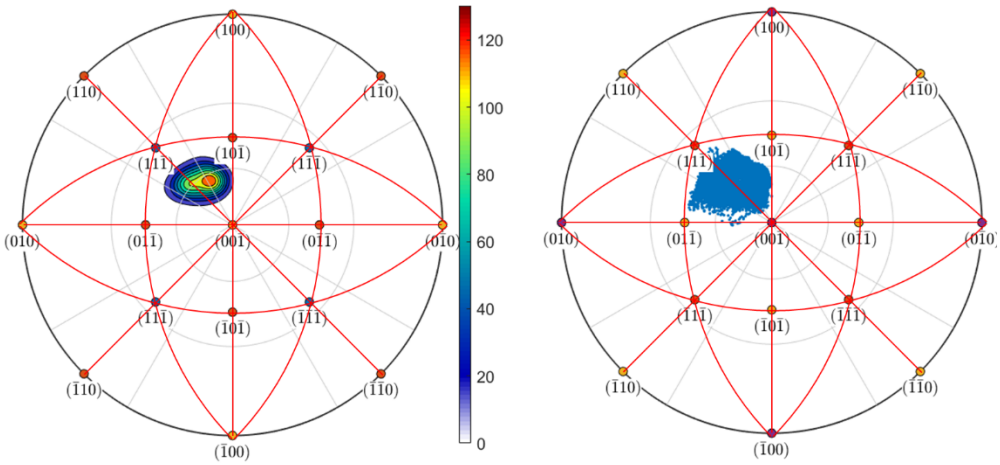

Plot of Ba75-Sr25 grain 7

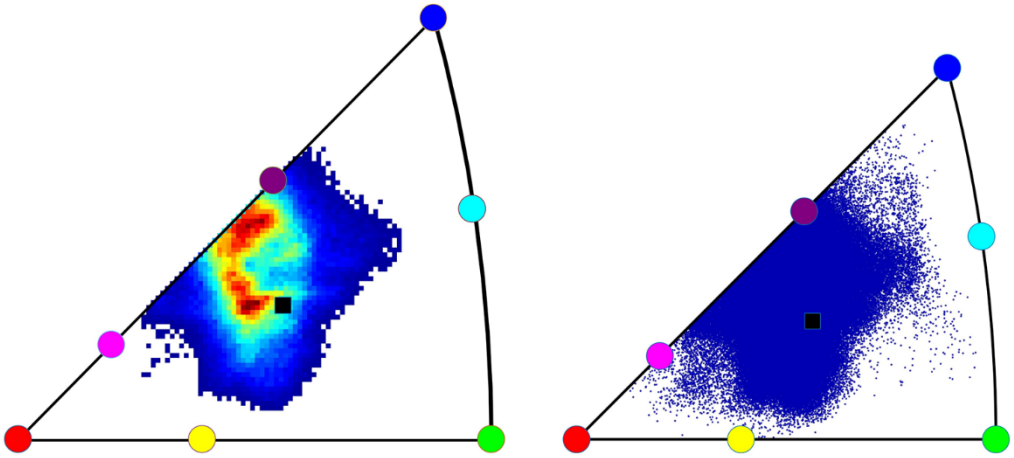

Plot of Ba25-Sr75 grain 7 with all data folded into one triangle of the stereographic projection

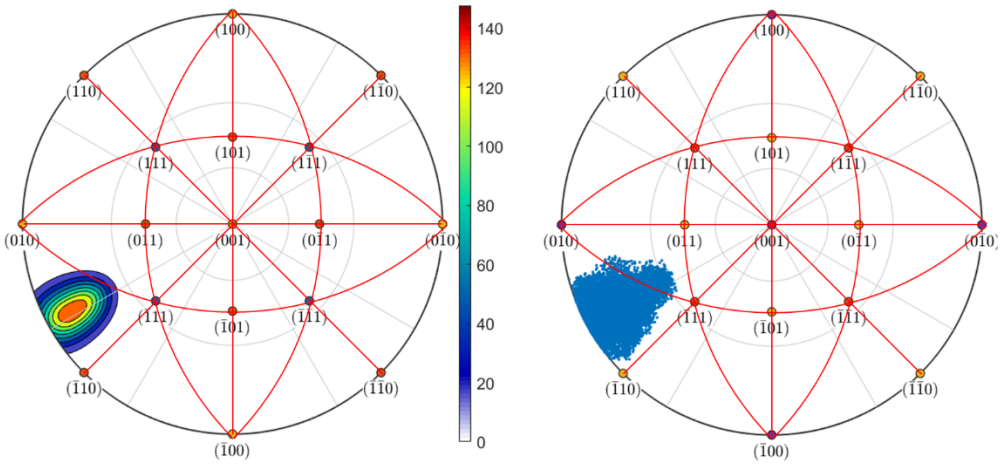

Plot of Ba75-Sr25 grain 8

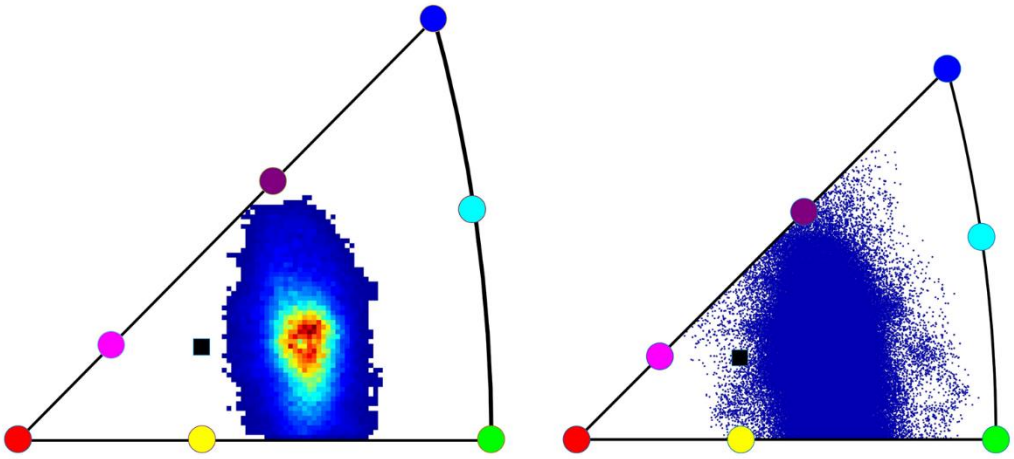

Plot of Ba25-Sr75 grain 8 with all data folded into one triangle of the stereographic projection

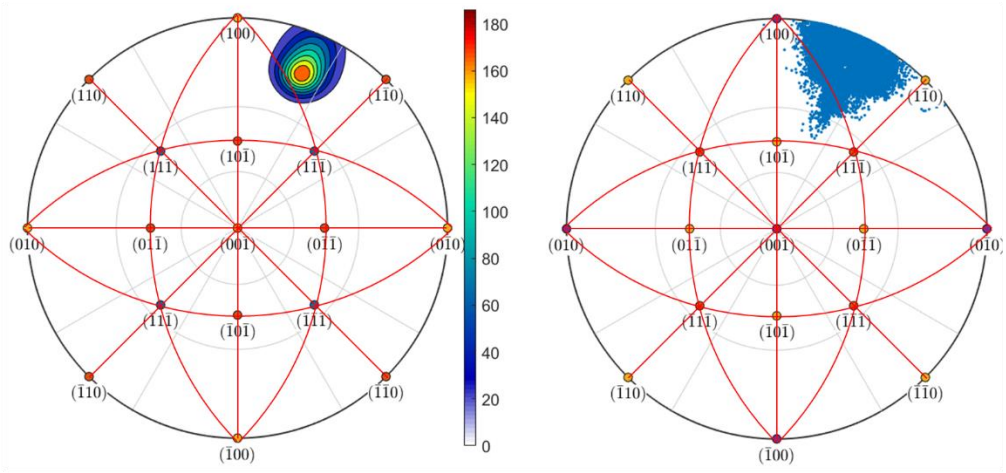

Plot of Ba75-Sr25 grain 9

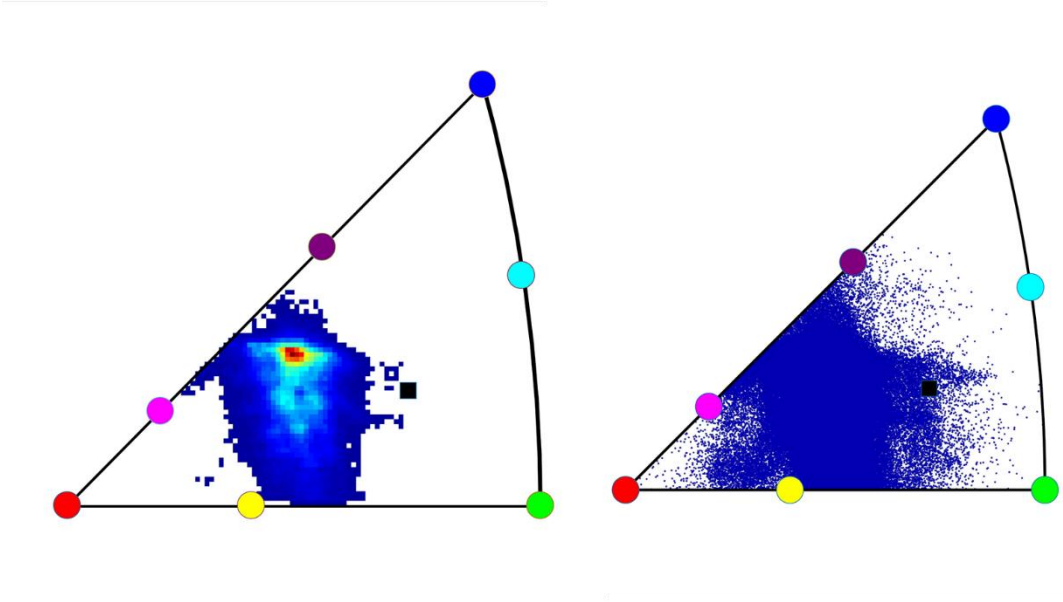

Plot of Ba25-Sr75 grain 9 with all data folded into one triangle of the stereographic projection

APPENDIX D. SURFACE FACETING DATA

Appendix D contains the SEM and EBSD data used to obtain the surface faceting behavior discussed in section 6.

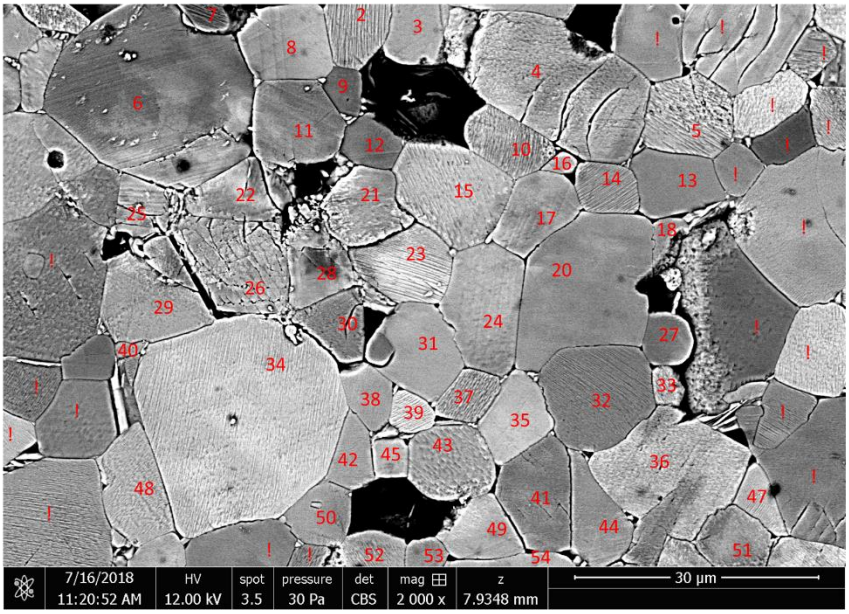

SEM micrograph of the area where surface faceting behavior was observed for Ba25%-Sr75% location 1.

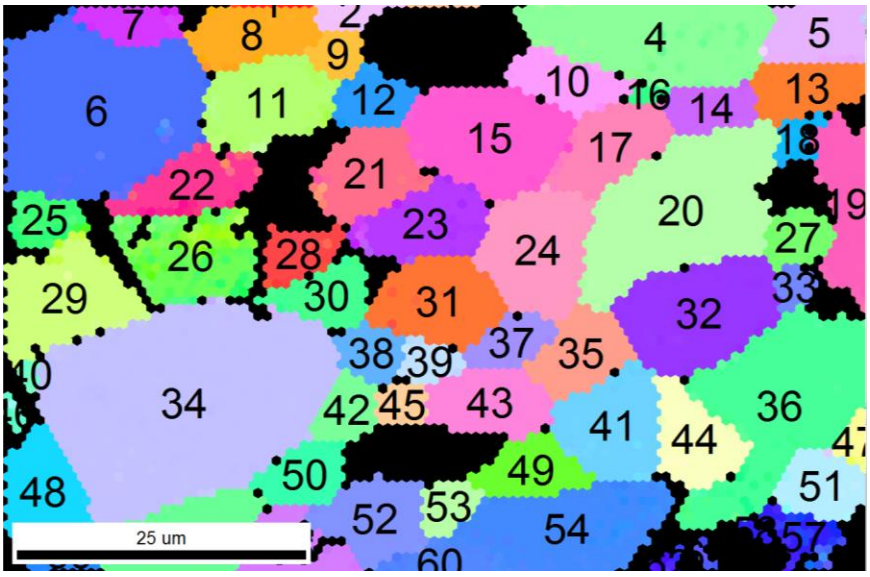

EBSD orientation map of Ba25%-Sr75% location 1.

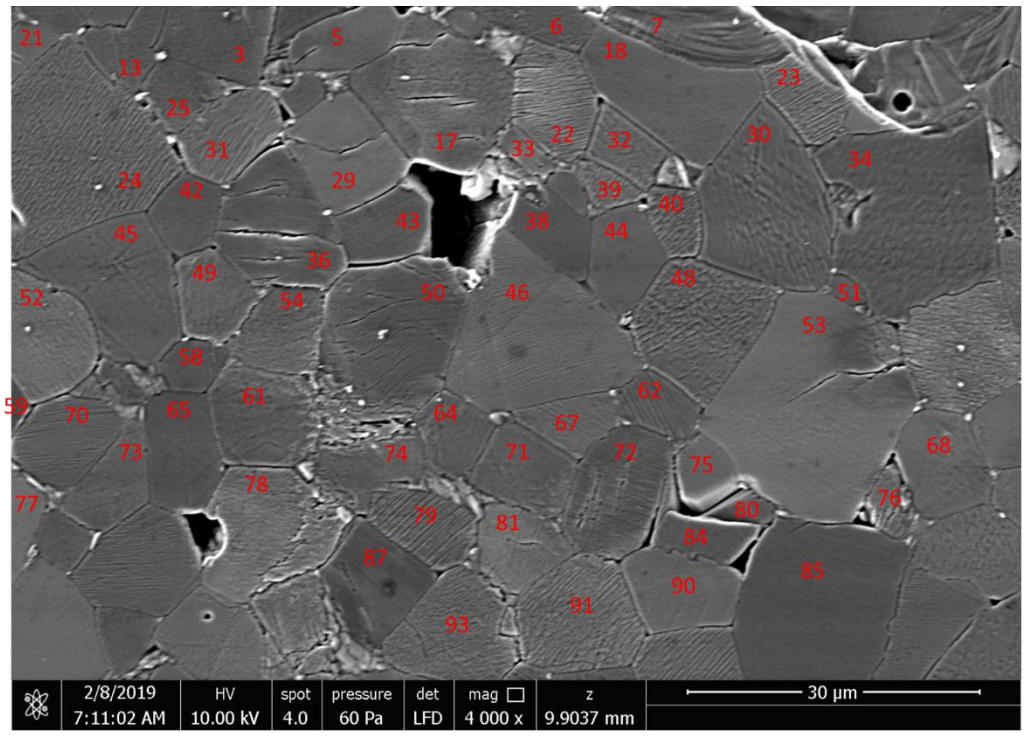

SEM micrograph of the area where surface faceting behavior was observed for Ba25%-Sr75% location 2.

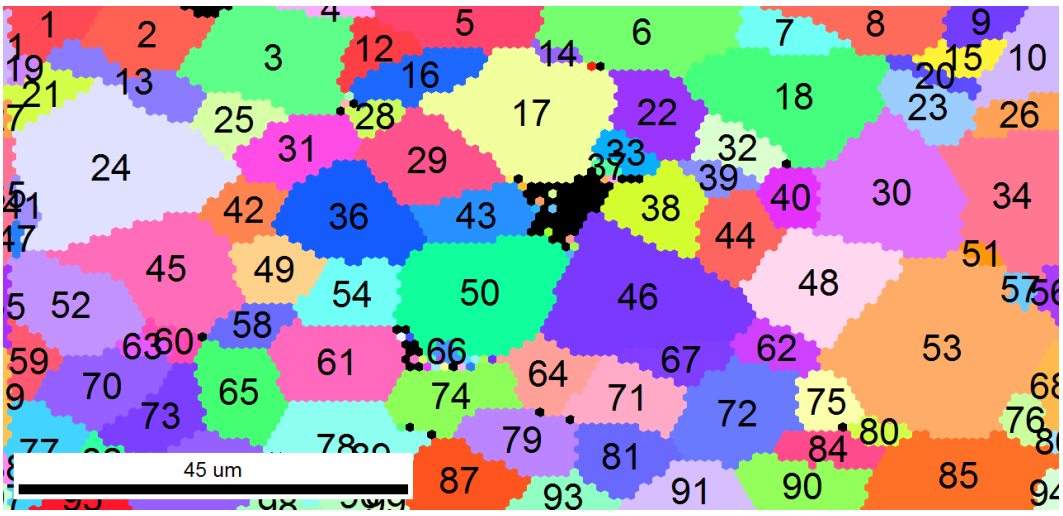

EBSD orientation map of Ba25%-Sr75% location 2.

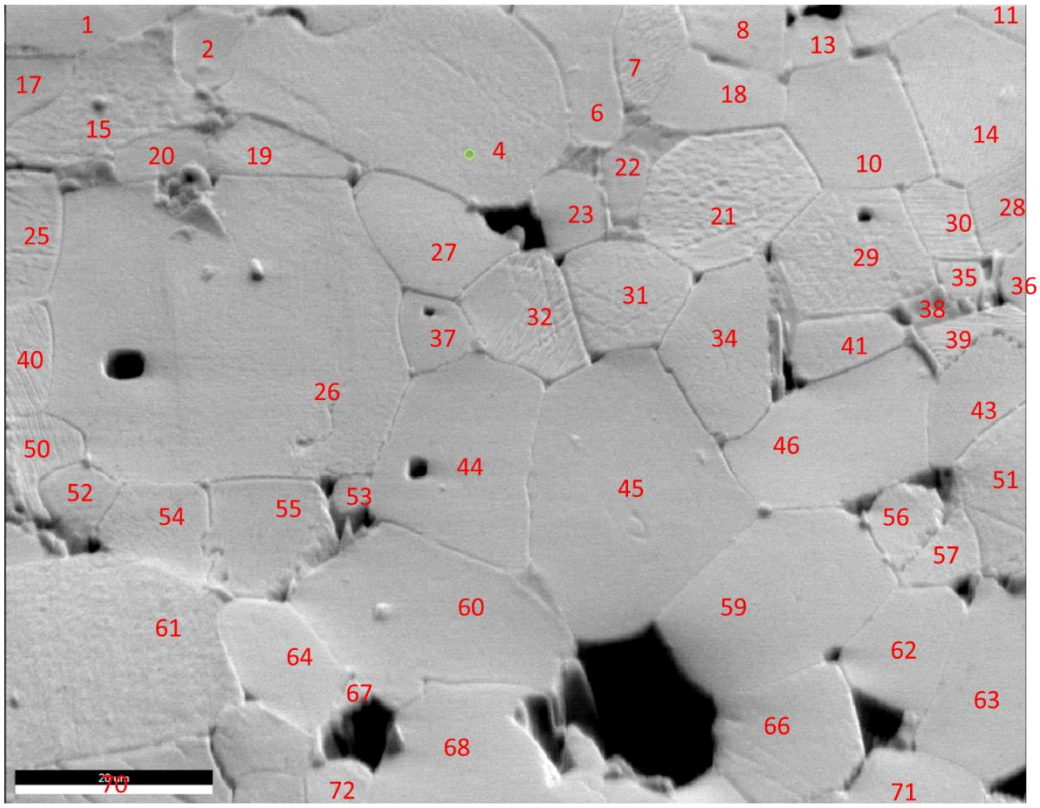

SEM micrograph of the area where surface faceting behavior was observed for Ba25%-Sr75% location 3.

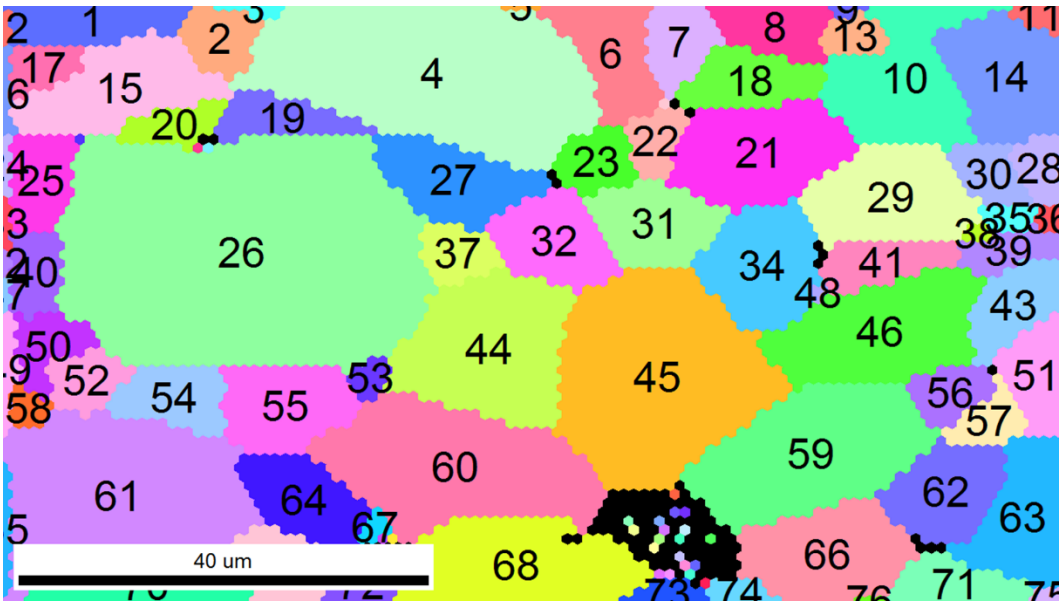

EBSD orientation map of Ba25%-Sr75% location 3.

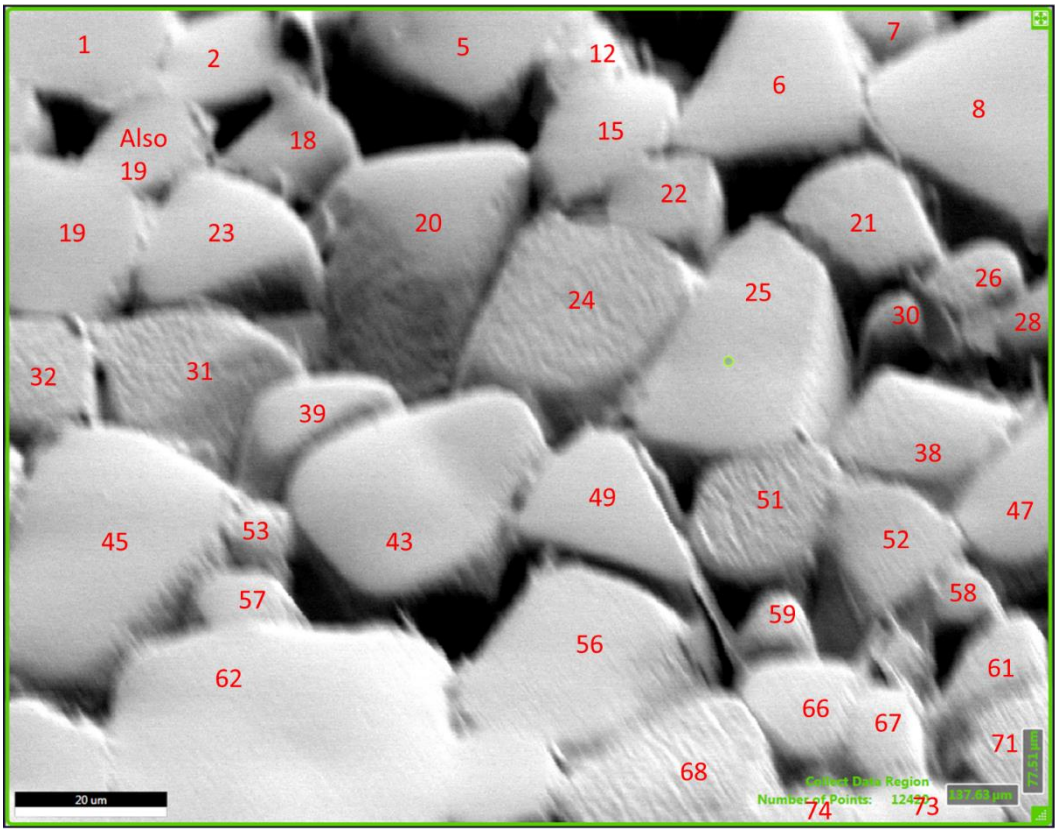

SEM micrograph of the area where surface faceting behavior was observed for Ba50%-Sr50% location 1.

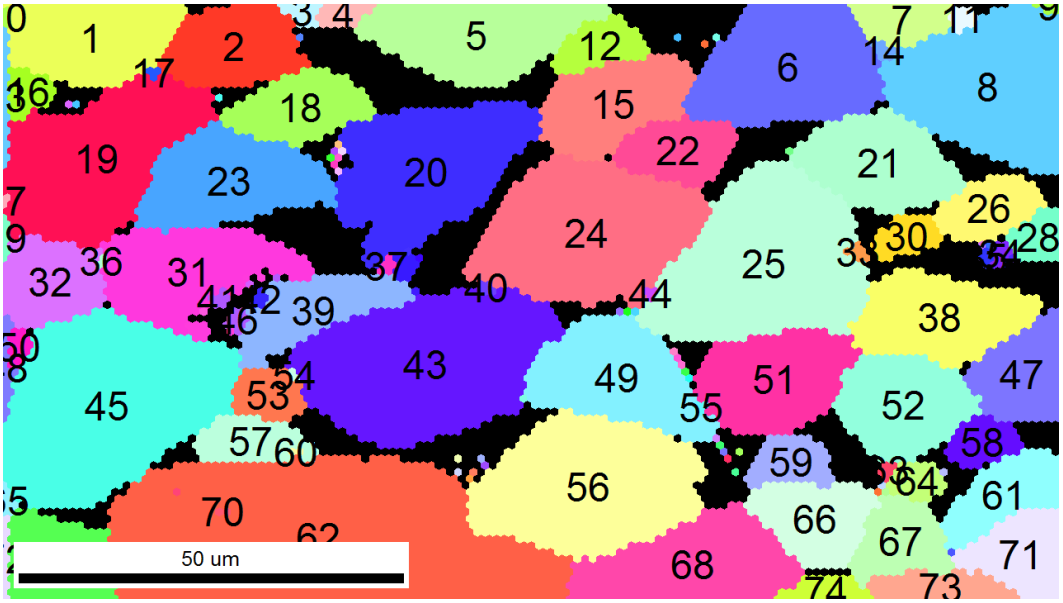

EBSD orientation map of Ba50%-Sr50% location 1.

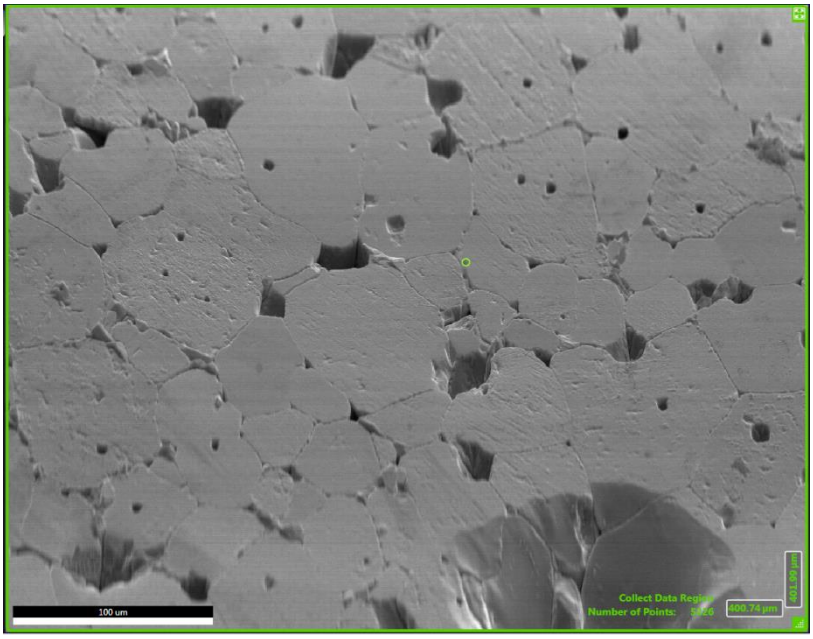

SEM micrograph of the area where surface faceting behavior was observed for Ba50%-Sr50% location 2.

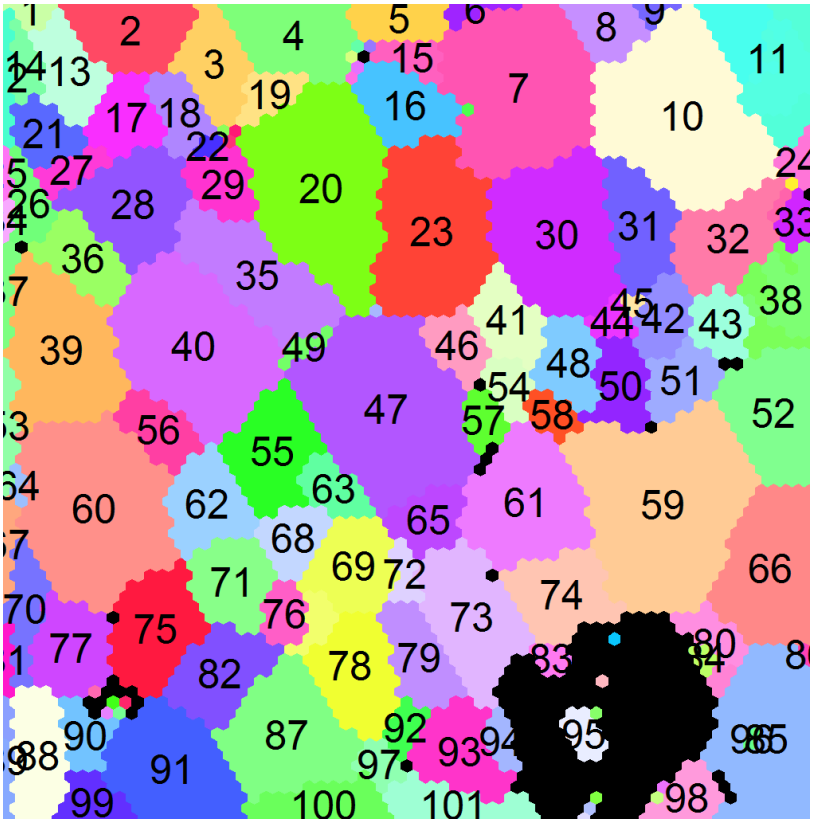

EBSD orientation map of Ba50%-Sr50% location 2.

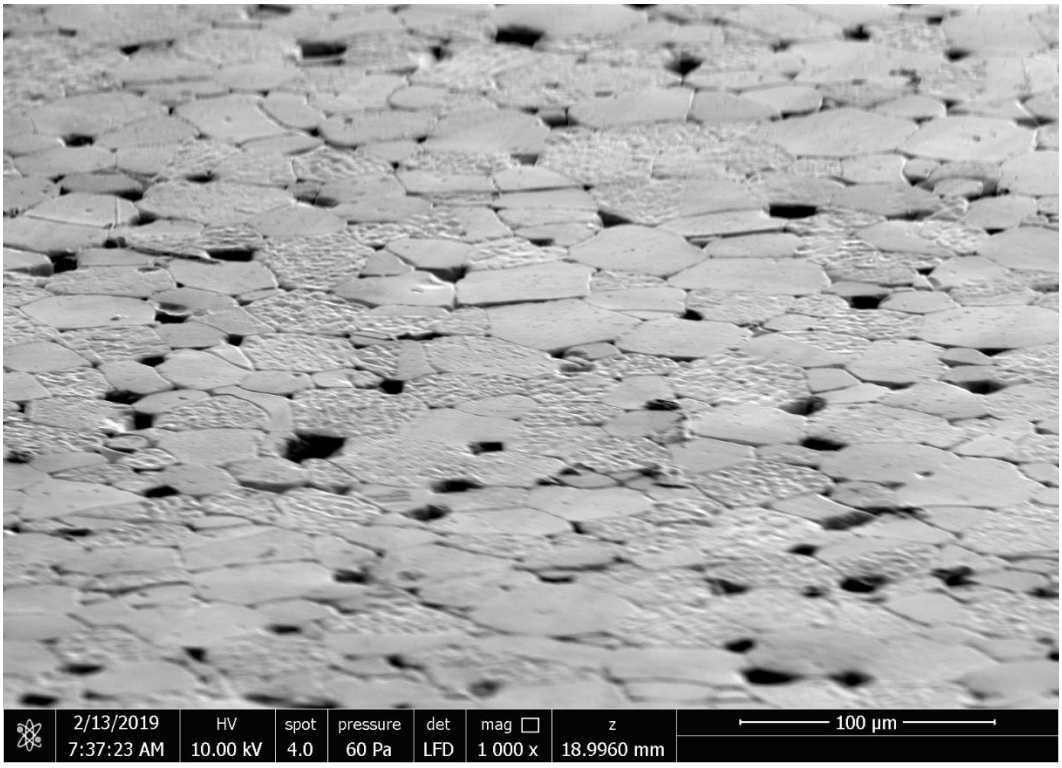

SEM micrograph of the area where surface faceting behavior was observed for Ba75%-Sr25% location 1.

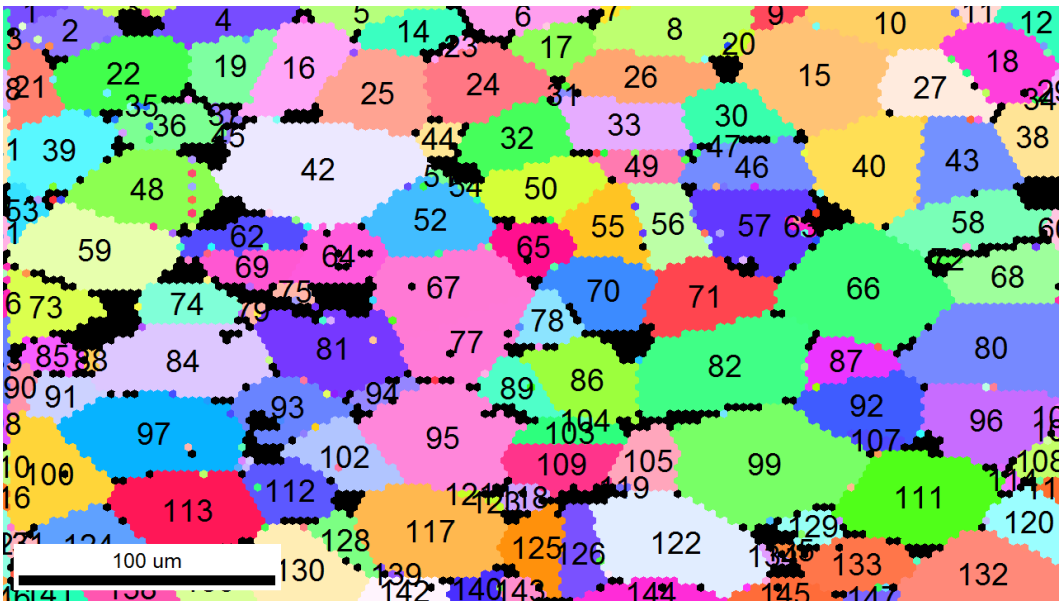

EBSD orientation map of Ba75%-Sr25% location 1.

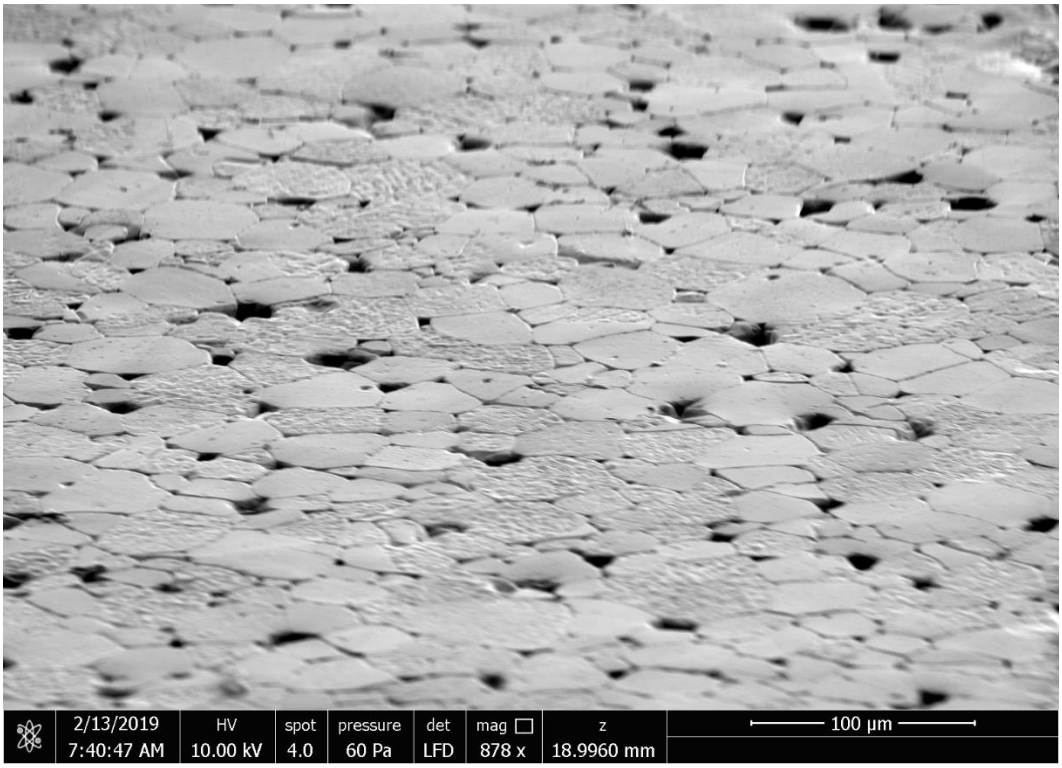

SEM micrograph of the area where surface faceting behavior was observed for Ba75%-Sr25% location 2.

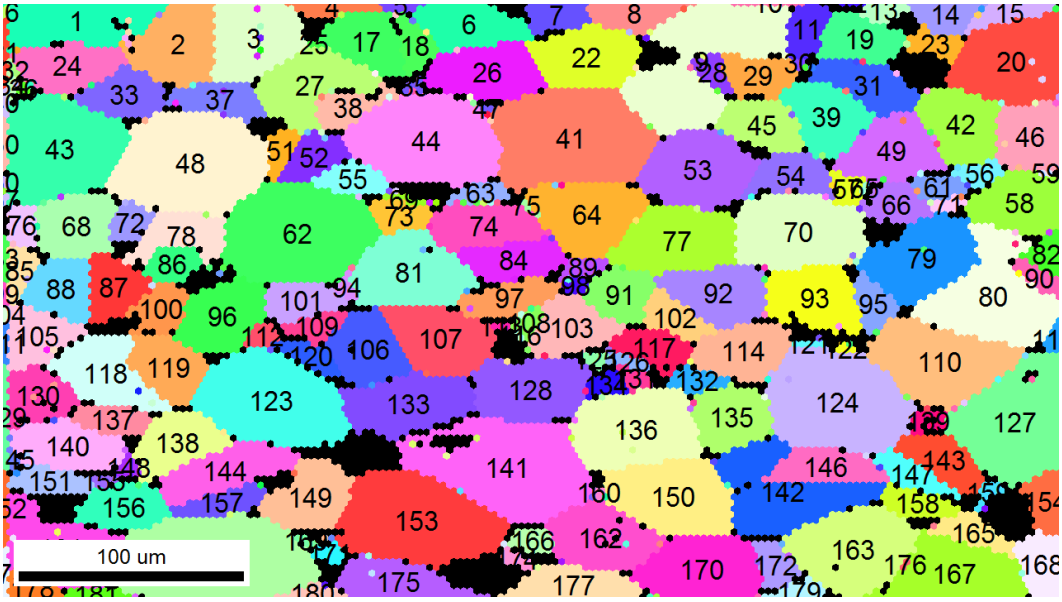

EBSD orientation map of Ba75%-Sr25% location 2.

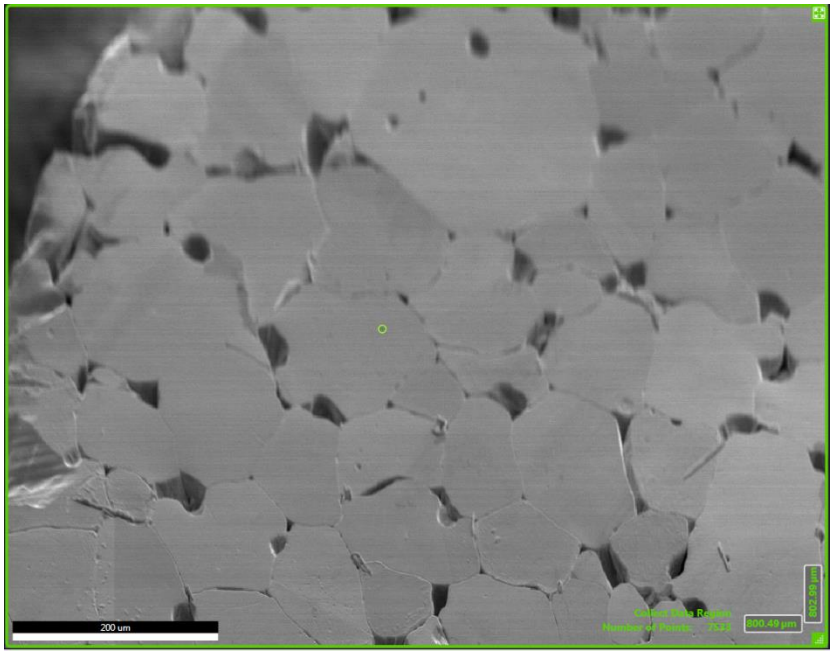

SEM micrograph of the area where surface faceting behavior was observed for Ba75%-Sr25% location 3.

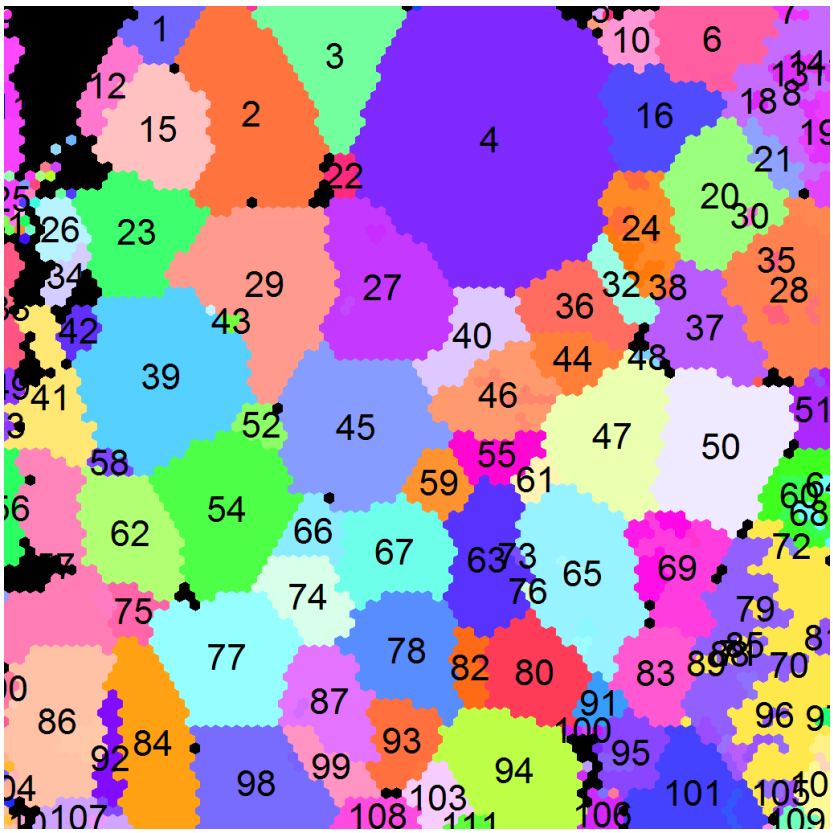

EBSD orientation map of Ba75%-Sr25% location 3.

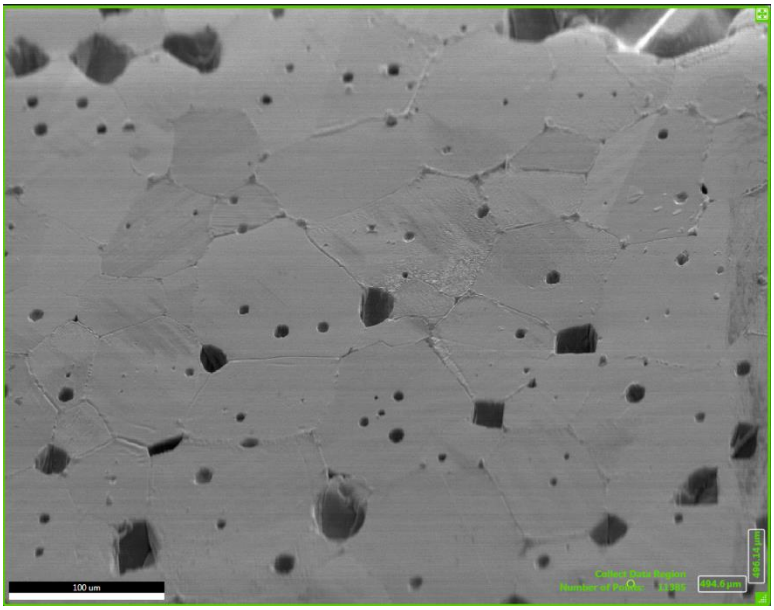

SEM micrograph of the area where surface faceting behavior was observed for $BaSrTiO_3$ location 1.

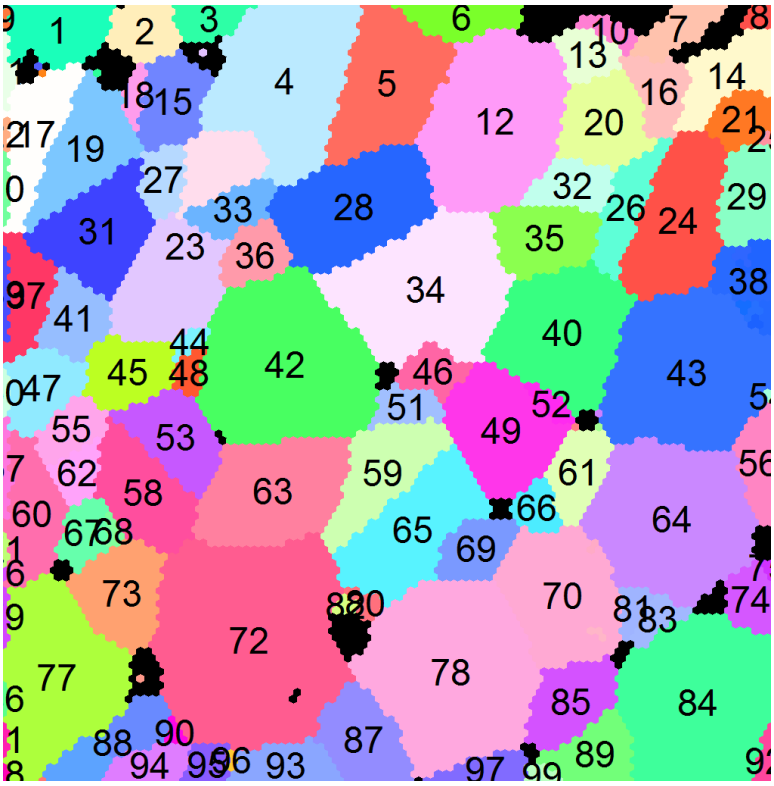

EBSD orientation map of $BaSrTiO_3$ location 1.

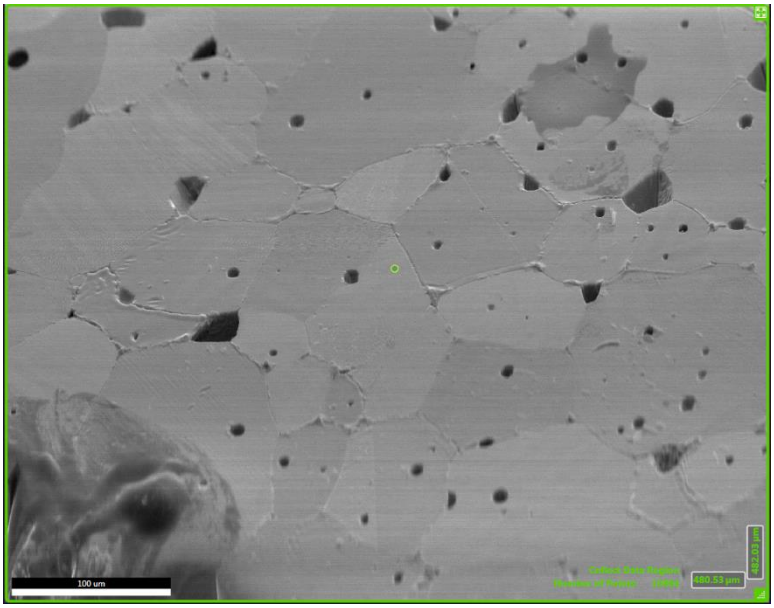

SEM micrograph of the area where surface faceting behavior was observed for $BaSrTiO_3$ location 2.

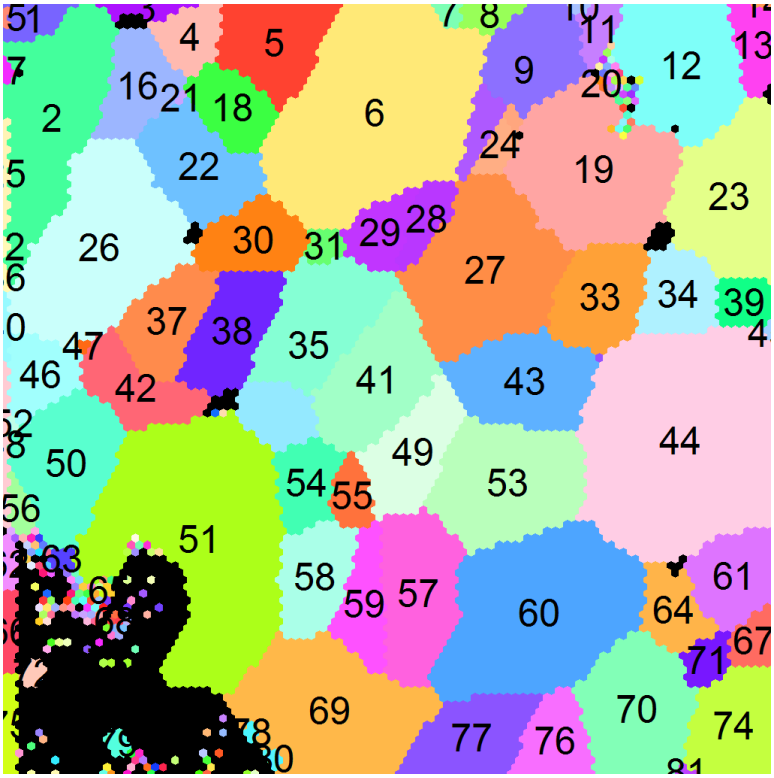

EBSD orientation map of $BaSrTiO_3$ location 2.

REFERENCES

[1] M.W. Barsoum, Fundamentals of Ceramics, IOP Publishing Ltd, 2003. doi:10.1887/0750309024.

[2] Global Ceramic Capacitor Market - Forecasts From 2018 to 2023, Knowl. Sourc. Intell. LLP. (2018) 104. https://www.researchandmarkets.com/research/zqw6fj/global_ceramic?w=4.

[3] Y.-M. Chiang, D.P. Birnie, W.D. Kingery, Physical Ceramics: Principles for Caramic Science and Engineering, 1st ed., John Wiley & Sons, Inc., 1997.

[4] E.I. Ltd., Observing Phase Transitions in a Halide Perovskite Using Temperature Dependent Photoluminescence Spectroscopy, Edinburgh Instruments. (n.d.). https://www.edinst.com/phase-transitions-halide-perovskite/.

[5] N. Rahaman, M., Ceramic processing and sintering, Int. Mater. Rev. 41 (1996) 36–37. doi:10.1179/095066096790151286.

[6] S.-J.L. Kang, Sintering: Densification, Grain Growth and Microstructure, Elsevier, 2004. doi:10.1016/B978-0-7506-6385-4.50000-5.

[7] A.P. Sutton, R.W. Balluffi, Interfaces in Crystalline Materials, Oxford University Press, 2007.

[8] C. HERRING, Some Theorems on the Free Energies of Crystal Surfaces, Phys. Rev. 82 (1951) 87–93.

[9] J.W. Cahn, D.W. Hoffman, A Vector Thermodynamics for Anisotropie Surfaces, Surf. Sci. 31 (1972) 368.

[10] D.A. Porter, K.E. Easterling, Phase Transformations in Metals and Alloys, 2nd ed., Springer US, Boston, MA, 1992. doi:10.1007/978-1-4899-3051-4.

[11] D. Wolf, A broken-bond model for grain boundaries in face-centered cubic metals, J. Appl. Phys. 68 (1990) 3221–3236. doi:10.1063/1.346373.

[12] G.S. Rohrer, V. Randle, Measurement of the Five-Parameter Grain Boundary Distribution from Planar Sections, in: Electron Backscatter Diffr. Mater. Sci., Springer US, Boston, MA, 2009: pp. 215–229. doi:10.1007/978-0-387-88136-2_16.

[13] J.E. Burke, D. Turnbull, Recrystallization and grain growth, Prog. Met. Phys. 3 (1952) 220–292. doi:10.1016/0502-8205(52)90009-9.

[14] M. Kitayama, A.M. Glaeser, The Kinetics of Pore Shape Evolution in Alumina, 6 (1998) 161–167. doi:10.4028/www.scientific.net/KEM.159-160.193.

[15] J.W. Cahn, The impurity-drag effect in grain boundary motion, Acta Metall. 10 (1962) 789–798. doi:10.1016/0001-6160(62)90092-5.

[16] J.D. Powers, A.M. Glaeser, Grain Boundary Migration in Ceramics, Interface Sci. 6 (1998) 23–39. doi:10.1023/A:1008656302007.

[17] C.H. Hsueh, A.G. Evans, R.L. Coble, Microstructure development during final/intermediate stage sintering—I. Pore/grain boundary separation, Acta Metall. 30 (1982) 1269–1279. doi:10.1016/0001-6160(82)90145-6.

[18] S.J. Dillon, M.P. Harmer, Diffusion Controlled Abnormal Grain Growth in Ceramics, Mater. Sci. Forum. 558–559 (2007) 1227–1236. doi:10.4028/www.scientific.net/MSF.558-559.1227.

[19] S.J. Dillon, M.P. Harmer, Multiple grain boundary transitions in ceramics: A case study of alumina, Acta Mater. 55 (2007) 5247–5254. doi:10.1016/j.actamat.2007.04.051.

[20] Z.X. Wu, Y.W. Zhang, D.J. Srolovitz, Grain boundary finite length faceting, Acta Mater. 57 (2009) 4278–4287. doi:10.1016/j.actamat.2009.05.026.

[21] P.R. Cantwell, M. Tang, S.J. Dillon, J. Luo, G.S. Rohrer, M.P. Harmer, Grain boundary complexions, Acta Mater. 62 (2014) 1–48. doi:10.1016/j.actamat.2013.07.037.

[22] S.M. An, B.K. Yoon, S.Y. Chung, S.J.L. Kang, Nonlinear driving force-velocity relationship for the migration of faceted boundaries, Acta Mater. 60 (2012) 4531–4539. doi:10.1016/j.actamat.2012.05.006.

[23] H. Sternlicht, W. Rheinheimer, M.J. Hoffmann, W.D. Kaplan, The mechanism of grain boundary motion in SrTiO3, J. Mater. Sci. 51 (2015). doi:10.1007/s10853-015-9058-1.

[24] W. Rheinheimer, M. Bäurer, H. Chien, G.S. Rohrer, C.A. Handwerker, J.E. Blendell, M.J. Hoffmann, The equilibrium crystal shape of strontium titanate and its relationship to the grain boundary plane distribution, Acta Mater. 82 (2015) 32–40. doi:10.1016/j.actamat.2014.08.065.

[25] A.P. Sutton, R.W. Balluffi, Overview no. 61 On geometric criteria for low interfacial energy, Acta Metall. 35 (1987) 2177–2201. doi:10.1016/0001-6160(87)90067-8.

[26] G.S. Rohrer, Grain boundary energy anisotropy : a review, (2011) 5881–5895. doi:10.1007/s10853-011-5677-3.

[27] D.M. Saylor, B. El Dasher, T. Sano, G.S. Rohrer, Distribution of Grain Boundaries in SrTiO 3 as a Function of Five Macroscopic Parameters, J. Am. Ceram. Soc. 76 (2004) 670–676.

[28] D.M. Saylor, A. Morawiec, G.S. Rohrer, Distribution of grain boundaries in magnesia as a function of five macroscopic parameters, Acta Mater. 51 (2003) 3663–3675. doi:10.1016/j.actamat.2004.04.018.

[29] J.E. Blendell, W.C. Carter, C. a Handwerker, Faceting and wetting transitions of anisotropic interfaces and grain boundaries, J. Am. Ceram. Soc. 82 (1999) 1889–1900. doi:10.1111/j.1151-2916.1999.tb02013.x.

[30] J.S. Wettlaufer, M. Jackson, M. Elbaum, A geometric model for anisotropic crystal growth, J. Phys. A. Math. Gen. 27 (1994) 5957–5967. doi:10.1088/0305-4470/27/17/027.

[31] M. Kitayama, T. Narushima, W.C. Carter, R.M. Cannon, A.M. Glaeser, The Wulff Shape of Alumina: I, Modeling the Kinetics of Morphological Evolution, J. Am. Ceram. Soc. 83 (2000) 2561–2531. doi:10.1111/j.1151-2916.2000.tb01591.x.

[32] J. W. Cahn, C. A. Handwerker, Equilibrium geometries of anisotropic surfaces and interfaces, Mater. Sci. Eng. A. 162 (1993) 83–95. doi:10.1016/0921-5093(90)90032-X.

[33] M. FUJIMOTO, W.D. KINGERY, Microstructures of SrTiO3 Internal Boundary Layer Capacitors During and After Processing and Resultant Electrical Properties, J. Am. Ceram. Soc. 68 (1985) 169–173. doi:10.1111/j.1151-2916.1985.tb15292.x.

[34] M. Bäurer, D. Weygand, P. Gumbsch, M.J. Hoffmann, Grain growth anomaly in strontium titanate, Scr. Mater. 61 (2009) 584–587. doi:10.1016/j.scriptamat.2009.05.028.

[35] S.J. Dillon, M. Tang, W.C. Carter, M.P. Harmer, Complexion: A new concept for kinetic engineering in materials science, Acta Mater. 55 (2007) 6208–6218. doi:10.1016/j.actamat.2007.07.029.

[36] W. Rheinheimer, M.J. Hoffmann, Grain growth in perovskites: What is the impact of boundary transitions?, Curr. Opin. Solid State Mater. Sci. (2016). doi:10.1016/j.cossms.2016.04.004.

[37] S.B. Lee, N.M. Hwang, D.Y. Yoon, M.F. Henry, Grain boundary faceting and abnormal grain growth in nickel, Metall. Mater. Trans. A. 31 (2000) 985–994. doi:10.1007/s11661-000-1016-z.

[38] S.B. Lee, W. Sigle, W. Kurtz, M. Rühle, Temperature dependence of faceting in Σ5(310)[001] grain boundary of SrTiO3, Acta Mater. 51 (2003) 975–981. doi:10.1016/S1359-6454(02)00500-1.

[39] B.K. Lee, S.Y. Chung, S.J.L. Kang, Grain boundary faceting and abnormal grain growth in BaTiO3, Acta Mater. 48 (2000) 1575–1580. doi:10.1016/S1359-6454(99)00434-6.

[40] Y. Jung, S. Choi, S.L. Kang, Grain-Growth Behavior during Stepwise Sintering of Barium Titanate in Hydrogen Gas and Air, 30 (2003) 2228–2230.

[41] S.Y. Choi, S.J.L. Kang, Sintering kinetics by structural transition at grain boundaries in barium titanate, Acta Mater. 52 (2004) 2937–2943. doi:10.1016/j.actamat.2004.02.039.

[42] S.M. Wang, S.J.L. Kang, Effect of grain boundary structure on diffusion-induced grain boundary migration in BaTiO 3, J. Am. Ceram. Soc. 88 (2005) 3267–3269. doi:10.1111/j.1551-2916.2005.00586.x.

[43] W. Rheinheimer, M.J. Hoffmann, Grain growth transitions of perovskite ceramics and their relationship to abnormal grain growth and bimodal microstructures, J. Mater. Sci. 51 (2015) 1756–1765. doi:10.1007/s10853-015-9535-6.

[44] J. Liou, M. Lin, H. Lu, Crystallographic Facetting in Sintered Barium Titanate, J. Am. Ceram. Soc. 85 (2002) 2931–2937. doi:10.1111/j.1151-2916.2002.tb00558.x.

[45] E.N. Bunting, G.R. Shelton, A.S. Creamer, Properties of Barium-Strontium Titanate Dielectrics, Am. Ceram. Soc. 30 (1947) 114–125. doi:10.1111/j.1151-2916.1947.tb18879.x.

[46] K. Gomann, G. Borchardt, A. Gunhold, W. Maus-Friedrichs, H. Baumann, Ti diffusion in La-doped SrTiO3 single crystals, Phys. Chem. Chem. Phys. 6 (2004) 3639–3644. doi:10.1002/chin.200441016.

[47] Y. Tsur, T.D. Dunbar, C.A. Randall, Crystal and Defect Chemistry of Rare Earth Cations in BaTiO 3, J. Electroceramics. 7 (2001) 25–34.

[48] M. Bäurer, S.-J. Shih, C. Bishop, M.P. Harmer, D.J.H. Cockayne, M.J. Hoffmann, Abnormal grain growth in undoped strontium and barium titanate, Acta Mater. 58 (2010) 290–300. doi:10.1016/j.actamat.2009.09.007.

[49] W. Rheinheimer, M. Bäurer, C.A. Handwerker, J.E. Blendell, M.J. Hoffmann, Growth of single crystalline seeds into polycrystalline strontium titanate: Anisotropy of the mobility, intrinsic drag effects and kinetic shape of grain boundaries, Acta Mater. 95 (2015) 111–123. doi:10.1016/j.actamat.2015.05.019.

[50] S. Lee, C.A. Randall, Z.K. Liu, BaO-TiO2 Phase Diagram, (2007) PED:12443.

[51] M. Drys, W. Trzebiatowski, SrO-TiO2 Phase Diagram, (1957) PED:297.

[52] J.-H. Choi, D.-Y. Kim, B.J. Hockey, S.M. Wiederhorn, C. a. Handwerker, J.E. Blendell, W.C. Carter, A.R. Roosen, Equilibrium Shape of Internal Cavities in Sapphire, J. Am. Ceram. Soc. 80 (1997) 62–68. doi:10.1111/j.1151-2916.1997.tb02791.x.

[53] R. Edwin García; John Blendell, Equilibrium Wulff Shape Generator, (2014). doi:10.4231/D3C53F234.

[54] M. Jin, E. Shimada, Y. Ikuma, Grain boundary grooving by surface diffusion in SrTiO3 bicrystal, 14 (1998) 2548–2553.

[55] D.A. Lowing, MICROSTRUCTURAL EVOLUTION IN NiO-MgO : LINKING EQUILIBRIUM CRYSTAL SHAPE AND GRAIN GROWTH, Purdue University, 2018.

[56] S.J. Dillon, M.P. Harmer, Comment on “effect of interface structure on the microstructural evolution of ceramics,” J. Am. Ceram. Soc. 90 (2007) 2291–2292. doi:10.1111/j.1551-2916.2007.01655.x.

[57] I.-J. Bae, S. Baik, Abnormal Grain Growth of Alumina, J. Am. Ceram. Soc. 80 (1997) 1149–1156. doi:10.1111/j.1151-2916.1997.tb02957.x.

[58] E.A. Holm, S.M. Foiles, How grain growth stops: A mechanism for grain-growth stagnation in pure materials, Science (80-.). 328 (2010) 1138–1141. doi:10.1126/science.1187833.

[59] H. Kishi, Y. Mizuno, H. Chazono, Base-metal electrode-multilayer ceramic capacitors: Past, present and future perspectives, Japanese J. Appl. Physics, Part 1 Regul. Pap. Short Notes Rev. Pap. 42 (2003) 1–5. doi:10.1143/JJAP.42.1.

[60] D. Liu, NEPP Capacitor Update - BME Technology for High- Reliability Applications, Nasa.Gov. (n.d.) 26. nepp.nasa.gov (accessed February 7, 2019).

[61] L. Smith, T. Ibn-Mohammed, S.C.L. Koh, I.M. Reaney, Life cycle assessment and environmental profile evaluations of high volumetric efficiency capacitors, Appl. Energy. 220 (2018) 496–513. doi:10.1016/j.apenergy.2018.03.067.

[62] S.O. Ojoawo, A.A. Gbadamosi, Application of TRACI and CML Modeling Tools in Life Cycle Impact Assessment of Municipal Wastes, J. Environ. Prot. (Irvine,. Calif). 04 (2013) 602–617. doi:10.4236/jep.2013.46070.

[63] E. Wolan-Sosna, Chloride TiO2 better than sulfate?, Eur. Coat. J. 49 (2002). http://www.european-coatings.com/Editorial-archive/Chloride-TiO2-better-than-sulfate.

[64] E. Chynoweth, France proposes carcinogen 1B classification for titanium dioxide, Chem. Watch. (2015). https://chemicalwatch.com/43791/france-proposes-carcinogen-1b-classification-for-titanium-dioxide.

[65] EFSA, EFSA statement on the review of the risks related to the exposure to the food additive titanium dioxide (E 171) performed by the French Agency for Food , Environmental and Occupational Health and Safety (ANSES), 17 (2019). doi:10.2903/j.efsa.2019.5714.

[66] M. Chen, J. Wang, H. Chen, O.A. Ogunseitan, M. Zhang, H. Zang, J. Hu, Electronic waste disassembly with industrial waste heat, Environ. Sci. Technol. 47 (2013) 12409–12416. doi:10.1021/es402102t.